Performance Evaluation for Future Wireless Communication Systems: Sensing Services and Intelligent Reflecting Surfaces

A thesis submitted to the University of Manchester for the degree of

Doctor of Philosophy

in the Faculty of Science and Engineering

2022

Mohammad A. Al-Jarrah

Department of Electrical and Electronic Engineering

Contents

The word count is approximately 48547.

List of Figures

List of Tables

List of Abbreviations

3GPP Third Generation Partnership Project

4G Fourth Generation

5G-NR Fifth Generation-New Radio

A2A Air-to-Air

AOA Angle of Arrival

ASK Amplitude Shift Keying

BER Bit Error Rate

BPSK Binary Phase Shift Keying

BS Base Station

BSC Binary Symmetric Channel

CG Connected Graph

CHD Cluster Head

CRLB Cramer-Rao Lower Bound

CSI Channel Side Information

CUE Communication User Equipment

CV Chair-Varshney

DFKF Distributed Fusion Kalman Filter

EB ExaByte

EC European Commission

ENN Energy Neutral Network

ESR Early Stage Researcher

ETN European Training Network

ETSI European Telecommunications Standards Institute

FC Fusion Center

FIRS Flying Intelligent Reflecting Surface

FN Furthest Neighbor

FR Fusion Rule

FSO Free Space Optical

Gbps Giga Bit per Second

GPS Global Positioning System

GU Ground User

HAA High Altitude Airship

HD Hard Decision

HDE Hard Decision Estimaator

IAB Integrated Access and Backhaul

ILA Individual Likelihood Approximation

ILS Ideal Local Sensor

IM Index Modulation

IoT Internet of Things

IRS Intelligent Reflecting Surface

ISAC Integrated Sensing And Communication

ISI Inter Symbol Interference

ITN Innovative Training Networks

KLD Kullback-Leibler Distance

KNN k Nearest Neighbor

LA-UAV Low Altitude Unmanned Aerial Vehicles

LAD Low Altitude Drone

LEC Localization with Error Concealment

LLR Log-Likelihood Ratio

LoRaWAN Long-Range Wide Area Network

LoS Line of Sight

LRT Likelihood Ratio Test

LS Least Square

LSCE Least Square Channel Estimator

LTE Long Term Evolution

LVA Local Voting Algorithm

LWA Leaky Wave Antenna

MAC Medium Access Control

MAR Major Axis Regression

mBS Macro Base Station

MIMO Multiple Input Multiple Output

MINLP Mixed Integer Nonlinear Program

ML Maximum Likelihood

MLD Maximum Likelihood Detection

MLE Maximum Likelihood Estimation

MLR Maximum Local Rate

mMIMO Massive Multiple Input Multiple Output

mmWave Millimtere Wave

MR Mobile Robot

MRT Maximum Ratio Transmission

MSCA Marie Skodowska-Curie Actions

MSE Mean Square Error

MU-MIMO Multi User Multiple Input Multiple Output

MVA Majority Voting Algorithm

NB-IoT Narrow Band Internet of Things

NCD Noncoherent Detection

NeDe Network Densification

NN Nearest Neighbor

NOMA Nonorthogonal Multiple Access

OP Outage Probability

OTFS Orthogonal Time Frequency Space

PA Position Aware

PAINLESS Portable Access Points for Infrastructure-less

PDF Probability Density Function

PHY Physical

PIN Positive Intrinsic Negative

PMF Probability Mass Function

POA Phase of Arrival

PSO Particle Swarm Optimization

QoS Quality of Service

QPSK Quadrature Phase Shift Keying

Radcom Radar-Communication

RB Resource Block

RE Relative Entropy

RF Radio Frequency

RFID Radio Frequency Identification

RIS Reader Interrogation Signal

RMSE Root Mean Square Error

RoI Region of Interest

RSMA Rate Splitting Multiple Access

RSS Received Signal Strength

RSSI Received Signal Strength Indication

Rx Receiver

RxBS Receive Base Station

SAT Sinusoidal Addition Theorem

sBS Small Base Station

SC-FDMA Single Carrier Frequency Division Multiple Access

SDE Soft Decision Estimator

SDP Semidefinite Programming

SER Symbol Error Rate

SINR Signal-to-Interference Noise Ratio

SNR Signal-to-Noise Ratio

SPRT Sequential Probability Ratio Test

SSK Space Shift Keying

SWIPT Simultaneous Wireless Information and Power Transfer

TDMA Time Division Multiple Access

TDOA Time Difference of Arrival

THz Tera Hertz

TIP Telecom Infra Project

TOA Time of Arrival

Tx Transmitter

TxBS Transmit Base Station

UAV Unmanned Aerial Vehicles

UDPN Unit Disk Planar Network

UE	User Equipment
UHF	Ultra High Frequency
URLLC	Ultra Reliable Low Latency Communication
VLC	Visible Light Communications
WAN	Wide Area Network
WF	Wireless First
WLAN	Wireless Local Area Network
WSN	Wireless Sensor Network
WSRE	Weighted Sum of Relative entropy
ZF	Zero Forcing

List of Mathematical Symbols

$\mathcal{N}(\cdot)$	Normal Distribution
$\Pr(\cdot)$	Probability Function
$\mathrm{E}(\cdot)$	Expected Value
$\mathrm{Var}(\cdot)$	Variance Operator
$\Pr(\cdot\|\cdot)$	Conditional Probability Function
$\mathcal{CN}(\cdot)$	Complex Normal Distribution
$\Re(\cdot)$	Real Part Operator
$\Im(\cdot)$	Imaginary Part Operator
$\ln(\cdot)$	Natural Logarithm
$\log(\cdot)$	Logarithm Function
$\sum$	Summation Operator
$\prod$	Product Operator
argmin	The Argument of the Minimum Function
argmax	The Argument of the Maximum Function
$(\cdot)^*$	Complex Conjugate
$\mathbf{X}^{\mathrm{H}}$	Hermitian of Matrix X
$\mathbf{X}^{\mathrm{T}}$	Transpose of Matrix X
$\mathbf{I}$	Identity Matrix
$\exp(\cdot)$	Exponential Function
$\mathrm{erf}(\cdot)$	Error Function

$\mathrm{erfc}(\cdot)$	Complementary Error Function
$Q(\cdot)$	Complementary Cumulative Distribution Function for Normal Distribution
$\hat{X}$	Estimate of X
$\bar{X}$	Average of X
∇	Gradient Operator
$\frac{\partial y}{\partial x_R}$	Partial Derivative of y with Respect to x
$J_m(\cdot)$	Bessel Function of the First Kind and Order m
$I_m(\cdot)$	Modified Bessel Function of the First Kind and Order m
$\mathcal{K}_{(m)}(\cdot)$	Modified Bessel Function of the Second Kind and Order m
$Q_m(\cdot,\cdot)$	mth Order Marcum Q-Function
$\mathcal{D}_{(\cdot)}(\cdot)$	Parabolic Cylinder Function
$\mathrm{B}(\cdot,\cdot)$	Beta Function
$\binom{\cdot}{\cdot}$	Binomial Coefficient
$f_X(x)$	The Probability Density Function of Random Variable x
$\lvert\cdot\rvert$	Absolute Value
$\Psi(\cdot)$	Digamma Function
$\mathrm{tr}(\cdot)$	Trace Operator
$(\cdot)!$	Factorial Operator
$(\cdot)!!$	Double Factorial Operator
$\mathrm{diag}(\cdot)$	Diagonal Matrix
$\Gamma(\cdot)$	Gamma Function
$\Gamma(\cdot,\cdot)$	Upper Incomplete Gamma Function
$\mathrm{GG}(\cdot,\cdot,\cdot)$	Generalized Gamma Distribution
$\mathrm{Gamma}(\cdot,\cdot)$	Gamma Distribution
$\mathcal{X}_2^2(\cdot)$	Noncentral Chi Squared Distribution
$\lVert\cdot\rVert$	Euclidian Norm

${}_{(\cdot)}F_{(\cdot)}(\cdot;\cdot;\cdot)$	Hypergeometric Function
$\mathcal{W}_{(\cdot,\cdot)}(\cdot)$	Whittaker Hypergeometric Function
$G^{(\cdot,\cdot)}_{(\cdot,\cdot)}\left(\cdot\middle\vert^{\cdot}_{\cdot,\cdot,\cdot}\right)$	Meijer G Function
$\sin(\cdot)$	Sine Trigonometric Function
$\cos(\cdot)$	Cosine Trigonometric Function
$\tan(\cdot)$	Tangent Trigonometric Function
$\arcsin(\cdot)$	Inverse Sine Function
$\arccos(\cdot)$	Inverse Cosine Function
$\arctan(\cdot)$	Inverse Tangent Function

Abstract

The deployment of small-size, low-cost and efficient internet-of-things (IoT) sensors has been growing rapidly to serve several applications like health monitoring, autonomous cars, spectrum sensing, environment monitoring, etc. As a result, there is a persistent need for efficient signal processing tools to efficiently make use of sensory data. As well as, the demands on low-energy and ultra high data rate telecommunication are obviously increasing, which considerably has led to increase the pressure on the existing backhaul links. Thus, adequate spectral and energy efficient communication technologies and network paradigms are required for current and future communications. Therefore, in this thesis, two emerging technologies in the areas of signal processing and wireless communications are explored, namely; sensing services and intelligent reflecting surfaces (IRSs) as a prominent technology for wireless backhauling.

Several aspects of wireless sensor networks (WSNs) and IoT are explored including target localization using radio frequency identification (RFID) network, decision fusion of multiple sensors, and integrated sensing and communication system (ISAC). Decision fusion rules and localization methods using a network of sensors and RFID tags are proposed, investigated and analyzed. The obtained results show the effectiveness of these proposed fusion rules and location estimators. Moreover, for ISAC system, a unified performance evaluation is introduced based on Kullback-Leibler divergence theorem, or so called the relative information theorem, where results clearly confirm that the relative information can efficiently characterize ISAC systems holistically.

Furthermore, the performance of IRS based communications is evaluated and their use in multi-hop wireless backhauling is explored. Multi-hop terrestrial backhauling is introduced first, where a small base-station communicating with a macro base-station through a number of small base-stations. The line-of-sight path between the small base-stations is dropped and communication takes place through IRS panels which provide virtual line-of-sight and thus the link is modeled using Rician channel. The bit error rate and outage probability are derived for the introduced system model and random number of hops is also considered. As well as, a multi-layer unmanned aerial vehicles (UAV) network is considered, in which an IRS panel is attached to a high altitude platform and provide line-of-sight paths to low altitude UAVs. Imperfect channel estimation and phase compensation at IRS are considered, and the bit error rate, outage probability and ergodic capacity are derived. Simulation and theoretical results are provided for the introduced system models and the performance limits are presented and investigated. Obtained results depicts a perfect match between the analysis and simulation when the number of reflectors is considerable, we well as the performance improvement gained by deploying IRS is shown.

Declaration

No portion of the work referred to in this thesis has been submitted in support of an application for another degree or qualification of this or any other university or other institute of learning.

Copyright

Acknowledgements

I would like to express my sincere appreciation to my supervisor, Dr Emad Alsusa, for his continuous guidance and inspiration through my PhD. His rich expertise, solid knowledge, enthusiasm and dedication to state-of-the-art research have remarkably contributed to my PhD and research career. I would like also to thank Dr A. Al-Dweik from Khalifa University for his cooperation and advice, in addition to fruitful discussions and constructive feedback.

I am delighted to know many friends and colleagues in the microwave and communications research group at The University of Manchester, as well as, the collaborative Early Stage Researchers (ESRs) of PAINLESS project . I appreciate all the refreshing times and scientific discussions we had while working on our research.

Furthermore, I would like to highlight that this work was supported by the European Union's Horizon 2020 Research and Innovation Programme through the Marie Sklodowska-Curie under Grant 812991.

Dedication

I dedicate this thesis to my parents, wife and daughter for their continuous support and encouragement.

Chapter 1

Introduction and Background

The increasing demands on modern telecommunication services such as high data rate and low latency services have created new challenges for network operators. Moreover, the network operators are expected to handle a tremendous number of connected Internet-of-Things (IoT) devices which typically have limited computational capabilities and operate with low energy consumption. Therefore, the deployment of energy and spectrally efficient wireless network solutions is indispensable. The work presented in this thesis represents my contributions to the Marie Sklodowska-Curie Innovative Training Networks (ITNs) on energy-autonomous portable access points for infrastructure-less networks (PAINLESS).

1.1 PAINLESS Project

The new advances in renewable sources of energy like solar, wind, and thermal sources, in addition to radio frequency (RF) energy harvesting, have created the potential for researchers to think about self-powered telecommunication networks [1,2]. PAINLESS was launched in 2018 by Horizon-2020-Marie Skłodowska-Curie actions (H2020-MSCA). The project aims to establish a platform for research and training for these kinds of networks in order to satisfy future demands with low dependency on the existing infrastructure. The main features of the nodes in PAINLESS network are their being pioneer green nodes, self-subsistent and limitlessly-scalable [3]. Fig. 1.1 shows a block diagram for the PAINLESS project. The PAINLESS project targets different practical indoor and outdoor scenarios including

1. Outdoor broadband access which is concerned in capacity and range extension in urban, sub-urban and rural areas, in addition to special and emergency events such as sports arenas, concerts, traffic jams, train accidents, etc.

2. Indoor broadband access such as public indoor access and large indoor areas such as special events, subways, malls, etc.

3. Outdoor massive IoT and large scale wireless sensor networks (WSNs).

4. Indoor ultra reliable low latency communication (URLLC) such as factory floors and indoor logistics.

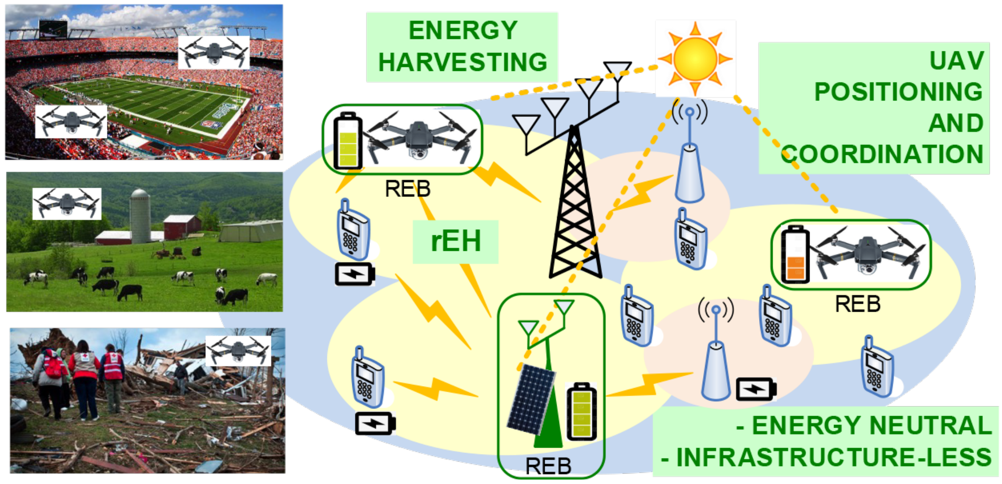

Figure 1.1: A block diagram for PAINLESS project.

Moreover, the objectives of PAINLESS project can be summarized in

1. The development and integration of energy and spectral efficient solutions into the wireless transmission (access/backhauling) and resource allocation of telecommunications networks.

2. The establishment of theoretical performance benchmarks for the combined power-and-information distribution in communication networks.

3. The development of innovative optimization and signal processing algorithms for the wide range of unmanned aerial vehicles (UAV) oriented networks, and introducing new communication paradigms and wireless solutions which guarantee efficient deployment for UAV networks.

4. The design of joint power-and-information management technologies.

5. The performance evaluation and design of efficient IoT and sensing networks paradigms and providing powerful signal processing algorithms.

6. The proof-of-concept demonstration of self-powered access points.

As can be noticed from Fig. 1.1 and the discussion above, several networking aspects are under the consideration of this project. For example, the project considers energy efficient backhauling, cells planning, energy neutrality, solar energy harvesting, and UAVs positioning and coordination. There are 16 early stage researchers (ESRs) who have been working on the project from different academic and industrial institutions around Europe, where each group of ESRs collaborated to contribute in certain parts of the project. The main interest of this thesis can be summarized as

1. The design and performance evaluation of reliable algorithms applicable for cooperative spectrum sensing in cognitive radio networks (CRNs) as CRNs are effective for utilizing the available bandwidth.

2. The design and analysis of efficient localization algorithms applicable for indoor radio frequency identification (RFID) networks.

3. The design and analysis of decision fusion rule for outdoor IoT-WSNs.

4. The development of unified theoretical performance framework for integrated sensing and communication (ISAC) systems.

5. The employment of new wireless solutions for wireless backhauling including the intelligent reflecting surfaces (IRSs) and the deployment of UAVs.

6. Performance evaluation for the performance of multi-hop networks including IRSs and UAV-IRS through providing derivations for the error rate, outage probability, and achievable capacity.

1.2 Background and Brief Review

My work in the PAINLESS project encompassed a number of topics as listed below. My contribution on these topics was concerned in introducing signal processing algorithms for WSNs applications, evaluating the performance of the introduced algorithms, and providing performance analysis for different system configurations in the presence of practical impairments. In the following, a brief background will be provided on each of these topics.

The request on sensing applications has been growing in the last few decades. Nowadays, sensing devices are widely implemented as an integral part in many today's applications including military and civilian applications. Examples for civilian applications in which sensors play a significant role include smart farms, smart cities, factories, medical applications, environment monitoring, spectrum sensing, etc. For more efficient utilization of sensors, WSNs, which mainly consist of large number of sensors deployed in the area of interest, have been adopted in many fields to add more mobility and flexibility to the considered application. Moreover, with the new advances in the development of IoT infrastructure, the functionality of WSNs has been expanded as sensory data can be processed globally over the internet cloud. With IoT-WSNs, a massive number of low-cost and low-power devices, such as sensors, actuators, smart meters, etc, can be easily accessed, monitored and controlled remotely. More recent studies have adopted the integration between sensing and data communication services, and thus it is expected that network operators will start providing both services in the future. Consequently, this PhD thesis explores a few sensing services such as cooperative spectrum sensing, target localization, decision fusion and ISAC.

The problem of target detection and localization using WSNs has been of interest for few decades. More recent works considered the localization problem using a network of RFID tags which has received a great deal of attention in the literature. For instance, a system to localize a mobile robot equipped with RFID reader sensors using a set of tags attached on the ceiling has been proposed in [9]. In [10], the received signal strength indicator (RSSI) measurements obtained by a set of passive RFID tags have been exploited for localization and tracking of an RFID reader to enhance the accuracy of localization. Directional antennas based localization method has been introduced in [11], where a novel particle swarm optimization (PSO) was applied. In addition, recursive Kalman filter has been considered in [12] to design a new localization and tracking algorithm aiming at minimizing the error in least squares sense, and a Bayesian filter has been employed in [13] with constant transmission power in order to localize RFID tags.

Generally speaking, WSN typically consists of large number of sensors distributed over a region and collects observations about the same phenomenon or a number of phenomena. Therefore, data obtained by different sensors are required to be jointly processed in order to obtain a final, or global, decision about the phenomena under interest. The process of combining and processing decisions taken from different sensors is called decision fusion. Several fusion rules (FRs) have been introduced in the literature for conventional WSNs, which can be also applicable for IoT infrastructure. For instance, the likelihood ratio test (LRT) under the Neyman-Pearson sense has been introduced in [14–16] to establish an optimum FR. However, the optimum rule suffers from considerable computational complexity which makes it impractical for applications in which network resources are limited. Therefore, researchers have dedicated their efforts to derive suboptimal FRs which have less computation complexity at the expense of performance. For example, as shown in [14] and [15], the Chair-Varshney suboptimal rule has been introduced and it has been shown that the probability of error performance asymptotically approaches the optimum fusion at high signal-to-noise ratios (SNRs). Moreover, other low-complexity FRs such as AND, OR, k out of N and majority voting rules, can be derived from the Chair-Varhsney rule by assuming identical sensors [17–19]. Although these rules have relatively low-complexity and do not depend on the local sensors' performance, their performance is worse than the Chair-Varshney rule, particularly when dissimilar sensors are used. Furthermore, the MaxLog rule has been proposed in [16] which generally provide better detection capabilities than the Chair-Varhsney rule, yet, it does not guarantee reliable performance for all system and channel conditions. Other rules based on diversity combining, such as the maximum ratio combining and equal gain combining, have been introduced and investigated in the literature as extremely low-complexity FRs; however, the required detection capability is not guaranteed [20].

More recently, the literature has proposed to promote the functionality of multiple-input-multiple-output (MIMO) base-stations for introducing sensing services in addition to the communication duties by exploiting the new development of multi-beam antenna arrays and/or by allocating some of the base-station resources for sensing services [21–24]. Two possible scenarios have been explored in the literature. The first one is referred to separated deployment, where the base-station antennas are distributed among each of the two sub-systems. On the other hand, all antennas are exploited for both sub-systems for the other scenario which is known as the shared deployment. Several designs for the signal waveforms and beampatterns can be found in [21–24] which aim at satisfying the requirements of communication users' rates and detection capability of the radar sub-system. A comprehensive survey for the employed signal processing tools in ISAC systems can be found in [25] for three possible scenarios, namely, radar-centric, communication-centric and joint design.

On the other hand, wireless backhauling is an integral technology of current and future generations of communication networks such as 6G and beyond. The main advantages of wireless backhauling over traditional wired backhauling include the ease, speed and low-cost of deployment and maintenance. Therefore, it has attracted researchers from both the business and academic sectors to propose solutions for efficient backhauling. For instance, Telecom Infra Project (TIP), which consists of more than 500 member organizations, has launched to accelerate the development of new solutions for future networks infrastructures [26]- [33].

Wireless backhauling can be achieved with several network topologies such as ring, tree and mesh; though the later is the most attractive because it provides backhauling with low-cost, flexible configuration, maintainable, and long distance coverage [34]- [37]. In general, wireless backhauling suffers from some limitations compared to optical fibres, such as, low capacity and disruptive interference. Therefore, several solutions haven been proposed to overcome these limitations such as millimeter-wave (mmWave) and free-space optical (FSO) signalling, as well as interference management protocols [38]- [40]. Some work has considered mixed radio RF-FSO links to combine the advantages of both communication technologies [41], [42]. Other technologies introduced in the literature to enhance wireless telecommunications in general include massive MIMO (mMIMO), visible light communications (VLCs), and network densification [43]- [60]. It is worthy to mention that the European Telecommunications Standards Institute (ETSI) and TIP backhaul group recommend the mmWave communications as a core technology [26], [27], [31]. Realistic experiments have been conducted for 1 giga bits per second (Gbps) average peak user throughput for a maximum range of 250 m [27]. In addition, the TIP backhaul team has proposed different methods for assessing the performance of mmWave, and provided a guidance for the installation process [32], [33].

A multihop wireless network is promising for wireless backhauling scheme, where it can provide reliable and flexible solution. In addition, advanced physical (PHY) layer technologies such as power control, resources allocation, rate control, and beamforming schemes can be emerged to satisfy the quality-of-service (QoS), and scalability [61]- [66]. In [61], a novel pricing-based rate allocation scheme is proposed for optical-wireless hybrid networks aiming at serving users with certain satisfaction levels and pricing affordability. The maximization of energy efficiency by user association, power and backhaul flow control is considered in [62]. The downlink of millimeter wave scenario is considered for backhaul heterogeneous networks, and the optimization problem is formulated using mixed-integer non-linear programing. In [63], resources allocation and power control are jointly optimized in cooperative small cell networks with constrained backhaul capacity by using sequential optimization algorithm. The problem of minimizing the energy consumption is formulated in [64] through concurrent transmission scheduling and power control. In this work, a mixed integer nonlinear program (MINLP) is applied, and then, an energy-efficient and practical mmWave backhauling scheme is developed. In [65], a heterogeneous network topology is presented, where the backhaul links are supported by mMIMO systems with full-duplex modes. Moreover, several routing protocols are proposed in the literature for multihop backhauling aiming at improving the connectivity and provide reliable backhaul access [67], [68]. In [67], the benefits of applying the software-define-radio is exploited for multihop wireless networks. A routing protocol for joint path selection and rate allocation is proposed in [68]. Reinforcement learning techniques are used in this work, and the successive convex approximation is used to convert the optimization problem to convex one.

Recent literature has considered UAVs to assist base-stations (BSs) and improve the quality of wireless backhauling due to their mobility and flexibility [69]- [74]. Spectrum allocation for a backhaul assisted by UAV is studied, and the achievable rate is optimized in [69]. In [70], UAVs are deployed as aerial relays to allow dynamic routing for mmWave signals while mitigating the impact of occlusions on the terrestrial links. The use of UAV as a BS with delay-sensitive and delay-tolerant users is investigated in [71]. The bandwidth, link rate and power are jointly optimized to guarantee the QoS requirements for the users. The optimal position of the UAV and resources allocation algorithms are proposed in [72]. In [73], the fixed-wing UAV is considered for providing wireless services to ground users, where dynamic allocation algorithm for the available resources is proposed. The authors in [74] have studied the improvement of the achievable end-to-end data rate of ground users assisted by UAVs and tethered balloons. The authors in [75] address the optimization of backhaul framework is considered, where multiple UAVs are deployed to configure the backhaul links for terrestrial BSs. The downlink throughput in mixed RF/FSO backhaul networks is maximized by optimizing resources and positions of the UAVs. Fig. 1.2 shows a typical example for wireless multihop backhauling with hybrid links and different kinds of BSs [76].

More recently, IRSs, sometimes called metasurfaces, have been introduced recently with the aim of controlling the propagation medium to enhance the QoS by boosting the energy and spectral efficiencies of the network. The IRS technology is expected to play a significant role in the future, where smartness, energy efficiency and spectral efficiency are the main requirements for the forthcoming wireless networks. IRS applies a large number of passive antenna elements which introduce a phase-shift to the received signals and reflect them back to the destination. For efficient transmission, multiple reflectors are used for a certain destination, and the introduced phase shifts are optimized by ensuring that the reflected signals are going to be added coherently in the channel. As a result, SNR is considerably increased, and consequently, the spectral efficiency is boosted [77]- [88]. In [77] and [78], a detailed overview about IRS and state-of-art solutions in addition to theoretical performance limits are provided. Energy-efficient approaches for the transmit power allocation and the phase shifts of the IRS elements is introduced in [79], and an accurate model for the power consumption of IRS-based systems is presented. A realistic

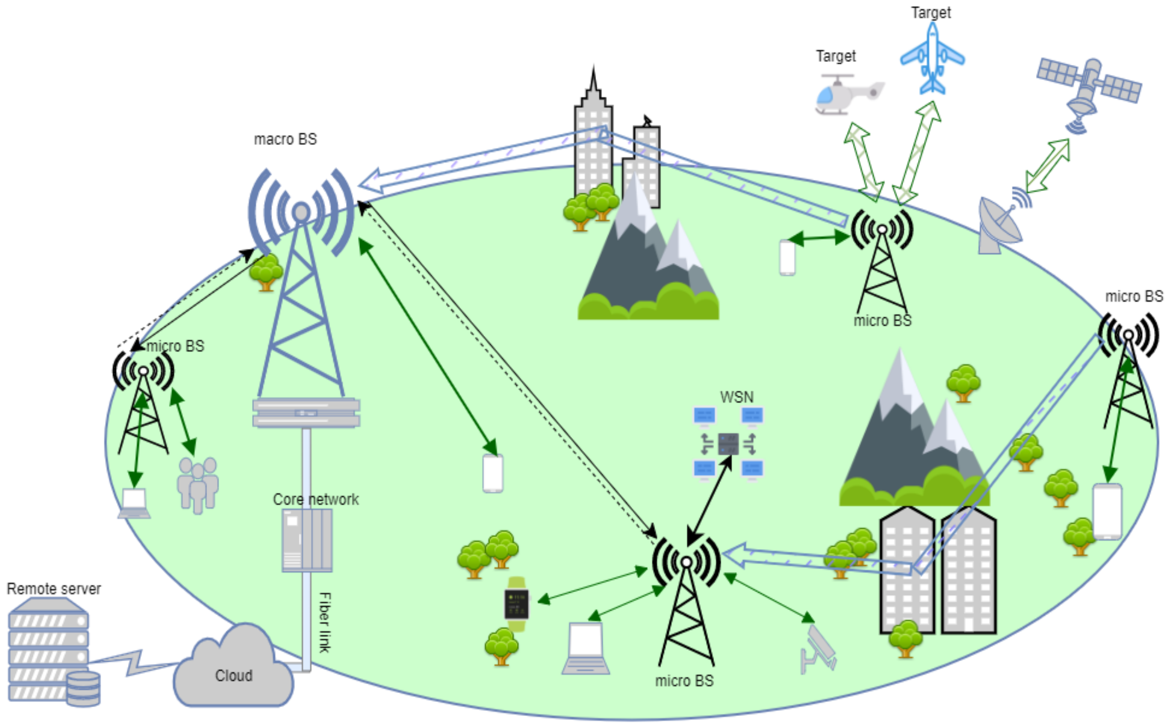

Figure 1.2: A typical wireless backhauling with different kinds of BSs.

implementation in outdoor environment has shown that the methods proposed in [79] for power allocation in IRS based systems could provide up to 300% higher energy efficiency when compared to multi-antenna amplify-and-forward systems. Joint active and passive beamforming is considered in [80] where some recommendations are provided for optimal deployment. Other research efforts are dedicated to study the performance of IRS with other existing signalling and communication technologies such as index modulation (IM) [81], space-shift-keying (SSK) [82], and non-orthogonal multiple access (NOMA) [88]. In [83], MIMO wireless communications assisted by IRS is investigated, where efficient algorithms for the phase shifts at the IRS and precoding at the transmitter are proposed with the aim of minimizing SER. Since the optimum values for the phase shift depends on the instantaneous channel side information (CSI), channel modeling and estimation are considered in [84]- [86]. In [89], the far-field pathloss model is derived for IRS based links using some optical physics techniques, and it has been shown that each reflecting element acts as a diffuse scatterer. A practical implementation for real IRS is introduced in [90], where a high-gain and low-cost IRS with 256 reflecting elements is designed in which positive intrinsic negative (PIN) diodes are used to design 2-bit phase shifters, and it was shown that a gain of 19.1 dBi can be achieved with the mmWave.

With all of IRS benefits and advantages mentioned above, we consider the deployment of IRS panels to assist wireless multi-hop backhauling. Terrestrial and aerial networks scenarios are studied. For the terrestrial network, multiple IRS panels are deployed to assist multi-hop wireless backhauling, where the error rate and outage probability are derived. Additionally, random number of hops with wired first protocol is considered. On the other hand, for the aerial networks, an IRS panel attached to high altitude

UAV is considered to reflect the base-station beams to unreachable low altitude UAVs. Multi layer UAV network is taken into account, where the error rate, outage probability and achievable ergodic capacity are derived.

1.3 Motivation

The requirements for the deployment of small-size and low-cost WSNs, which are the fundamental part of IoT, have been growing rapidly in the past period due to the wide area of useful applications they can serve. Such applications include military applications, health monitoring, autonomous cars, intelligent transportation systems, spectrum sensing, environment monitoring, smart cities, etc. By connecting WSNs to the internet cloud through IoT infrastructure, the opportunity for connecting the physical world to the computing world has become a reality and it has made it possible for humans to access, control and monitor their remote devices easily and effectively.

Likewise, the increasing demands for high QoS and high data rate real-time services will undoubtedly increase the amount of backhaul traffic between BSs. In addition, the integration of IoT will result in a massive number of low-cost and low-power devices, such as sensors, actuators, smart meters, etc, will further increase the pressure on the backhaul network. Consequently, the design of spectrum and energy efficient backhauling to satisfy these demands is a fundamental requirement for future generations of wireless networks. Moreover, the authors of [77] and [78] provide recommendations to rethink the current mathematical models for wireless communication and propose new appropriate models for the emerging IRS technology.

Motivated by the above mentioned, this thesis investigates mainly two enabling technologies for future wireless communications; namely, sensing services and IRS based wireless backhauling. Several aspects about sensing services and IoT have been thoroughly discussed and explored including spectrum sensing, target localization using RFID network, decision fusion for IoT-WSNs, and ISAC systems. Decision fusion algorithms based on statistical signal processing theorems have been proposed to assist the functionality of these networks. As well as, localization methods based on the maximum likelihood estimation have been explored and analyzed. In addition, performance evaluation for the introduced system models has been carried out using simulation, experiments and theoretical derivations, and the trade-off between computational complexity and achievable performance is discussed. Moreover, ISAC systems have been investigated and a unified performance evaluation is proposed based on Kullback-Leiber divergence theorem, or so called the relative information theorem.

Furthermore, the deployment of IRS panels to assist multiple hops wireless backhauling is investigated in this thesis. Two types of wireless backhauling are considered including including multi-hop terrestrial backhauling and multi-tier UAV networks. For the first scenario, a small BS intends to send data traffic to a remote macro BS with the assist of multiple small BSs, where the link between each pair of small BSs is assisted by an IRS panel due to lack of line-of-sight between small BSs. The bit error rate and outage probability are derived for the introduced system model and random number of hops is also considered. For UAV-IRS scenario, a multi-layer UAV network is considered, in which a high altitude UAV with an IRS panel attached is used to reflect signal from the BS to low altitude UAVs. The density function of the received SNR, bit error rate, outage probability and ergodic capacity are derived for the system model under imperfect channel estimation and compensation at IRS. Simulation and theoretical results are provided for the introduced system models and the performance limits are presented and investigated.

1.4 Thesis Organization

The rest of the thesis is organized as follows. The thesis consists of a total of nine chapters, where the first and tenth chapters provide an introduction and summery for the thesis, while the remaining seven chapters make up the core of the work. The core work (e.g. **Chapters 2** through **8**) is summarized below, where each of these chapters is a distinct journal publication as explained below. In addition, a footnote written on the first page of each chapter to relate the chapter with the corresponding publication.

In **Chapter 2**, RFID reader localization using hard decisions with error concealment is studied. An error concealment algorithm is proposed to enhance the accuracy of the estimated location by correcting the decisions of multiple deployed tags. The final location estimates are obtained a maximum likelihood estimator that takes into account imperfections in the sensing and transmission processes. **Chapter 3** discusses the joint estimation of location and orientation in wireless sensor networks using directional antennas. The directivity of the employed antenna is used to estimate the location and the facing direction of the receiver. The MR may use multiple directive antennas, or a single antenna whose beam can be steered electronically or mechanically. Moreover, majority voting and connected graph algorithms are employed to enhance the localization accuracy. As well as, **Chapter 4** investigates decision fusion for IoT-based wireless sensor networks. Multiple sensors transmit their decisions about a certain phenomenon to a remote fusion center (FC) over a wide area network are deployed and a novel decision fusion algorithm at FC is introduced. The proposed algorithm manage to reduce the decision fusion error probability performance while maintaining the low computational complexity. In **Chapter 5**, a unified performance framework for integrated sensing-communications (ISAC) based is proposed based on Kullback-Leibler divergence. The system model assumes a MIMO-BS providing ISAC services to multiple communication user equipments (CUEs) and a number of targets.

Furthermore, **Chapter 6** presents the performance analysis in terms of the error rate and outage probability of a multiple hop terrestrial network assisted by a number of IRS panels. In addition, **Chapter 7** introduces the performance evaluation for a multi-tier UAV network assisted by IRS with imperfect phase estimation and compensation where the error rate and outage probability are considered as performance measures. **Chapter 8** investigates the achievable ergodic capacity for UAV network assisted by IRS with imperfect phase estimation and compensation. Finally, **Chapter 9** summarizes the work and provides a future work plan.

1.5 List of Journal Publications

During my PhD at the University of Manchester, several research articles based on the PhD study have been published in top ranked journals/conferences, or accepted with revisions. These publications are listed below, where each of them is written as a distinct chapter in this thesis and they are ordered according to the sequence of **Chapters 2** through **8**. It should be noted that although these publications have multiple co-authors, the bulk of the work accomplished in [1-7] is my contribution. More specifically, the performance analysis, simulations, and the technical writing for the first draft of each of these papers have been accomplished by myself, whereas the contribution of the other co-authors is restricted to advisory role, consultation, revisions, and brainstorming.

1. **M. A. Al-Jarrah**, A. Al-Dweik, E. Alsusa and E. Damiani, "RFID reader localization using hard decisions with error concealment," *IEEE Sensors. J.*, vol. 19, no. 17, pp. 7534-7542, Sep. 2019, doi: 10.1109/JSEN.2019.2914914.

2. **M. A. Al-Jarrah**, A. Al-Dweik, N. T. Ali and E. Alsusa, "Joint estimation of location and orientation in wireless sensor networks using directional antennas," *IEEE Sensors. J.*, vol. 20, no. 23, pp. 14347-14359, Dec. 2020, doi: 10.1109/JSEN.2020.3008393.

3. **M. A. Al-Jarrah**, M. A. Yaseen, A. Al-Dweik, O. A. Dobre and E. Alsusa, "Decision fusion for IoT-based wireless sensor networks," *IEEE IoT. J.*, vol. 7, no. 2, pp. 1313-1326, Feb. 2020, doi: 10.1109/JIOT.2019.2954720.

4. **M. A. Al-Jarrah**, E. Alsusa and C. Masouros, "A unified performance framework for integrated sensing-communications based on KL-divergence," Submitted to *IEEE Trans. Wireless Commun.*, Sep. 2022.

5. **M. A. Al-Jarrah**, E. Alsusa, A. Al-Dweik and M.-S. Alouini, "Performance analysis of wireless mesh backhauling using intelligent reflecting surfaces," *IEEE Trans. Wireless Commun.*, vol. 20, no. 6, pp. 3597-3610, Jun. 2021, doi: 10.1109/TWC.2021.3052370.

6. **M. A. Al-Jarrah**, A. Al-Dweik, E. Alsusa, Y. Iraqi, and M.-S. Alouini, "On the performance of IRS-assisted multi-layer UAV communications with imperfect phase compensation," *IEEE Trans. Commun.*, vol. 69, no. 12, pp. 8551-8568, Dec. 2021, doi: 10.1109/TCOMM.2021.3113008.

7. **M. A. Al-Jarrah**, E. Alsusa, A. Al-Dweik, and D. K. C. So,"Capacity analysis of IRS-based UAV communications with imperfect phase compensation," *IEEE Wireless Commun. Lett.*, vol. 10, no. 7, pp. 1479-1483, Jul. 2021, doi: 10.1109/LWC.2021.3071059.

Furthermore, it is worth mentioning that in addition to the list of articles presented above, which form the core part of my submitted thesis, I have contributed in a few more published literature during my PhD which are listed below in [A] through [L]. Although I am the leading author of [A-D], these articles have not been included in this thesis due to the limitation on the number of pages. However, these articles are conference versions of the journal publications which have been included in the thesis, and thus the thesis covers the main contributions, ideas, models and findings. On the other hand, I had minor or reasonable contribution in the published material in [E-L], in which I performed partial system simulations and analysis, as well as, technical writing, revisions and editing. Those ones have not been included in the PhD thesis because I am not the main contributor, and might have, or might be, submitted for another degree by other students.

A. **M. Al-Jarrah**, E. Alsusa and C. Masouros, "Kullback-Leibler divergence analysis for integrated radar and communications (RadCom)," *2023 IEEE Wireless Commun. Netw. Conf. (WCNC)*, Glasgow, UK, Mar. 2023.

B. **M. Al-Jarrah**, A. Aldweik and E. Alsusa, "On the performance of downlink NOMA systems over hyper-Rayleigh fading channels," *2020 Int. Conf. Commun., Signal Processing, and their Appl. (ICCSPA)*, Sharjah, United Arab Emirates, 2021, pp. 1-6, doi: 10.1109/ICCSPA49915.2021.9385763.

C. **M. Al-Jarrah**, E. Alsusa and A. Al-Dweik, "Decision fusion for power-constrained wireless body sensor networks with amplify-and-forward relays," *2020 IEEE Int. Conf. Commun. Workshops (ICC Workshops)*, Dublin, Ireland, 2020, pp. 1-6, doi: 10.1109/ICCWorkshops49005.2020.9145150.

D. **M. Al-Jarrah**, A. Al-Dweik, S. S. Ikki and E. Alsusa, "Spectrum-occupancy aware cooperative spectrum sensing using adaptive detection," *IEEE Syst. J.*, vol. 14, no. 2, pp. 2225-2236, Jun. 2020, doi: 10.1109/JSYST.2019.2922773.

E. A. Alqahtani, E. Alsusa, A. Al-Dweik and **M. Al-Jarrah**, "Performance analysis for downlink NOMA Over $\alpha - \mu$ generalized fading channels," *IEEE Trans. Veh. Technol.*, vol. 70, no. 7, pp. 6814-6825, Jul. 2021, doi: 10.1109/TVT.2021.3082917.

F. A. Al-Dweik, Y. Iraqi, K.-H. Park, **M. Al-Jarrah**, E. Alsusa and M.-S. Alouini, "Efficient NOMA design without channel phase information using amplitude-coherent detection," *IEEE Trans. Commun.*, vol. 70, no. 1, pp. 245-263, Jan. 2022, doi: 10.1109/TCOMM.2021.3119368.

G. N. Babu Babu, M. Virgili, **M. Al-jarrah** *et al.*, "Energy-efficient trajectory design of a multi-IRS assisted portable access point," *IEEE Trans. Veh. Technol.*, vol. 72, no. 1, pp. 611-622, Jan. 2023, doi: 10.1109/TVT.2022.3202953.

H. M. AlaaEldin, E. Alsusa, K. G. Seddik and **M. Al-Jarrah**, "Optimizing IRS-assisted uplink NOMA system for power constrained IoT networks," *2022 IEEE 96th Veh. Technol. Conf. (VTC2022-Fall)*, London, United Kingdom, 2022, pp. 1-6, doi: 10.1109/VTC2022-Fall57202.2022.10012881.

I. Shuaishuai Han, **M. Al-Jarrah**, and E. Alsusa, "Efficient localization algorithms using a uniform rectangular array with model imperfections," *2023 IEEE Wireless Commun. Netw. Conf. (WCNC)*, Glasgow, UK, Mar. 2023.

J. Shuaishuai Han, **M. Al-Jarrah**, and E. Alsusa, "Joint DOA and Doppler frequency estimation for MIMO radars in the presence of array model imperfections," *2023 IEEE Wireless Commun. Netw. Conf. (WCNC)*, Glasgow, UK, Mar. 2023.

References

[1] O. Cetinkaya, E. Dinc, C. Koca, G. Merrett, and O. Akan, "Energy-neutral wireless-powered networks," *IEEE Wireless Commun. Lett.*, vol. 8, no. 5, pp. 1373-1376, Oct. 2019.

[2] H. Wang, G. Zhou, L. Bhatia, Z. Zhu, W. Li, and J. McCann, "Energy-neutral and QoS-aware protocol in wireless sensor networks for health monitoring of hoisting systems," *IEEE Trans. Ind. Inform.*, vol. 16, no. 8, pp. 5543-5553, Aug. 2020.

[3] "PAINLESS: An innovative training network (ITN) on energy-autonomous portable access points for infrastructure-less networks," [Online]. Available: `http://painless-itn.com/wp-content/uploads/2019/05/NEWSLETTER0.pdf`.

[4] M. Kader and M. Hoque, "Hybrid spectrum sharing with cooperative secondary user selection in cognitive radio networks," *KSII T. Internet Info.*, vol. 7, no. 9, pp. 2081-2100, Sep. 2013.

[5] W. Lee, and I. Akyildiz, "Optimal spectrum sensing framework for cognitive radio Networks," *IEEE Trans. Wireless Commun.*, vol. 7, no. 10, pp. 3845-3857, Oct. 2008.

[6] A. Ali and W. Hamouda, "Advances on spectrum sensing for cognitive radio networks: theory and applications," *IEEE Commun. Surveys Tuts.*, vol. 11, no. 2, pp. 1277-1304, Nov. 2016.

[7] Z. Qin, J. Wang, J. Chen, and L. Wang, "Adaptive compressed spectrum sensing based on cross validation in wideband cognitive radio system," *IEEE Syst. J.*, vol. 11, no. 4, pp. 2422-2431, Dec. 2017.

[8] O. Altrad, S. Muhaidat, A. Al-Dweik, A. Shami, and P. Yoo, "Opportunistic spectrum access in cognitive radio networks under imperfect spectrum sensing," *IEEE Trans. Veh. Technol.*, vol. 63, no. 2, pp. 920-925, Feb. 2014.

[9] E. DiGiampaolo and F. Martinelli, "Mobile robot localization using the phase of passive UHF RFID signals," *IEEE Trans. Ind. Electron.*, vol. 61, no. 1, pp. 365-376, Jan. 2014.

[10] S. Subedi, E. Pauls, and Y. Zhang, "Accurate localization and tracking of a passive RFID reader based on RSSI measurements," *IEEE Trans. Radio Freq. Identification*, vol. 1, no. 2, pp. 144-154, Jun. 2017.

[11] W. Shi, *et al.*, “Optimizing directional reader antennas deployment in UHF RFID localization system by using a MPCSO algorithm,” *IEEE Sensors J.*, vol. 18, no. 12, pp. 5035-5048, Jun. 2018.

[12] H. Xiong, J. Tang, H. Xu, W. Zhang, and Z. Du , “A robust single GPS navigation and positioning algorithm based on strong tracking filtering,” *IEEE Sensors J.*, vol. 18, no. 1, pp. 290-298, Jan. 2018.

[13] J. Zhang, Y. Lyu, J. Patton, S. Periaswamy, and T. Roppel, “BFVP: A probabilistic UHF RFID tag localization algorithm using Bayesian filter and a variable power RFID model,” *IEEE Trans. Ind. Electron.*, vol. 65, no. 10, pp. 8250-8259, Oct. 2018.

[14] B. Chen *et al.*, “Channel aware decision fusion in wireless sensor networks,” *IEEE Trans. Signal Process.*, vol. 52, no. 12, pp. 3454-3458, Dec. 2004.

[15] R. Niu *et al.*, “Fusion of decisions transmitted over Rayleigh fading channels in wireless sensor networks,” *IEEE Trans. Signal Process.*, vol. 54, no.3, pp. 1018-1027, Mar. 2006.

[16] A. Lei and R. Schober, “Multiple-symbol differential decision fusion for mobile wireless sensor networks,” *IEEE Trans. Wireless Commun.*, vol. 9, no. 2, pp. 778-790, Feb. 2010.

[17] K. Cichoń *et al.*, “Energy-efficient cooperative spectrum sensing: A survey,” *IEEE Commun. Surveys Tuts.*, vol. 18, no. 3, pp. 1861-1886, Third quarter 2016.

[18] S. Kim, “Simultaneous spectrum sensing and energy harvesting,” *IEEE Trans. Wireless Commun.*, vol. 18, no. 2, pp. 769-779, Feb. 2019.

[19] N. Banavathu and M. A. Khan, “Optimization of k-out-of-N rule for heterogeneous cognitive radio networks,” *IEEE Signal Process. Lett.*, vol. 26, no. 3, pp. 445-449, Mar. 2019.

[20] D. Hamza *et al.*, “Equal gain combining for cooperative spectrum sensing in cognitive radio networks,” *IEEE Trans. Wireless Commun.*, vol. 13, no. 8, pp. 4334-4345, Aug. 2014.

[21] F. Liu, C. Masouros, A. Li, and T. Ratnarajah, “Robust MIMO beamforming for cellular and radar coexistence,” *IEEE Wireless Commun. Lett.*, vol. 6, no. 3, pp. 374-377, Jun. 2017.

[22] F. Liu, L. Zhou, C. Masouros, A. Li, W. Luo, and A. Petropulu, “Toward dual-functional radar-communication systems: Optimal waveform design,” *IEEE Trans. Signal Process.*, vol. 66, no. 16, pp. 4264-4279, Aug. 2018.

[23] F. Liu, C. Masouros, A. Li, H. Sun, and L. Hanzo, “MU-MIMO communications with MIMO radar: From co-existence to joint transmission,” *IEEE Trans. Wireless Commun.*, vol. 17, no. 4, pp. 2755-2770, Apr. 2018.

[24] A. Liu *et al.*, "A survey on fundamental limits of integrated sensing and communication," *IEEE Commun. Surveys Tuts.*, *Early access*, 2022, doi: 10.1109/COMST.2022.3149272.

[25] J. A. Zhang *et al.*, "An overview of signal processing techniques for joint communication and radar sensing," *IEEE J. Sel. Topics Signal Process.*, vol. 15, no. 6, pp. 1295-1315, Nov. 2021, doi: 10.1109/JSTSP.2021.3113120.

[26] N. Kim and D. Cho, "A novel synchronous duplexing method for long distance wireless backhaul system," *IEEE Wireless Commun. Lett.*, vol. 8, no. 3, pp. 761-764, Jun. 2019.

[27] "Terragraph virtual fiber for high speed fixed broadband," Telecom infra project, White Paper, 2018. [Online]. Available: `https://terragraph.com/wp-content/uploads/2019/02/Terragraph_MikebudaTrial_Whitepaper.pdf`

[28] Ericsson Mobility Report 2019. Accessed: June 15, 2020. [Online]. Available: `https://www.ericsson.com/4acd7e/assets/local/mobility-report/documents/2019/emr-november-2019.pdf`.

[29] Cisco. 2020 Cisco annual internet report. [Online]. Available: `https://www.cisco.com/c/en/us/solutions/collateral/executiveperspectives/annual-internet-report/white-paper-c11-741490.html`.

[30] J. Rygaard, "Digitization, densification and why you should care," Nokia, Tech. Rep., Feb. 2017. [Online]. Available: https: `www.nokia.com/blog/digitization-densification-care/`

[31] M. Coldrey, "Maturity and field proven experience of millimetre wave transmission," Sophia Antipolis, France, ETSI White Paper, Sep. 2015. [Online]. Available: `https://www.etsi.org/images/files/ETSIWhitePapers/etsi_wp10_field_pr-oven_experience_of_mwt_20150923.pdf`

[32] "Telecom infra project mmWave radio link aspects," Telecom infra project, White Paper, 2018. [Online]. Available: `https://telecominfraproject.com/wp-content/uploads/TIP-mmWave_Radio-Link-Aspects_October-2018_vF.pdf`

[33] "Telecom infra project customer premises equipment (CPE) market adoption requirements," Telecom infra project, White paper, 2018. [Online]. Available: `https://telecominfraproject.com/wp-content/uploads/TIP-mmWave-CPE-Market-Adoption-Requirements_October-2018_vF.pdf`

[34] O. Tipmongkolsilp, S. Zaghloul and A. Jukan, "The evolution of cellular backhaul technologies: Current issues and future trends," *IEEE Commun. Surveys Tuts.*, vol. 13, no. 1, pp. 97-113, First Quarter 2011.

[35] K. Zheng, L. Zhao, J. Mei, M. Dohler, W. Xiang, and Y. Peng, “10 Gb/s hetsnets with millimeter-wave communications: Access and networking - challenges and protocols,” *IEEE Commun. Mag.*, vol. 53, no. 1, pp. 222-231, Jan. 2015.

[36] R. Favraud, C. Chang, and N. Nikaein, “Autonomous self-backhauled LTE mesh network with QoS guarantee,” *IEEE Access*, vol. 6, pp. 4083-4117, 2018.

[37] Y. Yu, T. Hsieh, and A. Pang, “Millimeter-wave backhaul traffic minimization for CoMP over 5G cellular networks,” *IEEE Trans. Veh. Technol.*, vol. 68, no. 4, pp. 4003-4015, Apr. 2019.

[38] M. Alzenad, M. Shakir, H. Yanikomeroglu, and M. Alouini, “FSO-based vertical backhaul/fronthaul framework for 5G+ wireless networks,” *IEEE Commun. Mag.*, vol. 56, no. 1, pp. 218-224, Jan. 2018.

[39] S. Samarakoon, M. Bennis, W. Saad, and M. Latva-aho, “Backhaul-aware interference management in the uplink of wireless small cell networks,” *IEEE Trans. Wireless Commun.*, vol. 12, no. 11, pp. 5813-5825, Nov. 2013.

[40] L. Sanguinetti, A. Moustakas, and M. Debbah, “Interference management in 5G reverse TDD HetNets with wireless backhaul: A large system analysis,” *IEEE J. Sel. Areas Commun.*, vol. 33, no. 6, pp. 1187-1200, Jun. 2015.

[41] Y. Al-Eryani, A. Salhab, S. Zummo, and M. Alouini, “Protocol design and performance analysis of multiuser mixed RF and hybrid FSO/RF relaying with buffers,” *IEEE/OSA J. Opt. Commun. Netw.*, vol. 10, no. 4, pp. 309-321, April 2018, doi: 10.1364/JOCN.10.000309.

[42] H. Lei *et al.*, “On secure mixed RF-FSO systems with TAS and imperfect CSI,” *IEEE Tran. Commun.*, vol. 68, no. 7, pp. 4461-4475, Jul. 2020, doi: 10.1109/TCOMM.2020.2985028.

[43] Q.-U.-A Nadeem, A. Kammoun, M. Debbah, and M. Alouini, “3D massive MIMO systems: Modeling and performance analysis,” *IEEE Trans. Wireless Commun.*, vol. 14, no. 12, pp. 6926-6939, Dec. 2015.

[44] H. Tabassum, A. Sakr, and E. Hossain, “Analysis of massive MIMO-enabled downlink wireless backhauling for full-duplex small cells,” *IEEE Trans. Commun.*, vol. 64, no. 6, pp. 2354-2369, Jun. 2016.

[45] M. Feng, S. Mao, and T. Jiang, “Joint frame design, resource allocation and user association for massive MIMO heterogeneous networks with wireless backhaul,” *IEEE Trans. Wireless Commun.*, vol. 17, no. 3, pp. 1937-1950, Mar. 2018.

[46] P. Anokye, R. Ahiadormey, C. Song, and K. Lee, “Achievable sum-rate analysis of massive MIMO full-duplex wireless backhaul links in heterogeneous cellular networks,” *IEEE Access*, vol. 6, pp. 23456-23469, 2018.

[47] A. Bonfante *et al.*, "5G massive MIMO architectures: self-backhauled small cells versus direct access," *IEEE Trans. Veh. Technol.*, vol. 68, no. 10, pp. 10003-10017, Oct. 2019.

[48] E. Calvanese Strinati *et al.*, "6G: The next frontier: From holographic messaging to artificial intelligence using subterahertz and visible light communication," *IEEE Veh. Technol. Mag.*, vol. 14, no. 3, pp. 42-50, Sep. 2019.

[49] X. Ge, S. Tu, G. Mao, C. Wang, and T. Han, "5G ultra-dense cellular networks," *IEEE Wireless Commun.*, vol. 23, no. 1, pp. 72-79, Feb. 2016.

[50] M. Mirahmadi, A. Al-Dweik, and A. Shami, "Interference modeling and performance evaluation of heterogeneous cellular networks," *IEEE Trans. Commun.*, vol. 62, no. 6, pp. 2132–2144, June 2014.

[51] J. G. Andrews, H. Claussen, M. Dohler, S. Rangan, and M. C. Reed, "Femtocells: Past, present, and future," *IEEE J. Sel. Areas Commun.*, vol. 30, no. 3, pp. 497–508, 2012.

[52] RSPG Report on Spectrum Issues on Wireless Backhaul, Radio Spectrum Policy Group, European Commission, Directorate-General for Communications Networks, Content and Technology, RSPG15-607, June 2015.

[53] W. Abderrahim, O. Amin, M. Alouini and B. Shihada, "Latency-aware offloading in integrated satellite terrestrial networks," *IEEE Open J. Commun. Soc.*, vol. 1, pp. 490-500, 2020.

[54] Y. Liu, A. Tang and X. Wang, "Joint incentive and resource allocation design for user provided network under 5G integrated access and backhaul networks," *IEEE Trans. Netw. Sci. Eng.*, vol. 7, no. 2, pp. 673-685, 1 Apr. 2020.

[55] C. Saha and H. S. Dhillon, "Millimeter wave integrated access and backhaul in 5G: performance analysis and design insights," *IEEE J. Sel. Areas Commun.*, vol. 37, no. 12, pp. 2669-2684, Dec. 2019.

[56] R. Mesleh, H. Haas, S. Sinanovic, C. Ahn, and S. Yun, "Spatial modulation," *IEEE Trans. Veh. Technol.*, vol. 57, no. 4, pp. 2228-2241, Jul. 2008.

[57] J. Jeganathan, A. Ghrayeb, L. Szczecinski, and A. Ceron, "Space shift keying modulation for MIMO channels," *IEEE Trans. Wireless Commun.*, vol. 8, no. 7, pp. 3692-3703, July 2009.

[58] M. Di Renzo, H. Haas, A. Ghrayeb, S. Sugiura, and L. Hanzo, "Spatial modulation for generalized MIMO: Challenges, opportunities, and implementation," *Proc. IEEE*, vol. 102, no. 1, pp. 56-103, Jan. 2014.

[59] P. Liu and A. Springer, "Space shift keying for LOS communication at mmWave frequencies," *IEEE Wireless Commun. Lett.*, vol. 4, no. 2, pp. 121-124, April 2015.

[60] E. Panayirci, A. Yesilkaya, T. Cogalan, H. Poor, and H. Haas, "Physical-layer security with optical generalized space shift keying," *IEEE Trans. Commun.*, *IEEE Early Access*, 2020. doi: 10.1109/TCOMM.2020.2969867

[61] S. Karar and A. Das-Barman, "Two-stage rate allocation game in wireless access networks with PON backhaul," *IEEE Commun. Lett.*, vol. 22, no. 9, pp. 1814-1817, Sep. 2018, doi: 10.1109/LCOMM.2018.2859414.

[62] S. Aboagye, A. Ibrahim, and T. Ngatched, "Energy efficient user association, power, and flow control in millimeter wave backhaul Heterogeneous networks," *IEEE Open J. Commun. Soc.,* vol. 1, pp. 41-59, 2020, doi: 10.1109/OJCOMS.2019.2953576.

[63] J. Jang, H. Yang, and H. Jwa, "Resource allocation and power control in cooperative small cell networks with backhaul constraint," *IEEE Trans. Veh. Technol.*, vol. 68, no. 11, pp. 10926-10942, Nov. 2019, doi: 10.1109/TVT.2019.2939885.

[64] Y. Niu *et al.*, "Energy-efficient scheduling for mmWave backhauling of small cells in heterogeneous cellular networks," *IEEE Trans. Veh. Technol.*, vol. 66, no. 3, pp. 2674-2687, March 2017, doi: 10.1109/TVT.2016.2582785.

[65] P. Anokye, R. Ahiadormey, C. Song, and K. Lee, "Achievable sum-rate analysis of massive MIMO full-duplex wireless backhaul links in heterogeneous cellular networks," *IEEE Access*, vol. 6, pp. 23456-23469, 2018, doi: 10.1109/ACCESS.2018.2828598.

[66] P. Anokye, R. Ahiadormey, C. Song, and K. Lee, "On the sum-rate of heterogeneous networks with low-resolution ADC quantized full-duplex massive MIMO-enabled backhaul," *IEEE Wireless Commun. Lett.*, vol. 8, no. 2, pp. 452-455, Apr. 2019, doi: 10.1109/LWC.2018.2875907.

[67] A. Zahmatkesh and T. Kunz, "Software defined multihop wireless networks: Promises and challenges," *J. Commun. Netw.*, vol. 19, no. 6, pp. 546-554, Dec. 2017, doi: 10.1109/JCN.2017.000094.

[68] T. Vu, M. Bennis, M. Debbah, and M. Latva-Aho, "Joint path selection and rate allocation framework for 5G self-backhauled mm-wave networks," *IEEE Trans. Wireless Commun.*, vol. 18, no. 4, pp. 2431-2445, Apr. 2019, doi: 10.1109/TWC.2019.2904275.

[69] L. Ji, J. Chen, and Z. Feng, "Spectrum allocation and performance analysis for backhauling of UAV assisted cellular network," *China Commun.*, vol. 16, no. 8, pp. 83-92, Aug. 2019, doi: 10.23919/JCC.2019.08.008.

[70] M. Gapeyenko, V. Petrov, D. Moltchanov, S. Andreev, N. Himayat, and Y. Koucheryavy, "Flexible and reliable UAV-assisted backhaul operation in 5G mmWave cellular networks," *IEEE J. Sel. Areas Commun.*, vol. 36, no. 11, pp. 2486-2496, Nov. 2018.

[71] Y. Huang, M. Cui, G. Zhang, and W. Chen, "Bandwidth, power and trajectory optimization for UAV base station networks with backhaul and user QoS constraints," *IEEE Access*, vol. 8, pp. 67625-67634, 2020.

[72] M. Youssef, J. Farah, C. Abdel-Nour, and C. Douillard, "Full-duplex and backhaul-constrained UAV-enabled networks using NOMA," *IEEE Trans. Veh. Technol.*, IEEE Early Access.

[73] C. Qiu, Z. Wei, Z. Feng, and P. Zhang, "Backhaul-aware trajectory optimization of fixed-wing UAV-mounted base station for continuous available wireless service," *IEEE Access*, vol. 8, pp. 60940-60950, 2020.

[74] A. Alzidaneen, A. Alsharoa, and M. Alouini, "Resource and placement optimization for multiple UAVs using backhaul tethered balloons," *IEEE Wireless Commun. Lett.*, vol. 9, no. 4, pp. 543-547, April 2020.

[75] J. Lee, K. Park, M. Alouini, and Y. Ko, "Optimal resource allocation and placement for terrestrial and aerial base stations in mixed RF/FSO backhaul networks," *2020 IEEE 91st Vehicular Technology Conference (VTC2020-Spring)*, Antwerp, Belgium, 2020, pp. 1-5.

[76] Y. Hu, M. Chen, and W. Saad, "Joint access and backhaul resource management in satellite-drone networks: A competitive market approach," *IEEE Trans. Wireless Commun.*, vol. 19, no. 6, pp. 3908-3923, June 2020.

[77] E. Basar, M. Di Renzo, J. De Rosny, M. Debbah, M.-S. Alouini and R. Zhang, "Wireless communications through reconfigurable intelligent surfaces," *IEEE Access*, vol. 7, pp. 116753-116773, 2019.

[78] M. Di Renzo *et al.*, "Smart radio environments empowered by reconfigurable AI meta-surfaces: An idea whose time has come," *EURASIP J. Wireless Commun. Netw.*, vol. 2019, p. 129, May 2019.

[79] C. Huang, A. Zappone, G. Alexandropoulos, M. Debbah, and C. Yuen, "Reconfigurable intelligent surfaces for energy efficiency in wireless communication," *IEEE Trans. Wireless Commun.*, vol. 18, no. 8, pp. 4157–4170, Aug. 2019.

[80] Q. Wu and R. Zhang, "Intelligent reflecting surface enhanced wireless network via joint active and passive beamforming," *IEEE Trans. Wireless Commun.*, vol. 18, no. 11, pp. 5394-5409, Nov. 2019.

[81] E. Basar, "Reconfigurable intelligent surface-based index modulation: A new beyond MIMO paradigm for 6G," *IEEE Trans. Commun.*, IEEE Early Access. doi: 10.1109/TCOMM.2020.2971486

[82] A. Canbilen, E. Basar, and S. Ikki, "Reconfigurable intelligent surface-assisted space shift keying," 2020. [Online]. Available: `https://arxiv.org/abs/2001.11287`.

[83] J. Ye, S. Guo, and M.-S. Alouini, "Joint reflecting and precoding designs for SER minimization in reconfigurable intelligent surfaces assisted MIMO systems," *to appear, IEEE Trans. Wireless Commun.* 2020. [Online]. Available: `https://arxiv.org/abs/1906.11466`.

[84] D. Mishra and H. Johansson, "Channel estimation and low-complexity beamforming design for passive intelligent surface assisted MISO wireless energy transfer, " *IEEE Int. Conf. Acoustics, Speech and Signal Process. (ICASSP)*, Brighton, United Kingdom, 2019, pp. 4659-4663.

[85] Z. He and X. Yuan, "Cascaded channel estimation for large intelligent metasurface assisted massive MIMO," *IEEE Wireless Commun. Lett.*, vol. 9, no. 2, pp. 210-214, Feb. 2020.

[86] Q.-U.-A. Nadeem, A. Kammoun, A. Chaaban, M. Debbah, M.-S. Alouini, "Intelligent reflecting surface assisted wireless communication: Modeling and channel estimation," *to appear, IEEE Open J. Commun. Soc.* 2020. [Online]. Available: `https://arxiv.org/abs/1906.02360`.

[87] Q. U. Nadeem, A. Kammoun, A. Chaaban, M. Debbah, and M. -S. Alouini, "Asymptotic max-min SINR analysis of reconfigurable intelligent surface assisted MISO systems," *to appear*, *IEEE Trans. Wireless Commun.*, 2020.

[88] Z. Ding and H. V. Poor, "A simple design of IRS-NOMA transmission," *IEEE Commun. Lett.*, *IEEE Early Access*, doi: 10.1109/LCOMM.2020.2974196

[89] Ö. Özdogan, E. Björnson, and E. Larsson, "Intelligent reflecting surfaces: Physics, propagation, and pathloss modeling," *IEEE Wireless Commun. Lett.*, IEEE Early Access. doi: 10.1109/LWC.2019.2960779

[90] L. Dai *et al.*, "Reconfigurable intelligent surface-based wireless communication: Antenna design, prototyping and experimental results," 2019. [Online]. Available: `https://arxiv.org/abs/1912.03620`.

Chapter 2

RFID Reader Localization Using Hard Decisions with Error Concealment[1]

Abstract

This paper presents an efficient reader localization algorithm in radio frequency identification (RFID) networks. In the proposed algorithm, it is assumed that no channel state information is available at the reader and the backscatters of all RFID tags are converted to hard decisions using an energy detector. The accuracy of the estimated location is improved using an error concealment algorithm that utilizes the fact that adjacent tags are expected to produce similar decisions. The final location estimates are obtained using Particle Swarm Optimization of a maximum likelihood estimator that takes into account imperfections in the sensing and transmission processes. The performance of the proposed algorithm is evaluated in terms of the root mean square error using Monte Carlo simulation, and compared to other well-established localization algorithms. Moreover, Cramer-Rao lower bound is derived to assess the efficiency of the new estimator. The obtained results show that the proposed algorithm estimation accuracy is up to 26.5% more than the other benchmark estimators.

Index Terms

RFID, localization, positioning, location estimation, received signal strength.

2.1 Introduction

Radio frequency identification (RFID) technology plays a key role in a wide-range of industrial, commercial, medical, transportation and environmental applications. Indoor localization using RFID networks is

[1]**M. A. Al-Jarrah**, A. Al-Dweik, E. Alsusa and E. Damiani, "RFID reader localization using hard decisions with error concealment," *IEEE Sensors. J.*, vol. 19, no. 17, pp. 7534-7542, Sep. 2019, doi: 10.1109/JSEN.2019.2914914.

a critical emerging application which has received extensive attention in the literature [1]- [12]. Generally speaking, the localization techniques reported in the literature aim at localizing the reader or one of the tags. In both cases, the required RFID infrastructure should include a reader and a grid of tags pre-deployed in the region of interest (RoI) [13]- [17]. For example, DiGiampaolo and Martinelli [5] proposed a system to localize a mobile robot equipped with RFID reader and odometry sensors with the tags fixed to the ceiling. The localization is based on measuring the phase of the signals transmitted by the tags with the aid of a multi-hypothesis Kalman filter. In [6], the influence of the tag interaction on the localization algorithm is studied. A two-dimensional localization system for passive ultra-high frequency (UHF) RFID tags based evaluating the backscattered transponder signals is proposed in [7], where the phase and amplitude of signals are jointly used to provide accurate localization. The authors of [8] developed methods for the purpose of pattern matching to mitigate the effect of measurements' errors by clustering the tags and considering only a few at a time, denoted as the neighbors tags, in the localization process. In [9], localization and tracking of an RFID reader is proposed to achieve accurate localization using received signal strength indicator (RSSI) measurements obtained from multiple distributed passive tags. A new deployment optimization approach for readers with directional antennas is proposed in [12], where a novel particle swarm optimization (PSO) is applied. A probabilistic model based on the recursive Kalman filter is considered in [10] to reduce errors in the least squares sense, while a Bayesian filter is applied in [14] using a fixed RF transmission power model to localize RFID tags. Moreover, hybrid RSSI and time of arrival (TOA) localization is considered in [16] to localize multiple targets, where an approximate solution for the positions is derived based on the weighted least squares criterion.

Although the aforementioned techniques offer high accuracy, their computational complexity and overhead are generally high. For example, the algorithms reported in [4]- [8], [12] employ TOA, time difference of arrival (TDOA), angle of arrival (AOA), or phase of arrival (POA). Such techniques require perfect time synchronization between all the transmitters and receivers, and accurate calculation for the entire cycle phase. Therefore, localization using RSSI can be considered as an efficient solution to reduce complexity, but it usually comes at the expense of reduced accuracy due to the impact of channel effects [6], [9], [18]. A fault-tolerant RFID reader localization approach, that can handle regional permanent faults is given in [2]. Although the proposed algorithm may provide reliable location estimates in certain scenarios, it is limited to dense distributions of passive tags, and its complexity is $O(n^3)$, where n is the number of tags. To overcome the fading effects, localization based on hard decision (HD) RSSI is considered in [11] where a local voting algorithm (LVA) is used to correct the hard decisions of certain tags before estimating the reader's location. However, the estimator is designed under the assumption of error-free link between the tags and the reader, and the distances between the reader and neighbor tags are equal. Therefore, the LVA accuracy deteriorates significantly at low signal-to-noise ratios (SNRs). A simplified version of [11] is reported in [20], but without local voting, and hence, its performance is worse than LVA at high SNRs. In addition, a soft range limited K-nearest neighbors (KNNs) localization fingerprinting algorithm is proposed in [21], where a scale factor related to the physical distance between the user's previous position and reference location is considered.

To the best of the authors' knowledge, there is no work in the literature that tackled the RFID reader localization problem while considering imperfect transmission and error concealment. Therefore, we propose an efficient reader localization algorithm for RFID networks where it is assumed that some of the tags do not receive the reader's signal, and hence do not respond to the reader interrogation signal (RIS). Moreover, the algorithm is designed while considering the impact of channel fading and the fact that adjacent tags are not necessarily at equal distance from the reader. The localization process is based on the maximum likelihood (ML) principle combined with a low complexity error concealment process to provide accurate location estimates. The system performance is evaluated in terms of the root mean square error (RMSE) for which the Cramer-Rao lower bound (CRLB) is derived.

The rest of the paper is organized as follows. In Section II, the system model is presented, followed by the proposed localization algorithm in Section III. In Section IV, the CRLB of the proposed localization algorithm is derived. Section V presents the analytical and simulation results. Finally, conclusions are provided in Section VI.

2.2 System Model and Problem Formulation

Consider an RFID network that consists of one reader and K tags distributed in the RoI with known positions. The reader sends its radio frequency (RF) interrogation signals at a particular frequency, and then listens to the return signals transmitted by the tags. A tag that detects the RIS responds by transmitting a confirmation signal back to the reader, otherwise it remains silent. As such, the reader and tags have two operating modes, the transmission and listening modes. To increase the probability of detecting its interrogation signals by the tags, the reader may send a sequence of L signals to enable the tag to combine these signals before it decides to respond back to the reader. In the listening mode, the reader receives only $U \leq K$ signals, where U is the number of tags that have successfully detected the RIS. The $K-U$ tags do not respond because they are outside the coverage range of the reader, or due to channel fading and/or system noise. The reader's objective is to determine its location based on the received U signals.

2.2.1 Received signal model at the tag

The baseband representation of the received signal at the kth tag during the lth signaling period can be written as

$$S_k[l] = \upsilon_k \sqrt{P_R \alpha_k} \hbar_k[l] + n_k[l],\; k = [1, 2, ..., K]\,,\; l = [1, 2, ..., L] \tag{2.1}$$

where P_R is the reader transmit power, $\upsilon_k \in [0,1]$ is an attenuation factor that captures the effect of the reader's antenna radiation pattern irregularity, $\hbar_k \sim \mathcal{CN}(0, \sigma_{\hbar}^2)$ is a complex Gaussian distributed channel gain, $n_k \sim \mathcal{N}(0, N_0/2)$ is the additive white Gaussian noise (AWGN) and α_k is the free space path loss,

$$\alpha_k = \left(\frac{\lambda}{4\pi d_k}\right)^2. \tag{2.2}$$

The wavelength of the RIS in (2.2) is denoted as λ and the distance between the kth tag and the reader is denoted as d_k, which can be computed as

$$d_k = \sqrt{\left(x_{G_k} - x_R\right)^2 + \left(y_{G_k} - y_R\right)^2} \tag{2.3}$$

where (x_R, y_R) and (x_{G_k}, y_{G_k}) are the Cartesian coordinates of the reader and kth tag, respectively.

To mitigate the impact of channel fading and noise, the participant tags may take repeated votes before deciding to respond to the RIS. Under power and delay constraints, the polling frequency L may be adaptable to minimize the probability of error [22]. However, such optimization could be computationally prohibitive in RFID scenarios due to computational power constraints, and thus, this work considers a fixed L for all tags. Given that the reader sends a sequence of L polling signals during its transmission mode that last for T_R seconds, combining the L RISs can be performed using various techniques, however equal gain combining is adopted in this context due to its simple implementation. Therefore, the combined L RISs can be written as

$$\begin{aligned} S_k &= \frac{1}{L}\sum_{l=1}^{L} \upsilon_k \sqrt{P_R \alpha_k} \rho_k[l] + n_k[l] \\ &= \upsilon_k A_k + w_k \end{aligned} \tag{2.4}$$

where $A_k = \frac{1}{L}\sqrt{P_R \alpha_k} \sum_{l=1}^{L} \rho_k[l]$, $w_k \sim \mathcal{N}(0, \sigma_w^2)$, and $\sigma_w^2 = N_0/2L$. For large values of L, the ensemble average can be approximated by the statistical average, and thus $A_k \approx \sqrt{P_R \alpha_k}\mathcal{E}\left\{\rho_k[l]\right\}$, where $\mathcal{E}\left\{\cdot\right\}$ represents the expectation process. Finally, the signal S_k is applied to the detector, which makes a binary decision (hard decision) whether to respond to the RIS or not. The decision at the tag can be described by

$$u_k = \begin{cases} 0, & S_k < \tau_k \\ 1, & S_k \geq \tau_k \end{cases}. \tag{2.5}$$

The detection threshold τ_k that can be selected to control the tags' sensitivity to the received signals. More specifically, τ_k can be adjusted to limit the number of tags that may receive and respond to the RIS. By noting that $A_k \approx \sqrt{P_R \alpha_k}\mathcal{E}\left\{\rho_k[l]\right\}$ and using (2.2), τ_k can be expressed as

$$\tau_k = \frac{\sqrt{P_R}}{4\pi d_0} \upsilon_k \lambda \mathcal{E}\left\{\rho_k[l]\right\} \tag{2.6}$$

where d_0 is the radius of the reader coverage area. It is worth noting that the effect of the free space path loss in (2.6) is based on the assumption that the radiation pattern of the reader is circular. Although it might be infeasible to design perfectly circular radiation patterns in practice, there are several antennas designed for RFID applications that has near-ideal omnidirectional antennas [23]- [25]. Consequently, the reader radiation pattern can be closely approximated by a circular pattern, and the free space path loss for all tags at a distance d_0 from the reader can be considered equivalent.

Based on (2.4) and (2.5), the probability that a tag successfully detects the RIS is given by

$$\Pr\left(u_k = 1\right) = Q\left(\frac{\tau_k - \upsilon_k A_k}{\sigma_w}\right) \tag{2.7}$$

where $Q\left(\cdot\right)$ is the Q-function. After the detection process, each tag with $u_k = 1$ will respond back to the reader by sending a continuous signal with average transmit power P_G and duration of T_G seconds.

2.2.2 Received signal model at the reader

In this work, it is assumed that the RFID system employs an anti-collision protocol, and hence there is no interference between the signals transmitted by the U active tags [4], [6]. In such protocols, the reader may interrogate the tags sequentially as in the case of tree-based splitting techniques [26]. Although the process is performed sequentially, off-the-shelf readers can read hundreds of tags in a fraction of a second [27]. Therefore, the received signal from the kth tag can be written as

$$y_k = \upsilon_k \sqrt{P_G} \hbar_k[l] \sqrt{\alpha_k}\ u_k + \varphi_k \tag{2.8}$$

where $\upsilon_k \hbar_k[l] \sqrt{\alpha_k} \triangleq h_k \sim \mathcal{CN}(0, \upsilon_k^2 \sigma_\hbar^2 \alpha_k)$ is the overall channel coefficient that captures the small and large scale fading effects, and $\varphi_k \sim \mathcal{CN}(0, \sigma_\varphi^2)$ is the AWGN. Thus, y_k can be written as

$$y_k = \sqrt{P_G} h_k\ u_k + \varphi_k. \tag{2.9}$$

To estimate its location, defined by $\theta \triangleq [x_R, y_R]$, the reader initially detects the responses collected from the K tags. To avoid the channel estimation overheads for K signals, the reader may use blind detection schemes such as energy detection [18], where the received signal energy can be expressed as

$$r_k = |y_k|^2 = |\sqrt{P_G} h_k u_k + \varphi_k|^2. \tag{2.10}$$

Generally speaking, the reader does not usually have the exact knowledge of its radiation pattern or its orientation with respect to the tags' grid. Therefore, the value of υ_k should be considered unknown by the reader, and hence the radiation pattern is considered to be circular where $\upsilon_k = 1\ \forall k$, which may cause some performance degradation. Based on (2.10), the ML estimator (MLE) using $\mathbf{r} = [r_1, r_2, \ldots, r_K]$ is given by

$$\begin{aligned}\hat{\theta} &= \arg\max_{\theta} \sum_{k=1}^{K} \ln f\left(r_k|\theta\right) \\ &= \arg\max_{\theta} \sum_{k=1}^{K} \ln \left(\sum_{u_k=0}^{1} f\left(r_k|u_k\right) \Pr\left(u_k|\theta\right) \right) \end{aligned} \tag{2.11}$$

where

$$\Pr\left(u_k|\theta\right) = 1 - u_k + (-1)^{u_k+1} Q\left(\frac{\tau_k - A_k}{\sigma_w}\right). \tag{2.12}$$

It is worth noting that θ in (2.12) is implicitly included in A_k. Since $y_k \sim \mathcal{CN}(0, P_G u_k^2 \sigma_h^2 + \sigma_\varphi^2)$, then r_k is exponentially distributed with mean $\beta_{u_k} = P_G u_k^2 \sigma_h^2 + \sigma_\varphi^2$, where $\sigma_h^2 = \sigma_{\bar{h}}^2 \alpha_k$. Consequently, the MLE can be written as

$$\hat{\theta}_{\text{SDE}} = \arg\max_{\theta} \sum_{k=1}^{K} \ln \left(\sum_{u_k=0}^{1} \frac{1}{\beta_{u_k}} \exp\left(\frac{-r_k}{\beta_{u_k}}\right) \Pr\left(u_k|\theta\right) \right). \tag{2.13}$$

Because the MLE in (2.13) is based on the unquantized values, i.e. soft values, of r_k, it is denoted as soft decision estimator (SDE) [18]. As can be noted from (2.13), it is infeasible to compute $\hat{\theta}$ analytically, and thus, exhaustive search methods should be used.

An alternative approach to estimate the location of the reader is to use r_k to generate hard decisions (binary decisions), for each tag individually, and then the likelihood function is derived based on the hard decisions, and hence it is denoted as the HD estimator (HDE) [20]. In other words, the reader tries to estimate u_k $\forall k$, and use the estimated values, denoted as $\hat{\mathbf{u}} = [\hat{u}_1, \hat{u}_2, ..., \hat{u}_K]$ to estimate its location. The optimum HD detector can be formulated as,

$$\begin{aligned}\hat{u}_k &= \arg \max_{u_k \in \{0,1\}} f\left(r_k|u_k\right), \, k = \{1, 2, ..., K\} \\ &= \arg \min_{u_k \in \{0,1\}} \frac{r_k}{\beta_{u_k}} + \ln \beta_{u_k}. \end{aligned} \tag{2.14}$$

After some manipulations, (2.14) can be written as

$$\hat{u}_k = \begin{cases} 0, & \gamma_0 \leq r_k \leq \gamma_1 \\ 1, & \gamma_1 \leq r_k \leq \gamma_2 \end{cases} \tag{2.15}$$

where $\gamma_0 = 0$, $\gamma_2 = \infty$ and

$$\gamma_1 = \frac{\ln \beta_1 - \ln \beta_0}{\beta_1 - \beta_0} \beta_1 \beta_0. \tag{2.16}$$

Thereafter, the MLE based on $\hat{\mathbf{u}}$ can be formulated as

$$\hat{\theta}_{\text{HDE}} = \arg\max_{\theta} \sum_{k=1}^{K} \ln \left(\sum_{u_k \in \{0,1\}} \Pr\left(\hat{u}_k|u_k\right) \Pr\left(u_k|\theta\right) \right). \tag{2.17}$$

The pairwise probability $\Pr(\hat{u}_k|u_k)$ can be derived from (2.15) and (2.16),

$$\Pr(\hat{u}_k = n|m) = e^{-\frac{\gamma_n}{\beta_m}} - e^{-\frac{\gamma_{n+1}}{\beta_m}} \tag{2.18}$$

where $\{n, m\} \in \{0, 1\}$.

In high signal to noise ratio (SNR) scenarios, the channel can be considered error free and $\Pr(u_k|\theta)$ is equal for nearby tags. Consequently, the decisions made by a particular tag can be corrected at the reader based on the decisions of the nearest M tags [11], and hence, this approach is denoted as the local voting algorithm (LVA). Given that the set of all tags in the RoI is denoted as $\mathbb{A}$, and the set of M neighboring tags is denoted as $\mathbb{B}$, where $\mathbb{B} \subseteq \mathbb{A}$, the decision correction process for each signal in $\mathbb{B}$ can be described as

$$\tilde{u}_k = \begin{cases} 1, & \mathcal{W}(\mathbf{u}_{\mathbb{B}}) \geq \epsilon_0 \\ 0, & \mathcal{W}(\mathbf{u}_{\mathbb{B}}) < \epsilon_0 \end{cases} \tag{2.19}$$

where $\mathbf{u}_{\mathbb{B}} = [u_1, u_2, ..., u_M]$, $\mathcal{W}(\cdot)$ is the Hamming weight, $\tilde{u}_k$ is the corrected decision and $\epsilon_0 \triangleq \lceil M/2 \rceil$, where $\lceil \cdot \rceil$ is the ceiling function. Therefore, the corrected decisions have the following probabilities,

$$\Pr(\tilde{u}_k = 1|\theta) = \sum_{i=\lceil \epsilon_0 \rceil}^{M} \binom{M}{i} (\Pr(u_k = 1|\theta))^i \times (1 - \Pr(u_k = 1|\theta))^{M-i} \tag{2.20}$$

and $\Pr(\tilde{u}_k = 0|\theta) = 1 - \Pr(\tilde{u}_k = 1|\theta)$. Therefore, the MLE based on the LVA algorithm is

$$\hat{\theta}_{\text{LVA}} = \arg\max_{\theta} \sum_{k=1}^{K} \ln(\Pr(\tilde{u}_k|\theta)). \tag{2.21}$$

Generally speaking, the signal transmitted/received by the tag depends on the tag model and frequency band used. In this work, we consider that all RFID tags are omnidirectional in both horizontal and vertical dimensions. Therefore, the transmitted/received signal models of the tags are independent of the tag orientation. The design of such tags at 925 MHz frequency is reported in [28].

2.3 The Proposed Localization Algorithm

To maintain low complexity of the MLE with hard decisions, the proposed algorithm is based on binary energy detection as the first stage to produce the vector $\hat{\mathbf{u}}$ as described in (2.15). In the second stage, error concealment is applied to correct the erroneous decisions and produce a new set of decisions denoted as $\tilde{\mathbf{u}}$. Finally, the MLE is applied to estimate the location of the reader. The proposed localization algorithm with error concealment (LEC) and the MLE are derived in the following two subsections.

Algorithm 1: Error Concealment Process

Input: $\hat{u}_k$, $k = \{1, 2, ..., K\}$, ϵ

1. Form the matrix $\hat{\mathbf{U}} : u_k \leftarrow \hat{U}_{a,b}$, $a = \left\lceil \frac{k}{\sqrt{K}} \right\rceil$, $b = k \mod \left(\sqrt{K}+1\right)$
2. **for** $m = 2 : \sqrt{K} - 1$
3. **for** $n = 2 : \sqrt{K} - 1$
4. compute $W\left(\hat{\mathbf{U}}(m-1 : m+1, n-1 : n+1)\right)$
5. set $\tilde{u}_k = \begin{cases} 1, & \mathcal{W} \geq \epsilon \\ 0, & \text{otherwise} \end{cases}$
6. **end for**
7. **end for**
8. **return:** $\tilde{u}_k$, $k = \{1, 2, ..., K\}$

2.3.1 The error concealment process

Due to channel impairments, it is highly likely that $\hat{\mathbf{u}}_{\mathbb{B}} \neq \mathbf{u}_{\mathbb{B}}$, and hence the performance of the MLE may deteriorate. In practical scenarios, tags in the vicinity of each other are expected to produce similar decisions, i.e., $u_1 = u_2 = \cdots = u_M$. Therefore, the LEC is designed to exploit such correlation to correct the errors before the location estimation process. An example for the LEC using $M = 9$ is given in **Algorithm 1**.

The correction threshold ϵ should be dynamically adjusted to consider the variable number of tags in $\mathbb{B}$ that detected the RIS as well as the imbalanced probability induced by the hard decision detector. By noting that ϵ is typically set to ϵ_0 in error free transmissions [11], it can be dynamically changed by considering the channel effects on the signals sent from the tags to the reader. Thus,

$$\begin{aligned} \epsilon &= \mathcal{E}\left[\mathcal{W}\left(\hat{\mathbf{u}}_{\mathbb{B}}\right) \left|\mathcal{W}\left(\mathbf{u}_{\mathbb{B}}\right) = \epsilon_0\right.\right] \\ &= \sum_{i=0}^{M} \mathcal{E}\left[\hat{u}_i \left|\mathcal{W}\left(\mathbf{u}_{\mathbb{B}}\right) = \epsilon_0\right.\right] \\ &= \sum_{i=0}^{M} \sum_{\hat{u}_i=\{0,1\}} \hat{u}_i \Pr\left(\hat{u}_i \left|\mathcal{W}\left(\mathbf{u}_{\mathbb{B}}\right) = \epsilon_0\right.\right). \end{aligned} \tag{2.22}$$

By noting that $\hat{u}_i \Pr\left(\hat{u}_i|\epsilon_0\right) = 0$ when $\hat{u}_i = 0$, then (2.22) can be simplified to

$$\epsilon = \sum_{i=0}^{M} \Pr\left(\hat{u}_i = 1 \left|\mathcal{W}\left(\mathbf{u}_{\mathbb{B}}\right) = \epsilon_0\right.\right). \tag{2.23}$$

Using the law of total probability, the summand in (2.23) can be written as

$$\begin{aligned} \Pr\left(\hat{u}_k = 1 \left|\mathcal{W}\left(\mathbf{u}_{\mathbb{B}}\right) = \epsilon_0\right.\right) = {} & \Pr\left(u_k = 1 \left|\mathcal{W}\left(\mathbf{u}_{\mathbb{B}}\right) = \epsilon_0\right.\right) \Pr\left(\hat{u}_k = 1 \left|u_k = 1\right.\right) \\ & + \Pr\left(u_k = 0 \left|\mathcal{W}\left(\mathbf{u}_{\mathbb{B}}\right) = \epsilon_0\right.\right) \Pr\left(\hat{u}_k = 1 \left|u_k = 0\right.\right). \end{aligned} \tag{2.24}$$

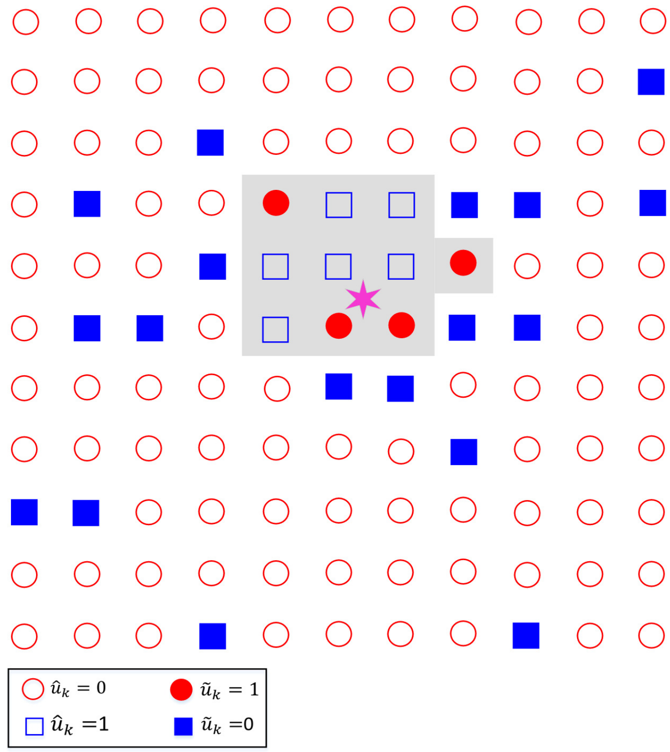

Figure 2.1: Example of the error concealment process for $M = 9$.

Given that $\mathcal{W}(\mathbf{u}_{\mathbb{B}}) = \epsilon_0$, then $\Pr(u_k = 1 \,|\mathcal{W}(\mathbf{u}_{\mathbb{B}}) = \epsilon_0) = \frac{\epsilon_0}{M}$, and thus

$$\Pr(\hat{u}_k = 1 \,|\mathcal{W}(\mathbf{u}_{\mathbb{B}}) = \epsilon_0) = \frac{\epsilon_0}{M}\Pr(\hat{u}_k = 1 \,|u_k = 1) + \left(1 - \frac{\epsilon_0}{M}\right)\Pr(\hat{u}_k = 1 \,|u_k = 0) \tag{2.25}$$

where $\Pr(\hat{u}_k = 1 \,|u_k = 1)$ and $\Pr(\hat{u}_k = 1 \,|u_k = 0)$ are given in (2.18).

In the special case that the average SNRs of the received signals from the tags in $\mathbb{B}$ are equal, then the probability of error for all tags in $\mathbb{B}$ is equal, which is mostly the case since all tags in $\mathbb{B}$ have approximately the same path loss. Moreover, by noting that for $\lceil M/2 \rceil \approx M/2$ for $M \gg 1$, then $\epsilon_0/M \approx 0.5$. By substituting $\epsilon_0/M = 0.5$ in (2.25), and substituting (2.25) in (2.23), then ϵ can be computed as

$$\epsilon = \frac{M}{2}\left(e^{-\left(\frac{\gamma_1}{\beta_1}\right)} + e^{-\left(\frac{\gamma_1}{\beta_0}\right)}\right). \tag{2.26}$$

Fig. 2.1 shows an example selected from one of the simulation results for the error concealment process for an 11×11 grid. The sliding window started from the top-left corner where $M = 9$ and $\epsilon = 5$. As can be noted from the figure, the concealment process inverted 22 values, 18 tags were excluded ($1 \rightarrow 0$) and 4 were included ($0 \rightarrow 1$). In this scenario, about 4 of the excluded tags are close to the reader and should have been considered. Nevertheless, the number of eliminated outliers is much larger than the number of legitimate tags that were erroneously excluded, which implies that the localization accuracy will eventually improve.

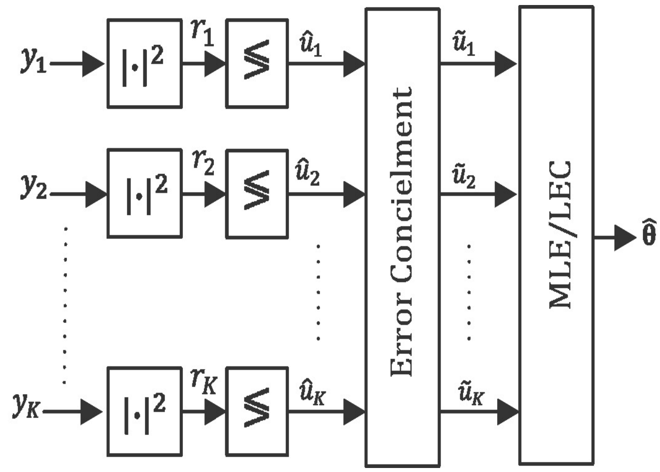

Figure 2.2: Block Diagram of the proposed LEC.

2.3.1.1 LEC based maximum likelihood estimator

The MLE is formulated based on the corrected decisions obtained from the LEC, and thus

$$\hat{\theta}_{\text{LEC}} = \arg\max_{\theta} \sum_{k=1}^{K} \ln\left(\Pr\left(\tilde{u}_k|\theta\right)\right). \tag{2.27}$$

By noting that $\tilde{u}_k \in \{0,1\}$, the summand in (2.27) $\sum_{k=1}^{K} \ln\left(\Pr\left(\tilde{u}_k|\theta\right)\right) \triangleq \Lambda_{\text{LEC}}\left(\theta\right)$ can be expressed as

$$\Lambda_{\text{LEC}}\left(\theta\right) = \sum_{k=1}^{K} \tilde{u}_k \ln\left(\Pr\left(\tilde{u}_k = 1|\theta\right)\right) + \left(1-\tilde{u}_k\right)\ln\left(\Pr\left(\tilde{u}_k = 0|\theta\right)\right). \tag{2.28}$$

Since $\mathcal{W}\left(\hat{\mathbf{u}}_{\mathbb{B}}\right)$ is a sum of M independent Bernoulli random variables with different probability of success, then $\tilde{u}_k$ is a Poisson-binomial distributed random variable with a cumulative distribution function (CDF) given by [29]

$$\begin{aligned}\Pr\left(\tilde{u}_k = 0|\theta\right) &= \Pr\left(\mathcal{W}\left(\hat{\mathbf{u}}_{\mathbb{B}}\right) < \epsilon|\theta\right)\\ &= \frac{\epsilon}{M+1} + \frac{1}{M+1}\sum_{i=1}^{M}\left(\frac{1-e^{-\frac{j2\pi i\epsilon}{M+1}}}{1-e^{-\frac{j2\pi i}{M+1}}} \times \prod_{l=1}^{M}\left(p_l e^{\frac{j2\pi i}{M+1}} + 1 - p_l\right)\right)\end{aligned} \tag{2.29}$$

where p_l is given by

$$\begin{aligned}p_l &= \Pr\left(\hat{u}_l = 1|\theta\right)\\ &= \sum_{u_l\in\{0,1\}} \Pr\left(\hat{u}_l = 1|u_l\right)\Pr\left(u_l|\theta\right).\end{aligned} \tag{2.30}$$

Finally, (2.29) is substituted in (2.28), and PSO is applied to compute $\hat{\theta} = \left(\hat{x}_R, \hat{y}_R\right)$ which maximizes $\Lambda_{\text{LEC}}\left(\theta\right)$.

To summarize the proposed system, Fig. 2.2 and **Algorithm 2** are presented, where the figure shows the system level block diagram while **Algorithm 2** describes the system in a step-by-step manner.

Algorithm 2: Proposed LEC
Input: y_k, $k = \{1, 2, ..., K\}$
1. **for** $k = 1 : K$
2. Compute r_k using (2.10)
3. Compute $\hat{u}_k$ using (2.15)
4. **end for**
5. Compute $\tilde{\mathbf{u}} = [\tilde{u}_1,\ \tilde{u}_2, ..., u_K]$ using **Algorithm 1**
6. **for** $k = 1 : K$
7. Compute p_l using (2.30)
8. Compute $\Pr(\tilde{u}_k = 0 \vert \theta)$ using (2.29)
9. **end for**
10. Compute $\Lambda_{\mathrm{LEC}}(\theta)$ using (2.28)
11. Compute $\hat{\theta}$ in (2.27) using PSO
12. **return** $\hat{\theta} = [\hat{x}_R, \hat{y}_R]$

Generally speaking, all HD based estimators [18]- [20] have comparable computational complexity, which is mostly determined by the maximization of the likelihood function. However, the proposed LEC and LVA [11] have some additional complexity over [20] caused by the error correction process. Nevertheless, the correction process is based on a low complexity majority voting operation within a small size sliding window, and hence, the computational complexity of the proposed LEC and [18]- [20] can be considered equivalent.

2.4 CRLB of the Proposed Estimator

The variance of an unbiased estimator is bounded by $\mathbf{F}^{-1}$, where $\mathbf{F}$ is the Fisher information matrix [26],

$$\mathcal{E}\left[\left(\hat{\theta} - \theta\right)\left(\hat{\theta} - \theta\right)^H\right] \geq \mathbf{F}^{-1} \tag{2.31}$$

where $(\cdot)^H$ is the Hermitian operator. The Fisher information matrix of $\hat{\theta} = \max_\theta \Lambda_{\mathrm{LEC}}(\theta)$ is given by

$$\begin{aligned} \mathbf{F} &= \mathcal{E}\left[-\nabla_\theta (\nabla_\theta)^t \left(\Lambda_{\mathrm{LEC}}(\theta)\right)\right] \\ &= -\mathcal{E}\begin{bmatrix} \frac{\partial^2 \Lambda_{\mathrm{LEC}}(\theta)}{\partial x_R^2} & \frac{\partial^2 \Lambda_{\mathrm{LEC}}(\theta)}{\partial x_R \partial y_R} \\ \frac{\partial^2 \Lambda_{\mathrm{LEC}}(\theta)}{\partial x_R \partial y_R} & \frac{\partial^2 \Lambda_{\mathrm{LEC}}(\theta)}{\partial y_R^2} \end{bmatrix} \end{aligned} \tag{2.32}$$

where ∇_θ and $(\cdot)^t$ are the gradient and transpose operators, respectively. The elements of $\mathbf{F}$ are

$$\mathbf{F}_{1,1} = \sum_{k=1}^{K} \sum_{\tilde{u}_k} \frac{1}{\Pr(\tilde{u}_k \vert \theta)} \left(\frac{\partial}{\partial x_R} \Pr(\tilde{u}_k \vert \theta)\right)^2 \tag{2.33}$$

$$\mathbf{F}_{2,2} = \sum_{k=1}^{K} \sum_{\tilde{u}_k} \frac{1}{\Pr(\tilde{u}_k \vert \theta)} \left(\frac{\partial}{\partial y_R} \Pr(\tilde{u}_k \vert \theta)\right)^2 \tag{2.34}$$

$$\mathbf{F}_{1,2} = \sum_{k=1}^{K} \sum_{\tilde{u}_k} \frac{1}{\Pr(\tilde{u}_k \vert \theta)} \frac{\partial}{\partial x_R} \Pr(\tilde{u}_k \vert \theta) \frac{\partial}{\partial y_R} \Pr(\tilde{u}_k \vert \theta) \tag{2.35}$$

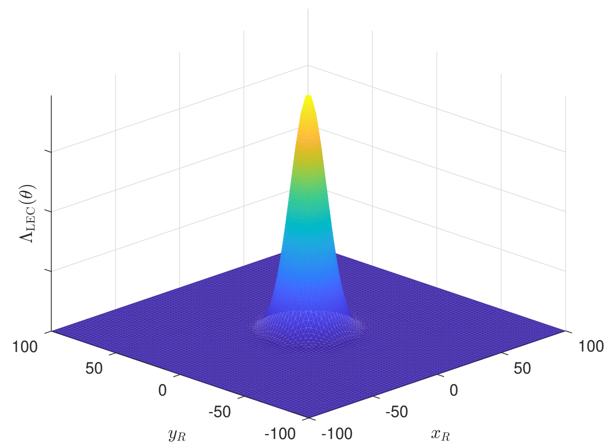

Figure 2.3: The log-likelihood function where $K = 256$, $L = 50$, SNR = 50 dB and $(x_R, y_R) = (0, 0)$.

$$\mathbf{F}_{2,1} = \mathbf{F}_{1,2} \tag{2.36}$$

and the derivative $\frac{\partial}{\partial x_R} \Pr(\tilde{u}_k|\theta)$ is given by

$$\frac{\partial}{\partial x_R} \Pr(\tilde{u}_k = 1|\theta) = \frac{-1}{M+1} \sum_{i=1}^{M} \left(\frac{1 - e^{-\frac{j2\pi i \epsilon}{M+1}}}{1 - e^{-\frac{j2\pi i}{M+1}}} \times \prod_{l=1}^{M} \left(p_l e^{\frac{j2\pi i}{M+1}} + 1 - p_l \right) \times \sum_{l=1}^{M} \frac{\partial p_l}{\partial x_R} \frac{\left(e^{\frac{j2\pi i}{M+1}} - 1 \right)}{p_l e^{\frac{j2\pi i}{M+1}} + 1 - p_l} \right) \tag{2.37}$$

where $j \triangleq \sqrt{-1}$, and

$$\frac{\partial p_l}{\partial x_R} = \frac{-\upsilon_l \sqrt{P_R} \mathcal{E}\left\{\rho_k[l]\right\} \lambda d_l^{-3}}{4\pi\sigma_l\sqrt{2\pi}} e^{-\frac{(\tau_l - \upsilon_l A_l)^2}{2\sigma_l^2}} (x_R - x_{G_k}) \times \left[\Pr(\hat{u}_l = 1|u_l = 1) - \Pr(\hat{u}_l = 1|u_l = 0)\right]. \tag{2.38}$$

It can be noted that $\frac{\partial}{\partial x_R} \Pr(\tilde{u}_k = 0|\theta) = -\frac{\partial}{\partial x_R} \Pr(\tilde{u}_k = 1|\theta)$ and $\frac{\partial}{\partial y_R} \Pr(\tilde{u}_k = 0|\theta) = -\frac{\partial}{\partial y_R} \Pr(\tilde{u}_k = 1|\theta)$ since $\Pr(\tilde{u}_k = 0|\theta) = 1 - \Pr(\tilde{u}_k = 1|\theta)$. Moreover, $(x_R - x_{G_k})$ in (2.37) and (2.38) can be replaced by $(y_R - y_{G_k})$ to find $\frac{\partial}{\partial y_R} \Pr(\tilde{u}_k|\theta)$.

2.5 Numeric Results

This section presents the simulation results for the proposed localization algorithm and compares them to those of the algorithms reported in [18]- [20]. The Monte Carlo simulation is configured to perform 500 runs for each simulation point, where a PSO with 12 particles and 10 generations is applied to find the global maximum of the log-likelihood function. The RFID tags with known positions are uniformly distributed over a grid with an area of (200 m × 200 m). The obtained results are generated for various operating scenarios such as the reader location, SNR and number of tags. The system and channel parameters for the downlink (reader→tag) are: $\mathcal{E}\{\rho_k[l]\} = 1\ \forall k$, $N_0 = 10^{-10}$ W/Hz, $P_R = 0$ dBW, $P_G = -10$ dBW, $\sigma_h^2 = 1$, $\lambda = 0.3$ m, and $d_0 = 30$ m. The RMSE is defined as $\sqrt{\mathcal{E}\left[(x_R - \hat{x}_R)^2 + (y_R - \hat{y}_R)^2\right]}$.

Fig. 2.3 depicts the log-likelihood function in three dimensional representation, where 256 tags are

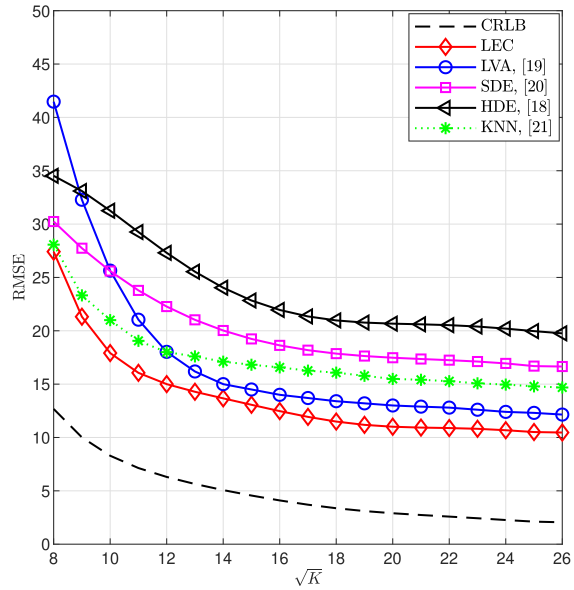

Figure 2.4: RMSE of the estimated position using the proposed LEC, LVA [11], SDE [20], HDE [18], and KNN [21] using SNR = 8 dB.

distributed over the RoI to localize an RFID reader located at $(x_R = 0, y_R = 0)$ position. The SNR $\triangleq P_G/\sigma_\varphi^2$ is set to 50 dB and the number of RISs $L = 50$. As can be noted from the figure, the log-likelihood function has a global maximum that corresponds to the Cartesian coordinates of the reader estimated location.

Fig. 2.4 shows the RMSE of the proposed estimator for different values of K using SNR = 8 dB, $(x_R = 5,\ y_R = 22)$ and $L = 10$. The figure also presents the RMSE of the LVA [11], SDE [18], HDE [20], KNN [21], and the CRLB. The results in the figure show that the proposed LEC outperforms all the other considered estimators for the entire range of K. However, the improvement depends on the values of K. The average relative improvement over the considered range of K with respect to the LVA, SDE, HDE and KNN is about 26.5%, 46.1%, 74.3%, and 26.9%, respectively. Moreover, it can be noted that the LVA performs poorly at low values of K since the correction window may include readings from distant tags. The KNN algorithm outperforms the HDE and SDE for the entire range of K, and the LVA for $K < 144$. The KNN and LEC demonstrate equivalent RMSE at $K = 64$.

Fig. 2.5 is generated using the same parameters used for Fig. 2.4 except that SNR = 15 dB. As can be seen from the figure, all the considered algorithms exhibit significant RMSE reduction, particularly the LVA one since the assumption that the tag→reader channel is error free becomes plausible at such high SNRs. The average relative improvement of the proposed LEC algorithm over the LVA, SDE, HDE, and KNN algorithms is about 4.5%, 55.1%, 67.5%, and 84%, respectively. The figure also shows that the KNN RMSE improves by increasing the SNR, though at a slower rate in comparison to the other considered techniques. Moreover, the results in Figs. 2.4 and 2.5 show that the RMSE of the proposed estimator approaches the CRLB when there is a large number of tags and high SNRs.

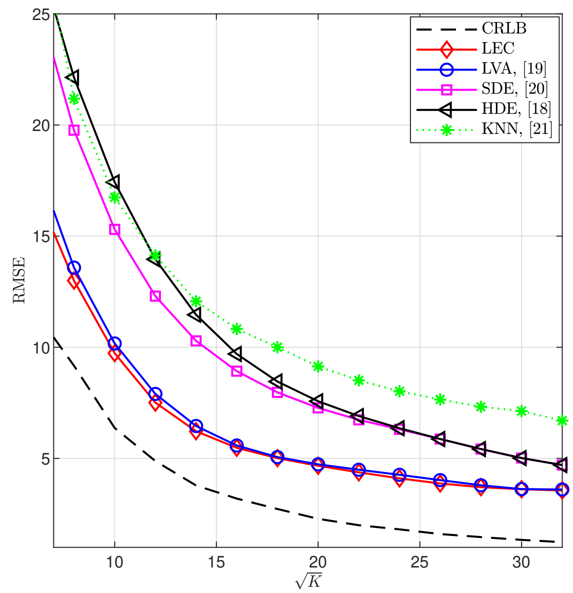

Figure 2.5: RMSE of the estimated position using the proposed LEC, LVA [11], SDE [20], HDE [18], and KNN [21] using SNR = 15 dB.

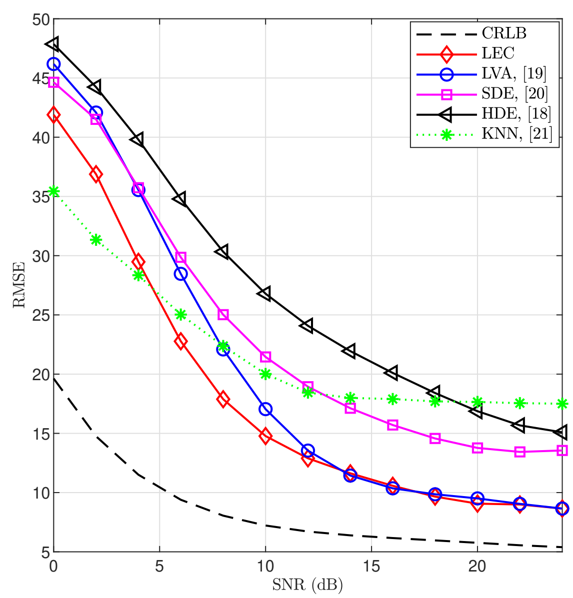

Figure 2.6: The RMSE of the estimated position using the proposed LEC, LVA [11], SDE [20], HDE [18], and KNN [21] versus SNR, $K = 100$.

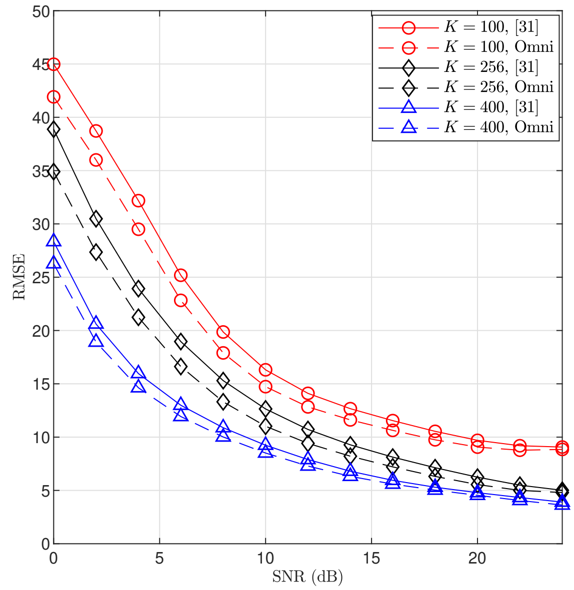

Figure 2.7: The impact of the antenna pattern on the LEC localization algorithm.

Fig. 2.6 shows the RMSE of the considered estimators versus SNR using $L = 10$, $K = 100$, and the reader is located at $(x_R = 10, y_R = 27)$. The results in the figure show that the proposed LEC noticeably outperforms the SDE and HDE for the considered range of SNRs, and the LVA at low SNRs. For SNR $\gtrsim$ 12 dB, the RMSE of the LEC and LVA converge since the tag→reader link becomes nearly error free. The KNN outperforms the proposed LEC at SNRs$\lesssim$ 4.7 dB, which is due to the fact the error concealment process fails to improve the performance at very low SNRs. The average improvement with respect to the LVA, SDE, HDE and KNN is about 12.2%, 31.5%, 53.5%, and 24.5%, respectively.

Fig. 2.7 illustrates the performance of the proposed localization algorithm using a practical antenna pattern, where the power radiation is non-uniform. More specifically, we consider the radiation pattern of the HyperLink HG908U-PRO from L-Com [31], which is ideally considered as an omnidirectional, but practically it may exhibit up to 37% (2 dB) irregularity in certain directions. As can be noted form the figure, the irregularity of the radiation pattern causes some performance degradation that depends on the grid size and SNR. At low SNRs, the degradation for all the considered cases is less than 1 dB because the performance is mostly determined by the AWGN at low SNRs. At moderate SNRs, the degradation increases to about 2 dB because the impact of the nonuniform radiation pattern become more apparent when the impact of the AWGN is not significant. At high SNRs, the RMSE of the practical and ideal patterns converge because in high power scenarios, all tags in the vicinity of the reader will received sufficient power to respond back to the reader.

2.6 Conclusion and Future Work

In this paper, the problem of RFID reader localization using distributed tags was considered. To mitigate the impact of channel impairments, a novel maximum likelihood estimator was proposed based on the signals received from the tags. By considering that the reader performs hard decisions on the signals received from the tags, a simple error concealment process is applied to improve the estimator's accuracy. The system was simulated for different cases of interest and the RMSE results were compared to four benchmark estimators. The obtained results showed that the proposed estimator considerably outperforms the other considered localization techniques. Moreover, the CRLB for the RMSE of the proposed algorithm was derived to asses its efficiency.

To capture the impact of various practical imperfections, evaluating the performance of the proposed algorithm experimentally is indispensable. Therefore, our future work includes developing a testbed to collect a large set of results in different channel conditions and compare the experimental results with the simulation and analytical results obtained in this work.

References

[1] A. Athalye, V. Savic, M. Bolic, and P. Djuric, “Novel semi-passive RFID system for indoor localization,” *IEEE Sensors J.*, vol. 13, no. 2, pp. 528-537, Feb. 2013.

[2] W. Zhu, J. Cao, Y. Xu, L. Yang and J. Kong, “Fault-tolerant RFID reader localization based on passive RFID tags,” *IEEE Trans. Parallel Distrib. Syst.*, vol. 25, no. 8, pp. 2065-2076, Aug. 2014.

[3] H. Yu, J. Chen, and T. Hsiang, “Design and implementation of a real-time object location system based on passive RFID tags,” *IEEE Sensors J.*, vol. 15, no. 9, pp. 5015-5023, Sep. 2015.

[4] L. Xie, Y. Yin, A. Vasilakos, and S. Lu, “Managing RFID data: challenges, opportunities and solutions,” *IEEE Commun. Surveys Tuts.*, vol. 16, no. 3, pp. 1294-1311, 2016.

[5] E. DiGiampaolo and F. Martinelli, “Mobile robot localization using the phase of passive UHF RFID signals,” *IEEE Trans. Ind. Electron.*, vol. 61, no. 1, pp. 365-376, Jan. 2014.

[6] Z. Zhang, *et al.*, “Item-level indoor localization with passive UHF RFID based on tag interaction analysis,” *IEEE Trans. Ind. Electron.*, vol. 61, no. 4, pp. 2122-2135, Apr. 2014.

[7] M. Scherhäufl, M. Pichler, and A. Stelzer, “UHF RFID localization based on evaluation of backscattered tag signals,” *IEEE Trans. Instrum. Meas.*, vol. 64, no. 11, pp. 2889-2899, Nov. 2015.

[8] Y. Zhao, *et al.*, “Similarity analysis-based indoor localization algorithm with backscatter information of passive UHF RFID tags,” *IEEE Sensors J.*, vol. 17, no. 1, pp. 185-193, Jan. 2017.

[9] S. Subedi, E. Pauls, and Y. Zhang, “Accurate localization and tracking of a passive RFID reader based on RSSI measurements,” *IEEE Trans. Radio Freq. Identification*, vol. 1, no. 2, pp. 144-154, Jun. 2017.

[10] H. Xiong, J. Tang, H. Xu, W. Zhang, and Z. Du , “A robust single GPS navigation and positioning algorithm based on strong tracking filtering,” *IEEE Sensors J.*, vol. 18, no. 1, pp. 290-298, Jan. 2018.

[11] C. Yao and W. Hsia, “An indoor positioning system based on the dual-channel passive RFID technology,” *IEEE Sensors J.*, vol. 18, no. 11, pp. 4654-4663, 1 Jun. 2018.

[12] W. Shi, *et al.*, "Optimizing directional reader antennas deployment in UHF RFID localization system by using a MPCSO algorithm," *IEEE Sensors J.*, vol. 18, no. 12, pp. 5035-5048, Jun. 2018.

[13] M. El-Absi, A. Abbas, A. Abuelhaija, F. Zheng, K. Solbach, and T. Kaiser, "High-accuracy indoor localization based on chipless RFID systems at THz band," *IEEE Access*, vol. 6, pp. 54355-54368, Sep. 2018.

[14] J. Zhang, Y. Lyu, J. Patton, S. Periaswamy, and T. Roppel, "BFVP: A probabilistic UHF RFID tag localization algorithm using Bayesian filter and a variable power RFID model," *IEEE Trans. Ind. Electron.*, vol. 65, no. 10, pp. 8250-8259, Oct. 2018.

[15] H. Xiong, *et al.*, "Efficient bias reduction approach of time-of-flight-based wireless localization networks in NLOS states," *IET Radar Sonar Nav.*, vol. 12, no. 11, pp. 1353-1360, Nov. 2018.

[16] H. Xiong, M. Peng, S. Gong, and Z. Du, "A novel hybrid RSS and TOA positioning algorithm for multi-objective cooperative wireless sensor networks," *IEEE Sensors J.*, vol. 18, no. 22, pp. 9343-9351, Nov. 2018.

[17] M. Scherhäufl, B. Rudić, A. Stelzer, and M. Pichler-Scheder, "A blind calibration method for phase-of-arrival-based localization of passive UHF RFID transponders," *IEEE Trans. Instrum. Meas.*, vol. 68, no. 1, pp. 261-268, Jan. 2019.

[18] O. Ozdemir, R. Niu, and P. Varshney, "Channel aware target localization with quantized data in wireless sensor networks," *IEEE Trans. Signal Process.*, vol. 57, no. 3, pp. 1190-1202, Mar. 2009.

[19] N. Katenka, E. Levina, and G. Michailidis, "Tracking multiple targets using binary decisions from wireless sensor networks," *J. Am. Stat. Assoc.*, vol. 108, no. 502, pp. 398-410, Feb. 2013.

[20] R. Niu, A. Vempaty, and P. Varshney, "Received-signal-strength-based localization in wireless sensor network," *Proc. IEEE*, vol. 106, no. 7, pp. 1166-1182, Jul. 2018.

[21] M. Hoang, *et al.*, "A soft range limited K-nearest neighbors algorithm for indoor localization enhancement," *IEEE Sensors J.*, vol. 18, no. 24, pp. 10208-10216, Dec. 2018.

[22] M. Anisetti, C. Ardagna, V. Bellandi, E. Damiani, and S. Reale, "Map-based location and tracking in multipath outdoor mobile networks," *IEEE Trans. Wireless Commun.*, vol. 10, no. 3, pp. 814-824, Mar. 2011.

[23] K. Wei, Z. Zhang, Z. Feng, and M. Iskander, "A MNG-TL loop antenna array with horizontally polarized omnidirectional patterns," *IEEE Trans. Antennas Propag.*, vol. 60, no. 6, pp. 2702-2710, Jun. 2012.

[24] J. Shi, X. Wu, X. Qing, and Z. Chen, “An omnidirectional circularly polarized antenna array,” *IEEE Trans. Antennas Propag.*, vol. 64, no. 2, pp. 574-581, Feb. 2016.

[25] K. Wei, Z. Zhang, and Z. Feng, “Design of a wideband horizontally polarized omnidirectional printed loop antenna,” *IEEE Antennas Wireless Propag. Lett.*, vol. 11, pp. 49-52, 2012.

[26] J. Su, Z. Sheng, L. Xie, G. Li and A. X. Liu, “Fast splitting-based tag identification algorithm for anti-collision in UHF RFID system,” *IEEE Trans. Commun.*, vol. 67, no. 3, pp. 2527-2538, Mar. 2019.

[27] `https://www.zebra.com/us/en/products/rfid/rfid-handhelds/rfd2000.html`.

[28] S. Chen, K. Lin, and R. Mittra, “Miniature and near-3D omnidirectional radiation pattern RFID tag antenna design,” *Electron. Lett.*, vol. 45, no. 18, pp. 923-924, 27, Aug. 2009.

[29] M. Fernandez and S. Williams, “Closed-form expression for the Poisson-binomial probability density function,” *IEEE Trans. Aerosp. Electron. Syst.*, vol. 46, no. 2, pp. 803–817, Apr. 2010.

[30] H. Poor. An introduction to signal detection and estimation, 2nd ed. New York: Springer-Verlag, 1994.

[31] L-Com Global Connectivity, “Hyperlink wireless 900 MHz 8 dBi professional high performance omni antenna ,” HG908U-PRO datasheet.

Chapter 3

Joint Estimation of Location and Orientation in Wireless Sensor Networks using Directional Antennas[1]

Abstract

This paper presents a joint location and orientation estimation algorithm for a mobile robot (MR) equipped with directional antennas in wireless sensor networks (WSNs). The proposed algorithm utilizes the antennas' directivity and signals received from a set of distributed sensors to estimate the location and the facing direction of the receiver. The MR may use multiple directive antennas, or a single antenna whose beam can be steered electronically or mechanically. The received signals from each antenna, or antenna direction, are applied to a simple linear regression algorithm that decides the direction of the object for that particular beam scan. The process is repeated for different angles, and the results obtained are used to estimate the location and orientation of the MR. Moreover, error concealment techniques are used to improve the estimation accuracy by applying the local majority voting and connected graph algorithms. The obtained experimental and simulation results show that the proposed approach can estimate the location and orientation with high accuracy, especially at high signal-to-noise-ratio (SNR).

Index Terms

Target localization, location estimation, orientation estimation, Rician fading, majority voting algorithm, connected graph, linear regression.

[1]**M. A. Al-Jarrah**, A. Al-Dweik, N. T. Ali and E. Alsusa, "Joint estimation of location and orientation in wireless sensor networks using directional antennas," *IEEE Sensors. J.*, vol. 20, no. 23, pp. 14347-14359, Dec. 2020, doi: 10.1109/JSEN.2020.3008393.

3.1 Introduction

Indoor localization of humans and assets is challenging because of the lack of line of sight (LoS) signals, and severe multipath and shadow fading problems, making it difficult to accurately locate objects. Using wireless sensor networks has attracted many researchers because of the increased accuracy of location estimation and the high number of possible applications. Various technologies have been proposed in the literature used for indoor positioning including, wireless local area networks (WLANs), infrared, radio frequency identification (RFID), ultra-sound, radio, Bluetooth, etc. [4, 6, 12, 14, 15, 19]. Generally, localization techniques use basic measurements to extract features such as received signal strength (RSS) [7, 16], time of arrival (ToA), time difference of arrival (TDoA) [11, 13, 22] and angle of arrival (AoA) [12]. Both, ToA and TDoA, require precise time synchronization to produce accurate results, which is difficult to realize using current buildings' infrastructure, while the computational complexity of the AoA is prohibitively high. RSS, however, is simple to implement but not sufficiently accurate for most localization applications.

Although the RSS approach suffers from low positioning accuracy, it is considered a good candidate for wireless sensor networks (WSNs) due to the ease of implementation, as well as the fact that many low energy sensors can perform the detection without additional requirements. Several algorithms were proposed to improve the RSS based target location estimation such as the maximum likelihood (ML), least square (LS), and semidefinite programming (SDP). For instance, in [16], a location estimator is proposed based on SDP [14, 58], for either unknown or inaccurate transmit powers and path losses. The authors in [34] used an error correction technique to enhance the accuracy of target location estimation when the exact sensor locations are included. The presented results show that their method outperforms the LS [22], and the computationally expensive ML estimator (MLE) [35]. Moreover, using machine learning techniques demonstrated some promising results in certain scenarios, but such techniques are unsuitable for low power WSN applications [17, 18].

Because most WSNs are based on battery-powered sensors, reducing the transmission and processing energy consumption is paramount. Towards this goal, the authors in [33] applied the Cramer-Rao lower bound (CRLB) criterion to design a quantized-data based MLE, which is optimized using a sensor selection approach. Channel information is also considered to increase the localization accuracy with a manageable increase in power consumption. Another location estimator based on ML with a low complexity error concealment for RFID networks is proposed in [12], where a target, such as a mobile robot (MR), can talk only to selected sensors that are within its antenna detection range. The algorithm considers the multipath effects and radio frequency (RF) tags with unequal separation distances.

Location estimation algorithms can be also designed using directional antennas, because they have several desirable features such as high gain, reduced interference and less reflections from the surroundings [20–30]. However, using a particular directional antenna may influence the system performance in terms of size, hardware compatibility, power consumption and production cost. Therefore, optimizing the directional antenna design is critical for efficient system realization.

In the literature, the antenna design for various localization algorithms has received extensive attention. For example, the antenna design for RSS-based location and orientation estimation is considered in [20,23,24,31,32] for objects in the antenna near-field while the far-field is considered in [25–29]. Passive planar directional antennas, such as planar array, amplitude monopulse antenna array, frequency steered leaky wave antennas (LWAs), etc., are popular choices because they can be produced with low cost using microstrip technology, and their performance and operation are reliable and well understood. For example, in [23], [26], [29], electronically steered amplitude monopulse antennas are deployed to improve the estimation of localization and DoA of mobile devices using RSS fingerprinting. The authors in [24], [27], demonstrated the benefits of adopting directional LWAs for powering sensors in a WSN using frequency hopping to steer the antenna beam. LWAs are also used with low energy Bluetooth sensors to construct an inexpensive WSN [28]. The battery life of the Bluetooth sensors is extended by allowing the mobile device to process the RSSI information.

Robot localization has attracted significant attention because of the extensive indoor and outdoor applications such as industrial automation, search and rescue missions, autonomous vehicles tracking and surveillance [34, 39]. In [39], robot navigation is achieved by using colored line sensors to enhance the accuracy of the RFID technology in following paths designated using Petri nets approach. In another work [34], robot localization and steering accuracy were enhanced by feeding data from multiple sensors, gyroscope, magnetometer, and a direction sensor, into a specifically developed orientation algorithm. The algorithm is based on Kalman filter and a gross error recognizer. Nevertheless, location knowledge could be insufficient in certain scenarios such as autonomous robots, or when the human controlling the robot does not have a clear view of the robot orientation [35, 36].

As can be noted from the aforementioned discussion, developing an efficient algorithm for joint localization and orientation estimation in the context of low energy WSN is indispensable. Consequently, we propose a simple and computationally efficient mathematical procedure for localizing an MR using distributed sensors with known locations. The proposed scheme exploits the antenna directivity to jointly estimate the location and orientation of the MR using linear regression. Moreover, error concealment algorithms such as the majority voting algorithm (MVA) and connected graph (CG) theory are applied to increase the accuracy of the location and orientation estimation. The obtained results show that the proposed scheme provides accurate estimation for the location and orientation at considerable values of signal-to-noise-ratio (SNR).

The rest of the paper is organized as follows. In Section II, the system model and problem formulation are provided. Section III shows the proposed joint direction-location estimation procedure. Sections IV and V present the numerical results and conclusion, respectively.

3.2 System Model and Problem Formulation

Generally, a WSN consists of a massive number of sensors deployed in a geographical area to collect data from the environment and forward it to a central device through wireless transmissions. The central device aggregates the data of all sensors in the network and applies certain operations to this data such as fusion and storage, and may perform certain actions such as sending commands to various actuators or generating alerts. In several applications, an MR, possibly an unmanned aerial vehicle (UAV), is used to collect the data from the sensors. Hence, the estimation of location and orientation of the aggregating device is necessary to follow a certain planned trajectory. In this work, we consider joint estimation of the location and orientation of an MR in the context of WSNs. The WSN is assumed to have $N \times N$ sensors that are distributed according to a two-dimensional (2D) grid topology, and the network covers a certain area, which has a range $0 \to x_U$ in the x-direction and $0 \to y_U$ in the y-direction. The sensors' coordinates are assumed to be known by the MR, which can be achieved through the network initial deployment and configuration, where the coordinates and sensor identification (ID) information are provided to the MR. Due to its power efficiency and low complexity, the sensors use amplitude shift keying (ASK) modulation to communicate with the MR.

Without loss of generality, the considered MR is assumed to be located at (x_0, y_0), and it is equipped with a directional antenna for transmission and reception. The antenna beam is assumed to be with rotation angle θ^o from the positive x-axis, and has a beam-width of ϕ^o. The MR transmits an interrogation signal to the sensors located within its antenna coverage area, and in turn the sensors respond by sending any collected information. This information may include temperature, humidity, etc. As a result, the sensors inside the coverage area will respond to the MR by sending the information they collected to the MR. In this work, we assume that the sensors respond to the MR through using interference-free multiple access (MAC) protocol, such as time division multiple access (TDMA). Therefore, each sensor transmits according to a certain timing schedule. This enables the MR to identify the sensor ID through the allocated time slot.

Although a contention-free MAC protocol is considered in this work, contention-based protocols can be also adopted [37, 38]. In most contention-based protocols, severe interference is produced when two or more sensors attempt to access the channel simultaneously, i.e., when a collision occurs. In such protocols, to inform the sensor that the data was delivered correctly, the MR sends a short packet to acknowledge correctly received packets. Otherwise, after waiting for a certain time period, the sensor retransmits the same packet again. Although adopting such protocols is attractive due to their low complexity, their throughput is less than contention-free protocols. In the context of MR localization, the MR speed should be sufficiently low to allow the MR to complete the transaction with the sensor. If the MR moves or rotates during a transaction, some packets might be lost due to the lack of proper flow control between the MR and sensor. Moreover, missing positive acknowledgements from the MR makes the sensor retransmit

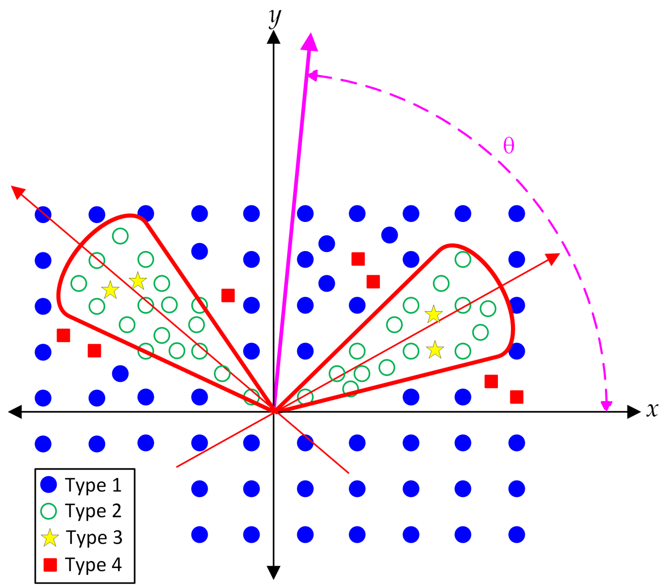

Figure 3.1: Illustrative diagram for the proposed algorithm.

the packet several times, which causes energy efficiency problems. In contention-based protocols, each sensor has to transmit its identity to enable the MR to link it with the sensor location.

3.2.1 Channel Model

In WSNs with MR, there is a high probability that the MR and each of the sensors will have an LoS component, in addition to a number of multipath reflections. Therefore, the MR-sensor link, denoted as h, can be modeled as a non-zero mean complex Gaussian random variable, $h \sim \mathcal{CN}(m_h, 2\sigma_h^2)$. Moreover, the transmission rate in WSNs is generally low, which makes the delay spread of the channel much smaller than the symbol rate. Consequently, the channel does not introduce inter-symbol interference (ISI), i.e., the channel is flat for at least one symbol period. By noting that the sensors spacing is much larger than the transmitted signals' wavelength, then the channels between the MR and all sensors are independent and identically distributed (i.i.d.). The marginal probability density function (PDF) of the channel fading amplitude $\alpha \triangleq |h|$, is given by [76],

$$f(\alpha) = \frac{2(1+K)}{\Omega} \alpha \, \mathrm{e}^{-K} \, \mathrm{e}^{-\frac{(1+K)}{\Omega}\alpha^2} \; I_0\left(2\alpha\sqrt{\frac{K(1+K)}{\Omega}}\right) \tag{3.1}$$

where $\Omega = \mu_h^2 + 2\sigma_h^2$, $K = \frac{\mu_h^2}{2\sigma_h^2}$, $\mu_h = |m_h|$, and $I_0(\cdot)$ is the modified Bessel function of the first kind with 0 order. On the other hand, the PDF of the channel phase, i.e., $\theta \triangleq \arg\{h\}$, is given by,

$$f(\theta) = \frac{1}{2\pi}\, \mathrm{e}^{-K} + \sqrt{\frac{K}{\pi}} \cos(\theta+\phi) \times \exp\left(-K \sin^2(\theta+\phi)\right) Q\left(-\sqrt{2K}\cos(\theta+\phi)\right) \tag{3.2}$$

where $\phi = \tan^{-1}\left(\frac{\mu_{h,Q}}{\mu_{h,I}}\right)$, $\mu_{h,I} \triangleq \Re\{m_h\}$, $\mu_{h,Q} = \Im\{m_h\}$, and $Q(\cdot)$ is the Q-function. Unlike the independent channels scenario, deriving the PDF of the amplitude and phase when the channels between the sensors and MR are correlated is intractable when the number of sensors is greater than two [40].

3.2.2 Signal Detection Model

Given that an interference-free MAC is adopted, the MR receives the signals transmitted from a random number of sensors that are mostly within the antenna beams, as shown in Fig. 3.1. Assuming that the sensors that receive the interrogation signal from the MR respond with a short frame with a non-zero header value. The complex baseband representation of the received signal from the kth sensor can be represented as

$$r_k = \sqrt{P_s} s_k h_k + \varphi_k,\ 0 \leq k \leq N^2 \tag{3.3}$$

where the headers' symbols $s_k \in \{0, 1\}$, P_s is the average transmission power for each sensor, $h_k \sim \mathcal{CN}(m_h, 2\sigma_h^2)$ is a complex channel gain, and $\varphi_k \sim \mathcal{CN}(0, 2\sigma_\varphi^2)$ is the additive white Gaussian noise (AWGN). Because the MR power is significantly higher than the sensors, it is assumed that all sensors within the coverage of the antenna beams receive the interrogation signal.

The received signal can be detected by applying coherent, amplitude-coherent, or noncoherent detection (NCD) [41, 42, 76]. To keep the receiver design structure simple, NCD is adopted at the MR, which does not require knowledge of the instantaneous channel state information (CSI). By noting that $r_k \sim \mathcal{CN}(\sqrt{P_s} m_h s_k, 2P_s s_k^2 \sigma_h^2 + 2\sigma_\varphi^2)$, the NCD can be formulated as,

$$\hat{s}_k = \arg \max_{s_k \in \{0,1\}} f(r_k) \tag{3.4}$$

where

$$f(r_k) = \frac{1}{\sqrt{2\pi \left(P_s \sigma_h^2 s_k^2 + \sigma_\varphi^2\right)}} \exp\left(-\frac{\left|r_k - \sqrt{P_s} s_k m_h\right|^2}{2P_s s_k^2 \sigma_h^2 + 2\sigma_\varphi^2}\right). \tag{3.5}$$

By taking the natural logarithm of $f(r_k)$ and dropping the constant terms, the NCD can be reduced to,

$$\hat{s}_k = \arg \min_{s_k \in \{0,1\}} \ln\left(P_s s_k^2 \sigma_h^2 + \sigma_\varphi^2\right) + \frac{\left|r_k - \sqrt{P_s} s_k m_h\right|^2}{2P_s s_k^2 \sigma_h^2 + 2\sigma_\varphi^2} \tag{3.6}$$

which can be further simplified to

$$\hat{s}_k = \arg \min_{s_k \in \{0,1\}} \ln\left(P_s s_k^2 \sigma_h^2 + \sigma_\varphi^2\right) + \frac{|r_k|^2 - 2\sqrt{P_s} s_k \Re\left(r_k m_h^*\right) + P_s s_k^2 \mu_h^2}{2P_s s_k^2 \sigma_h^2 + 2\sigma_\varphi^2}. \tag{3.7}$$

Because $s_k \in \{0, 1\}$, the NCD can be written as

$$\gamma_1 |r_k|^2 + 2\sqrt{P_s} \Re\left(r_k m_h^*\right) \underset{\hat{s}_k=0}{\overset{\hat{s}_k=1}{\gtrless}} \frac{\ln(1+\gamma_1)}{\gamma_2} + P_s \mu_h^2 \tag{3.8}$$

where $\frac{P_s \sigma_h^2}{\sigma_\varphi^2} \triangleq \gamma_1$ and $\frac{1}{\sigma_\varphi^2(\gamma_1+1)} \triangleq \gamma_2$. By noting that $2\sqrt{P_s} \Re\left(r_k m_h^*\right) \ll \gamma_1 |r_k|^2$ at high SNR values, the second term can be dropped without a noticeable impact on the detector error probability. Consequently, the resultant detector can be expressed as

$$|r_k|^2 \underset{\hat{s}_k=0}{\overset{\hat{s}_k=1}{\gtrless}} \tau_0 \tag{3.9}$$

where

$$\begin{aligned} \tau_0 &= \frac{1}{\gamma_1}\left[\frac{\ln(1+\gamma_1)}{\gamma_2} + P_s\mu_h^2\right] \\ &= \frac{\ln(1+\gamma_1)}{\gamma_1\gamma_2} + 2K\sigma_\varphi^2. \end{aligned} \tag{3.10}$$

Therefore, the suboptimal NCD requires the knowledge of the channel statistical information, which are K, σ_φ^2, and σ_h^2. For high SNRs, we may consider that $\gamma_1 + 1 \approx \gamma_1$, and hence, the threshold τ_0 can be written as,

$$\tau_0 \approx [\ln(\gamma_1) + 2K]\,\sigma_\varphi^2. \tag{3.11}$$

As can be noted from (3.9) and (3.11), the suboptimal NCD can be expressed as an energy detector, and the detector threshold τ_0 does not require the knowledge of any instantaneous CSI. Moreover, the computational complexity of the suboptimal NCD is substantially less than the optimal NCD (3.8).

Although the NCD complexity is less than the coherent detector, it suffers from a BER degradation of about 6 dB [41]. Nevertheless, as demonstrated in Sec. 3.5, the location estimates accuracy is mostly determined by the sensor spacing for moderate and high SNRs. Therefore, unless accurate estimates at low SNRs are required, using the NCD would be preferable due to its low complexity.

3.2.3 Probability of Error Analysis

Although it is considered that all sensors receive the MR interrogation signal and respond accordingly, the sensors' power is usually very limited, and hence, the MR might miss some of the sensors' signals, or might erroneously decide that a particular sensor has responded to the interrogation message. The probability of error for the suboptimal NCD given in (3.9) can be derived by noting that the decision variable $|r_k|^2$ can be expressed as

$$|r_k|^2 = \left(r_k^I\right)^2 + \left(r_k^Q\right)^2 \tag{3.12}$$

where $r_k^I = \Re(r_k) \sim \mathcal{N}(\sqrt{P_s}\mu_{h,I}s_k, P_s s_k^2\sigma_h^2 + \sigma_\varphi^2)$ and $r_k^Q = \Im(r_k) \sim \mathcal{N}(\sqrt{P_s}\mu_{h,Q}s_k, P_s s_k^2\sigma_h^2 + \sigma_\varphi^2)$. Consequently, $|r_k|^2 \triangleq y_k$ has a non-central Chi-square distribution with two degrees of freedom and uncertainty parameter $P_s s_k^2\mu_h^2$, where the PDF and cumulative distribution function (CDF) are respectively given by [70],

$$f_{y_k}(y_k|s_k) = \frac{1}{2\sigma_y^2}e^{-\frac{\lambda_k^2+y_k}{2\sigma_y^2}} I_0\left(\frac{\lambda_k}{\sigma_y^2}\sqrt{y_k}\right), \, y_k > 0 \tag{3.13}$$

$$F_{y_k}\left(y_k|s_k\right) = 1 - Q_1\left(\frac{\lambda_k}{\sigma_y}, \frac{\sqrt{y_k}}{\sigma_y}\right),\ y_k > 0 \tag{3.14}$$

where $\lambda_k = \sqrt{P_s} s_k \mu_h$, $\sigma_y^2 = P_s s_k^2 \sigma_h^2 + \sigma_\varphi^2$ and $Q_1(\cdot,\cdot)$ is the first order Marcum Q-function. Therefore, the pairwise error probabilities (PEPs) are given by

$$\begin{aligned}
\Pr\left(\hat{s}_k = 1|s_k = 0\right) &= \int_{\tau_0}^{\infty} f_{y_k}\left(y_k|s_k = 0\right) dy_k \\
&= 1 - F_{y_k}\left(y_k = \tau_0|s_k = 0\right) \\
&= Q_1\left(0, \frac{\sqrt{\tau_0}}{\sigma_\varphi}\right)
\end{aligned} \tag{3.15}$$

and

$$\begin{aligned}
\Pr\left(\hat{s}_k = 0|s_k = 1\right) &= \int_{0}^{\tau_0} f_{y_k}\left(y_k|s_k = 1\right) dy_k \\
&= F_{y_k}\left(y_k = \tau_0|s_k = 1\right) \\
&= 1 - Q_1\left(\sqrt{\frac{P_s \mu_h^2}{\gamma_1 \sigma_\varphi^2}}, \sqrt{\frac{\tau_0}{\gamma_1 \sigma_\varphi^2}}\right).
\end{aligned} \tag{3.16}$$

3.3 Location and Orientation Estimation

In WSNs with data harvesting, the MR transmits an interrogation signal, and then listens to the responses from the sensors. The sensors that receive the interrogation signal respond by sending the information symbols s_k, $k \in \{0, 1, \ldots, \mathbb{N}_1\}$. When directional antennas are used, the sensors that are expected to respond are the ones within the coverage area of the antenna, Fig. 3.1 shows an example of an antenna with two main lobes. However, in practical operating conditions, channel fading, noise, interference, antenna sidelobes, and radiation pattern imperfections may trigger out of range sensors to respond, or some in-range sensors to be ignored. Therefore, the interrogation and response activities between the sensors and the MR can be classified into four types. Type 1 corresponds to the sensors that did not receive the interrogation signal, did not respond, and the MR correctly decided that they did not respond. Type 2, the sensors received the interrogation signal, responded, and the MR correctly decided that they responded. Type 3, the sensors are within the antenna coverage area and received the interrogation signal, but the MR missed the response; and finally Type 4 when sensors are outside the antenna coverage region, yet the MR erroneously decided that they have responded. The probabilities associated with the four types are as follows:

- $\Pr\left(Type\ 1\right) = \Pr\left(\hat{s}_k = 0|s_k = 0\right)$
- $\Pr\left(Type\ 2\right) = \Pr\left(\hat{s}_k = 1|s_k = 1\right)$
- $\Pr\left(Type\ 3\right) = \Pr\left(\hat{s}_k = 0|s_k = 1\right) = 1 - \Pr\left(Type\ 2\right)$

- $\Pr(Type\ 4) = \Pr(\hat{s}_k = 1 | s_k = 0) = 1 - \Pr(Type\ 1)$

The probabilities $\Pr(s_k)$ $\forall k$ depend on the location of the sensor, the direction of the antenna, the channel between the MR and the sensor, and the distance between the MR and the sensor. Therefore, it is generally difficult to measure or estimate $\Pr(s_k)$ accurately. The probability of each type can be computed using (3.15) and (3.16).

After the interrogation-listening phase, the MR should create a virtual map similar to the one in Fig. 3.1 with clusters of responding sensors. However, the number of clusters may vary depending on the number of antenna beams used. In such maps, the resulting clusters may give clear indications about the location of the MR as well as its orientation. Although there are several approaches to identify the clusters and use them to estimate the location and orientation of the MR, in this work, the axial symmetry of the transmitting horn antenna main beam in the azimuth plane is exploited [44–46]. By identifying the symmetry axis of at least two antennas or antenna orientations, it would be possible to compute the location and orientation of the MR. Towards this goal, and to keep the complexity low, linear regression is used to estimate the beams symmetry axes. Among several linear regression techniques, the major axis regression (MAR) was able to provide the most accurate results, and hence, has been adopted in this work.

According to this algorithm, the sum of perpendicular distances between each point and the regression line is minimized. According to Fig. 3.1, two different directions for the antenna are considered, and the corresponding straight lines are plotted based on the received hard decisions from the sensors. In general, the estimated straight line that represents the symmetry axis of the antenna main beam radiation pattern can be expressed as

$$l_i = a_i t_i + b_i. \tag{3.17}$$

At least two lines are required to estimate the location of the MR, which is their intersection point. If three or more lines are used, however, the location of the MR is estimated by computing the average of all intersection points. For a pair of lines l_i and l_j, $i \neq j$, the intersection point can be written as

$$\hat{x}_{i,j} = \frac{b_j - b_i}{a_i - a_j} \tag{3.18}$$

$$\hat{y}_{i,j} = a_i \hat{x}_{i,j} + b_i \tag{3.19}$$

For the case of using more than two lines

$$\hat{x} = \frac{1}{L} \sum_{i=1}^{L} \sum_{j>i}^{L} \hat{x}_{i,j}, \quad L > 2 \tag{3.20}$$

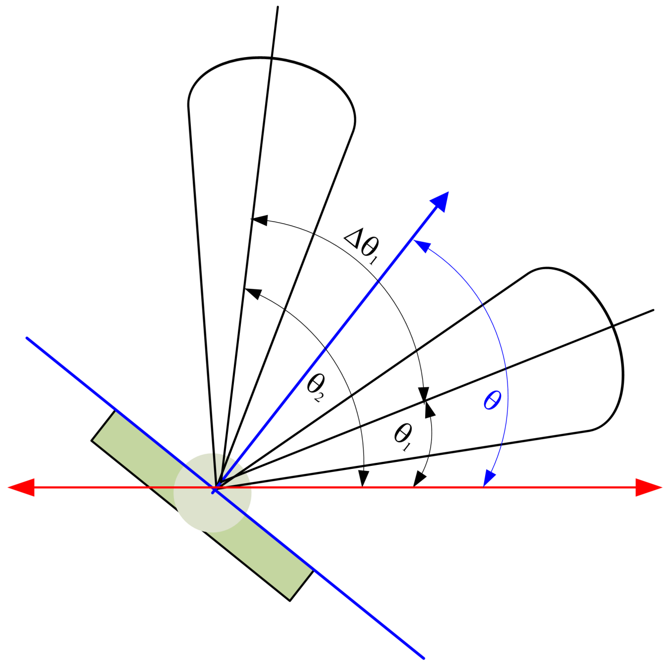

Figure 3.2: Orientation calculation example using two beams.

and

$$\hat{y} = \frac{1}{L}\sum_{i=1}^{L}\sum_{j>i}^{L}\hat{y}_{i,j},\ L > 2 \tag{3.21}$$

where L is the total number of lines used. It should be noted that the estimated location must be inside the grid boundaries, i.e., $\hat{x}_0 \in \{0,\ x_U\}$ in the x-direction and $\hat{y}_0 \in \{0,\ y_U\}$, otherwise, the point $(\hat{x}_0, \hat{y}_0)$ must be ignored and other beams should be considered. Moreover, if the MR is close to and facing the grid boundaries, the number of responding sensors might be very small, leading to unreliable results. In such scenarios, the MR should steer the antenna beams towards the center of the grid to increase the number of responding sensors. In this work we use a threshold τ_2 to indicate if the MR should collect data from other directions or not. While increasing τ_2 improves the estimates accuracy, it also increases the delay. Therefore, the value of τ_2 should be selected such that adequate accuracy is achieved with minimum delay. As reported in [47], using a sample size of five is sufficient to provide a plausible straight-line regression, and hence, we set $\tau_2 = 5$.

The orientation of the MR can be generally obtained using a single beam where the rotation angle of the ith beam can be computed as $\hat{\theta}_i = \arctan(a_i)$. For multiple lines, the average can be computed as

$$\hat{\theta} = \frac{\Delta\theta_1}{2} + \frac{1}{L}\sum_{i=2}^{L}\left[\hat{\theta}_1 + \left(\hat{\theta}_i - \Delta\theta_i\right)\right] \tag{3.22}$$

where $\Delta\theta_i$ is the angle difference between the first beam and the ith beam when $i > 1$. Fig. 3.2 shows the orientation estimation example using $L = 2$.

As can be noted from the aforementioned discussion for the case when more than two beams are used, it is suggested to average the multiple obtained positions to produce a single position and orientation estimates. However, by noting that not all lines have the same reliability, then combining different estimates should take the reliability of each point into consideration. For example, a line generated using a small number of sensors is less reliable than a line generated with a large number of symbols. Consequently, a weighted average based on the reliability of each estimated point can be adopted. However, computing an accurate reliability factor is not straightforward. More sophisticated methods such as the one reported in [48] can be adopted as well. Nevertheless, deriving the joint PDF for the case of WSNs with hard detection and regression operations is prohibitively complex. Based on the results in Sec. 3.5, it can be noted that simple averaging can produce sufficiently accurate results, hence, it is adopted in this work.

3.3.1 The Local Majority Voting Algorithm (MVA)

The MVA algorithm can mitigate the errors caused by non-ideal transmission and reception, and thus, can improve the localization and orientation estimation accuracy [6], [49]. In the MVA, each of the detected decisions is corrected based on the decisions of its neighbors. Without loss of generality, let us assume that the set of all sensors in the grid is defined as $\mathbf{A}$, and the set of the M neighboring sensors is $\mathbf{B}$, i.e., $\mathbf{B} \subseteq \mathbf{A}$. Consequently, each decision in $\mathbf{B}$ is corrected based on the following metric

$$\hat{d}_k \approx \begin{cases} 1, & N \geq M/2 \\ 0, & N < M/2 \end{cases} \tag{3.23}$$

where $\hat{d}_k$ is the corrected decision for all $k \in \mathbf{B}$, and N is the total number of detected ones in $\mathbf{B}$.

3.3.2 The Connected Graph (CG)

Another error concealment algorithm can be applied is the CG, which is one of the basic concepts in the graph theory [50]. According to this theorem, in an undirected graph G, two vertices u and v are considered to be connected if G contains a path from u to v, otherwise, they are called disconnected. Due to non-ideal reception, the extracted decisions could have more than one group of connected graphs; and thus, the biggest group of decisions equal to 1 is chosen because it is expected to be the most accurate cluster of sensors inside the coverage area of the beam. In addition, sensors with decision 0 inside this cluster are corrected to 1, while other connected clusters are set to 0 because they are expected to be erroneous decisions.

3.3.3 Correlated Fading

Generally speaking, increasing the sensors' density may improve the location estimation accuracy of the proposed algorithm. Nevertheless, if the density is increased such that the distance between adjacent sensors is equal or less than the transmitted signal wavelength, then the channels between adjacent sensors and the MR become spatially correlated. In such scenarios, the improvement gained by increasing

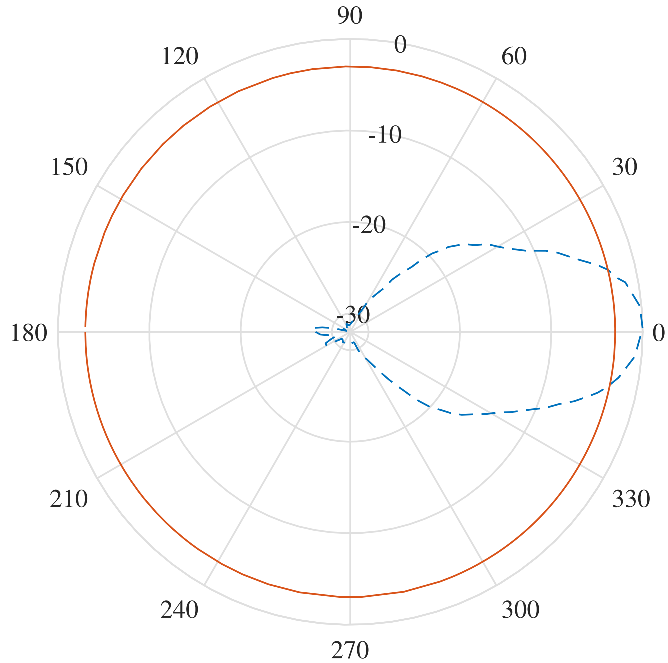

Figure 3.3: Radiation pattern of the horn antenna LB-430-10-A at 2 GHz in the azimuth plane.

the network density may vanish, or even degrade for power-constrained WSNs. Mitigating the channels' correlation typically requires sophisticated designs, and the improvement gained is generally limited [51]. Therefore, the network design should avoid unnecessary network densification and prohibitively complex receiver designs.

3.4 Measurements Setup and Results

In this work, the location data were collected by conducting time domain channel measurements in a very large room, 29.4 m×19.6 m. An open area in the room of 16 m ×15 m was divided into a uniform grid with a 1 m spacing. The sensor spacing is selected to be much larger than the wavelength to guarantee that the channels between various sensors and the MR are mutually independent. The time domain measurements of the wireless channel were carried out using the DSOS204A High-Definition Digital Storage Oscilloscope, and the E4421B Analog RF Signal Generator, both from Keysight Technologies. The measurement system also included low loss RF cables, an LB-430-10-A standard gain horn antenna type from Ainfo corp. [44], at the transmitter, while the receiver was equipped with an omni-directional antenna. Fig. 3.3 shows the radiation pattern of the vertically polarized horn antenna with an azimuth half power beam width (HPBW) of about 24^o and a peak gain of 16 dBi. The transmitter and receiver heights were fixed at 1.5 m. During the measurements, the transmitting horn antenna was fixed in one location and a particular direction, while the receiver was moved across the whole 271 grid points, 17×16 points less the transmitter point. A snapshot of the measurement setup showing the transmitter and receiver is shown in Fig. 3.4.

At each grid point, the channel was measured with a signal frequency 2 GHz, a wavelength $\lambda_o = 15$

Figure 3.4: A snapshot of the measurement process showing the transmitter and receiver.

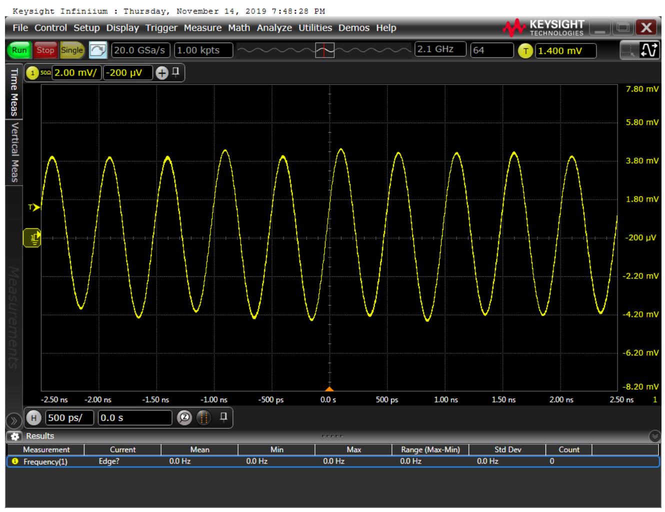

Figure 3.5: The signal captured by the Oscilloscope at one of the grid locations.

cm, a time period 5 ns, i.e., 10 periods. It is worth noting that the 2 GHz frequency was selected because it was the upper limit of the oscilloscope. Nevertheless, operating at the ISM 2.4-2.5 GHz band should not affect the outcome of this work. The power is then calculated for the 10 cycles. Each measurement sweep contained 800 time samples for high resolution. The measurements were then repeated for another orientation for the transmitting antenna but in the same location. Fig. 3.5 shows the measure signal captured by the Oscilloscope during the measurements process.

Fig. 3.6 shows how the proposed location estimation works using the experimental setup described earlier. In this example, the MR gathers data from the 16×16 grid of sensors while located at Cartesian coordinates $(5, 3)$ with orientation $\theta = 45^o$. In order to estimate the location and actual orientation θ, two data sets were collected by rotating the MR antenna in the positive x-axis and positive y-axis directions. The number of antenna rotations is pre known to the MR, and the direction of rotations are calculated by the robot based on the responding sensors. The number of responding sensors, within the antenna coverage area, is determined according to the sensors' minimum RSS threshold (or power threshold). From Fig. 3.3, the back lobes are at least 27 dB lower than the main lobe, and hence, by carefully setting the sensor threshold, the effect of the sidelobes can be reduced. The MVA was then applied on both sets separately to enhance the accuracy of the estimated location, and then the corresponding major symmetry axis for each set was obtained as explained earlier. The two obtained lines are

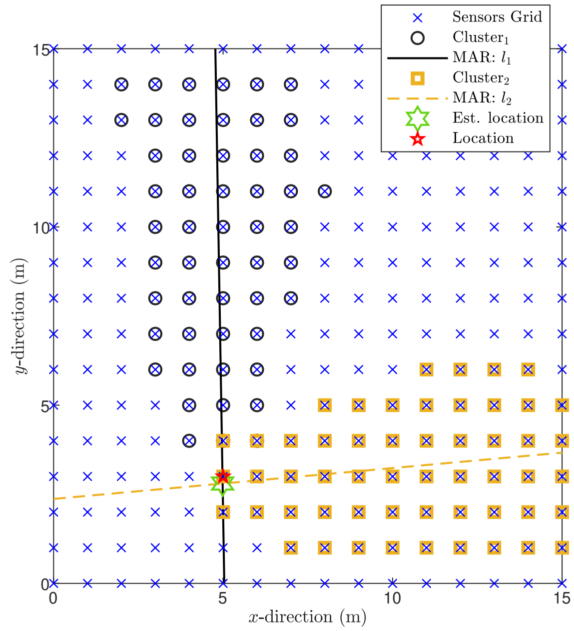

Figure 3.6: Location estimation for the MR based on experimental results.

Table 3.1: The estimated locations and orientations for different scenarios.

	Case 1	Case 2	Case 3	Case 4
(x_0, y_0)	$(5, 3)$	$(2.5, 10)$	$(13, 10)$	$(13, 5)$
θ	45^o	135^o	225^o	315^o
l_1	$0.086535t_1 + 2.37$	$-0.15t_1 + 3.96$	$0.16t_1 + 11.24$	$-0.156t_1 + 13.58$
l_2	$-56.955t_2 + 286.76$	$297.45t_2 - 3003$	$-297.5t_2 + 3019$	$297.5t_2 - 1442$
$(\hat{x}_0, \hat{y}_0)$	$(5, 2.9)$	$(2.4, 10.1)$	$(12.83, 10.1)$	$(13.1, 4.89)$
$\hat{\theta}$	47.97^o	139.5^o	229.5^o	319^o
RMSE$_l$	0.1 m	0.14 m	0.20 m	0.148 m
RMSE$_\theta$	0.05 rad	0.078 rad	0.078 rad	0.069 rad

$$l_1 = 0.086535t_1 + 2.37 \tag{3.24}$$

$$l_2 = -56.955t_2 + 286.76. \tag{3.25}$$

Based on these two lines, the intersection point can be obtained as $(5, 2.9)$, and the orientation is $\hat{\theta} = 47.97^o$.

Figs. 3.7 and 3.8 show the power map of the received signals in the vertical and horizontal orientations, respectively. The figures are obtained using the same experimental setup used with Fig. 3.6. The power profile is very similar to a typical horn antenna radiation pattern given in Fig. 3.3. The major axis of the radiation pattern passes through the location of the MR, and the intersection of the major axes of both patterns is the estimated MR location.

The experiment was repeated using three additional locations and orientations, which are $[(2.5, 10), 135^o]$, $[(13, 10), 225^o]$ and $[(13, 5), 315^o]$. As shown in Table 3.1, the two symmetry lines l_1 and l_2 are obtained

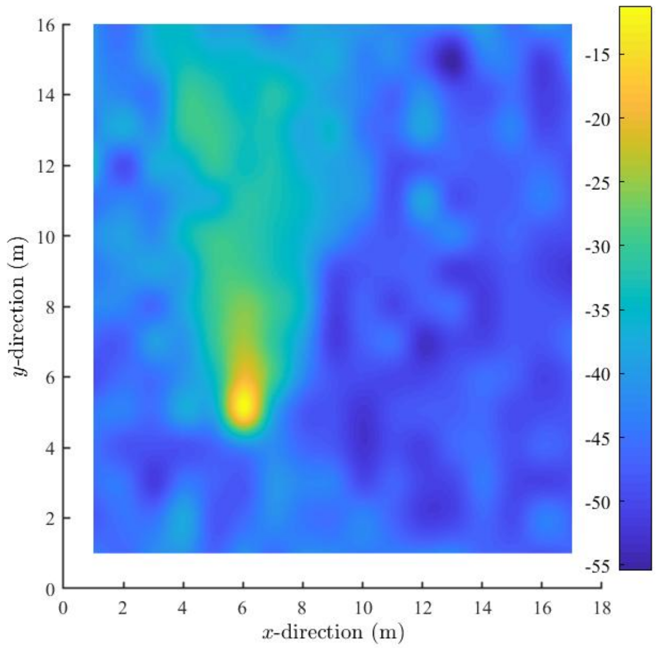

Figure 3.7: Power map for the received power when the MR has vertical orientation.

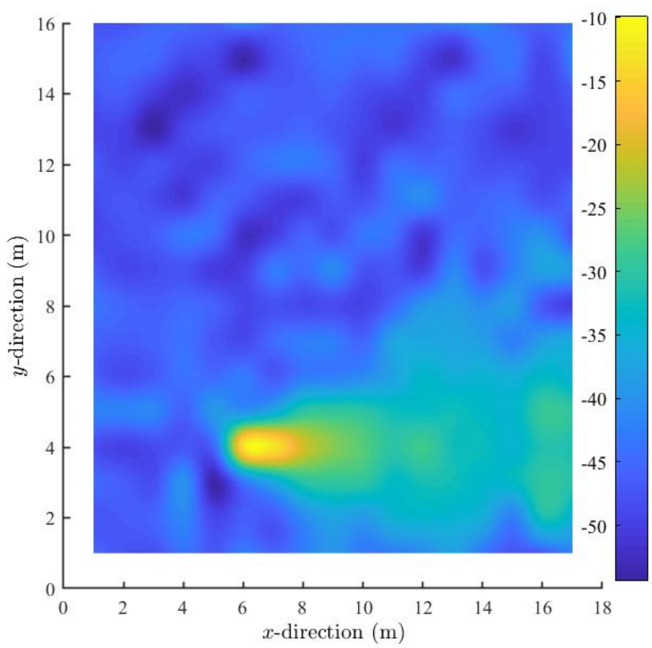

Figure 3.8: Power map for the received power when the MR has horizontal orientation.

for each case, and then the estimated location $(\hat{x}_0, \hat{y}_0)$ and orientation $\hat{\theta}$ are computed accordingly. The root mean square error (RMSE) of the location and orientation is defined as

$$\mathrm{RMSE}_l \triangleq \sqrt{(x_0 - \hat{x}_0)^2 + (y_0 - \hat{y}_0)^2} \tag{3.26}$$

$$\mathrm{RMSE}_\theta \triangleq \left|\theta - \hat{\theta}\right|. \tag{3.27}$$

The table shows that the proposed algorithm provides fairly accurate approximation for the location and orientation, where $\mathrm{RMSE}_l \leq 0.2$ m and $\mathrm{RMSE}_\theta \leq 0.078$ rad.

As compared to other alternative approaches [23–29], the method described in this work intends to estimate the location of a device moving within a fairly dense sensor network where the sensors act as omni-directional beacons, and are only required to transmit their identity. The moving device must either rotate or use a multi-beam antenna, preferably with no overlapping, then the location and orientation are obtained as the spatial intersection of the two beams, as shown in Figs. 3.1 and 3.2. The method in [26] aims to determine an accurate DoA for signals from a moving device as seen from several fixed stations that use a split beam or monopulse method with only a small spacing between overlapping beams. The demonstration devices use two planar antennas with a small azimuthal deviation between them to generate the overlapping beams. Therefore, both the proposed technique and [26] are amplitude-only methods. Moreover, it can be noted that neither method depends crucially on the technology of the directional antenna nor the azimuthal beam shape, provided that the beams are symmetric and have reasonably well-formed main lobe. In the proposed method, the beamwidth is a compromise between angular resolution and the number of sensors required to overcome propagation effects. For proof of concept, the horn antenna used in this work appears to give quite satisfactory results. A similar mechanically rotatable antenna is also used in [52]. The two inexpensive planar antennas used here and in [52] are similar to those in [26, 29], but with a greater relative angle.

Other papers have described LWAs with beam frequency scanning applied to both power transfer [27] and localization [28, 29]. Steering by frequency hopping between channels adds a slight complexity, but these antennas remain inexpensive, compact and lightweight, which makes them a good substitute to the horn antenna. Active antenna structures are also suitable when used by the central node, or MR in this case [53–56]. Multiple beams can be generated using adaptive antenna array, smart antenna array, or electronically steerable parasitic array radiator to enable simultaneous angular scanning of different sets of sensors located in different directions. Such approach offers a fast method for processing the information and estimate the position and/or direction of the target.

Mechanically rotated horn antennas can be used to provide a steerable beam, however, such systems are prone to mechanical failures, and consume high power. In addition, rotating the horn antenna is time consuming and should be performed while the MR is stationary to avoid unnecessary channel

Table 3.2: The system simulation parameters .

P_s	f_0	c	K	Ω	τ_2	N
1	1 GHz	3×10^8 m/s	10	1	5	16

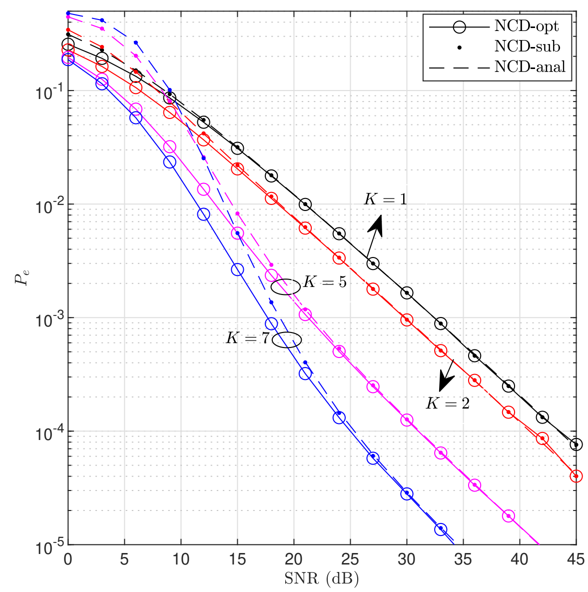

Figure 3.9: The BER of the optimal and suboptimal NCD over Rician fading channel with different K.

disturbance, which can make the MR motion discretized and slow. Unlike the mechanically steered antennas, the aforementioned passive and active directive antenna structures do not produce perfectly consistent patterns when the beam is steered in different directions [26, 29, 30]. In such scenarios, an elaborate calibration process is required to compensate for the beam width and power level variation. A comprehensive overview of mechanical, electronic and multi-beam antennas can be found in [57–59], respectively.

3.5 Simulation Results

In this section, the performance of the proposed localization algorithm is presented, and compared with a benchmark algorithm referred to MLE [6]. The RMSE is used as a performance measure. Monte Carlo simulations with 10^4 runs are performed to obtain the results. The system parameters considered in the simulation results are included in Table 3.2, where f_0 and c are the operating frequency and speed of light, respectively.

Fig. 3.9 shows the BER of the optimal and suboptimal NCD over the Rician fading channel with different K. Clearly, the optimal and suboptimal detection provide comparable performance for small values of K. As can be observed also, when the Rician factor K increases the gap between both detectors increases at low SNR values; however, they converge at high SNR. In addition, the obtained results show a perfect match between the simulation results and derived analytical BER for the suboptimal detector.

Fig. 3.10 shows an example of the actual and estimated trajectory for the MR with different trajectories

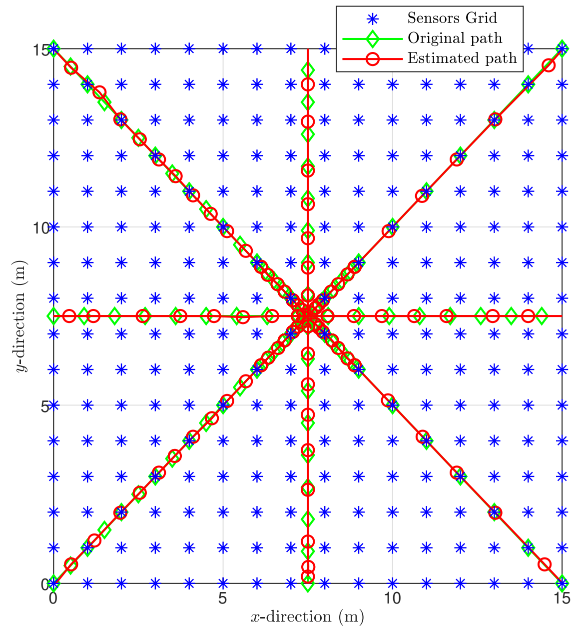

Figure 3.10: The actual and estimated trajectory of the MR for different paths.

when applying MAR-CG based localization. The SNR is fixed at 30 dB, and the antenna was rotated 4 times with angles $\{0, 45^o, 90^o, 135^o\}$ resulting in 4 lines, where the location of the MR is evaluated by calculating the mean of the intersection points between each pair of the lines. As can be noticed, the proposed MAR-CG provides a very good estimate for the path trajectory.

Fig. 3.11 compares the proposed localization algorithms with the MLE based localization over a wide range of SNR, where the MR is located at $(7.5, 7.5)$ and $(7.5, 0)$. Two lines were considered, i.e., $\{0, 90^o\}$, and the intersection point between them is the estimated location of the MR. It is clear from the figure that the MLE outperforms the proposed algorithms when the MR is located at $(7.5, 0)$, while the proposed algorithms provide better results when the location is $(7.5, 7.5)$. This behavior means that the proposed algorithms may suffer from considerable estimation errors at the borders of the grid because the presence of the concrete posts in the experimental space which disturbed the symmetry of the antenna beam. Here, the MAR-CG based localization outperforms the MAR-MVA for almost the whole range of SNR and the two considered locations. The main trend of the figure is that applying error concealment algorithms, i.e., MVA and CG, improves the RMSE. However, the standard MAR (MAR-Std), which refers to MAR localization without CG or MVA, provides lower RMSE than MAR-CG and MAR-MVA for the case of $(7.5, 7.5)$ when SNR$\lesssim$ 4 dB. This behavior is due to the fact that at very low SNR, the probability of error is very high, and thus applying MVA or CG may increase the errors.

Fig. 3.12 shows the effect of applying the non-optimum NCD at the MR on both the MVA and CG based localization algorithms. For the non-optimum ED, the detection threshold is considered as a static (Stc) value of 0.5, while for the optimum NCD an adaptive (Adpt) threshold is evaluated using (3.10). Similar to Fig. 3.11, two locations for the MR, $(7.5, 7.5)$ and $(7.5, 0)$, and two beams, $\{0, 90^o\}$, are

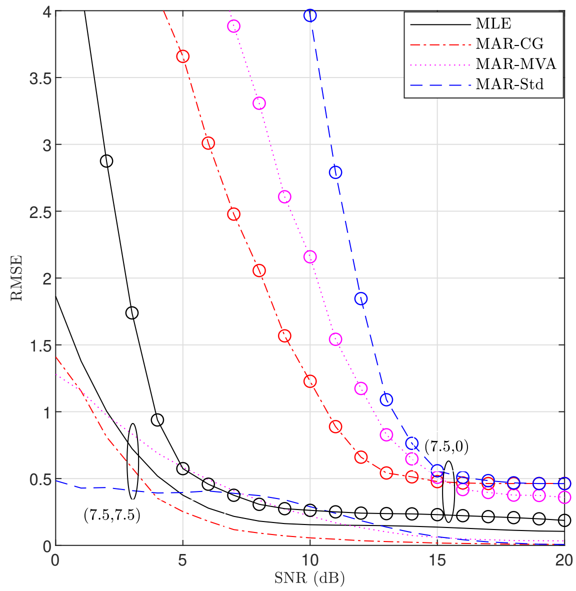

Figure 3.11: A comparison between different localization algorithms for different locations of the MR, i.e., $(7.5, 7.5)$ and $(7.5, 0)$.

considered. It is clear from the figure that there is a considerable performance degradation by applying a static threshold, especially at low and mid-range SNR. However, at high SNR, both detectors provide the same RMSE except for MVA when the location is $(7.5, 0)$.

Fig. 3.13 shows the effect of increasing the number of beams on the RMSE. The lines $\{0^o, 45^o\}$, $\{0^o, 45^o, 90^o\}$, and $\{0^o, 45^o, 90^o, 135^o\}$ are used for the cases of 2, 3, and 4 beams; respectively, and the MR is fixed at $(7.5, 7.5)$. As can be seen by comparing the two subplots, the MAR-CG outperforms the MAR-MVA. Moreover, both MAR-MVA and MAR-CG outperform the MLE for SNR$\gtrsim$ 14 dB and SNR$\gtrsim$ 9 dB, respectively. Although increasing the number of beams from 2 to 3 manages to improve the RMSE, the performance of the 4 beams case is worse than the 2 beams. This indicates that increasing the number of beams does not necessarily improve the system performance.

Fig. 3.14 shows the RMSE in estimating the orientation in rad using MVA and CG based techniques. The MR is located at $(7.5, 7.5)$ and $(7.5, 0)$, and the orientation of the MR is $\theta = \frac{\pi}{4}$. Two beams are considered to estimate the orientation of the MR; namely, the horizontal and vertical beams, where $\hat{\theta}$ is estimated according to (3.22). It can be observed from the figure that CG outperforms the MVA for almost the whole range of SNR and the two locations. An error floor of about 0.12 rad is achieved by applying MVA at the location $(7.5, 0)$. However, the RMSE in estimating θ approaches 0 rad for the MVA at $(7.5, 7.5)$ when SNR$\geq$ 13 dB, while it approaches 0 for SNR$\geq$ 9 for the CG at both locations. It should be highlighted that the MLE is not included in this figure because it cannot be used for inferring the direction as it assumes an omni-directional antenna.

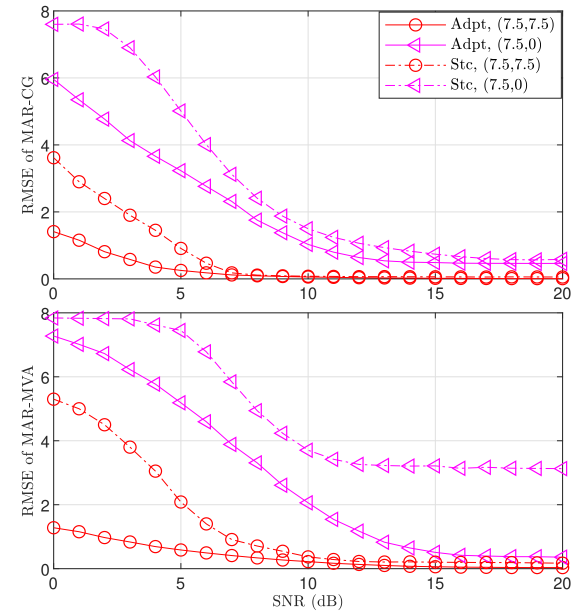

Figure 3.12: The effect of using optimal NCD on the RMSE.

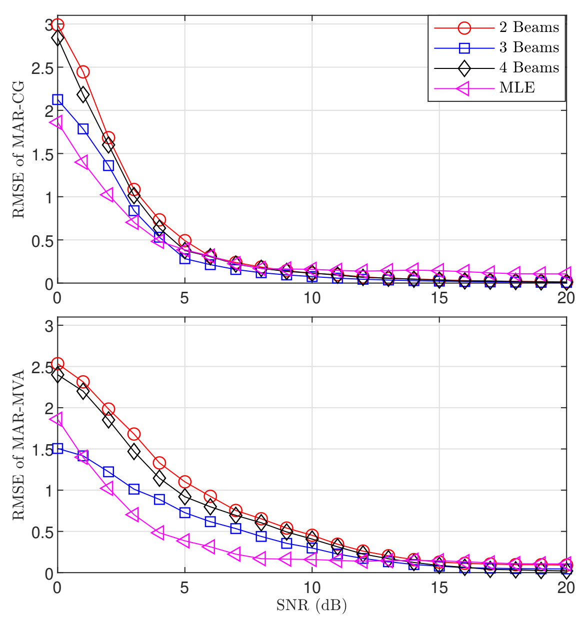

Figure 3.13: The RMSE of MAR-CG and MAR-MVA based localization for different number of beams.

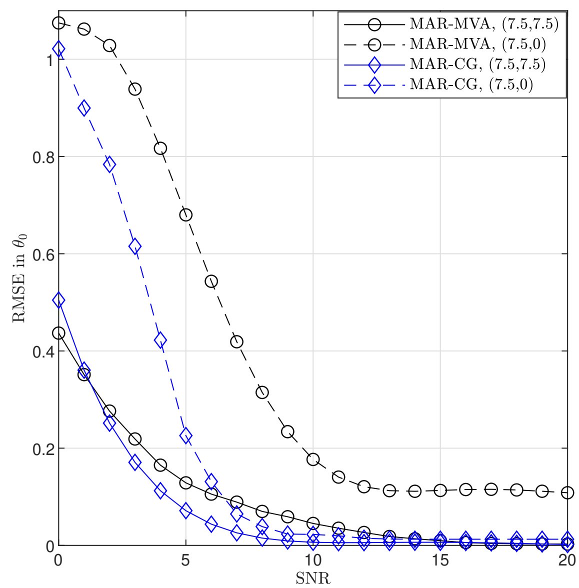

Figure 3.14: The RMSE in estimating the orientation of the MR in rad versus SNR in dB.

3.6 Conclusion and Future Work

In this paper, an efficient algorithm was proposed to jointly estimate the location and orientation of an MR. The MR utilizes a directional antenna to collect information from a sensor grid, and linearly fits the locations of the responding sensors. The MAR regression technique was used the with two error concealment algorithms, namely, the CG and MVA. The orientation of the MR was estimated by considering the slope of the fitted lines of symmetry while the location of the MR was estimated by intersecting two or more lines. The multiple lines were obtained by rotating the antenna for different orientations. The numeric results confirmed the superior performance of the proposed algorithm compared to MLE algorithm at high SNR. In contrast, the highly complex MLE based algorithm outperformed the proposed techniques at low SNR. Unlike the MLE, the proposed algorithms provide an advantage of estimating the orientation of the MR's antenna. In addition, applying error concealment algorithms such as MVA and CG noticeably reduces the RMSE of the proposed algorithms, where the MAR-CG based localization provides better RMSE than the MAR-MVA. However, the results also showed that increasing the number of beams does not always improve RMSE when multiple intersection points are combined using simple averaging, because each line might have different reliability.

In future work, the measurements setup could be substituted using commercially available platforms to capture the impact of various hardware imperfections when using inexpensive devices [26–28]. Moreover, the system performance will be evaluated using various detection schemes and antenna technologies. Another interesting dimension that worth considering is the case where some of the sensing nodes are mobile and has predefined position. In such scenarios, the MR has to perform hybrid localization for sensors with known and unknown positions, or each mobile node estimates its positions and sends it to the MR.

References

[1] S. Kim and B. Kim, “Accurate hybrid global self-localization algorithm for indoor mobile robots with two-dimensional isotropic ultrasonic receivers,” *IEEE Trans. Instrum. Meas.*, vol. 60, no. 10, pp. 3391-3404, Oct. 2011.

[2] N. Al-Khanbashi *et al.* “Real time evaluation of RF fingerprints in wireless LAN localization systems,” *10th Workshop on Positioning, Navigation and Commun.* (WPNC2013), Mar. 2013, Dresden, Germany.

[3] D. Ayllón, H. Sánchez-Hevia, R. Gil-Pita, M. Manso, and M. Zurera, “Indoor blind localization of smartphones by means of sensor data fusion,” *IEEE Trans. Instrum. Meas.*, vol. 65, no. 4, pp. 783-794, Apr. 2016.

[4] R. Al-Jarrah, M. Al-Jarrah, and H. Roth, “A novel edge detection algorithm for mobile robot path planning,” *J. Robot.*, vol. 2018, 2018.

[5] L. Chen and J. Lain, “Two-dimensional indoor visible light positioning using smartphone image sensor,” *IEEE Int. Conf. on Consumer Electron.*, Taiwan, 2018.

[6] M. Al-Jarrah, A. Al-Dweik, E. Alsusa, and E. Damiani, “RFID reader localization using hard decisions with error concealment,” *IEEE Sensors J.*, vol. 19, no 17, pp. 7534-7542.

[7] F. Bandiera, A. Coluccia, and G. Ricci, “A cognitive algorithm for received signal strength based localization,” *IEEE Trans. Signal Process.*, vol. 63, no. 7, pp. 1726-1736, Apr. 2015.

[8] Y. Hu and G. Leus, “Robust differential received signal strength based localization,” *IEEE Trans. Signal Process.*, vol. 65, no. 12, pp. 3261-3276, Jun. 2017.

[9] E. Xu, Z. Ding, and S. Dasgupta, “Wireless source localization based on time of arrival measurement,” *in Proc. IEEE Int. Conf. Acoust. Speech Signal (ICASSP)*, Dallas, TX, USA, Mar. 2010, pp. 2842-2845.

[10] K. Yang, J. An, X. Bu, and G. Sun, “Constrained total least-squares location algorithm using time-difference-of-arrival measurements,” *IEEE Trans. Veh. Technol.*, vol. 59, no. 3, pp. 1558-1562, Mar. 2010.

[11] Y. Sun, F. Zhang, and Q. Wan , "Wireless sensor network-based localization method using TDOA measurements in MPR," *IEEE Sensors J.*, vol. 19, no. 10, pp. 3741-3750, May 2019.

[12] S. Xu and K. Dogançay, "Optimal sensor placement for 3-D angle-of-arrival target localization," *IEEE Trans. Aerosp. Electron. Syst.*, vol. 53, no. 3, pp. 1196-1211, Jun. 2017.

[13] C. Meng, Z. Ding, and S. Dasgupta, "A semidefinite programming approach to source localization in wireless sensor networks," *IEEE Signal Process. Lett.*, vol. 15, pp.253-256, 2008.

[14] R. Ouyang, A.-S. Wong, and C.-T. Lea, "Received signal strength-based wireless localization via semidefinite programming: Noncooperative and cooperative schemes," *IEEE Trans. Veh. Technol.*, vol. 59, no. 3, pp. 1307-1318, 2010.

[15] C. Wei, H. Lin, P. Chen, Y. Han, and P. Varshney, "Target localization using sensor location knowledge in wireless sensor networks" *IEEE Wireless Commun. Lett.*, vol. 7, no. 3, pp. 456-459, Jun. 2018.

[16] X. Sheng and Y.-H. Hu, "Maximum likelihood multiple-source localization using acoustic energy measurements with wireless sensor networks," *IEEE Trans. Signal Process.*, vol. 53, no. 1, pp. 44-53, Jan. 2005.

[17] M. AlHajri, N. Ali, and R. Shubair, "Classification of indoor environments for IoT applications: A machine learning approach," *IEEE Antennas Wireless Propag. Lett.*, vol. 17, no. 12, pp. 2164-2168, Dec. 2018.

[18] M. AlHajri, N. Ali, and R. Shubair, "Indoor localization for IoT using adaptive feature selection: A cascaded machine learning approach," *IEEE Antennas Wireless Propag. Lett.*, vol. 18, no. 11, pp. 2306-2310, Nov. 2019.

[19] R. Niu, A. Vempaty, and P. K. Varshney, "Received-signal-strength-based localization in wireless sensor networks," *IEEE Proc.*, vol. 106, no. 7, pp. 1166-1182, Jul. 2018.

[20] H. Schantz, "A real-time location system using near-field electromagnetic ranging," 2007 *IEEE Antennas and Propagation Int. Symposium*, pp. 3792-3795, Jun. 2007.

[21] H.-N. Dai, K.-W. Ng, M. Li, and M.-Y. Wu, "An overview of using directional antennas in wireless networks," *Int. J. Commun. Syst.*, vol. 26, no. 4, pp. 413-448, 2013.

[22] O. Ben Smida, S. Zaidi, S. Affes, and S. Valaee, "Robust distributed collaborative beamforming for wireless sensor networks with channel estimation impairments," Sensors, vol. 19, pp. 1061, Mar. 2019.

[23] J. López-Pastor, A. Gómez-Alcaraz, D. Cañete-Rebenaque, A. Martinez-Sala, and J. Gómez-Tornero, "Near-field monopulse DoA estimation for angle-sensitive proximity WiFi readers," *IEEE Access*, vol. 7, no. 1, pp. 88450-88460, Jun. 2019.

[24] M. Poveda-García, *et al.*, “Frequency-scanned focused leaky-wave antennas for direction-of-arrival detection in proximity BLE sensing applications,” *European Conf. Antennas and Propagation (EuCAP 2020)*, Copenhagen, Denmark, 15-20 Mar. 2020, pp.1-4.

[25] R. Guzmán-Quirós, A. Martínez-Sala, J. Gómez-Tornero, and J. García-Haro, “Integration of directional antennas in an RSS fingerprinting-based indoor localization system,” *Sensors, Special Issue Sensors for Indoor Mapping and Navigation*, vol. 16, no. 4, pp. 1-23, Dec. 2015.

[26] J. Gómez-Tornero, D. Cañete-Rebenaque, J. López-Pastor, and A. Martínez-Sala, “Hybrid analog-digital processing system for amplitude-monopulse RSSI-based MiMoWiFi direction-of-arrival estimation,” *IEEE J. Sel. Topics Signal Process.*, vol. 12, no.3, pp. 529-540, Jun. 2018.

[27] M. Poveda-García, J. Oliva-Sánchez, R. Sanchez-Iborra, D. Cañete-Rebenaque, and J. Gomez-Tornero, “Dynamic wireless power transfer for cost-effective wireless sensor networks using frequency-scanned beaming,” *IEEE Access*, vol. 7, pp. 8081–8094, Jan. 2019.

[28] M. Poveda-García, A. Gómez-Alcaraz, D. Cañete-Rebenaque, A. Martinez-Sala, and J. L. Gómez-Tornero, “RSSI-based direction-of-departure estimation in Bluetooth low energy using an array of frequency-steered leaky-wave antennas,” *IEEE Access*, vol. 8, pp. 9380-9394, Jan. 2020.

[29] M. Poveda-García, et al., “Frequency-scanned monopulse pattern synthesis using leaky-wave antennas for enhanced power-based direction-of-arrival estimation”, *IEEE Trans. Antennas Propag.*, vol. 67, no. 11, pp. 7071-7086, Nov. 2019.

[30] D. Ren and J. H. Choi, “Full-sphere frequency scanning array antenna based on passive dual-band CRLH series integrated feeding network,” *IEEE MTT-S Int. Microwave Symp. (IMS)*, Boston, MA, USA, 2019, pp. 1462-1465.

[31] C. Javali, G. Revadigar, L. Libman, S. Jha, “SeAK: Secure authentication and key generation protocol based on dual antennas for wireless body area networks,” *in Proc. 10th Workshop on RFID Security (RFIDsec)*, Oxford, UK, 2014.

[32] T. J. Pierson, X. Liang, R. Peterson and D. Kotz, “Wanda: Securely introducing mobile devices,” *IEEE INFOCOM*, San Francisco, CA, 2016, pp. 1-9.

[33] F. Da Mota, M. Rocha, J. Rodrigues, V. De Albuquerque, and A. De Alexandria. “Localization and navigation for autonomous mobile robots using Petri nets in indoor environments,” *IEEE access*, vol. 6, pp. 31665-31676, Jun. 2018.

[34] W. Lv, Y Kang, and J. Qin, “Indoor localization for skid-steering mobile robot by fusing encoder, gyroscope, and magnetometer,” *IEEE Trans. Syst., Man, Cybern. Syst.*, vol. 49, no. 6, pp. 1241-1253, Jun. 2019.

[35] R. Moses, D. Krishnamurthy, and R. Patterson, "A self-localization method for wireless sensor networks," *EURASIP Journal on Advances in Signal Processing*, p. 348-358, vol. 4, 2003.

[36] J. Jiang, C. Lin, and Y. Hsu, "Localization with rotatable directional antennas for wireless sensor networks," 39th *Int. Conf. on Parallel Processing*, San Diego, CA, 2010, pp. 542-548.

[37] A. Bachir, M. Dohler, T. Watteyne and K. K. Leung, "MAC essentials for wireless sensor networks," *IEEE Commun. Surveys Tuts.*, vol. 12, no. 2, pp. 222-248, Second Quarter 2010.

[38] A. Kumar, M. Zhao, K. Wong, Y. Guan and P. Chong, "A comprehensive study of IoT and WSN MAC protocols: research issues, challenges and opportunities," *IEEE Access*, vol. 6, pp. 76228-76262, 2018.

[39] M. Al-Jarrah, K.-H. Park, A. Al-Dweik, and M.-S. Alouni, "Error rate analysis of amplitude-coherent detection over Rician fading channels with receiver diversity," *IEEE Trans. Wireless Commun.*, vol. 19, no. 1, pp. 134-147, Jan. 2020.

[40] P. Dharmawansa, N. Rajatheva and C. Tellambura, "Envelope and phase distribution of two correlated gaussian variables," *IEEE Trans. Commun.*, vol. 57, no. 4, pp. 915-921, Apr. 2009.

[41] A. Al-Dweik and Y. Iraqi, "Error probability analysis and applications of amplitude-coherent detection in flat Rayleigh fading channels," *IEEE Trans. Commun.*, vol. 64, no. 5, pp. 2235-2244, May 2016.

[42] M. Al-Jarrah and M. Yaseen, "Performance evaluation of amplitude coherent detection over Nakagami-m fading channels with multiple receiving antennas," *Electr. Comput. Technol. Appl. (ICECTA) 2019 Int. Conf.*, pp. 1-6, 2019.

[43] J. Proakis, Digital Communications, 3rd Ed. New York: McGraw-Hill, 1995.

[44] Standard gain horn antenna LB430-15, from Ainfo Inc, [available online] at `http://www.ainfoinc.com/en/p_ant_h_std.asp`, last accessed 05/02/2020.

[45] F. Ulaby and U. Ravaioli, Fundamentals of Applied Electronics, USA: Prentice Hall, 2015.

[46] C. Balanis, Antenna Theory: Analysis and Design, 4th Ed. USA: Wiley, 2016. ISBN: 978-1-118-64206-1.

[47] D. Jenkins and P. Ascencio, "A solution to minimum sample size for regressions," *PloS One*, vol. 15(2), e0229345, Feb. 2020.

[48] R. Tazawa, N. Honma, A. Miura, and H. Minamizawa, "RSSI-based localization using wireless beacon with three-element array," *IEICE Trans. Commun.* vol. E101-B, no. 2, Feb. 2018.

[49] N. Katenka, E. Levina, and G. Michailidis, “Local vote decision fusion for target detection in wireless sensor networks,” *IEEE Trans. Signal Process.*, vol. 56, no. 1, pp. 329-338, Jan. 2008.

[50] R. Wilson, Introduction to Graph Theory, 4th Ed. UK: Addison Wesley Longman Limited, 1996.

[51] R. Vaghefi and R. Buehrer, “Received signal strength-based sensor localization in spatially correlated shadowing,” *IEEE Int. Conf. on Acoustics, Speech and Signal Processing (ICASSP)*, Vancouver, BC, Canada, 2013, pp. 4076-4080.

[52] J. Vongkulbhisal and Y. Zhao, “An RFID-based indoor localization system using antenna beam scanning,” *9th Int. Conf. Electr. Eng./Electron., Computer, Telecomm. Info. Technol.*, Phetchaburi, 2012, pp. 1-4.

[53] A. Erdogan, V. Coskun, and A. Kavak, “The sectoral sweeper scheme for wireless sensor networks: Adaptive antenna array based sensor node management and location estimation”, *Wireless Pers. Commun.*, vol. 39, no. 415, pp. 415-433, Dec. 2006.

[54] A. Cidronali, S. Maddio, G. Giorgetti, and G. Manes, “Analysis and performance of a smart antenna for 2.45-GHz single-anchor indoor positioning,” *IEEE Trans. Microw. Theory Techn.*, vol. 58, no. 1, pp. 21-31, Jan. 2010.

[55] L. Kulas, “RSS-based DoA estimation using ESPAR antennas and interpolated radiation patterns,” *IEEE Antennas Wireless Propag. Lett.*, vol. 17, no. 1, pp. 25-28, Jan. 2018.

[56] M. Plotka, M. Tarkowski, K. Nyka, and L. Kulas, “A novel calibration method for RSS-based DoA estimation using ESPAR antennas,” 22*nd Int. Microw. and Radar Conf. (MIKON)*, Poznan, 2018, pp. 65-68.

[57] A. Mirkamali, R. Deban, F. Siaka and J. Laurin, “Fast and low-cost beam steering using an agile mechanical feed system for exciting circular arrays,” *IET Microw. Antenna P.*, vol. 10, no. 4, pp. 378-384, 19 3 2016.

[58] L. Xing, J. Zhu, Q. Xu, D. Yan and Y. Zhao, “A circular beam-steering antenna with parasitic water reflectors,” *IEEE Antennas Wireless Propag. Lett.*, vol. 18, no. 10, pp. 2140-2144, Oct. 2019.

[59] W. Hong e*t al.*, “Multibeam antenna technologies for 5G wireless communications,” *IEEE Trans. Antennas Propag.*, vol. 65, no. 12, pp. 6231-6249, Dec. 2017.

Chapter 4

Decision Fusion for IoT-Based Wireless Sensor Networks[1]

Abstract

This paper presents a novel decision fusion algorithm for Internet-of-Things based wireless sensor networks, where multiple sensors transmit their decisions about a certain phenomenon to a remote fusion center (FC) over a wide area network. The proposed algorithm, denoted as the individual likelihood approximation (ILA), can significantly reduce the decision fusion error probability performance while maintaining the low computational complexity of other state-of-the-art fusion algorithms. The performance of the ILA rule is evaluated in terms of the global fusion probability of error, and an efficient analytical expression is derived in terms of a single integral. The analytical results corroborated by Monte Carlo simulation show that the ILA significantly outperforms all other considered rules, such as the Chair-Varshney (CV) and MaxLog rules. Moreover, the impact of the link from the cluster head to the FC, which is modeled as a binary symmetric channel with unknown transition probabilities, has been investigated. It is shown that the probability of error over such links should not exceed 10^{-3} to avoid sever performance degradation. Furthermore, we derive a closed-form expression for the system fusion error probability of the CV rule for the most general system parameters.

Index Terms

Global connectivity, Internet-of-Things, IoT, wireless sensor network, data fusion, LoRaWAN, NB-IoT.

[1]**M. A. Al-Jarrah**, M. A. Yaseen, A. Al-Dweik, O. A. Dobre and E. Alsusa, "Decision fusion for IoT-based wireless sensor networks," *IEEE IoT. J.*, vol. 7, no. 2, pp. 1313-1326, Feb. 2020, doi: 10.1109/JIOT.2019.2954720.

4.1 Introduction

The Internet-of-Things (IoT), machine-to-machine communications and cloud computing are among the main game-changing technologies for the wireless communications sector [1]. The integration of these technologies will enable the deployment of a massive number of low-cost and low-power devices, such as sensors, actuators, smart meters, etc. The IoT infrastructure will enable the connectivity of such massive number of compatible devices, and will allow the design of low-power consumption networks by realizing the global connectivity vision [2]. More specifically, if a sensor is in close proximity of a base-station, WiFi access point, etc., then the transmission power of the sensor can be reduced significantly [1]. The cloud computing technology enables transferring the computational capabilities of the communicating devices to the cloud, which can simultaneously reduce the cost, size and processing power of these devices [3], [4]. According to the Cisco internet business solutions group report [5], it is predicted that fifty billion IoT devices will be connected to the Internet by 2020. This explains the researchers' global and growing interest in IoT in recent years. Consequently, developing reliable rules to fuse all collected data from sensors to get reliable decisions is crucial for the success of wireless sensor network (WSN)/IoT integration [6]- [11].

Generally speaking, a WSN consists of a group of spatially distributed sensors with limited capabilities in a certain space, where they cooperate to perform a certain task. WSNs are widely adopted for a vast number of applications in various fields, including environmental, military, medical, and industrial applications [12]- [18]. Cooperative spectrum sensing is an emerging application of WSNs and data fusion [19]- [21]. The design of small-size and low-cost sensing nodes facilitates the deployment of WSNs in various environments and locations that might be harsh and unreachable. With the aid of IoT and cloud computing technologies, achieving such objectives becomes feasible. Consequently, it is crucial to develop efficient decision fusion algorithms that can be used with a very large number of sensors, as well as to evaluate the performance of such algorithms in the context of IoT [22].

In an IoT-based WSN, the region of interest can be much larger than for a conventional WSN, where the sensors are distributed over a local area. The network configuration might follow the typical WSN, where each group of sensors is initially connected to a cluster head (CHD), and all CHDs are connected to the fusion center (FC) through an IoT infrastructure, which might include base-station, denoted as eNB in the long-term evolution (LTE) terminology, core network components, etc. Figure. 4.1 shows a simple example of an WSN-IoT with two clusters and two CHDs; each CHD collects information from three sensors. Alternatively, each sensor might be connected directly to the cloud via a particular modem. In both configurations, the fusion process should be performed at the FC, which can be hosted at the cloud. Fusion over the cloud is very popular nowadays for applications such as sensing as a service [23]. Moreover, the FC can be also hosted at a fog node in time-sensitive applications. In the first configuration, which is the model considered in this work, the WSN will experience the same constraints and limitations of a con-

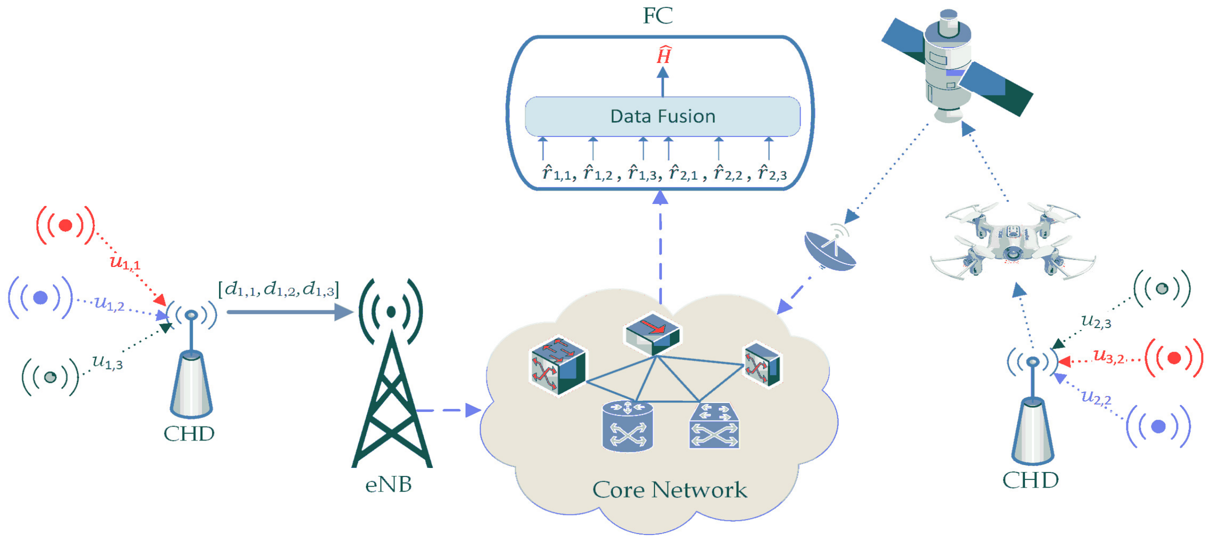

Figure 4.1: Example of IoT-based data fusion with two-cluster WSN with different connectivity to the fusion center.

ventional WSN, which include limited bandwidth, energy, power, memory, and computational capability. Techniques proposed in the literature to reduce the energy consumption are based on compressive sensing, energy-efficient routing, optimum clustering, and scheduling data communications between sensors and sink nodes [24]- [27]. Energy-efficient techniques were also introduced to limit the number of transmitting sensors by applying a certain criterion such as censoring [28] and ordered transmission [29]. To satisfy the limited bandwidth, [30] suggested that only selected parts of the sensor's decisions to be transmitted to the FC, which applies distributed fusion Kalman filter (DFKF) to compensate for the missing decisions. In [31], an algorithm referred to the finite-time average-consensus is provided to achieve distributed average consensus in finite time, while maintaining low-computational and memory requirements. Different congestion control mechanisms and protocols for WSNs can be found in [32].

4.1.1 Related Work

In the literature, various fusion rules (FRs) have been proposed for conventional WSNs, which can be also used for fusion over IoT infrastructure. For example, the likelihood ratio test (LRT) under the Neyman-Pearson sense is applied in [33]- [35] to develop an optimum FR. However, the complexity of the optimum rule and the enormous amount of computations, which are unsuitable to resources-constrained networks, have motivated researchers to search for less complex rules, which are typically suboptimum in terms of fusion error performance. One of the most efficient suboptimum FRs is the Chair-Varshney (CV) rule, which is a two-stage FR. As shown in [33] and [34], the CV probability of error performance asymptotically approaches the optimum fusion at high signal-to-noise ratios (SNRs). Other low-complexity FRs such as AND, OR, k out of N and majority voting rules, can be derived from the CV rule by assuming that the sensors are identical [36]- [38]. Although these rules have relatively low-complexity and do not depend on the local false alarm and detection probabilities, their performance is worse than the CV rule, particularly for networks with non-identical sensors. The MaxLog rule proposed in [35] performs generally better than the CV rule, yet, it does not guarantee reliable performance for all system and channel conditions. Other rules based on diversity combining, such as the maximum ratio combining and equal gain combining, are presented in the literature as very low-complexity FRs; however, these rules do not satisfy the required detection accuracy [39]. In [15], [17], Al-Jarrah *et al.* explored the decision fusion problem in cooperative WSNs, and considered several conventional FRs such as, ILS [35], MaxLog [35], CV [34]. The complexity of the conventional rules is reduced using various approximations for the decision statistics. However, the performance of the approximated and exact rules suffer a noticeable performance degradation due to the simplifying assumptions used to derive these rules. In [40], an impulse radio wide-band system is proposed with massive antenna arrays applied at the FC, where the trade-off between coherent and non-coherent detection based fusion rules is studied. However, the decision variable in [40] is based on the combined signal at the FC, while other types of fusion rules are not considered.

4.1.2 Motivation and Contribution

Although the problem of decision fusion of distributed sensors has been widely investigated, it is apparent from the extensive literature review that the problem remains open due to the conflict between complexity and fusion error performance. Most of the techniques reported in the literature are designed to trade-off one parameter versus the other. Moreover, to the best of the authors' knowledge, no work has been reported in the literature that considers the impact of having multiple heterogeneous hops with unknown characteristics as in the case of IoT applications. The main challenge in such distributed topologies is that optimum fusion requires knowledge of channel state information (CSI) on all links between any sensor and the FC. Nevertheless, it is infeasible to have such information in practical scenarios due to the fact that several communications nodes actually act as decode-and-forward relays, and hence, the CSI on such links will be suppressed. Moreover, even if the CSI can be estimated for certain links, sending the CSI to the FC will mostly incur some errors, which may jeopardize the benefit of having such information at the FC. Therefore, the main contributions of this paper can be summarized as follows:

1. Proposes a procedure for deploying WSNs over IoT infrastructure to enable decision fusion over wide area networks (WANs).

2. Derives a novel efficient decision FR, referred to the individual likelihood approximation (ILA) rule, which offers near-optimum fusion error performance with complexity that is comparable to conventional suboptimum rules. Based on the derived FR, we specify all the information required to perform reliable fusion, discuss the feasibility of having such information at the FC, and evaluate the performance of the FR under imperfect information conditions. Moreover, the derived algorithm is not based on any simplifying assumption, which makes its performance superior as compared to conventional algorithms.

3. The probability of detection and false alarm are derived at the FC in terms of a single integral that can be evaluated numerically.

4. Investigates the performance of the proposed ILA rule with and without sending the decisions over IoT infrastructure, and evaluates the required core network reliability for near-perfect fusion.

5. Derives a closed-form expression for the performance of the CV rule in the most general case where each sensor in the network may have its own characteristics. To the best of the authors' knowledge, none of the work reported in the literature considered the most general case [15], [21], [28], [34], [41]-[48]. Such analysis is more realistic because it is practically very challenging to deploy all sensors with identical characteristics. Moreover, the sensor performance generally depends on many other factors.

It is worth noting that unlike the other common FRs, the ILA is derived by approximating the likelihood ratio function without considering any other simplifying assumptions. Therefore, a significant performance improvement can be gained as compared to conventional rules such as the ones described in [15], [17], and the references listed therein.

4.1.3 Paper organization

The rest of the paper is organized as follows. Section II describes the system model of a WSN. Section III introduces the optimum decision FR. The CV rule is revisited in Section IV. The proposed FR and its performance analysis are presented in Sections V and VI, respectively. Sections VII and VIII provide simulation results and conclusions, respectively.

4.2 System Model

As depicted in Fig. 4.1, this work considers an integrated WSN-IoT configuration. The main components of the WSN are the sensing nodes, also referred to sensors, and one or more CHDs. The sensors are divided into clusters, and the sensors in each cluster are connected to the CHD in a star topology via a wired/wireless link. The CHD is the interface between the sensors and IoT infrastructure, which refers to all components that link the CHD to the FC, which may include eNBs, WiFi access points, cellular modems, unmanned aerial vehicles (UAVs) and satellites [49]. Such components are also denoted as IoT nodes. The IoT infrastructure also includes the core network, which comprises several wireless and wired links.

The WSN that consists of $K \times L$ distributed wireless sensors deployed in a specific region to collect observations about a certain phenomenon. The sensors are divided into K clusters, where the sensors in each cluster communicate with a CHD as shown in Fig. 4.1. All CHDs are connected to an FC through a particular wireless link such as cellular/WiFi networks, satellite links, or UAV [9], which is a typical structure for rural area communications [50]. The UAVs can be used to collect data from the CHDs and pass it to the FC through a satellite connection or other available connections, or may act as flying CHD if the WSN density is low [50]. Each sensor makes a binary decision about the existence of the phenomenon independently and sends the decision to the CHD. Because WSNs may need to provide connectivity to a large number of sensors, the adopted multiple access (MAC) protocol and network topology should be designed to support such scenarios. However, WSNs typically have low data rate requirements, and hence, orthogonal MACs can be used to connect massive number of sensors. For example, the narrowband IoT (NB-IoT) standard [51], [52] has a bandwidth of 180 kHz, with a possible subcarrier spacing of 3.75 kHz. Each subcarrier can be allocated to a different user for a period of 32 ms. Therefore, if the sensing duty cycle for each sensor is one second, then the system can support more than $1,500$ sensors in each cell. On the other hand, non-orthogonal MACs are also adopted in some industrial standards such as the Long-Range wide area network (LoRaWAN) network protocol [53], [54]. In this work, the considered MAC protocol follows the NB-IoT uplink , which is based on single carrier frequency division multiple access (SC-FDMA), and thus, all sensors send their decisions to the CHD through orthogonal channels [51].

The signal generated by a given sensor during the tth sensing period can be defined as [17], [21]

$$\chi_{k,l}[t]|H_1 = \hbar_{k,l}x[t] + \xi_{k,l}[t] \tag{4.1a}$$

$$\chi_{k,l}[t]|H_0 = \xi_{k,l}[t] \tag{4.1b}$$

where l and k denote the sensor and cluster indices, respectively, H_1 and H_0 denote the presence and absence of the phenomenon, respectively, x is the signal produced by the sensor due to the observed phenomenon, $\hbar_{k,l}$ is a random variable that captures the different signal strengths that the observed phenomenon would generate at each sensor, and the additive white Gaussian noise (AWGN) $\xi_{k,l} \sim \mathcal{N}\left(0,\, \sigma_\xi^2\right)$. It is worth noting that $\chi_{k,l}$ $\forall k$ and l are independent because the AWGN samples and $\hbar_{k,l}$ are independent. The signal at the kth sensor $\chi_{k,l}[t]$ is then compared to threshold $\tau_{k,l}$ to make a binary decision $u_{k,l} \in \{-1,\, 1\}$. The decision-making process of the sensor can be characterized by its detection probability $P_{k,l}^{\mathrm{d}} = \Pr\left(u_{k,l} = 1|H_1\right)$ and false alarm probability $P_{k,l}^{\mathrm{fa}} = \Pr\left(u_{k,l} = 1|H_0\right)$, where they can be given by

$$\begin{aligned} P_{k,l}^{\mathrm{d}} &= \Pr\left(\chi_{k,l}[t] > \tau_{k,l}|H_1\right) \\ &= Q\left(\frac{\tau_{k,l} - \hbar_{k,l}x[t]}{\sigma_\xi}\right) \end{aligned} \tag{4.2a}$$

$$\begin{aligned} P_{k,l}^{\mathrm{fa}} &= \Pr\left(\chi_{k,l}[t] > \tau_{k,l}|H_0\right) \\ &= Q\left(\frac{\tau_{k,l}}{\sigma_\xi}\right) \end{aligned} \tag{4.2b}$$

where $Q(\cdot)$ is the complementary cumulative distribution function of the standard normal distribution.

A typical example for such model is the fire detection system using WSNs. In such a system, the sensors keep sensing the temperature, which is a continuous value, yet, the sensors do not send any alarm unless the temperature is lager than a predefined threshold. Therefore, $u_{k,l} = 1$ corresponds to the case where $\chi_{k,l}$ is greater than the threshold [55], [56]. Using such approach is necessary to reduce the energy and bandwidth requirements of the WSN because the continuous data should be represented by a large number of bits as compared to a single bit in the binary case.

After the generation of the binary decisions, each sensor modulates its decision using binary phase-shift-keying (BPSK) and transmits it to the CHD. Low-order modulation schemes such as BPSK are usually adopted in WSN and IoT applications because of their high power efficiency as in the case of the NB-IoT standard which may use only BPSK or quadrature phase-shift-keying (QPSK) [57]. The wireless links between the sensors and their corresponding CHDs are assumed to be mutually independent and identically distributed (i.i.d.) flat fading channels with Rayleigh distribution. At the kth CHD, the received signal from the lth sensor can be represented as

$$r_{k,l} = \sqrt{\mathcal{P}_{k,l}} h_{k,l} u_{k,l} + n_{k,l} \tag{4.3}$$

where $h_{k,l} \sim \mathcal{CN}(0,\sigma_h^2)$ is the fading coefficient, $n_{k,l} \sim \mathcal{CN}(0,\sigma_n^2)$ is the AWGN, and $\mathcal{P}_{k,l}$ is the average transmission power. It is worth noting that most IoT standards, such as the NB-IoT, apply error control coding in the form of repetition codes [52], and hence, the received signal at the CHD (4.3) remains unchanged with and without coding.

To perform global fusion at the FC, all CHDs should forward their signals $r_{k,l}\ \forall \{k, l\}$ to the FC. For example, given that each CHD is connected to the FC via a single-hop wireless link, and the CHD is configured to relay $r_{k,l}$ in an amplify-and-forward manner; then, the received signal of the lth sensor and kth cluster at the FC can be expressed as [17], [21],

$$\mathfrak{r}_{k,l} = \mathfrak{a}_{k,l} \mathfrak{h}_{k,l} r_{k,l} + \mathfrak{n}_{k,l} \tag{4.4}$$

where $\mathfrak{h}_{k,l}$ is an arbitrary channel gain between the CHD and FC, $\mathfrak{a}_{k,l}$ is the relaying gain introduced by the CHD, and $\mathfrak{n}_{k,l} \sim \mathcal{CN}(0, \sigma_{\mathfrak{n}}^2)$. Moreover, the FC must have knowledge of $\left\{\mathfrak{h}_{k,l}, h_{k,l}, P^{\mathrm{d}}_{k,l}, P^{\mathrm{fa}}_{k,l}\right\} \forall \{k, l\}$, σ_n^2 and $\sigma_{\mathfrak{n}}^2$ [17], [21]. However, for WANs such as the one depicted in Fig. 4.1, it is generally infeasible to estimate the end-to-end (CHD→FC) CSI because of the large number of intermediate links and relays with unknown characteristics [11]. Moreover, the signals over the core network are typically digital, and hence, a quantized and maybe erroneous versions of $r_{k,l}$, denoted as $\hat{r}_{k,l}$, will be received by the FC. Therefore, the link between the CHD and FC is modeled as a binary symmetric channel (BSC) with an unknown transition probability ρ_e. As the values of $h_{k,l}$ can not be estimated directly at the FC, the CHD has to package and transmit both $r_{k,l}$ and $h_{k,l}$ to the FC. The values of $P^{\mathrm{d}}_{k,l}$ and $P^{\mathrm{fa}}_{k,l}$ can be estimated at the CHD and forwarded to the FC, or estimated directly at the FC, which is the scenario considered in this work. The value of σ_n^2 is typically fixed for relatively long time periods; hence, it is considered to be known perfectly at the FC. Consequently, the main overhead associated with the fusion process at the fusion center is the channel fading coefficients $h_{k,l}\ \forall\{k,l\}$. Because wireless channels can not be considered static over long time periods, $h_{k,l}$ should be updated for each fusion process, which may affect the overall system throughput. Moreover, in the case that $P^{\mathrm{d}}_{k,l}$ and $P^{\mathrm{fa}}_{k,l}$ are estimated at the CHD and forwarded to the FC, then they will also contribute to the system overhead. Nevertheless, the varying rate of $P^{\mathrm{d}}_{k,l}$ and $P^{\mathrm{fa}}_{k,l}$ is typically much less than the transmission rate, and hence, their impact on the system overhead is very limited.

4.3 Optimum Fusion Rule (FR)

Using the signals $\hat{r}_{k,l}\ \forall\{k,l\}$ received by the FC, the LRT under Neyman-Pearson sense can be used to derive the optimum FR that maximizes the system probability of detection P_D for a given probability of false alarm P_{FA} [17]. Therefore [58],

$$\begin{aligned}\hat{H}_{\mathrm{opt}} &= \arg\max_{H_i}\left\{f\left(H_i|\hat{\mathbf{R}}\right)\times\kappa_i\right\}\\ &= \arg\max_{H_i}\left\{\frac{f\left(\hat{\mathbf{R}}|H_i\right)\times\Pr\left(H_i\right)}{f\left(\hat{\mathbf{R}}\right)}\times\kappa_i\right\}\end{aligned}\tag{4.5}$$

where $\hat{\mathbf{R}}=\left[\hat{\mathbf{r}}_1^T,\hat{\mathbf{r}}_2^T,...,\hat{\mathbf{r}}_K^T\right]$, $\hat{\mathbf{r}}_k=\left[\hat{r}_{k,1},\hat{r}_{k,2},...,\hat{r}_{k,L}\right]$ and κ_i is a factor used to give priority to a hypothesis or to satisfy some constraints on the fusion level false alarm rate. By noting that $f\left(\hat{\mathbf{R}}\right)$ can be dropped without affecting the optimization process, then

$$\begin{aligned}\hat{H}_{\mathrm{opt}} &= \arg\max_{H_i}\left\{f\left(\hat{\mathbf{R}}|H_i\right)\times\Pr\left(H_i\right)\times\kappa_i\right\}\\ &= \arg\max_{H_i}\prod_{k=1}^{K}\prod_{l=1}^{L}\left\{f\left(\hat{r}_{k,l}|H_i\right)\times\Pr\left(H_i\right)\times\kappa_i\right\}\end{aligned}\tag{4.6}$$

which can be simplified by computing the logarithm of the argument in (4.6), which gives

$$\hat{H}_{\mathrm{opt}}=\arg\max_{H_i}\sum_{k=1}^{K}\sum_{l=1}^{L}\ln\left\{f\left(\hat{r}_{k,l}|H_i\right)\times\Pr\left(H_i\right)\times\kappa_i\right\}.\tag{4.7}$$

However, given that $r_{k,l}$ is quantized sufficiently and the CHD-FC link is fairly reliable, i.e., $\rho_e = 0$, then $\hat{r}_{k,l} \approx r_{k,l}$. Consequently, the optimum rule can be expressed as

$$\hat{H}_{\widetilde{\text{opt}}} = \begin{cases} H_1, & \sum_{k=1}^{K} \sum_{l=1}^{L} \text{LLR}_{k,l}^{\widetilde{\text{opt}}} > \tau_g \\ H_0, & \text{otherwise} \end{cases} \tag{4.8}$$

where $\tau_g = \ln\left(\frac{\kappa_0 \Pr(H_0)}{\kappa_1 \Pr(H_1)}\right)$, and

$$\text{LLR}_{k,l}^{\widetilde{\text{opt}}} = \ln\left(\frac{f\left(r_{k,l}|H_1\right)}{f\left(r_{k,l}|H_0\right)}\right). \tag{4.9}$$

According to the law of total probability, $f\left(r_{k,l}|H_i\right)$ can be written as

$$f\left(r_{k,l}|H_i\right) = \sum_{u_{k,l}\in\{-1,1\}} f\left(r_{k,l}|u_{k,l}\right) \Pr\left(u_{k,l}|H_i\right). \tag{4.10}$$

By noting that the probability density function (PDF) of the received signal conditioned on $u_{k,l}$ is $f\left(r_{k,l}|u_{k,l}\right) \sim \mathcal{CN}(m_{k,l}|u_{k,l}, \sigma_n^2)$, where $m_{k,l}|u_{k,l} = \sqrt{\mathcal{P}_{k,l}} h_{k,l} u_{k,l}$, the $\text{LLR}_{k,l}^{\widetilde{\text{opt}}}$ given in (4.9) can be expanded as shown in (4.11), where $\mu_{k,l} = \sqrt{\mathcal{P}_{k,l}} h_{k,l}$.

$$\text{LLR}_{k,l}^{\widetilde{\text{opt}}} = \ln\left(\frac{P_{k,l}^{\text{d}} \exp\left(\frac{-|r_{k,l}-\mu_{k,l}|^2}{\sigma_n^2}\right) + \left(1-P_{k,l}^{\text{d}}\right)\exp\left(\frac{-|r_{k,l}+\mu_{k,l}|^2}{\sigma_n^2}\right)}{P_{k,l}^{\text{fa}} \exp\left(\frac{-|r_{k,l}-\mu_{k,l}|^2}{\sigma_n^2}\right) + \left(1-P_{k,l}^{\text{fa}}\right)\exp\left(\frac{-|r_{k,l}+\mu_{k,l}|^2}{\sigma_n^2}\right)}\right) \tag{4.11}$$

After some mathematical manipulations, $\text{LLR}_{k,l}^{\widetilde{\text{opt}}}$ can be simplified to

$$\text{LLR}_{k,l}^{\widetilde{\text{opt}}} = \ln\left(\frac{P_{k,l}^{\text{d}} + \left(1-P_{k,l}^{\text{d}}\right)\exp\left(-y_{k,l}\right)}{P_{k,l}^{\text{fa}} + \left(1-P_{k,l}^{\text{fa}}\right)\exp\left(-y_{k,l}\right)}\right) \tag{4.12}$$

where $y_{k,l} = \frac{4}{\sigma_n^2}\Re\left[r_{k,l}\left(\mu_{k,l}\right)^*\right]$, and thus, it is necessary to know σ_n^2 to be able to compute $y_{k,l}$.

Although the FR in (4.8) results in near-optimum detection performance, it suffers from the drawbacks of high computational complexity and numerical problems which may occur at high SNRs; these may limit its potential for practical implementation. The computational complexity arises because the rule requires evaluating KL logarithmic and exponential functions for wide range of arguments. The numerical instability may result from evaluating exponential functions when $\sigma_n^2 \to 0$, and thus, $\exp\left(-y_{k,l}\right) \to \infty$ or 0 depending on the sign of $y_{k,l}$. In an alternative realization, the decision variable of the optimum rule (4.8) can be written as

$$\ln\left(\prod_{k=1}^{K}\prod_{l=1}^{L}\frac{P_{k,l}^{\text{d}} + \left(1-P_{k,l}^{\text{d}}\right)\exp\left(-y_{k,l}\right)}{P_{k,l}^{\text{fa}} + \left(1-P_{k,l}^{\text{fa}}\right)\exp\left(-y_{k,l}\right)}\right) \tag{4.13}$$

and thus, the KL logarithmic operations can be reduced to one at the expense of an additional $KL - 1$ multiplications. Although the complexity of the multiplication operation is generally less than the logarithm, it is typically difficult to compute the LLR values accurately due to the large number of multiplication operations. More specifically, when $y_{l,k} \ll 1$, or $y_{l,k} \gg 1$, the result of the product will be either substantially large or small, which makes it infeasible to implement using reasonable hardware complexity. Therefore, using the form in (4.8) is generally more preferable.

4.4 Existing Suboptimum Rules

This section presents the well-established FRs, which are used in this work for benchmarking purposes. Although these rules are described in the literature, they are briefly listed in this paper for the sake of completeness.

4.4.1 Chair-Varshney (CV) Rule [41]

The CV rule is widely considered for applications that require fusing 1-bit decisions transmitted from distributed sensors, as in the case of cooperative spectrum sensing [21]. The pivotal requirement for implementing the CV rule is the knowledge of the local probability of detection and false alarm at each sensor.

In the CV rule, the fusion process is performed in two stages. In the first stage, a hard decision detector based on the maximum likelihood criterion is applied to detect the transmitted BPSK signals. Therefore, the estimated nodes' decisions at the FC are given by

$$\hat{u}_{k,l}^{\mathrm{CV}} = \begin{cases} 1, & \frac{4\sqrt{\mathcal{P}_{k,l}}}{\sigma_n^2} \Re\left(r_{k,l}(h_{k,l})^*\right) > \ln \frac{P_1}{P_0} \\ -1, & \text{otherwise} \end{cases} \tag{4.14}$$

where $P_1 = \Pr\left(u_{k,l} = 1\right)$ and $P_0 = \Pr\left(u_{k,l} = -1\right)$. In general, obtaining accurate estimates for P_1 and P_0 is challenging because they depend on $\Pr\left(H_0\right)$ and $\Pr\left(H_1\right)$ [21]. Therefore, most of the works reported in the literature assume that $\Pr\left(u_{k,l} = 1\right) = \Pr\left(u_{k,l} = -1\right) = 0.5$, and thus, $\ln \frac{\Pr(u_{k,l}=1)}{\Pr(u_{k,l}=-1)} = 0$.

In the second stage, the resulted decisions $\hat{u}_{k,l}^{\mathrm{CV}}\ \forall \{k,l\}$ are sent for fusion using the CV rule,

$$\hat{H}_{\mathrm{CV}} = \begin{cases} H_1, & \sum_k \sum_l \mathrm{LLR}_{k,l}^{\mathrm{CV}} > \tau_{\mathrm{CV}} \\ H_0, & \text{otherwise} \end{cases} \tag{4.15}$$

where

$$\mathrm{LLR}_{k,l}^{\mathrm{CV}} = \begin{cases} a_{k,l}, & \hat{u}_{k,l}^{\mathrm{CV}} = 1 \\ b_{k,l} & \hat{u}_{k,l}^{\mathrm{CV}} = -1 \end{cases} \tag{4.16}$$

$a_{k,l} = \ln\left(\frac{P_{k,l}^{\mathrm{d}}}{P_{k,l}^{\mathrm{fa}}}\right)$, $b_{k,l} = \ln\left(\frac{1-P_{k,l}^{\mathrm{d}}}{1-P_{k,l}^{\mathrm{fa}}}\right)$, and τ_{CV} is a fusion threshold used to satisfy certain constraints on the fusion level false alarm rate. Figure 4.2 shows the $\mathrm{LLR}_{k,l}^{\mathrm{CV}}$. As can be noted from (4.15), the CV rule does not require evaluating logarithmic and exponential functions, but the values of $P_{k,l}^{\mathrm{d}}$ and $P_{k,l}^{\mathrm{fa}}$ are required at the FC.

Although the CV rule is highly reliable at high SNRs, the hard detection leads to significant performance loss at low and moderate SNRs, which are typically the operating ranges of WSNs due to power constraints. Consequently, applying the CV rule with hard detection may lead to modest error performance, in addition to the degradation caused by assuming that $\Pr(u_{k,l}=1)=\Pr(u_{k,l}=-1)$.

4.4.2 MaxLog Fusion Rule [41]

In this rule, using the fact that only one term in the denominator and numerator of (4.12) is dominant, the optimum rule can be approximated by

$$\hat{H}_{\text{MaxLog}} = \begin{cases} H_1, & \sum_{k=1}^{K}\sum_{l=1}^{L} \text{LLR}_{k,l}^{\text{MaxLog}} > \tau_g \\ H_0, & \text{otherwise} \end{cases} \tag{4.17}$$

where

$$\text{LLR}_{k,l}^{\text{MaxLog}} = \begin{cases} b_{k,l}, & y_{k,l} \leq e_{k,l} \\ y_{k,l} + c_{k,l}, & e_{k,l} < y_{k,l} < d_{k,l} \\ a_{k,l}, & y_{k,l} \geq d_{k,l} \end{cases} \tag{4.18}$$

where $c_{k,l} = \ln\left(\frac{P_{k,l}^{\text{d}}}{1-P_{k,l}^{\text{fa}}}\right)$, $d_{k,l} = \ln\left(\frac{1-P_{k,l}^{\text{fa}}}{P_{k,l}^{\text{fa}}}\right)$, and $e_{k,l} = \ln\left(\frac{1-P_{k,l}^{\text{d}}}{P_{k,l}^{\text{d}}}\right)$. Compared to the CV rule, the MaxLog rule has the same requirements, and comparable computational complexity.

4.4.3 Ideal Local Sensors Rule (ILS) [35]

In this rule, it is assumed that the FC does not have knowledge of $P_{k,l}^{\text{d}}$ and $P_{k,l}^{\text{fa}}$, and thus, it assumes ideal sensors, i.e., $P_{k,l}^{\text{d}}=1$ and $P_{k,l}^{\text{fa}}=0$, which after substitution in (4.12) yields,

$$\hat{H}_{\text{ILS}} = \begin{cases} H_1, & \sum_{k=1}^{K}\sum_{l=1}^{L} \frac{4\sqrt{\mathcal{P}_{k,l}}}{\sigma_n^2} \Re\left[r_{k,l}\left(h_{k,l}\right)^*\right] > \tau_g \\ H_0, & \text{otherwise} \end{cases}. \tag{4.19}$$

Unlike all other FRs considered in this paper, the ILS rule does not require $P_{k,l}^{\text{d}}$ and $P_{k,l}^{\text{fa}}$, and hence, it has a computational complexity advantage. However, it is at the expense of error probability performance. Another advantage in terms of computational complexity is that it does not require the evaluation of exponential or logarithmic functions, but only of a small number of arithmetic operations.

4.5 Proposed ILA Rule

As can be noted from the discussion of the existing FRs in Section 4.4, the main goal of these techniques is to reduce the complexity of the optimum FR by simplifying the $\widetilde{\text{LLR}}_{k,l}^{\text{opt}}$. Nevertheless, each of these techniques seems to perform reliably only when the condition used for the simplification is accurate, i.e., none of them performs well for general operating conditions. For example, the CV rule is designed by assuming that $\Pr(u_{k,l}=1) = \Pr(u_{k,l}=-1)$. However, as demonstrated in [21], this assumption may lead to significant probability of fusion error (PFE) degradation. Therefore, the proposed ILA rule is designed to provide an accurate approximation for the $\widetilde{\mathrm{LLR}_{k,l}^{\mathrm{opt}}}$ that offers reliable PFE performance for a wide range of operating conditions while maintaining low-complexity.

As can be noted from Fig. 4.2, the $\widetilde{\mathrm{LLR}_{k,l}^{\mathrm{opt}}}$ passes through the point $(0,0)$ and the mid-point of the nonlinear region $\left(y_{k,l}^{\mathrm{mid}}, z_{k,l}^{\mathrm{mid}}\right)$, where $z_{k,l}^{\mathrm{mid}} = \frac{a_{k,l}+b_{k,l}}{2}$, and then $y_{k,l}^{\mathrm{mid}}$ can be evaluated based on (4.12) as

$$y_{k,l}^{\mathrm{mid}} = \ln\left(\frac{1-P_{k,l}^{\mathrm{d}} - \left(1-P_{k,l}^{\mathrm{fa}}\right)e^{z_{k,l}^{\mathrm{mid}}}}{P_{k,l}^{\mathrm{fa}}e^{z_{k,l}^{\mathrm{mid}}} - P_{k,l}^{\mathrm{d}}}\right) \tag{4.20}$$

Based on the points $(0,0)$ and $\left(y_{k,l}^{\mathrm{mid}}, z_{k,l}^{\mathrm{mid}}\right)$, the slope of the line can be calculated as $\alpha_{k,l} = \frac{z_{k,l}^{\mathrm{mid}}}{y_{k,l}^{\mathrm{mid}}}$. Recalling the equation of a straight line, i.e., $y = \alpha x + b$, and noting that $b = 0$ since the line passes through the point $(0,0)$, the equation of the line can be simply expressed as $\mathrm{LLR}_{k,l}^{\mathrm{Line}} = \alpha_{k,l}y_{k,l}$. Moreover, referring to Fig. 4.2, it can be observed that this line is bounded by $a_{k,l}$ and $b_{k,l}$, and thus, the interval of the straight line can be evaluated by finding the intersection points between $\alpha_{k,l}y_{k,l}$ and $b_{k,l}$, and $\alpha_{k,l}y_{k,l}$ and $a_{k,l}$. Consequently, $\mathrm{LLR}_{k,l}^{\mathrm{ILA}}$ can be approximated as

$$\mathrm{LLR}_{k,l}^{\mathrm{ILA}} = \begin{cases} b_{k,l}, & y_{k,l} \leq \frac{b_{k,l}}{\alpha_{k,l}} \\ \alpha_{k,l}y_{k,l}, & \frac{b_{k,l}}{\alpha_{k,l}} < y_{k,l} < \frac{a_{k,l}}{\alpha_{k,l}} \\ a_{k,l}, & y_{k,l} \geq \frac{a_{k,l}}{\alpha_{k,l}} \end{cases} \tag{4.21}$$

Similar to (4.12), the approximated individual LLR functions are added and compared to the fusion threshold in order to obtain the final decision $\hat{H}_{\mathrm{ILA}}$ given by,

$$\hat{H}_{\mathrm{ILA}} = \begin{cases} H_1, & \sum_{k=1}^{K}\sum_{l=1}^{L}\mathrm{LLR}_{k,l}^{\mathrm{ILA}} > \tau_g \\ H_0, & \text{otherwise} \end{cases}. \tag{4.22}$$

The accuracy of the approximated $\mathrm{LLR}_{k,l}^{\mathrm{ILA}}$ is shown in Fig. 4.3, where the normalized error is computed as

$$\text{Normalized Error} = \left|\frac{\mathrm{LLR}_{k,l}^{\mathrm{ILA}} - \widetilde{\mathrm{LLR}_{k,l}^{\mathrm{opt}}}}{\widetilde{\mathrm{LLR}_{k,l}^{\mathrm{opt}}}}\right| \tag{4.23}$$

and compared to the other considered fusion rules. As can be noted from the figure, the $\mathrm{LLR}_{k,l}^{\mathrm{ILA}}$ has the minimum error as compared to the considered fusion rules for $y_{k,l} \lesssim 3$. Otherwise, all LLRs converge and approach zero, except for the ILS. By noting that $y_{k,l} \gg 3$ at high SNRs, then it is expected that the fusion error probability for all fusion rules, except the ILS, are equivalent.

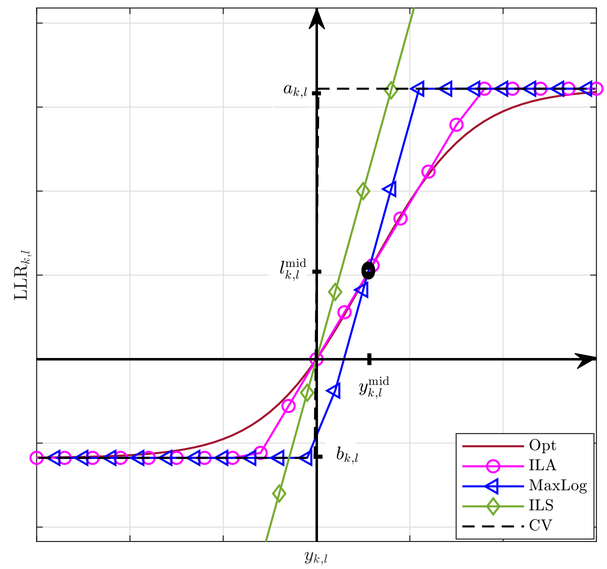

Figure 4.2: A plot for the individual $\mathrm{LLR}_{k,l}$ for the decision fusion rules.

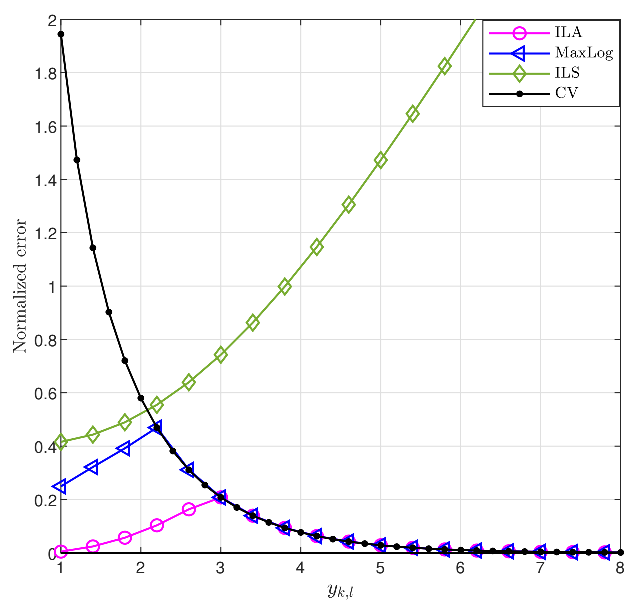

Figure 4.3: The normalized error of $\mathrm{LLR}_{k,l}$ for the suboptimum fusion rules, using $P_{k,l}^{\mathrm{d}} = 0.8$ and $P_{k,l}^{\mathrm{fa}} = 0.1$.

Quantizer Design: As can be noted from (4.21), the FC requires knowledge of $r_{k,l}$, $h_{k,l}$, σ_n^2, and $\mathcal{P}_{k,l}$, and hence, the data overhead will be large because $r_{k,l}$ is the only signal that carries sensing information while other variables are side information required for the fusion process. However, because the fusion center actually requires the knowledge of $y_{k,l} = \frac{4\sqrt{\mathcal{P}_{k,l}}}{\sigma_n^2}\Re\left[r_{k,l}\left(h_{k,l}\right)^*\right]$ rather than knowing each parameter individually, then it is more efficient just to quantize $y_{k,l}$ and then send it to the FC. Consequently, the CHD should estimate $h_{k,l}$, compute and quantize $y_{k,l}$, and pass it to the FC through the available links. By noting that $r_{k,l}$ is complex while $y_{k,l}$ is real, then $r_{k,l}$ generally requires more bits to provide a certain quantization error. Therefore, the overhead associated with $h_{k,l}$, σ_n^2, and $\mathcal{P}_{k,l}$ can be considered negligible. Consequently, certain quality of service (QoS) requirements such as the service rate, queuing delay and data drop should not be affected because the network does not allocate any noticeable transmission resources for overhead data [60].

Given that a q-bit quantizer is employed, then $y_{k,l}$ is compared to a set of thresholds λ_i, where $i = \{0, 1, \ldots, 2^q\}$, $\lambda_0 = -\infty$ and $\lambda_{2^q} = \infty$. It should be observed that $y_{k,l}$ is a real-valued random variable with conditional PDF given in the Appendix, where $\mu_y = 0$, $\sigma_y^2 = \frac{16\mathcal{P}_{k,l}}{\sigma_n^4}\left[2\mathcal{P}_{k,l}\sigma_h^4 + \frac{\sigma_n^2\sigma_h^2}{4}\right]$. Let $\psi(\cdot)$ and Δ denote the quantization process and interval, respectively; then, the quantizer can be represented as

$$d_{k,l} = \begin{cases} \mathbf{0}_q, & \lambda_0 \leq y_{k,l} < \lambda_1 \\ \psi\left(y_{k,l}\right), & \lambda_i \leq y_{k,l} < \lambda_{i+1} \\ \mathbf{1}_q, & \lambda_{2^q-1} \leq y_{k,l} < \lambda_{2^q} \end{cases} \tag{4.24}$$

where $d_{k,l}$ is the generated codeword, $\lambda_1 = -5\sigma_y^2$, $\lambda_{2^q-1} = 5\sigma_y^2$, $\mathbf{1}_q$ and $\mathbf{0}_q$ represent the all ones and all zeros vectors with q elements. The interval Δ and λ_i for $2 \leq i \leq 2^q - 2$ can be evaluated as

$$\Delta = \frac{2^q - 2}{10\sigma_r^2} \tag{4.25}$$

$$\begin{aligned} \lambda_i &= \lambda_{i-1} + \Delta \\ &= \lambda_1 + (i-1) \times \Delta. \end{aligned} \tag{4.26}$$

The overall process to deploy the proposed ILA in an IoT-based WSN can be summarized as depicted in ***Procedure I***.

As can be noted from (4.22), the ILA complexity is mostly determined by the $\mathrm{LLR}_{k,l}^{\mathrm{ILA}}$ (4.21). Given that $P_{k,l}^{\mathrm{d}}$ and $P_{k,l}^{\mathrm{fa}}$ varying rate is much less than the transmission rate, which is typically the case, then $b_{k,l}$, $y_{k,l}^{\mathrm{mid}}, z_{k,l}^{\mathrm{mid}}$, $\alpha_{k,l}$, and $a_{k,l}$ can be evaluated only once for several fusion operations, and thus, their computational complexity can be dropped. Consequently, the main arithmetic operations required to evaluate the ILA rule are $6KL$ multiplication/division operations, and $6KL - 1$ additions/subtractions. The complexity of the other considered algorithms can be evaluated in a similar approach using (4.14)

***Procedure I*: ILA deployment over WSN-IoT.**	
1.	**for each sensor do:**
2.	Sense the environment, and generate the local decision $u_{k,l}$
3.	Send the local decision $u_{k,l}$ to the corresponding CHD
4.	**end**
5.	**for each CHD do:**
6.	Update the values of $h_{k,l}$, $\mathcal{P}_{k,l}$, and σ_n^2
7.	Compute $y_{k,l} = \frac{4\sqrt{\mathcal{P}_{k,l}}}{\sigma_n^2} \Re\left[r_{k,l}\left(h_{k,l}\right)^*\right]$
8.	Digitize $y_{k,l}$ using (4.24) to produce $d_{k,l}$
9.	Forward $d_{k,l}$ to the FC through IoT infrastructure
10.	**end**
11.	**FC do:**
12.	Update $P_{k,l}^{\mathrm{d}}$ and $P_{k,l}^{\mathrm{fa}}$
13.	Regenerate $y_{k,l}$
14.	Compute $\hat{H}_{\mathrm{ILA}}$ using (4.22)
15.	**end**
16.	**Output:** $\hat{H}_{\mathrm{ILA}}$

Table 4.1: Computational complexity of the considered fusion rules.

	Opt.	**CV**	**MaxLog**	**ILS**	**ILA**
$\pm$	$6KL-1$	$2KL-1$	$3KL-1$	$2KL-1$	$2KL-1$
$\times$	$6KL$	$4KL$	$4KL$	$4KL$	$5KL$
$\div$	$2KL$	KL	KL	KL	KL
log	KL	-	-	-	-
exp	KL	-	-	-	-

and (4.15) for the CV, (4.17) and (4.18) for the MaxLog, and (4.19) for the ILS. Table 4.1 summarizes the computational complexity of all considered algorithms, which reveals that all rules have generally equivalent complexity, except for the optimum, which requires several additional operations. In addition to the high computational complexity, the optimum rule suffers from an instability problem which arises at high SNR [17].

4.6 Performance Analysis

In this section, the performance analysis for both ILA and CV rules is presented for the most general case in which $P_{k,l}^{\mathrm{d}}$ and $P_{k,l}^{\mathrm{fa}}$ are different for each sensor. The $P_{D/FA}$ of the ILA rule is derived by evaluating the numerical integration (4.30), while it is derived in closed-form for the CV rule. To simplify the analysis, the channel between the CHDs and FC is assumed to be error-free. Moreover, the quantization error is typically small, and hence, can be ignored.

4.6.1 ILA Rule

The $P_{D/FA}$ for the ILA rule can be formulated as

$$P_{D/FA}^{\mathrm{ILA}} = \tfrac{1}{2\pi j} \int_{q-j\infty}^{q+j\infty} \phi^{-\mathrm{ILA}}\left(s|H_{1/0}\right) \frac{e^{-\tau_g s}}{s} ds \tag{4.27}$$

where $\phi^{-\mathrm{ILA}}\left(s|H_{1/0}\right)$ is the Laplace transform of the PDF of $-\mathrm{LLR}^{\mathrm{ILA}}$, with $\mathrm{LLR}^{\mathrm{ILA}} = \sum_k \sum_l \mathrm{LLR}_{k,l}^{\mathrm{ILA}}$, which is given by

$$\phi^{-\mathrm{ILA}}\left(s|H_{1/0}\right) = \prod_{k=1}^{K} \prod_{l=1}^{L} \sum_{u_{k,l}} \phi_{k,l}^{-\mathrm{ILA}}\left(s|u_{k,l}\right) \Pr\left(u_{k,l}|H_{1/0}\right). \tag{4.28}$$

However, the PDF of $\mathrm{LLR}^{\mathrm{ILA}}$ is discontinuous, and thus, direct application of the Gauss-Chebyshev quadrature integration is not feasible. Consequently, $\phi^{-\mathrm{ILA}}\left(s|H_{1/0}\right)$ can be separated into two parts: ϕ_{C} for the continuous part and ϕ_{D} for the terms which cause discontinuities

$$\begin{aligned}\phi^{-\mathrm{ILA}}\left(s|H_{1/0}\right) &= \phi_{\mathrm{C}}\left(s|H_{1/0}\right) + \phi_{\mathrm{D}}\left(s|H_{1/0}\right) \\ &= \left(\phi^{-\mathrm{ILA}}\left(s|H_{1/0}\right) - \phi_{\mathrm{D}}\left(s|H_{1/0}\right)\right) + \phi_{\mathrm{D}}\left(s|H_{1/0}\right).\end{aligned} \tag{4.29}$$

Thus, $P_{D/FA}^{\mathrm{ILA}}$ can be written as

$$P_{D/FA}^{\mathrm{ILA}} = \underbrace{\tfrac{1}{2\pi j} \int_{q-j\infty}^{q+j\infty} \phi_{\mathrm{D}}\left(s|H_{1/0}\right) \frac{1}{s} e^{-\tau_g s} ds}_{\Gamma_{\mathrm{D}}|H_{1/0}} + \tfrac{1}{2\pi j} \int_{q-j\infty}^{q+j\infty} \frac{1}{s} e^{-\tau_g s} \left(\phi^{-\mathrm{ILA}}\left(s|H_{1/0}\right) - \phi_{\mathrm{D}}\left(s|H_{1/0}\right)\right) ds. \tag{4.30}$$

The first integral $\Gamma_{\mathrm{D}}|H_{1/0}$ can be evaluated in closed-form using the inverse Laplace transform, while the second integral can be efficiently evaluated using the Gauss-Chebyshev quadrature rule. The integral of the discontinuous term $\Gamma_{\mathrm{D}}|H_{1/0}$ is derived in Appendix in closed-form.

4.6.2 Chair-Varshney (CV) Rule with Different $P_{k,l}^{\mathbf{d}}$ and $P_{k,l}^{\mathbf{fa}}$

Similar to the ILA case, the system level detection and false alarm probabilities for the CV rule, $P_{D/FA}^{\mathrm{CV}}$, can be formulated as

$$\begin{aligned}P_{D/FA}^{\mathrm{CV}} &= \Pr\left(-\mathrm{LLR}^{\mathrm{CV}} < -\tau_g|H_{1/0}\right) \\ &= \tfrac{1}{2\pi j} \int_{q-j\infty}^{q+j\infty} \phi^{-\mathrm{CV}}\left(s|H_{1/0}\right) \frac{e^{-\tau_g s}}{s} ds\end{aligned} \tag{4.31}$$

where $\mathrm{LLR}^{\mathrm{CV}} = \sum_k \sum_l \mathrm{LLR}_{k,l}^{\mathrm{CV}}$ and $\phi^{-\mathrm{CV}}\left(s|H_{1/0}\right)$ is the Laplace transform of the PDF of $-\mathrm{LLR}^{\mathrm{CV}}$, which can be expressed as

$$\begin{aligned}
\phi^{-\mathrm{CV}}\left(s|H_{1/0}\right) &= \prod_{k=1}^{K}\prod_{l=1}^{L}\phi_{k,l}^{-\mathrm{CV}}\left(s|H_{1/0}\right) \\
&= \prod_{k=1}^{K}\prod_{l=1}^{L}\sum_{u_{k,l}}\phi_{k,l}^{-\mathrm{CV}}(s|u_{k,l})\,\mathrm{Pr}\left(u_{k,l}|H_{1/0}\right) \\
&= \prod_{k=1}^{K}\prod_{l=1}^{L}\left(e^{sb_{k,l}}\phi_{b_{k,l}}^{\mathrm{CV}} + e^{sa_{k,l}}\phi_{a_{k,l}}^{\mathrm{CV}}\right)
\end{aligned} \tag{4.32}$$

where

$$\phi_{b_{k,l}}^{\mathrm{CV}} = \sum_{u_{k,l}}\frac{v_2}{v_2+v_1}\,\mathrm{Pr}\left(u_{k,l}|H_{1/0}\right) \tag{4.33}$$

and

$$\phi_{a_{k,l}}^{\mathrm{CV}} = \sum_{u_{k,l}}\frac{v_1}{v_2+v_1}\,\mathrm{Pr}\left(u_{k,l}|H_{1/0}\right). \tag{4.34}$$

The variables v_1 and v_2 are defined in the Appendix.

For the sake of abbreviation, the final expression for $P_{D/FA}^{\mathrm{CV}}$ is presented below, as the derivation is a special case of that presented in the Appendix for the ILA rule, where the multi-binomial theorem and then the Laplace inverse transform are applied to evaluate $P_{D/FA}^{\mathrm{CV}}$ in closed-form as given by

$$\begin{aligned}
P_{D/FA}^{\mathrm{CV}} = \sum_{n_1=0}^{1}\sum_{t_1=0}^{1}\cdots\sum_{n_K=0}^{1}\sum_{t_L=0}^{1}\phi_{b_{1,1}}^{n_1}\phi_{a_{1,1}}^{1-n_1}\times\cdots\times\phi_{b_{K,L}}^{t_L}\phi_{a_{K,L}}^{1-t_L} \\
\times\,\Phi\left[-\tau_g + n_1 b_{1,1} + (1-n_1)\,a_{1,1} + \cdots + t_L b_{K,L} + (1-t_L)\,a_{K,L}\right]
\end{aligned} \tag{4.35}$$

where

$$\phi_{b_{k,l}} = \sum_{u_{k,l}}\frac{v_2 e^{\frac{v_1 b_{k,l}}{\alpha_{k,l}}}}{v_2+v_1}\,\mathrm{Pr}\left(u_{k,l}|H_{1/0}\right) \tag{4.36}$$

and

$$\phi_{a_{k,l}} = \sum_{u_{k,l}}\frac{v_1 e^{-\frac{v_2 a_{k,l}}{\alpha_{k,l}}}}{v_2+v_1}\,\mathrm{Pr}\left(u_{k,l}|H_{1/0}\right). \tag{4.37}$$

4.7 Simulation Results

In this section, the detection performance of all decision FRs considered in this paper is evaluated and compared. Simulation results are obtained using Monte Carlo simulations, where each simulation run consists of 10^7 realizations. Analytical results are also presented and compared with simulation results. The links between the sensors and CHDs are considered i.i.d. flat Rayleigh fading with unit power; thus, $h_{k,l} \sim \mathcal{CN}(0,1)\ \forall\ k,l$. The total transmission power for the network is normalized to 1, and thus, $\mathcal{P}_{k,l} = \frac{1}{KL}$ per sensor and the total SNR of network is defined as $\overline{\gamma}_T = \frac{1}{\sigma_n^2}$, which can be easily estimated as

Table 4.2: The detection and false alarm probabilities for sensors in each cluster.

Cluster (k)	$P_{k,l}^{\mathrm{d}} \forall l$	$P_{k,l}^{\mathrm{fa}} \forall l$
1	0.50	0.05
2	0.55	0.07
3	0.60	0.09
4	0.65	0.10

Table 4.3: System parameters used in simulations.

	Fig. 4.4a	Fig. 4.4b	Fig. 4.5a	Fig. 4.5b	Fig. 4.6	Fig. 4.7
K	4	4	4	4	4	4
L	4	16	16	8	8	8
P_{FA}	0.01	0.010	-	-	-	-
τ_g	-	-	0	0	-	0
$\bar{\gamma}_T$	-	-	-	-	10 dB	-
ρ_e	0	0	0	0	0	-

described in [59]. The detection and false alarm probabilities for the individual sensors in each cluster are given in Table 4.2, while Table 4.3 shows the simulation parameters for each of the figures. The values of $P_{k,l}^{d}$ and $P_{k,l}^{fa}$ are typical in decision fusion systems where multiple low-cost sensors are utilized to produce accurate decisions about certain events [61]- [64]. Unless otherwise mentioned, the link between the CHDs and FC is considered error free, and the signal has no quantization errors. It is also worth noting that evaluating the performance the proposed and other fusion algorithms using a physical WSN-IoT testbed may offer great benefit because it considers comprehensive real-life scenarios. However, developing such a testbed and testing the network under different scenarios can be quite challenging [60], and hence, requires a dedicated work.

Figure 4.4 shows the system level detection probability P_D for the considered FRs, i.e., the optimum, ILA, MaxLog, CV and ILS rules. The results in Fig. 4.4a are obtained for a system with four clusters, each of which has four sensors, i.e., $K = 4$ and $L = 4$, whereas $K = 4$ and $L = 16$ are considered in Fig. 4.4b. The fusion threshold τ_g is adjusted such that the system level false alarm probability is fixed at $P_{FA} = 0.01$ for both subplots and all SNRs. As can be noted from the figure, analytical results for the proposed ILA and CV rules perfectly match simulation results. In terms of detection capability, it is clear that the ILA rule outperforms all the other considered suboptimum rules, and is actually comparable to the optimum. The MaxLog rule performance is close to ILA, with a fraction of 1 dB difference. For ILS and CV rules, the performance depends on SNR and the number of sensors. For the 16 sensors case in Fig. 4.4a, the ILS offers higher P_D when compared to the CV rule at $\bar{\gamma}_T \lesssim 11$ dB. For the case of 64 sensors in Fig. 4.4b, the ILS rule consistently outperforms the CV for low and moderate SNRs, while they converge for $\bar{\gamma}_T \gtrsim 16$ dB. It can be also noted from Fig. 4.4a that the ILS rule suffers a fixed error when the number of sensors is small even at very high SNRs.

Figure 4.5 shows the probability of fusion error P_e for the considered FRs, where $P_e = \Pr(H_1)(1 - P_D) + \Pr(H_0) P_{FA}$. The number of sensors is 64 for Fig. 4.5a and 32 for Fig. 4.5b, where the number of sensors per cluster is $L = 16$ and 8, respectively. The fusion threshold τ_g is set to 0 for all considered cases. As

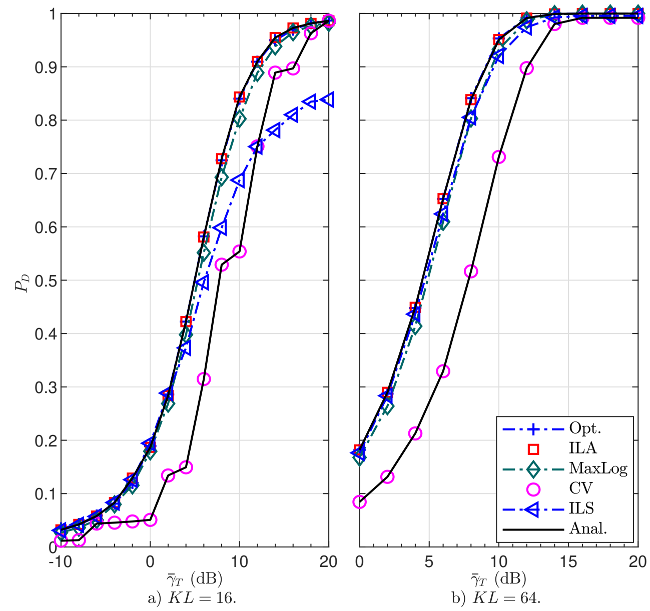

Figure 4.4: The detection probability P_D for $KL = 16$ and 64 sensors, respectively, where $P_{FA} = 0.01$.

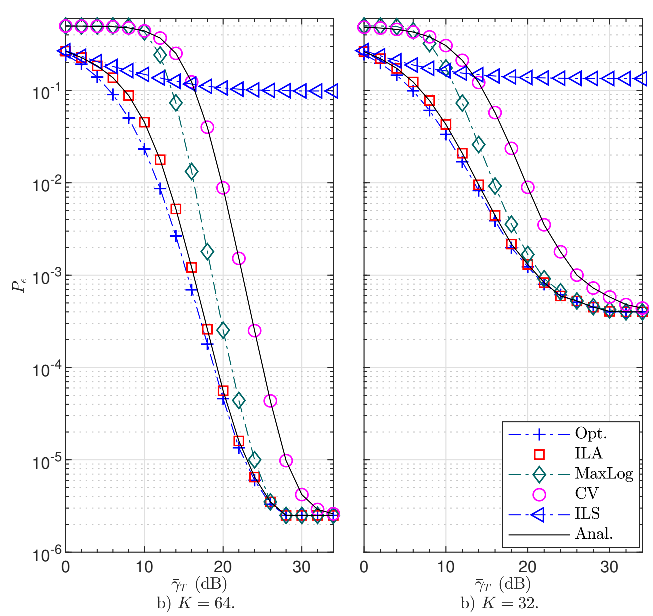

Figure 4.5: The probability of error fusion P_e for $KL = 64$ and 32, respectively, where τ_g is set to 0.

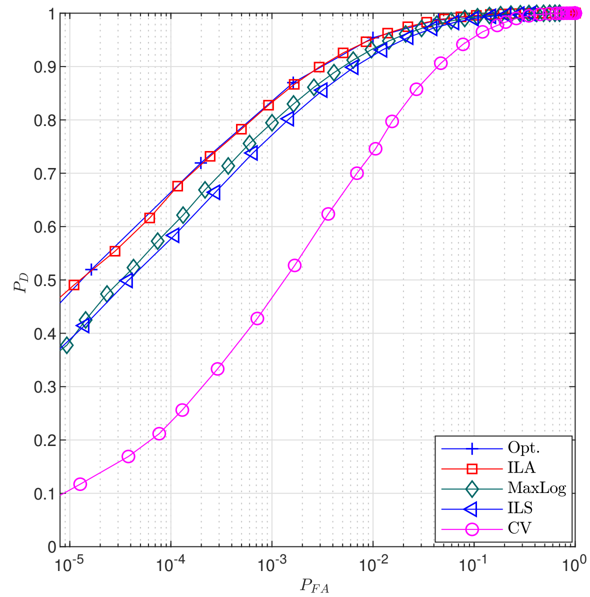

Figure 4.6: The receiver operating characteristics for $\overline{\gamma}_T = 10$ dB, where $KL = 32$.

can be noted from Fig. 4.5a, P_e generally suffers from error floor at high SNRs for all FRs, which is caused by $P_{k,l}^{\mathrm{d}}$ and $P_{k,l}^{\mathrm{fa}}$. However, the ILS rule is the most sensitive with high error floor of about 0.1, while it is about 2.5×10^{-6} for the other rules. Moreover, P_e of the proposed ILA rule remains very close to the optimum rule for the entire range of SNRs, particularly at high SNR where the two curves merge. Unlike the case in Fig. 4.4, the MaxLog performance at low and moderate SNRs shows significant degradation with respect to the optimum and ILA rules. This performance degradation is caused by the biasing in $\mathrm{LLR}_{k,l}^{\mathrm{MaxLog}}$ as shown in Fig. 4.2, where $\mathrm{LLR}_{k,l}^{\mathrm{MaxLog}} \neq 0$ at $y_{k,l} = 0$, and thus, the optimum threshold for the MaxLog case is not $\tau_g = 0$. The effectiveness of the proposed ILA rule is clear in this figure, where it considerably outperforms all other suboptimum FRs. For the case of $L = 16$ in Fig. 4.5b, reducing the number of sensors increases the error floor substantially. Nevertheless, the ILA rule maintained its superiority with respect to the other considered rules. Similar to the case of 64 sensors, P_e for all rules converge except for the ILS. Moreover, analytical and simulation results show perfect match.

Figure 4.6 shows the receiver operating characteristics for the system, where P_D is plotted versus P_{FA} using $\overline{\gamma}_T = 10$ dB. The number of sensors per cluster is $L = 8$. The results in the figure emphasize the efficiency of the ILA rule for wide range of P_{FA} and P_D, where its performance is comparable with the optimum rule and better than the other rules. For example, the optimum and ILA rules provide $P_D \approx 0.7$ at $P_{FA} \approx 10^{-4}$, while the MaxLog, ILS and CV rules provide $P_D \approx 0.6$, 0.59 and 0.24, respectively. Moreover, to achieve $P_D = 0.9$ using all rules, P_{FA} should be about 2×10^{-3} for the optimum and ILA rules, while it is about 5×10^{-3}, 6.5×10^{-3}, and 4×10^{-2} for the MaxLog, ILS, and CV rules, respectively.

Figure 4.7 evaluates the impact of the BSC on P_e for the ILA rule; therefore, $y_{k,l}$ at all CHDs is

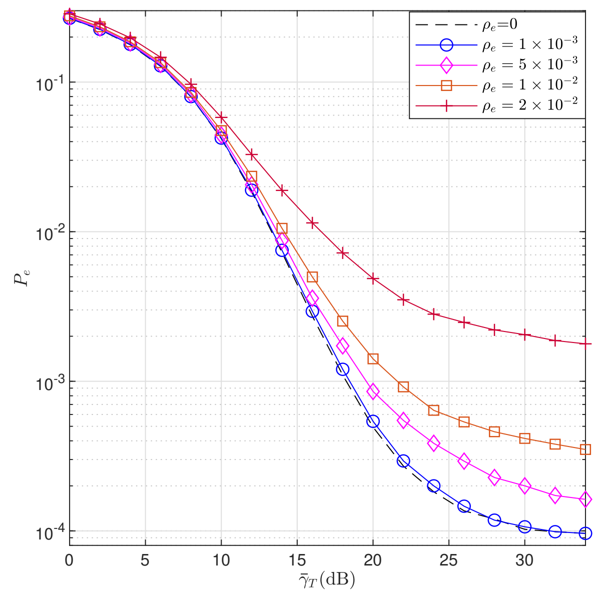

Figure 4.7: The impact of the BSC between the CH and FC for different values of ρ_e, where $L = 8$ and $q = 8$.

quantized using an 8-bit quantizer. As can be noted from the figure, the transition probability ρ_e of the BSC may have significant impact on the FC performance. More specifically, the transition probability of the core network should be kept below 10^{-3} to achieve near-ideal performance. For example, for $\rho_e = 5 \times 10^{-3}$, the performance deteriorates by about 5 dB at $P_e = 10^{-4}$.

The run-time for the proposed ILA, optimum and other suboptimum rules is given in Fig. 4.8 versus the number of sensors in the network KL. As can be noted from the figure, the ILA, CV and MaxLog have generally equivalent run-time while the optimum has the maximum. The ILS rule has less run-time requirements, but it is at the expense of the modest performance.

4.8 Conclusion and Future Work

In this work, the decision fusion problem for IoT-based clustered WSN has been investigated. A new decision FR denoted as the ILA rule was proposed and analyzed, where an analytical expression in terms of a single integral has been derived. Moreover, a closed-form expression has been obtained for the CV rule. The process of fusing the collected sensors' decisions after passing through an unknown channel was considered, where the channel is modeled as BSC, and received decisions are quantized at the CHDs. The analytical results corroborated by simulation revealed that the ILA rule offers near-optimum performance for various operating conditions, and the transition probability of the BSC should be less than 10^{-3} to obtain reliable decisions at the fusion center. Moreover, the computational complexity of the ILA, CV and MaxLog are generally comparable.

While there are some WSN platforms with MAC protocols that support orthogonal and interference-free transmission, there are other MAC protocols that do not guarantee interference-free transmission.

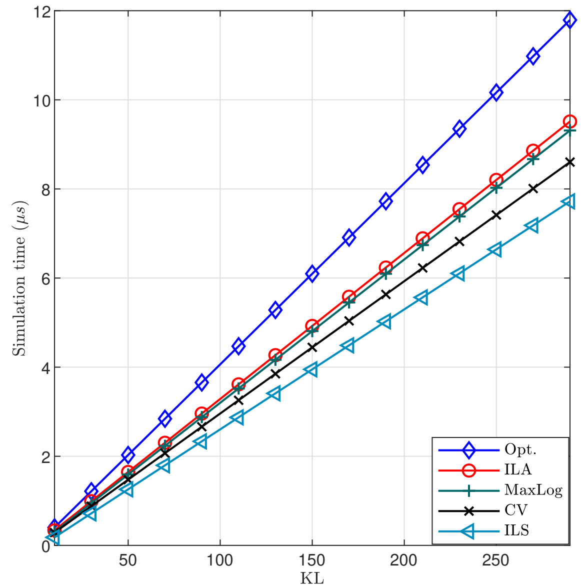

Figure 4.8: The run-time results for the optimum and suboptimum fusion rules.

Therefore, it would be crucial to evaluate the performance of various fusion rules in the presence of interference and derive efficient algorithms to reduce its impact. Moreover, evaluating the performance the proposed and other fusion algorithms using a physical WSN-IoT testbed may offer great benefit to corroborate the analytical and simulation results in real-life scenarios.

Appendix

The PDF of $y_{k,l}$ is [17]

$$f\left(y_{k,l}|u_{k,l}\right)=\frac{v_1 v_2}{v_2+v_1}\left(e^{v_1 y_{k,l}}\Phi\left(-y_{k,l}\right)+e^{-v_2 y_{k,l}}\Phi\left(y_{k,l}\right)\right) \tag{4.38}$$

where $\Phi\left(\cdot\right)$ is the unit step function and v_i $\forall i\in\{1,\,2\}$ can be expressed as

$$v_i=\sqrt{w_{k,l}^2+\frac{1}{C_{k,l}^2\left(\sigma_{r_{k,l}}^2\sigma_h^2-\mu_{r_{k,l},h_{k,l}}^2\right)}}-(-1)^i w_{k,l}. \tag{4.39}$$

The parameters required to compute v_i are defined as

$$w_{k,l}=\frac{\mu_{r_{k,l},h_{k,l}}}{C_{k,l}\left(\sigma_{r_{k,l}}^2\sigma_{h_{k,l}}^2-\mu_{r_{k,l},h_{k,l}}^2\right)},\; C_{k,l}=\frac{2}{\sigma_n^2}\sqrt{\mathcal{P}_{k,l}},$$

$$\mu_{r_{k,l},h_{k,l}}=\sqrt{\mathcal{P}_{k,l}}\sigma_h^2 u_{k,l},\text{ and }\sigma_{r_{k,l}}^2=\mathcal{P}_{k,l}\sigma_h^2+\sigma_n^2. \tag{4.40}$$

Therefore, $\phi_{k,l}^{-\mathrm{ILA}}\left(s|u_{k,l}\right)$ can be evaluated as

$$\phi_{k,l}^{-\mathrm{ILA}}\left(s|u_{k,l}\right)=\int_{-\infty}^{\frac{b_{k,l}}{\alpha_{k,l}}} e^{sb_{k,l}} f\left(y_{k,l}|u_{k,l}\right) dy_{k,l}+\int_{\frac{b_{k,l}}{\alpha_{k,l}}}^{\frac{a_{k,l}}{\alpha_{k,l}}} e^{s\alpha_{k,l}y_{k,l}} f\left(y_{k,l}|u_{k,l}\right) dy_{k,l}+\int_{\frac{a_{k,l}}{\alpha_{k,l}}}^{\infty} e^{sa_{k,l}} f\left(y_{k,l}|u_{k,l}\right) dy_{k,l} \tag{4.41}$$

$$\begin{aligned}\phi_{k,l}^{-\mathrm{ILA}}\left(s|u_{k,l}\right)=\frac{v_1v_2}{v_2+v_1}\Bigg(&\int_{-\infty}^{\frac{b_{k,l}}{\alpha_{k,l}}} e^{sb_{k,l}} e^{v_1y_{k,l}} dy_{k,l}+\int_{\frac{b_{k,l}}{\alpha_{k,l}}}^{0} e^{s\alpha_{k,l}y_{k,l}} e^{v_1y_{k,l}} dy_{k,l}+\int_{0}^{\frac{a_{k,l}}{\alpha_{k,l}}} e^{s\alpha_{k,l}y_{k,l}} e^{-v_2y_{k,l}} dy_{k,l}\\ &+\int_{\frac{a_{k,l}}{\alpha_{k,l}}}^{\infty} e^{sa_{k,l}} e^{-v_2y_{k,l}} dy_{k,l}\Bigg)\end{aligned} \tag{4.42}$$

which can be evaluated as

$$\phi_{k,l}^{-\mathrm{ILA}}\left(s|u_{k,l}\right)=\frac{v_1v_2}{v_2+v_1}\left(\frac{e^{sb_{k,l}+\frac{v_1b_{k,l}}{\alpha_{k,l}}}}{v_1}+\frac{e^{sa_{k,l}-\frac{v_2a_{k,l}}{\alpha_{k,l}}}}{v_2}+\frac{1-e^{\frac{\left(\alpha_{k,l}s+v_1\right)b_{k,l}}{\alpha_{k,l}}}}{\alpha_{k,l}s+v_1}+\frac{e^{\frac{\left(\alpha_{k,l}s-v_2\right)a_{k,l}}{\alpha_{k,l}}}-1}{\alpha_{k,l}s-v_2}\right). \tag{4.43}$$

It should be observed that the inverse of $\phi_{k,l}^{-\mathrm{ILA}}\left(s|u_{k,l}\right)$ has discontinuities, and thus, $\phi^{-\mathrm{ILA}}\left(s|H_{1/0}\right)$ is separated into two parts: $\phi^{-\mathrm{ILA,C}}$ for the continuous part and $\phi^{-\mathrm{ILA,D}}$ for the terms which cause discontinuities. These terms are evaluated separately and results are obtained in closed-form, where $\phi^{-\mathrm{ILA,D}}$ is

$$\phi^{-\mathrm{ILA,D}}\left(s|H_{1/0}\right)=\prod_{k=1}^{K}\prod_{l=1}^{L}\left(e^{sb_{k,l}}\phi_{b_{k,l}}+e^{sa_{k,l}}\phi_{a_{k,l}}\right) \tag{4.44}$$

and can be expanded as

$$\phi^{-\mathrm{ILA,D}}\left(s|H_{1/0}\right)=\left(e^{sb_{1,1}}\phi_{b_{1,1}}+e^{sa_{1,1}}\phi_{a_{1,1}}\right)\times\cdots\times\left(e^{sb_{K,L}}\phi_{b_{K,L}}+e^{sa_{K,L}}\phi_{a_{K,L}}\right) \tag{4.45}$$

where

$$\phi_{b_{k,l}}=\sum_{u_{k,l}}\frac{v_2e^{\frac{v_1b_{k,l}}{\alpha_{k,l}}}\Pr\left(u_{k,l}|H_{1/0}\right)}{v_2+v_1} \tag{4.46}$$

and

$$\phi_{a_{k,l}}=\sum_{u_{k,l}}\frac{v_1e^{-\frac{v_2a_{k,l}}{\alpha_{k,l}}}\Pr\left(u_{k,l}|H_{1/0}\right)}{v_2+v_1}. \tag{4.47}$$

By applying the multi-binomial theorem in (4.45) yields

$$\phi^{-\mathrm{ILA,D}}\left(s|H_{1/0}\right)=\sum_{n_1=0}^{1}\sum_{t_1=0}^{1}\cdots\sum_{n_K=0}^{1}\sum_{t_L=0}^{1}\left\{\binom{1}{n_1}\binom{1}{t_1}\cdots\binom{1}{n_K}\binom{1}{t_L}\times\left(e^{sb_{1,1}}\phi_{b_{1,1}}\right)^{n_1}\left(e^{sa_{1,1}}\phi_{a_{1,1}}\right)^{1-n_1}\right.$$
$$\left.\cdots\left(e^{sb_{K,L}}\phi_{b_{K,L}}\right)^{t_L}\left(e^{sa_{K,L}}\phi_{a_{K,L}}\right)^{1-t_L}\right\} \quad (4.48)$$

which can be written as

$$\phi^{-\mathrm{ILA,D}}\left(s|H_{1/0}\right)=\sum_{n_1=0}^{1}\sum_{t_1=0}^{1}\cdots\sum_{n_K=0}^{1}\sum_{t_L=0}^{1}\left\{\binom{1}{n_1}\binom{1}{t_1}\cdots\binom{1}{n_K}\binom{1}{t_L}\times\phi_{b_{1,1}}^{n_1}\phi_{a_{1,1}}^{1-n_1}\cdots\phi_{b_{K,L}}^{t_L}\phi_{a_{K,L}}^{1-t_L}\right.$$
$$\left.\times e^{s[n_1b_{1,1}+(1-n_1)a_{1,1}+\cdots+t_Lb_{K,L}+(1-t_L)a_{K,L}]}\right\}. \quad (4.49)$$

Therefore, $\Gamma_{\mathrm{D}}|H_{1/0}$ can be evaluated using the inverse Laplace transform tables [65] as

$$\Gamma_{\mathrm{D}}|H_{1/0}=\sum_{n_1=0}^{1}\sum_{t_1=0}^{1}\cdots\sum_{n_K=0}^{1}\sum_{t_L=0}^{1}\left\{\binom{1}{n_1}\binom{1}{t_1}\cdots\binom{1}{n_K}\binom{1}{t_L}\times\phi_{b_{1,1}}^{n_1}\phi_{a_{1,1}}^{1-n_1}\cdots\phi_{b_{K,L}}^{t_L}\phi_{a_{K,L}}^{1-t_L}\right.$$
$$\left.\times\Phi\left(-\tau_g+n_1b_{1,1}+\left(1-n_1\right)a_{1,1}+\cdots+t_Lb_{K,L}+\left(1-t_L\right)a_{K,L}\right)\right\}. \quad (4.50)$$

Since $\binom{1}{n_k}=1$ for $n_k\in\{0,1\}$, $\Gamma_{\mathrm{D}}|H_{1/0}$ is reduced to

$$\Gamma_{\mathrm{D}}|H_{1/0}=\sum_{n_1=0}^{1}\sum_{t_1=0}^{1}\cdots\sum_{n_K=0}^{1}\sum_{t_L=0}^{1}\left\{\phi_{b_{1,1}}^{n_1}\phi_{a_{1,1}}^{1-n_1}\cdots\phi_{b_{K,L}}^{t_L}\phi_{a_{K,L}}^{1-t_L}\times\Phi\left(-\tau_g+n_1b_{1,1}+\left(1-n_1\right)a_{1,1}+\right.\right.$$
$$\left.\left.\cdots+t_Lb_{K,L}+\left(1-t_L\right)a_{K,L}\right)\right\}. \quad (4.51)$$

References

[1] A. Ali *et al.*, "Next generation M2M cellular networks: challenges and practical considerations," *IEEE Commun. Mag.*, vol. 53, no. 9, pp. 18-24, Sep. 2015.

[2] V. Petrov *et al.*, "When IoT keeps people in the loop: a path towards a new global utility," *IEEE Commun. Mag.*, vol. 57, no. 1, pp. 114-121, Jan. 2019.

[3] X. Zhang *et al.*, "Towards an elastic application model for augmenting the computing capabilities of mobile devices with cloud computing," *Mobile Netw. Appl.,* vol. 16, no. 3, pp. 270-284, Jun. 2011.

[4] X. Li *et al.*, "Optimal cloud resource allocation with cost performance trade-off based on Internet of Things," *IEEE Internet Things J.*, vol. 6, no. 4, pp. 6876-6886, Aug. 2019.

[5] D. Evans, "The Internet of Things: How the next evolution of the internet is changing everything," Cisco IBSG., US, Apr. 2011. [Online]. Available: https://www.cisco.com/c/dam/en_us/about/ac79/docs/innov/IoT_IBSG_04 11FINAL.pdf

[6] N. Nesa and I. Banerjee, "IoT-based sensor data fusion for occupancy sensing using Dempster–Shafer evidence theory for smart buildings," *IEEE Internet Things J.*, vol. 4, no. 5, pp. 1563-1570, Oct. 2017.

[7] J. Yuan and X. Li, "A reliable and lightweight trust computing mechanism for IoT edge devices based on multi-source feedback information fusion," *IEEE Access*, vol. 6, pp. 23626-23638, Apr. 2018.

[8] Y. Zhang *et al.*, "Collaborative fusion for distributed target classification using evidence theory in IOT environment," *IEEE Access*, vol. 6, pp. 62314-62323, Oct. 2018.

[9] D. Ebrahimi *et al.*, "UAV-aided projection-based compressive data gathering in wireless sensor networks," *IEEE Internet Things J.*, vol. 6, no. 2, pp. 1893-1905, Apr. 2019.

[10] A. Al-Dweik *et al.*, "IoT-based multifunctional scalable real-time enhanced road side unit for intelligent transportation systems," *In Proc. IEEE 30th Canadian Conf. Electrical and Computer Engineering* (CCECE), Windsor, ON, 2017, pp. 1-6.

[11] T. Jiang, Y. Shi, J. Zhang, and K. Letaief, "Joint activity detection and channel estimation for IoT networks: Phase transition and computation-estimation tradeoff," *IEEE Internet Things J.*, Early access.

[12] J. Callaway, *Wireless Sensor Networks: Architectures and Protocols*, 1st ed. CRC Press, 2003.

[13] A. Garca-Hernando *et al.*, *Problem Solving for Wireless Sensor Networks.* London: Springer-Verlag, 2008.

[14] S. Faye and C. Chaudet, "Characterizing the topology of an urban wireless sensor network for road traffic management," *IEEE Trans. Veh. Technol.*, vol. 65, no. 7, pp. 5720 - 5725, Jul. 2016.

[15] M. Al-Jarrah *et al.*, "Efficient decision fusion for cooperative wireless sensor networks," *In Proc. ICECTA*, Ras Al Khaimah, UAE, Nov. 2017, pp. 1–5.

[16] F. Al-Turjman, *Wireless Sensor Networks: Deployment Strategies for Outdoor Monitoring*, 1st ed. CRC Press, 2018.

[17] M. Al-Jarrah *et al.*, "Decision fusion in distributed cooperative wireless sensor networks," *IEEE Trans. Veh. Technol.*, vol. 68, no. 1, pp. 797-811, Jan. 2019.

[18] M. Wu *et al.*, "Adaptive range-based target localization using diffusion Gauss-Newton method in industrial environments," *IEEE Trans. Ind. Informat.*, Early access, DOI: 10.1109/TII.2019.2909135.

[19] O. Saukh, *Efficient Algorithms for Structuring Wireless Sensor Networks.* Logos Verlag Berlin GmbH, 2009.

[20] D. Joshi *et al.*, "Gradient-based threshold adaptation for energy detector in cognitive radio systems," *IEEE Commun. Lett.*, vol. 15, no. 1, pp. 19-21, Jan. 2011.

[21] M. Al-Jarrah *et al.*, "Spectrum-occupancy aware cooperative spectrum sensing using adaptive detection," *IEEE Syst. J.*, Early access.

[22] Y. Kuo *et al.*, "Design of a wireless sensor network-based IoT platform for wide area and heterogeneous applications," *IEEE Sensors J.*, vol. 18, no. 12, pp. 5187-5197, Jun. 2018.

[23] "Sensing as a service, existing assets, new revenue streams". Available online at `https://www.nokia.com/networks/services/sensing-as-a-service`.

[24] J. Leu *et al.*, "Energy efficient clustering scheme for prolonging the lifetime of wireless sensor network with isolated nodes," *IEEE Commun. Lett.*, vol. 19, no. 2, pp. 259-262, Feb. 2015.

[25] L. Tan and M. Wu, "Data reduction in wireless sensor networks: A hierarchical LMS predictionapproach," *IEEE Sensors J.*, vol. 16, no. 6, pp. 1708-1715, Mar. 2016.

[26] H. Liu *et al.*, "On energy-efficient straight-line routing protocol for wireless sensor networks," *IEEE Syst. J.*, vol. 11, no. 4, pp. 2374-2382, Dec. 2017.

[27] N. Jain *et al.*, "IDEG: Integrated data and energy gathering framework for practical wireless sensor networks using compressive sensing," *IEEE Sensors J.*, vol. 19, no. 3, pp. 1040-1051, Feb. 2019.

[28] V. Cheng and T. Wang, "Performance analysis of distributed decision fusion using a multilevel censoring scheme in wireless sensor networks," *IEEE Trans. Veh. Technol.*, vol. 61, no. 4, pp. 1610-1619, May 2012.

[29] N. Sriranga *et al.*, "Shared channel ordered transmissions for energy-efficient distributed signal detection," *IEEE Commun. Lett.*, vol. 23, no. 1, pp. 96-99, Jan. 2019.

[30] B. Chen *et al.*, "Distributed finite-horizon fusion kalman filtering for bandwidth and energy constrained wireless sensor setworks," *IEEE Trans. Signal Process.*, vol. 62, no. 4, pp. 797-812, Feb. 2014.

[31] G. Oliva *et al.*, "Distributed finite-time average-consensus with limited computational and storage capability," *IEEE Trans. Control Netw. Syst.*, vol. 4, no. 2, pp. 380-391, Jun. 2017.

[32] C. Sergiou *et al.*, "A comprehensive survey of congestion control protocols in wireless sensor networks," *IEEE Commun. Surveys Tuts.*, vol. 16, no. 4, pp. 1839-1859, Fourth quarter 2014.

[33] B. Chen *et al.*, "Channel aware decision fusion in wireless sensor networks," *IEEE Trans. Signal Process.*, vol. 52, no. 12, pp. 3454-3458, Dec. 2004.

[34] R. Niu *et al.*, "Fusion of decisions transmitted over Rayleigh fading channels in wireless sensor networks," *IEEE Trans. Signal Process.*, vol. 54, no.3, pp. 1018-1027, Mar. 2006.

[35] A. Lei and R. Schober, "Multiple-symbol differential decision fusion for mobile wireless sensor networks," *IEEE Trans. Wireless Commun.*, vol. 9, no. 2, pp. 778-790, Feb. 2010.

[36] K. Cichoń *et al.*, "Energy-efficient cooperative spectrum sensing: A survey," *IEEE Commun. Surveys Tuts.*, vol. 18, no. 3, pp. 1861-1886, Third quarter 2016.

[37] S. Kim, "Simultaneous spectrum sensing and energy harvesting," *IEEE Trans. Wireless Commun.*, vol. 18, no. 2, pp. 769-779, Feb. 2019.

[38] N. Banavathu and M. A. Khan, "Optimization of k-out-of-N rule for heterogeneous cognitive radio networks," *IEEE Signal Process. Lett.*, vol. 26, no. 3, pp. 445-449, Mar. 2019.

[39] D. Hamza *et al.*, "Equal gain combining for cooperative spectrum sensing in cognitive radio networks," *IEEE Trans. Wireless Commun.*, vol. 13, no. 8, pp. 4334-4345, Aug. 2014.

[40] S. Sharma *et al.*, "IR-UWB sensor network using massive MIMO decision fusion: Design and performance analysis," *IEEE Sensors J.*, vol. 18, no. 15, pp. 6290-6302, Aug. 2018.

[41] D. Ciuonzo *et al.*, "Channel-aware decision fusion in distributed MIMO wireless sensor networks: Decode-and-fuse vs. decode-then-fuse," *IEEE Trans. Wireless Commun.*, vol. 11, no. 8, pp. 2976-2985, Aug. 2012.

[42] M. Al-Jarrah *et al.*, "Cooperative OFDM for semi distributed detection in wireless sensor networks," *Int. J. Electron. Commun.*, vol. 68, no. 10, pp.1022-1029, Oct. 2014.

[43] D. Ciuonzo *et al.*, "Massive MIMO channel-aware decision fusion," *IEEE Trans. Signal Process.*, vol. 63, no. 3, pp. 604-619, Feb. 2015.

[44] P. Rossi *et al.*, "Energy detection for MIMO decision fusion in underwater sensor networks," *IEEE Sensors J.*, vol. 15, no. 3, pp. 1630-1640, Mar. 2015.

[45] S. Javadi and A. Peiravi, "Fusion of weighted decisions in wireless sensor networks," *IET Wireless Sensor Syst.*, vol. 5, no. 2, pp. 97-105, Apr. 2015.

[46] N. Maleki *et al.*, "Distributed binary detection over fading channels: Cooperative and parallel architectures," *IEEE Trans. Veh. Technol.*, vol. 65, no. 9, pp. 7090-7109, Sep. 2016.

[47] D. Duan *et al.*, "LD approach to asymptotically optimum sensor fusion," *IET Commun.*, vol. 11, no. 5, pp. 680-686, Apr. 2017.

[48] M. Al-Jarrah *et al.*, "Decision fusion in mobile wireless sensor networks using cooperative multiple symbol differential space time coding," *Int. J. Electron. Commun.*, vol. 80, pp.127-136, Oct. 2017.

[49] H. Ye *et al.*, "Joint access and backhaul resource management in satellite-drone networks: A competitive market approach," arXiv preprint, arXiv:1908.11038 (2019).

[50] L. Chiaraviglio *et al.*, "Bringing 5G into rural and low-income areas: Is it feasible?," *IEEE Commun. Standards Mag.*, vol. 1, no. 3, pp. 50-57, Sep. 2017.

[51] L. Feltrin *et al.*, "Narrowband IoT: A survey on downlink and uplink perspectives," *IEEE Wireless Commun.*, vol. 26, no. 1, pp. 78-86, Feb. 2019.

[52] B. Martinez *et al.*, "Exploring the performance boundaries of NB-IoT," *IEEE Internet Things J.*, vol. 6, no. 3, pp. 5702-5712, Jun. 2019.

[53] F. Van den Abeele *et al.*, "Scalability analysis of large-scale LoRaWAN networks in ns-3," *IEEE Internet Things J.*, vol. 4, no. 6, pp. 2186-2198, Dec. 2017.

[54] M. Mohammadkarimi, M. A. Raza and O. A. Dobre, "Signature-based nonorthogonal massive multiple access for future wireless networks: uplink massive connectivity for machine-type communications," *IEEE Veh. Technol. Mag.*, vol. 13, no. 4, pp. 40-50, Dec. 2018.

[55] S. Mohapatra and P. Khilar, "Forest fire monitoring and detection of faulty nodes using wireless sensor network," *IEEE Region 10 Conf. (TENCON)*, Singapore, 2016, pp. 3232-3236.

[56] T. Zhang *et al.*, "Faulty sensor data detection in wireless sensor networks using logistical regression," *IEEE 37th Int. Conf. Distrib. Comput. Sys. Workshops (ICDCSW)*, Atlanta, GA, 2017, pp. 13-18.

[57] W. Ayoub *et al.*, "Internet of mobile things: Overview of LoRaWAN, DASH7, and NB-IoT in LPWANs standards and supported mobility," *IEEE Commun. Surveys Tuts.*, vol. 21, no. 2, pp. 1561-1581, Secondquarter 2019.

[58] H. Poor, *An Introduction to Signal Detection and Estimation*, 2nd ed. New York: Springer-Verlag, 1994.

[59] M. Suliman *et al.*, "SNR estimation in linear systems with Gaussian matrices," *IEEE Signal Process. Lett.*, vol. 24, no. 12, pp. 1867-1871, Dec. 2017.

[60] S. Ezdiani, *et al.*, "Wireless sensor network softwarization: Towards WSN adaptive QoS," *IEEE Internet Things J.*, vol. 4, no. 5, pp. 1517-1527, Oct. 2017.

[61] E. Onur *et al.*, "Analysis of target detection probability in randomly deployed sensor networks," *IEEE Commun. Lett.*, vol. 11, no. 10, pp. 778-780, Oct. 2007.

[62] R. Stolkin and I. Florescu, "Probability of detection and optimal sensor placement for threshold based detection systems," *IEEE Sensors J.*, vol. 9, no. 1, pp. 57-60, Jan. 2009.

[63] J. Wu *et al.*, "Channel-aware decision fusion with unknown local sensor detection probability," *IEEE Trans. Signal Process.*, vol. 58, no. 3, pp. 1457-1463, Mar. 2010.

[64] M. Brämming *et al.*, "BOF process control and slopping prediction based on multivariate data analysis," *Steel Research Int.*," vol. 87 no. 3, pp. 301-310, Mar. 2016.

[65] A. Papoulis, *Signal Analysis*. New York: McGraw-Hill, 1977.

Chapter 5

A Unified Performance Framework for Integrated Sensing- Communications based on KL- Divergence[1]

Abstract

The need for integrated sensing and communication (ISAC) services has significantly increased in the last few years. This integration imposes serious challenges such as joint system design, resource allocation, optimization, and analysis. Since sensing and telecommunication systems have different approaches for performance evaluation, introducing a unified performance measure which provides a perception about the quality of sensing and telecommunication is very beneficial. To this end, this paper provides performance analysis for ISAC systems based on the information theoretical framework of the Kullback-Leibler divergence (KLD). The considered system model consists of a multiple-input-multiple-output (MIMO) base-station (BS) providing ISAC services to multiple communication user equipments (CUEs) and targets (or sensing-served users). The KLD framework allows for a unified evaluation of the error rate performance of CUEs, and the detection performance of the targets. The relation between the detection capability for the targets and error rate of CUEs on one hand, and the proposed KLD on the other hand is illustrated analytically. Theoretical results corroborated by simulations show that the derived KLD is very accurate and can perfectly characterize both subsystems, namely the communication and radar subsystems.

[1] **M. A. Al-Jarrah**, E. Alsusa and C. Masouros, "A Unified performance framework for integrated sensing-communications based on KL-divergence," Submitted to *IEEE Trans. Wireless Commun.*, Sep. 2022.

Index Terms

Integrated sensing and communication (ISAC), relative information, Kullback-Leibler distance, zero forcing (ZF) precoding, maximum ratio transmission (MRT) precoding, MIMO radar, multiple targets.

5.1 Introduction

With the immensely successful deployment of fifth generation (5G) networks worldwide, many technologies, services and applications have been created. Examples for such technologies, include massive connectivity for internet-of-things (IoT) devices [1–3], autonomous or self-driving vehicles [4], and unmanned aerial vehicles (UAVs) [5,6], which all rely on sensing and are subject to future developments. Therefore, sensing services such as detection, localization, tracking, navigation and environmental surveillance are expected to be supplied by network operators in the future to support these kinds of technologies. However, sensing services would add extra challenges due to limited network resources including spectrum, time and energy. Therefore integrating telecommunication services and sensing functionalities to optimize network resources have become an active research area for the past few years [7–13].

Generally speaking, remote sensing can be defined as the collection of measurements and data from the surroundings without physical contact with objects or the phenomena of interest [3,14]. Sensing is used in a massive number of daily applications such as radar, LiDAR, IoT applications, electromagnetic sensing, underwater sensing, environmental sensing and monitoring, medical applications, global positioning systems (GPS), etc [1,15–18]. Two main categories can be used to classify sensing systems, which are passive and active sensing. Whilst passive detectors rely on signals emitted from sources (e.g. infrared, the sunlight and smoke detectors) or reflected by objects as the case of cameras, energy is intentionally emitted from a source and the reflected or backscattered signals are detected and measured by sensors in the case of active type sensing. Examples for active sensing applications include conventional and multiple-input-multiple-output (MIMO) radars, LiDAR and sonar. In MIMO radars, the one intended in this work, multiple antennas are employed with digital receivers and waveform generators feeding the aperture. Unlike phased array radars in which the separation between the antenna elements is typically small, MIMO radars employ relatively widely separated antennas (e.g. $d \geq \lambda/2$, where d is the antenna separation and λ is the wavelength). Therefore, MIMO radars have the ability to integrate energy from different waveforms to obtain diversity gain which results in high resolution detection and localization capabilities [21–23].

On the other hand, in multi-user MIMO (MU-MIMO) communication systems, multiple beams can be transmitted from a base-station (BS) to serve a number of users with adequate data rates and quality-of-service (QoS). MIMO has become an integral element in wireless communications and has been adopted by several global standards and specifications such as 4G, 5G, IEEE 802.11n and WiMax, etc [24,25]. More recently, massive MIMO BSs which are equipped with a large number of antennas, practically up to 256, are employed to provide connectivity to a significant number of users simultaneously. Moreover, by using a large number of antennas, inter-user interference can be efficiently eliminated due to the asymptotic orthogonality of the channels. Other significant advantages of massive MU-MIMO is achieving a huge capacity, enhancing the spectral efficiency without network densification, improving the energy efficiency, providing the ability to generate focused beams that feed small areas [24–27].

Evidently, there is a persistent evolution in wireless communication networks in general where BSs equipped with a large number of antennas play a main role in this evolution. Moreover, promoting the functionality of BSs to be able to provide sensing services in addition to their fundamental communication duties is unavoidable for efficient deployment of IoT and sensing systems. Therefore, exploiting the large number of antennas to provide integrated sensing and communication (ISAC) services simultaneously is expected play a significant role in the future [7–13]. Therefore, this paper investigates ISAC system and studies the performance trade-off using the relative entropy (RE) theorem, or so called Kullback-Leibler divergence (KLD). Although KLD has been used in the literature to evaluate the detection capability of sensing systems [28–32], it is not commonly used to describe a communication systems. However, we will show that KLD can also capture the detection performance of a communication system and has a direct relation to the symbol error rate (SER). With this introduced performance measure, both subsystems, namely, the radar and the communication subsystems, can be characterized, and thus the capability of an ISAC system can be evaluated holistically using a unified performance measure rather than using a different performance measure for each individual subsystem.

5.1.1 Related work

5.1.1.1 MIMO Radar

In [19], MIMO based radars have been firstly proposed as an alternative solution to phased array radars, where it is shown that the new concept of MIMO radars is able to provide a spatial diversity. The performance of MIMO and phased array radars have been compared using analytical derivations for the detection and false alarm probabilities. The principle of MIMO radar is generalized to the case of non-orthogonal signal waveforms in [20]. In addition, the effect of interfering signals on the detection capability is considered in [33], and the effect of a gamma fluctuating target and synchronization errors are taken into account in [34] and [35], respectively.

The problem of target detection with MIMO radar for multi-target scenarios has also been considered in the literature [36–41]. In [36], for instance, the statistical angle resolution has been investigated and the performance is evaluated using derived detection and false alarm probabilities, and the clutter impact on the radar resolution is considered in [37]. A multiple hypotheses testing problem based multi-target detection is considered in [38] for passive MIMO radar in which targets illuminate signals rather that acting as scatterers or reflectors. Another effort on multi-target multi-hypothesis detection scenario using cognitive MIMO radars can be found in [39], where an adaptive waveform design algorithm is proposed. Moreover, a joint multi-target detection and localization problem is investigated in [40], where low-complex suboptimal detection algorithms have been proposed. Furthermore, a sequential probability ratio test (SPRT) based method is introduced in [41] to resolve close targets in co-located MIMO radars.

5.1.1.2 ISAC

More recently, ISAC systems have been introduced in the literature and attracted the attention of both academic research and industrial fields. Generally speaking, ISAC implies the use of the telecommunication network resources for both sensing and telecommunication services [10]. In such scenario, a multi-antenna BS can be applied to provide both services simultaneously by exploiting multiple beams generated in the transmission mode. In the reception mode, a portion of the antennas can be used for radar reception, or time division multiple access (TDMA) can be applied to reduce the interference. Alternatively, one can apply interference cancellation algorithms to separate radar signals from communication signals [10, 42, 43].

In [7], a robust beamforming matrix is proposed for a MU-MIMO communication system that shares the same spectrum with a MIMO radar system with the objective of maximize the detection probability of the radar system. The concept of ISAC is introduced in [8, 9] in which a single BS is dedicated for both functionalities of communications and sensing. Two models, referred to as separated deployment and shared deployment are presented, where the BS antennas are distributed among each sub-system in the separated deployment whereas all antennas are exploited for both sub-systems in the latter case. Several designs for the signals waveforms and beampatterns are proposed in [8, 9] to satisfy the requirements of communication users' rates and detection capability of the radar sub-system. A comprehensive survey for the signal processing tools that can be applied for ISAC systems can be found in [11] for three possible scenarios, namely, radar-centric, communication-centric and joint design.

In [12] and [13], a dual-functional communication and radar system with massive MIMO-OFDM is considered for downlink and uplink scenarios, respectively. The achievable rate and detection capability for both sub-systems are derived and discussed under perfect and imperfect channel side information (CSI). In [44], the dual functional system is optimized aiming at maximizing the achievable sum-rate and energy-efficiency while satisfying a minimum required target detection probability and the individual users' rates. A novel approach for ISAC system which considers IEEE 802.11ad-based long range radar operating at 60 GHz is investigated in [45], where the preamble of a single-carrier frame with good correlated sequences is exploited for the radar signal.

An optimization algorithm to jointly design the transceiver of BS and power allocation for uplink users is introduced in [46] aiming at maximizing the radar detection probability, while maintaining a desirable quality-of-service for the individual communication user equipment (CUEs). In [47], the optimal power distribution among the communication and training symbols is derived, and the waveform design is considered to maximize the weighted sum of mutual information for communication and sensing parts. Rate-splitting multiple access (RSMA) based ISAC system is introduced in [48] based on optimizing the weighted sum-rate for CUEs while satisfying a pre-defined radar beampattern under constrained average transmit power. A comprehensive literature survey about resource allocation methods is provided in [49].

Performance trade-off of ISAC system is analyzed in [50] using the detection probability and achievable rate for radar and communication users, respectively. The power resources of BS is allocated for the radar waveforms and information signals such that the probability of detection for the radar is maximized with a minimum required information rate for CUEs. In [51] and [52], the performance of uplink and downlink integrated ISAC is analyzed in terms of the outage probability, ergodic communication rate, diversity order, and sensing rate. A full-duplex ISAC scheme that exploits the waiting time of a pulsed radar to transmit communication signals is proposed in [53]. Besides, the probability of detection for the radar sensing part and the spectrum efficiency of the communication subsystem are analyzed. In [54], an ISAC system which employs OFDM and orthogonal time frequency space (OTFS) modulation is considered, where a vehicle equipped with a mono-static radar is communicating with a receiver and simultaneously measures some parameters about that receiver by exploiting the backscattered signal. The maximum likelihood estimator and its corresponding Cramer-Rao bound have been derived for a single target scenario, and the root mean square error and data rate have been used to evaluate the performance of radar and communication subsystems, respectively. A similar setup is considered in [55] under a memoryless channel assumption and the system is analyzed using capacity-distortion trade-off, which is defined as the maximum achievable communication rate at which the data can be reliably decoded by the receiver while keeping the sensing distortion at a desirable value.

5.1.2 Motivation and contribution

As can be depicted from the introduction and literature survey above, ISAC systems are expected to play a pivotal role in future wireless networks such as 6G and beyond. Researches in the literature usually use different metric for the performance evaluation of sensing and communication subsystems. For example, sum-rate, bit/symbol error rate, and outage probability are typically used for the communication part, whereas estimation rate, detection probability, false alarm probability and mean square error (MSE) are utilized to evaluate the performance of the radar systems. Motivated by this fact, this paper considers an ISAC system which consists of MIMO-BS serving a number of CUEs and aims at detecting a number of targets with a main objective concerns in providing a unified performance measure to evaluating the efficiency of communication and radar subsystems at the same time. The proposed performance measure is based on the Kullback-Leibler divergence theorem, also referred to the relative information theorem, which provides a measure for how different is a certain probability density function (PDF) from another one. Mathematically, it can be defined as the expectation of the log-likelihood ratio (LLR), and thus it is asymptotically related to the detection performance of radar systems. More specifically, according to Stein's lemma, a higher KLD measure implies a better detection performance for a certain radar system [30, 32].

Although KLD is well-known in the field of sensing and target detection, it is not widely used to characterize the performance of wireless communication systems. However, we will show in this paper that KLD can be employed to infer the symbol error rate of the detector at the CUEs, in addition to being informative of the detection capability of MIMO radars. Consequently, such a measure can be effectively used to evaluate the performance of ISAC systems as a single entity instead of two separated (unlinked) performance measures. Accordingly, we consider a generalized system model with a MIMO-BS, multiple users and multiple targets, where the weighted sum of the relative entropy (WSRE) is proposed to infer the efficiency of ISAC systems as one system rather than two subsystems. The contribution of this paper can be summarized in the following.

1. Providing a framework for the statistics of received signals as well as a KLD based analysis for CUEs using two well-known precoding techniques employed by the MIMO-BS, namely, the zero forcing (ZF) and the maximum ratio transmission (MRT) precoders. It is worth noting that although MRT is widely used in the literature, to the best of authors knowledge, the analysis of the statistics of the received signals and interference from other users and radar signal has not been well investigated.

2. Inspired by full-duplex communications, an interference cancellation (IC) approach, which is applicable at the MIMO-BS before employing targets detection, is proposed in order to cancel out the communication signal reflected from the environment.

3. Providing a unique KLD analysis for the MIMO radar sub-system. The uniqueness of this KLD comes from two facts. The first one is that KLD analysis with noncentral Chi-squared observations, which is the case in most of MIMO radars, has not been derived in the literature. The second fact is that the analysis takes into account the imperfect cancellation for the communication waveform portion reflected by the environment.

4. Proposing a unified performance measure for ISAC systems using WSRE for the case of multiple CUEs and targets.

5. Introducing KLD as a measure for communication systems, and illustrating its relation to SER. Additionally, the relation between KLD and the detection probability in MIMO radars is investigated.

6. Evaluating the performance of the proposed WSRE using the derived formulas, and validating the analysis by simulations.

The obtained results show that the derived KLD is very accurate and can be efficiently used to infer the efficiency of both parts of the ISAC systems, namely, the communication and radar subsystems.

5.1.3 Paper Organization

Sec. II presents the system model for the ISAC scenario of interest and a background about KLD. Sec. III, provides the KLD analysis for the communication subsystem, and the relation between KLD and SER is investigated in Sec. IV. Sec. V shows the derivation of KLD for a MIMO radar system considering a multiple targets scenario, and relates KLD to the detection probability of radar. Sec. VI introduces the WSRE performance measure for ISAC while Sec. VII provides the numerical results and Sec. VIII concludes the paper.

5.2 System Model

As illustrated in Fig. 5.1, this work considers an ISAC system which consists of MIMO-BS with a total of N antennas serving a number of single antenna K CUEs in the downlink direction and aims at detecting T targets which can be ground targets, unmanned aerial vehicles (UAVs) or a mix of ground targets and UAVs, where the radar-targets propagation medium obeys a line-of-sight channel model. The separated deployment, in which the BS antennas are distributed among the communication and radar subsystems, is the scenario of this paper's interest. The transmitter employs linear precoding techniques such as ZF and MRT to precode the information intended to CUEs before the transmission process takes place through the allocated $N_C \leq N$ antennas. Moreover, the power budget at BS is limited to P_{T} which is supposed to be exploited for data transmission and sensing, and thus $P_{\mathrm{T}} = P_{\mathrm{C}} + P_{\mathrm{rad}}$ where P_{C} and P_{rad} denote the amounts of power allocated for the communication and radar subsystems, respectively. It is worth mentioning that although there are several precoding methods in the literature such as interference aware precoding and dirty paper coding which could outperform ZF and MRT, the later two precoders, ZF and MRT, are the most attractive solutions due to their low-complexity, implementation feasibility in practice and reasonable performance [24–27]. On the other hand, the radar matrix is assumed to be designed using a desired radar signal $\mathbf{s}_l$ which satisfies a covariance matrix of $\mathbf{R}_s \triangleq \frac{1}{L}\sum_{l=1}^{L}\mathbf{s}_l\mathbf{s}_l^H$ with L being the number of snapshots. The radar signal vector $\mathbf{s}_l$ is emitted towards the targets using the remaining $N_R = N - N_C$ antennas assigned for the radar service.

5.2.1 Communication Subsystem

For a given transmission interval l, a data symbol $d_k\left[l\right]$ intended for the kth CUE is picked from a normalized constellation with $\mathbb{E}\left[\left|d_k\left[l\right]\right|^2\right] = 1$, and precoded using a linear precoder with a precoding vector $\mathbf{w}_k \in \mathbb{C}^{N_C\times 1}$, and thus the precoded information symbols for all users $\mathbf{d}_{\mathbf{w}} \in \mathbb{C}^{N_C\times 1}$ can be written

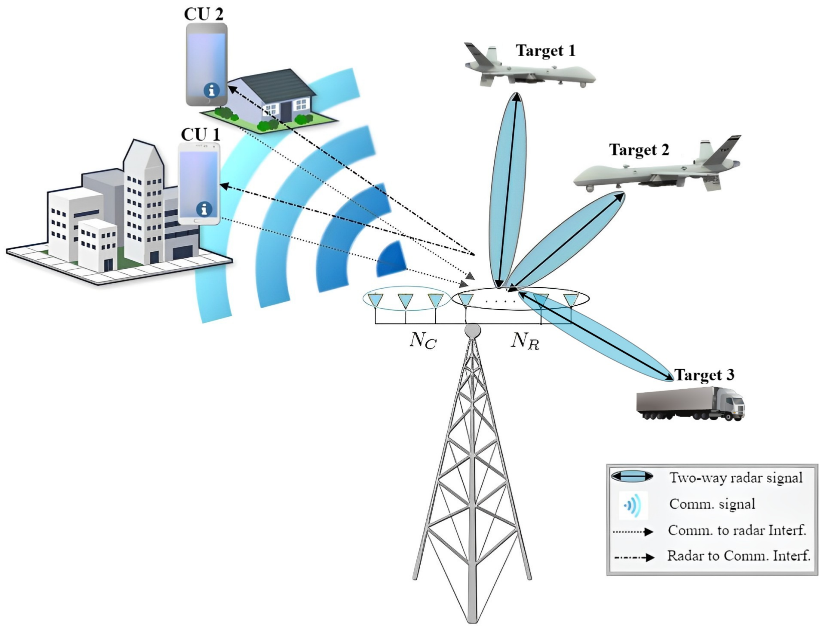

Figure 5.1: An illustration diagram for separated deployment based ISAC.

as

$$\mathbf{d}_{\mathbf{w}}\left[l\right]=\sum_{i=1}^{K}\sqrt{p_i}\mathbf{w}_i d_i\left[l\right], \tag{5.1}$$

where p_i is a power control factor. Consequently, the received signal at the kth CUE considering the interference caused by the radar signal is

$$y_k\left[l\right]=\mathbf{g}_k^T\mathbf{d}_{\mathbf{w}}\left[l\right]+\sqrt{\frac{P_{\text{rad}}}{N_R}}\mathbf{f}_k^T\mathbf{s}_l+n_k[l], \tag{5.2}$$

where P_{rad} is the power allocated to the radar subsystem, $\mathbf{g}_k\in\mathbb{C}^{N_C\times 1}\sim\mathcal{CN}\left(0,2\sigma_g^2\right)$ is a flat Rayleigh channel gain vector from the communication antennas to the kth CUE, $\mathbf{f}_k^T\in\mathbb{C}^{N_R\times 1}\sim\mathcal{CN}\left(0,2\sigma_f^2\right)$ with $(\cdot)^T$ denoting the transpose operation is a flat Rayleigh channel vector which captures the channel between the radar antennas and CUEs, $\mathbf{s}_l$ is the radar waveform, and $n_k\sim\mathcal{CN}\left(0,2\sigma_n^2\right)$ is the additive white Gaussian noise (AWGN). In this paper, channels are assumed independent identically distributed (i.i.d) and follow flat Rayleigh fading.

5.2.2 Sensing Subsystem

Generally speaking, in MIMO radar, a signal vector $\mathbf{s}\left(t\right)$ is transmitted from BS towards the targets, which reflect the signals that are captured at the receiver, which is the same BS in the case of monostatic scenario. Moreover, due to the multipath nature of the wireless medium, the signals which get reflected from a target might be received at BS through multiple paths with different amplitudes and phases. In such scenarios, virtual targets, also known as ghost targets, which are virtual copies of the actual target with different values of the angle-of-arrival (AoA), will appear. Ray tracing techniques, the uniform diffraction theory and the law of reflection can be employed to separate the actual target from ghost targets [56–58]. However, similar to many existing work in the literature, this work is concerned with the scenario in which the radar-targets channels are subject to direct path propagation model [20,23,33]. It is noteworthy mentioning that since monostatic MIMO radar with direct path channel is considered, antennas have almost equal distance to a certain target and thus they are subject to equal pathloss values. Therefore, unlike wireless communication systems, it is unlikely to have preference for one antenna over another, and thus P_{rad} can be evenly distributed over the radar antennas. Consequently, for interference free environment, the baseband representation of the radar return signals from the direct path with time delay τ_{d} and Doppler shift ω_{d} can be written as,

$$\tilde{\mathbf{y}}_{\mathrm{rad}}\left(t\right)=\sum_{t=1}^{T}\alpha_{t}\sqrt{\frac{P_{\mathrm{rad}}}{N_{R}}}\mathbf{a}_{\mathrm{R}}\left(\theta_{t}\right)\mathbf{a}_{\mathrm{T}}\left(\theta_{t}\right)^{T}\mathbf{s}\left(t-\tau_{t,\mathrm{d}}\right)\mathrm{e}^{j\omega_{t,\mathrm{d}}t}+\mathbf{n}_{\mathrm{rad}}\left(t\right), \tag{5.3}$$

where α_t is the channel gain for BS-Target-BS path, $\mathbf{a}_{\mathrm{T}}\left(\theta_t\right)$ and $\mathbf{a}_{\mathrm{R}}\left(\theta_t\right)$ denote the transmit and receive array gain, respectively, and $\mathbf{n}_{\mathrm{rad}}\left(t\right)$ is AWGN. The received signals vector $\tilde{\mathbf{y}}_{\mathrm{rad}}\left(t\right)$ is typically processed through a bank of matched filters which are tuned to a Doppler frequency of ω_{d} and a time delay of τ_{d}. In other words, the detection process is applied to a certain range-Doppler bin and could be repeated for other range-Doppler bins separately [20,23,33]. Therefore, let the desired radar waveform in signal domain $\mathbf{s}_l \in \mathbb{C}^{N_R\times 1}$ $\forall l \leq L$, where L is the number of snapshots, $\mathbf{a}_{\mathrm{T}}\left(\theta\right)$ and $\mathbf{a}_{\mathrm{R}}\left(\theta\right)$ are the transmit and receive array gains of a uniform linear array (ULA), respectively, the signals vector reflected by the targets and received at BS, which is processed through a bank of filters tuned to τ_{d} and ω_{d} and impinged by communication signal interference, can be expressed as

$$\tilde{\mathbf{y}}_{\mathrm{rad}}\left[l\right]=\sum_{t=1}^{T}\alpha_{t}\sqrt{\frac{P_{\mathrm{rad}}}{N_{R}}}\mathbf{a}_{\mathrm{R}}\left(\theta_{t}\right)\mathbf{a}_{\mathrm{T}}\left(\theta_{t}\right)^{T}\mathbf{s}_{l}+\mathbf{G}_{\mathrm{rad}}\mathbf{d}_{\mathbf{w}}\left[l\right]+\mathbf{n}_{\mathrm{rad}}\left[l\right], \tag{5.4}$$

where the term $\mathbf{G}_{\mathrm{rad}}\mathbf{d}_{\mathbf{w}}\left[l\right]$ represents the interference from the communication subsystem which is caused by backscattering the communication signal from the environment, $\mathbf{G}_{\mathrm{rad}} \in \mathbb{C}^{N_R\times N_C}$ is the channel matrix from the N_C communication antennas to N_R radar antennas, and $\mathbf{n}_{\mathrm{rad}} \in \mathbb{C}^{N_R\times 1}$is the AWGN, i.e., $\mathbf{n}_{\mathrm{rad}} \sim \mathcal{CN}\left(0, 2\sigma_n^2\mathbf{I}_{N_R}\right)$ where $\mathbf{I}_{N_R}$ is the identity matrix.

Interestingly, it can be observed from (5.4) that the interference caused by the communication signal consists of the channel gain of the BS (Communication transmitter)-Environment-BS (radar receiver) link and the data vector $\mathbf{d}_{\mathbf{w}}\left[l\right]$ which has been already transmitted from BS. Since $\mathbf{d}_{\mathbf{w}}\left[l\right]$ is previously known at BS, interference cancellation (IC) process can be very beneficial if the estimate of $\mathbf{G}_{\mathrm{rad}}$ is available at BS. It worth noting that the estimation of $\mathbf{G}_{\mathrm{rad}}$ can be performed at BS in a previous phase through pilot signals. Therefore, inspired by full duplex communication systems, we propose such IC process which is very useful for real life ISAC systems and analyze the radar system considering that the IC process is not perfect. Given the estimated channel matrix $\hat{\mathbf{G}}_{\mathrm{rad}}$, the received signals in (5.4) after applying IC can be rewritten as

$$\mathbf{y}_{\text{rad}}[l] = \sum_{t=1}^{T} \alpha_t \sqrt{\frac{P_{\text{rad}}}{N_R}} \mathbf{A}(\theta_t) \mathbf{s}_l + \omega_{\text{rad}} + \mathbf{n}_{\text{rad}}[l], \tag{5.5}$$

where a monostatic radar is considered with $\mathbf{a}(\theta_t) \triangleq \mathbf{a}_{\text{R}}(\theta_t) = \mathbf{a}_{\text{T}}(\theta_t) \triangleq \left[1, \mathrm{e}^{j\frac{2\pi\Delta}{\lambda_0}\sin\theta_t}, \cdots, \mathrm{e}^{j\frac{2\pi\Delta}{\lambda_0}(N_R-1)\sin\theta_t}\right]^T$, Δ is the antenna spacing, λ_0 is the signal wavelength, $\mathbf{A}(\theta_t) \in \mathbb{C}^{N_R \times N_R} = \mathbf{a}(\theta_t)\mathbf{a}(\theta_t)^T$ is the equivalent array manifold, and $\omega_{\text{rad}} \in \mathbb{C}^{N_R \times 1} = \mathbf{G}_{\text{err}}\mathbf{d}_{\mathbf{w}}[l] = \mathbf{G}_{\text{err}} \sum_{k=1}^{K} \sqrt{p_k}\mathbf{w}_k d_k[l]$ is the interference from the communication subsystem to radar subsystem after employing IC with $\mathbf{G}_{\text{err}} \triangleq \mathbf{G}_{\text{rad}} - \hat{\mathbf{G}}_{\text{rad}}$ representing channel estimation errors.

5.2.3 The Relative Entropy or Kullback-Leibler Divergence (KLD)

The relative entropy, or KLD, for a pair of random PDFs is defined in **Definition 1** below. Although the KLD measure is originally defined for a pair of PDFs, it can be extended for multiple PDFs by considering every pair separately and then evaluating the average for all possible unequal pairs.

Definition 1: For a pair of continuous PDFs, $f_m(x)$ and $f_n(x)$, $\text{KLD}_{n\to m}$ is defined as the relative entropy from $f_n(x)$ to $f_m(x)$ or a measure of how different a PDF $f_n(x)$ is from another PDF $f_m(x)$. In general , KLD is an asymmetric measure, and mathematically $\text{KLD}_{n\to m}$ for continuous random variable can be represented as [30]

$$\text{KLD}(f_m \parallel f_n) = \int_{-\infty}^{\infty} f_m(x) \log_2\left(\frac{f_m(x)}{f_n(x)}\right) dx, \tag{5.6}$$

where $\text{KLD}(f_m \parallel f_n) \triangleq \text{KLD}_{n\to m} \forall m \neq n$. For multivariate Gaussian distributed random variables having mean vectors of μ_m and μ_n and covariance matrices of Σ_m and Σ_n, it can be derived as

$$\text{KLD}_{n\to m} = \frac{1}{2\ln 2}\left(\text{tr}\left(\Sigma_n^{-1}\Sigma_m\right) - 2 + \left(\mu_{k,n} - \mu_{k,m}\right)^T \Sigma_n^{-1}\left(\mu_{k,n} - \mu_{k,m}\right) + \ln\frac{|\Sigma_n|}{|\Sigma_m|}\right), \tag{5.7}$$

Since KLD is generally asymmetric, the average KLD can be evaluated wherever $\text{KLD}_{n\to m} \neq \text{KLD}_{m\to n}$, i.e., $\text{KLD}_{n,m} \triangleq \frac{1}{2}(\text{KLD}_{n\to m} + \text{KLD}_{m\to n})$. It worth noting that when the logarithm function with base 2, i.e., $\log_2(\cdot)$, is considered, KLD is measured in bits, whereas it is measured in nats when the natural logarithm $\ln(\cdot)$ is used. In this work, we consider the first case and KLD is measured in bits.

KLD, or the relative entropy, has a wide range of applications in several science and engineering disciplines such as comparing the information gain of different statistical models for model selection, machine learning to measure the information gain achieved by using the distribution f_m rather than the current distribution f_n, information coding to measure the expected number of extra bits required to encode samples taken from the distribution f_m using a code optimized for another distribution f_n, and quantum information science where the minimum $\text{KLD}(f_m \parallel f_n)$ over all possible separable states f_n is used to model the entanglement in state f_m. According to the well known Neyman-Pearson lemma, the best way to separate or distinguish between two random variables through an observation X taken from one of them is obtained by using the log-likelihood ratio test, i.e., $\log_2(\frac{f_m(x)}{f_n(x)})$, where the performance can be assessed using the expected value of the log-likelihood ratio which represents the relative entropy or KLD as defined in (5.6). Moreover, $\mathrm{KLD}_{n\to m}$, or equivalently $\mathrm{KLD}\left(f_m \parallel f_n\right)$, with f_m and f_n respectively represent the distribution of received samples under hypotheses H_1 and H_0, can be interpreted as the expected discrimination information or information gain for discriminating hypothesis H_1 against hypothesis H_0 when H_1 is the true hypothesis [59–62].

Clearly, KLD is an informative measure that can be applied for inferring systems to assess the discrimination process between a set of candidates such as the data detection process in communication systems and hypothesis testing problem in sensing systems. Moreover, unlike traditional metrics such as SER, detection probability and false alarm probability, KLD is independent of the detection process and detection thresholds applied at the receiver. By using KLD as a unified performance measure, the performance of the two subsystems of ISAC are put on the same scale rather than two different scales. It is noteworthy to mention that according to [30, Ch. 2], KLD is a generalization for the concept of mutual information which in one role generalizes the Shannon entropy. Therefore, our core aim in this work is to develop a unified performance framework for both sensing and communications, departing from separate performance metrics, which is very beneficial for the design of integrated waveforms for ISAC systems. Additionally, it is worth noting that the trade-off between the two subsystems is not always clear when different metrics are employed to evaluate the performance of ISAC.

5.3 Relative Entropy Analysis for Communication Subsystem

The received signal at the kth CUE in (5.2) can be represented as

$$y_k\left[l\right] = \sqrt{p_k}\mathbf{g}_k^T\mathbf{w}_k d_k\left[l\right] + \mathbf{g}_k^T\sum_{\substack{i=1\\i\neq k}}^{K}\sqrt{p_i}\mathbf{w}_i d_i\left[l\right] + \eta_k[l], \tag{5.8}$$

where $\eta_k[l] \triangleq \sqrt{\frac{P_{\mathrm{rad}}}{N_R}}\mathbf{f}_k^T\mathbf{s}_l + n_k[l]$ is the radar interference plus noise. It can be shown that the distribution of $\mathbf{f}_k^T\mathbf{s}_l$ follows complex Gaussian with a mean of $\mathbb{E}\left[\mathbf{f}_k^T\mathbf{s}_l\right] = 0$ and a variance of

$$\mathbb{E}\left[\mathbf{f}_k^H\mathbf{s}_l\mathbf{s}_l^H\mathbf{f}_k\right] = 2\sigma_f^2\mathbb{E}\left[\mathrm{tr}\left(\mathbf{s}_l\mathbf{s}_l^H\right)\right] = 2\sigma_f^2\mathrm{tr}\left(\mathbf{R}_s\right) = 2\sigma_f^2 N_R, \tag{5.9}$$

where the last equality is obtained given the fact that the elements of the main diagonal of $\mathbf{R}_s$ are typically normalized to ones. Consequently, the distribution of $\eta_k[l] = \sqrt{\frac{P_{\mathrm{rad}}}{N_R}}\mathbf{f}_k^T\mathbf{s}_l + n_k[l]$ is complex Gaussian with $\eta_k \sim \mathcal{CN}\left(0, 2\sigma_\eta^2\right)$ where $\sigma_\eta^2 = P_{\mathrm{rad}}\sigma_f^2 + \sigma_n^2$.

For the design of the data beamforming matrix $\mathbf{W} = [\mathbf{w}_1, \mathbf{w}_2, \cdots, \mathbf{w}_K]$, we consider the widely accepted ZF and MRT in the following two sections. Generally speaking, for a linear precoding matrix $\mathbf{W}$, the received data vector at CUEs can be written in a matrix form as

$$\mathbf{y}\left[l\right] = \mathbf{G}^T\mathbf{W}\mathbf{P}\mathbf{d}[l] + \eta[l], \tag{5.10}$$

where $\mathbf{G} \in \mathbb{C}^{N_C \times K} = [\mathbf{g}_1, \mathbf{g}_2, \cdots, \mathbf{g}_K]$, $\mathbf{W} \in \mathbb{C}^{N_C \times K} = [\mathbf{w}_1, \mathbf{w}_2, \cdots, \mathbf{w}_K]$ is the precoding matrix, $\mathbf{P} \in \mathbb{C}^{K \times K} = \text{diag}\left(\sqrt{p_1}, \sqrt{p_2}, \cdots, \sqrt{p_K}\right)$ is power control matrix, $\mathbf{d}[l] \in \mathbb{C}^{K \times 1} = \left[d_1\left[l\right], d_2\left[l\right], \cdots, d_K\left[l\right]\right]^T$, $\mathbf{F} \in \mathbb{C}^{N_R \times K} = \left[\mathbf{f}_1^T, \mathbf{f}_2^T, \cdots, \ \mathbf{f}_K^T\right]$ is the interfering channel matrix between the radar antennas and CUEs, $\mathbf{n}[l] \in \mathbb{C}^{K \times 1} = \left[n_1\left[l\right], n_2\left[l\right], \cdots, n_K\left[l\right]\right]^T$, and $\eta[l] \in \mathbb{C}^{K \times 1} = \left[\eta_1\left[l\right], \eta_2\left[l\right], \cdots \ , \eta_K\left[l\right]\right]^T$, which is defined as $\eta[l] \triangleq \sqrt{\frac{P_{\text{rad}}}{N_R}}\mathbf{F}^T\mathbf{s}_l + \mathbf{n}[l]$, is the radar interference plus noise term with $\eta_k \sim \mathcal{CN}\left(0, 2\sigma_\eta^2\right)$ where $\sigma_\eta^2 = P_{\text{rad}}\sigma_f^2 + \sigma_n^2$.

5.3.1 ZF based Data Precoding

Here, we assume ZF is employed at BS to precode the users' data, which is able to cancel out the interference between the users. Using such precoder, the precoding matrix $\mathbf{W}$ is generally given by $\mathbf{W} = \mathbf{G}^*\left(\mathbf{G}^T\mathbf{G}^*\right)^{-1}$, where $(\cdot)^*$ is the conjugate operator. Consequently, by substituting $\mathbf{W}$ in (5.10) and noting that $\mathbf{G}^T\mathbf{W} = \mathbf{I}_K$ with $\mathbf{I}_K$ represents the identity matrix, we obtain

$$\mathbf{y}\left[l\right] = \mathbf{P}\mathbf{d}[l] + \eta[l], \tag{5.11}$$

where $\mathbf{P}$ depends on the normalization scheme employed as discussed in the next two subsections.

5.3.1.1 ZF based on vector normalization

With vector normalization based ZF (VNZF), $\mathbf{P} = \text{diag}\left(\alpha_{1,\text{ZF}}, \alpha_{2,\text{ZF}}, \cdots, \alpha_{K,\text{ZF}}\right)\mathbf{P}_{\text{com}}$ where $\alpha_{k,\text{ZF}} = \frac{1}{\|\mathbf{w}_k\|}$ is a normalization factor and $\mathbf{P}_{\text{com}} \triangleq \text{diag}\left(\sqrt{P_{1,\text{com}}}, \sqrt{P_{2,\text{com}}}, \cdots, \sqrt{P_{K,\text{com}}}\right)$ with constraint $P_{\text{C}} = \sum_k P_{k,\text{com}}$ is used to control the average transmission power for CUEs. It is worthy to mention that for users with equal priorities, $P_{k,\text{com}}$ can be selected such that $P_{k,\text{com}} = \frac{P_{\text{C}}}{K}$. Anyway, for the general case with unequal $P_{k,\text{com}}$'s, the received signal at the kth CUE is

$$y_k\left[l\right] = \sqrt{P_{k,\text{com}}}\alpha_{k,\text{ZF}}d_k\left[l\right] + \eta_k[l]. \tag{5.12}$$

Based on the received signal $y_k\left[l\right]$, the conditional density function of $y_k|\left\{d_k\left[l\right], \alpha_{k,\text{ZF}}\right\}$ is complex Gaussian (or bivariate Gaussian), which can be expressed as

$$f\left(y_k|\left\{d_k\left[l\right], \alpha_{k,\text{ZF}}\right\}\right) = \frac{1}{\sqrt{\left(2\pi\right)^2|\Sigma|}}\exp\left(-\left(\mathbf{y}_k - \mu_k\right)^T \ \Sigma^{-1}\left(\mathbf{y}_k - \mu_k\right)\right), \tag{5.13}$$

where $\mathbf{y}_k \triangleq [y_{k,\Re}, y_{k,\Im}]^T$ with $y_{k,\Re} \triangleq \mathrm{Re}(y_k)$ and $y_{k,\Im} = \mathrm{Im}(y_k)$ denote the real and imaginary components of y_k, respectively, and $\mu_k \triangleq [\mu_{k,\Re}, \mu_{k,\Im}]^T$ with $\mu_{k,\Re} = \sqrt{P_{k,\mathrm{com}}}\alpha_{k,\mathrm{ZF}}\mathrm{Re}(d_k[l])$ and $\mu_{k,\Im} = \sqrt{P_{k,\mathrm{com}}}\alpha_{k,\mathrm{ZF}}\mathrm{Im}(d_k[l])$. The covariance matrix $\Sigma = \sigma_\eta^2\mathbf{I}_2$ with $|\Sigma| = \sigma_\eta^4$ and $\Sigma^{-1} = \dfrac{1}{\sigma_\eta^2}\mathbf{I}_2$.

Corrolary 1: For a generalized M-ary signal constellation, KLD can be evaluated for each possible pair of unequal data symbols $\{d_{k,n}[l], d_{k,m}[l]\}, n \neq m$. Let us consider a pair of symbols $\left\{d_{k,n}[l] \triangleq |a_{k,n}| e^{j\phi_{k,n}}, d_{k,m}[l] \triangleq |a_{k,m}| e^{j\phi_{k,m}}\right\} \forall n \neq m$, with corresponding received signals density functions $f_n \sim \mathcal{CN}(\mu_{k,n}, \Sigma_n)$ and $f_m \sim \mathcal{CN}(\mu_{k,m}, \Sigma_m)$, thus the relative entropy for the kth CUE measured in bits from f_m to f_n is denoted as $\mathrm{KLD}_{m\to n}$ and can be derived using **Definition 1** as

$$\mathrm{KLD}_{k,m\to n} = \frac{1}{2\ln 2}\left(\mathrm{tr}\left(\Sigma_m^{-1}\Sigma_n\right) - 2 + (\mu_{k,m} - \mu_{k,n})^H \Sigma_m^{-1}(\mu_{k,m} - \mu_{k,n}) + \ln\frac{|\Sigma_m|}{|\Sigma_n|}\right). \tag{5.14}$$

By noting that $\Sigma_n = \Sigma_m = \sigma_\eta^2\mathbf{I}_2$, and given that $\mu_{k,m} = \left[\sqrt{P_{k,\mathrm{com}}}\alpha_{k,\mathrm{ZF}}\cos\phi_{k,m}, \sqrt{P_{k,\mathrm{com}}}\alpha_{k,\mathrm{ZF}}\sin\phi_{k,m}\right]$, $\mathrm{KLD}_{m\to n}$ can be simplified to

$$\begin{aligned}
\mathrm{KLD}_{k,m\to n} &= \frac{1}{2\ln 2\sigma_\eta^2}(\mu_{k,m} - \mu_{k,n})^H(\mu_{k,m} - \mu_{k,n}) \\
&= \frac{1}{\ln 2}\gamma_{\mathrm{VNZF}}\left(|a_m|^2 + |a_n|^2 - 2|a_m||a_n|\cos(\phi_{k,m} - \phi_{k,n})\right) \\
&= \frac{1}{\ln 2}\gamma_{\mathrm{VNZF}}|d_{k,n}[l] - d_{k,m}[l]|^2,
\end{aligned} \tag{5.15}$$

where $\gamma_{k,\mathrm{VNZF}} = \dfrac{\alpha_{k,\mathrm{ZF}}^2 P_{k,\mathrm{com}}}{2\sigma_\eta^2}$.

As stated earlier, since KLD is measured for a pair of PDFs, the average KLD, $\mathrm{KLD}_{k,\mathrm{VNZF}}$, is evaluated by considering all possible pairs of dissimilar symbols, which can be represented as

$$\mathrm{KLD}_{k,\mathrm{VNZF}} = \frac{\gamma_{\mathrm{VNZF}}}{\ln 2}\sum_{m=1}^{M}\sum_{\substack{n=1\\n\neq m}}^{M}\Pr(\phi_{k,m}, \phi_{k,n})|d_{k,n}[l] - d_{k,m}[l]|^2, \tag{5.16}$$

and for equal likelihood symbols, it can be reduced to

$$\mathrm{KLD}_{k,\mathrm{VNZF}} = \frac{\gamma_{\mathrm{VNZF}}}{M(M-1)\ln 2}\sum_{m=1}^{M}\sum_{\substack{n=1\\n\neq m}}^{M}|d_{k,n}[l] - d_{k,m}[l]|^2 = \frac{\lambda}{M(M-1)\ln 2}\gamma_{\mathrm{VNZF}}, \tag{5.17}$$

where $\lambda = \sum_{m=1}^{M}\sum_{\substack{n=1\\n\neq m}}^{M}|d_{k,n}[l] - d_{k,m}[l]|^2$ which depends on the transmitted data constellation, and thus λ is a constant for a given constellation. For MPSK signalling, as an example, with a normalized constellation, $\mathrm{KLD}_{k,\mathrm{VNZF},m\to n}^{\mathrm{MPSK}} = \dfrac{2}{\ln 2}\gamma_{\mathrm{VNZF}} \times (1 - \cos(\phi_{k,m} - \phi_{k,n}))$ and $\mathrm{KLD}_{k,\mathrm{VNZF}}^{\mathrm{MPSK}} = \dfrac{\lambda}{M(M-1)\ln 2}\gamma_{\mathrm{VNZF}}$ with $\lambda_{\mathrm{MPSK}} = 2\sum_{m=1}^{M}\sum_{\substack{n=1\\n\neq m}}^{M}(1 - \cos(\phi_{k,m} - \phi_{k,n}))$ are obtained.

The KLD derivations have not considered the randomness nature of the communication channel so far, which results in a random normalization factor $\alpha_{k,\mathrm{ZF}}$, and thus averaging over $\alpha_{k,\mathrm{ZF}}$ must be taken into account for the sake of completeness. Towards this goal, the distribution of $\alpha_{k,\mathrm{ZF}}^2 \triangleq \frac{1}{\left[(\mathbf{G}^T\mathbf{G}^*)^{-1}\right]_{k,k}}$ is found first, which under Rayleigh fading follows a Gamma random variable with a scale factor of 1 and a shape factor of $L_{\mathrm{G}} = N_C - K + 1$ [63], i.e., $x \triangleq \alpha_{k,\mathrm{ZF}}^2 \sim \mathrm{Gamma}(L_{\mathrm{G}}, 1)$.

$$f_x\left(x\right) = \frac{1}{\Gamma\left(L_{\mathrm{G}}\right)} x^{L_{\mathrm{G}}-1} \mathrm{e}^{-x}, x \geq 0. \tag{5.18}$$

Therefore, $\alpha_{k,\mathrm{ZF}}$ follows the generalized Gamma distribution with the following PDF

$$f_{\alpha_{k,\mathrm{ZF}}}\left(\alpha_{k,\mathrm{ZF}}\right) = \frac{2}{\Gamma\left(L_{\mathrm{G}}\right)} \alpha_{k,\mathrm{ZF}}^{2L_{\mathrm{G}}-1} \mathrm{e}^{-\alpha_{k,\mathrm{ZF}}^2}, \alpha_{k,\mathrm{ZF}} \geq 0. \tag{5.19}$$

Consequently, by evaluating the average of (5.17) the relative entropy for the kth CUE is

$$\mathrm{KLD}_{k,\mathrm{IVNZF,avg}} = \frac{\lambda}{M\left(M-1\right)\ln 2} \mathbb{E}\left[\gamma_{\mathrm{VNZF}}\right]. \tag{5.20}$$

Substituting the density function given by (5.19) in (5.20), $\mathrm{KLD}_{k,\mathrm{IVNZF,avg}}$ can be expressed as

$$\mathrm{KLD}_{k,\mathrm{IVNZF,avg}} = \frac{\lambda}{M\left(M-1\right)\ln 2} \frac{P_{k,\mathrm{com}}}{2\sigma_\eta^2} \frac{2}{\Gamma\left(L_{\mathrm{G}}\right)} \int_0^\infty \alpha_{k,\mathrm{ZF}}^{2L_{\mathrm{G}}+1} \mathrm{e}^{-\alpha_{k,\mathrm{ZF}}^2} d\alpha_{k,\mathrm{ZF}}. \tag{5.21}$$

By using integration by substitution with $y = \alpha_{k,\mathrm{ZF}}^2$, and noting that $\alpha_{k,\mathrm{ZF}}^{2L_{\mathrm{G}}} = \left(\alpha_{k,\mathrm{ZF}}^2\right)^{L_{\mathrm{G}}} = y^{L_{\mathrm{G}}}$ and $d\alpha_{k,\mathrm{ZF}} = \frac{1}{2\alpha_{k,\mathrm{ZF}}} dy$, $\mathrm{KLD}_{k,\mathrm{IVNZF,avg}}$ is reduced to

$$\mathrm{KLD}_{k,\mathrm{IVNZF,avg}} = \frac{\lambda}{M\left(M-1\right)\ln 2} \frac{P_{k,\mathrm{com}}}{2\sigma_\eta^2} \frac{1}{\Gamma\left(L_{\mathrm{G}}\right)} \int_0^\infty y^{L_{\mathrm{G}}} \mathrm{e}^{-y} dy. \tag{5.22}$$

Thereafter, with the aid of the definition of the Gamma function, i.e., $\Gamma\left(L_{\mathrm{G}}\right) = \int_0^\infty y^{L_{\mathrm{G}}-1} \mathrm{e}^{-y} dy$, thus $\int_0^\infty y^{L_{\mathrm{G}}} \mathrm{e}^{-y} dy = \Gamma\left(L_{\mathrm{G}}+1\right)$, and using the fact that $\Gamma\left(L_{\mathrm{G}}+1\right) = L_{\mathrm{G}}!$ since L_{G} is a positive integer value, $\mathrm{KLD}_{k,\mathrm{IVNZF,avg}}$ can be found as

$$\mathrm{KLD}_{k,\mathrm{IVNZF,avg}} = \frac{\lambda}{M\left(M-1\right)\ln 2} \frac{P_{k,\mathrm{com}}}{2\sigma_\eta^2} L_{\mathrm{G}}. \tag{5.23}$$

5.3.1.2 ZF with instantaneous matrix normalization

With instantaneous channel matrix based normalization, $\mathbf{P} \triangleq \tilde{\alpha}_{\mathrm{ZF}} \mathbf{P}_{\mathrm{com}}$ with $\tilde{\alpha}_{\mathrm{ZF}} = \sqrt{\frac{1}{\left(\mathbf{d}^H \mathbf{W} \mathbf{W}^H \mathbf{d}\right)}}$, and the received signal at the kth CUE can be written as

$$y_k\left[l\right] = \sqrt{P_{k,\mathrm{com}}} \tilde{\alpha}_{\mathrm{ZF}} d_k\left[l\right] + \eta_k[l]. \tag{5.24}$$

Following the derivations in the previous case, it can be easily shown that $\tilde{\alpha}_{\mathrm{ZF}}$ follows a generalized Gamma distribution, i.e., $\tilde{\alpha}_{\mathrm{ZF}} \sim \mathrm{GG}(a = 1, d = 2L_{\mathrm{G}} = 2\left(N_C - K + 1\right), p = 2)$. Based on the received signal $y_k\left[l\right]$, the density function of $y_k | \left\{\tilde{\alpha}_{\mathrm{ZF}}, d_k\left[l\right]\right\}$ is complex Gaussian (or bivariate Gaussian), and thus the instantaneous and average KLD for the kth CUE can be respectively expressed as

$$\mathrm{KLD}_{k,\mathrm{IZF}|\alpha_{\mathrm{ZF}}} = \frac{\lambda}{M\left(M-1\right)\ln 2}\frac{P_{k,\mathrm{com}}}{2\sigma_{\eta}^{2}}\tilde{\alpha}_{\mathrm{ZF}}^{2}, \tag{5.25}$$

with an average value of

$$\mathrm{KLD}_{k,\mathrm{IZF,avg}} = \frac{\lambda}{M\left(M-1\right)\ln 2}\frac{P_{k,\mathrm{com}}}{2\sigma_{\eta}^{2}}\int_{0}^{\infty}\tilde{\alpha}_{\mathrm{ZF}}^{2} f_{\tilde{\alpha}_{\mathrm{ZF}}}\left(\tilde{\alpha}_{\mathrm{ZF}}\right) d\tilde{\alpha}_{\mathrm{ZF}}. \tag{5.26}$$

By substituting the generalized Gamma distribution for $f_{\tilde{\alpha}_{\mathrm{ZF}}}\left(\tilde{\alpha}_{\mathrm{ZF}}\right)$, and then employing the integration by substitution theorem with $x = \tilde{\alpha}_{\mathrm{ZF}}^{2}$ and using the definition of Gamma function, $\mathrm{KLD}_{k,\mathrm{IZF,avg}}$ can be derived as

$$\mathrm{KLD}_{k,\mathrm{IZF,avg}} = \frac{\lambda}{M\left(M-1\right)\ln 2}\frac{P_{k,\mathrm{com}}}{2\sigma_{\eta}^{2}}\left(N_C - K + 1\right). \tag{5.27}$$

Interestingly, by comparing (5.27) with (5.23), it can be realized that the KLDs for ZF with instantaneous vector normalization and matrix normalization are equal. Therefore, we will consider ZF with instantaneous matrix normalization in our investigations henceforth.

5.3.2 MRT based Data Precoding with Vector Normalization

To employ MRT, sometimes called the matched filter (MF), for data precoding, the precoding vector for the kth user data, $\mathbf{w}_k$, is evaluated based on the channel vector $\mathbf{g}_k$ only, and thus $\mathbf{w}_k$ is independent of $\mathbf{g}_i \forall i \neq k$. For MRT, we consider the instantaneous vector based normalization with $\mathbf{w}_k = \mathbf{g}_k^{*}$ and thus the received signal at the kth user can be written as

$$y_k\left[l\right] = \frac{\mathbf{g}_k^T}{\left\|\mathbf{g}_k\right\|}\sum_{i=1}^{K}\sqrt{P_{i,\mathrm{com}}}\mathbf{w}_i d_i\left[l\right] + \sqrt{\frac{P_{\mathrm{rad}}}{N_R}}\mathbf{f}_k^T\mathbf{s}_l + n_k[l] = \sqrt{P_{k,\mathrm{com}}}\left\|\mathbf{g}_k\right\| d_k\left[l\right] + \tilde{\omega}_{\mathrm{MRT}}[l], \tag{5.28}$$

where the equivalent inter-user and radar interference plus noise term $\tilde{\omega}_{\mathrm{MRT}} = \omega_{\mathrm{MRT}} + \eta_k$ with $\omega_{\mathrm{MRT}} = \mathbf{g}_k^T\sum_{\substack{i=1\\ i\neq k}}^{K}\sqrt{P_{i,\mathrm{com}}}\breve{\mathbf{g}}_i d_i\left[l\right]$ is the inter-user interference, where $\breve{\mathbf{g}}_i = \mathbf{g}_i^{*}/\left\|\mathbf{g}_i\right\|$. To find the statistical distribution of $\tilde{\omega}_{\mathrm{MRT}}$, we first evaluate the statistical properties of ω_{MRT}. Towards this goal, let us define new variables as $\tilde{v}_{k,i} = \sqrt{P_{i,\mathrm{com}}}\frac{t_{k,i}}{z_i}$, $z_i = \left\|\mathbf{g}_i\right\| \triangleq \sqrt{\sum_{n_c=1}^{N_C}\left|\mathbf{g}_{i,n_c}\right|^2}$, and $t_{k,i} = \sum_{n_c=1}^{N_C} d_i\left[l\right]\mathbf{g}_{k,n_c}^T\mathbf{g}_{i,n_c}^{*}\forall i\neq k$, and thus ω_{MRT} can be written as

$$\omega_{\mathrm{MRT}} = \sum_{\substack{i=1\\ i\neq k}}^{K}\sqrt{P_{i,\mathrm{com}}}\frac{\sum_{n_c=1}^{N_C} d_i\left[l\right]\mathbf{g}_{k,n_c}^T\mathbf{g}_{i,n_c}^{*}}{\left\|\mathbf{g}_i\right\|} = \sum_{\substack{i=1\\ i\neq k}}^{K}\tilde{v}_{k,i}. \tag{5.29}$$

As shown in Appendix I, with the aid of the central limit theorem (CLT), the density of $\tilde{v}_{k,i}$ can be approximated as a complex Gaussian distribution, $\tilde{v}_{k,i} \sim \mathcal{CN}\left(0, 2P_{i,\mathrm{com}}\sigma_v^2\right)$, and thus $\omega_{\mathrm{MRT}} \sim \mathcal{CN}\left(0, 2\sigma_v^2\sum_{\substack{i=1\\ i\neq k}}^{K}P_{i,\mathrm{com}}\right)$. Therefore, the equivalent inter-user and radar interference plus noise $\tilde{\omega}_{\mathrm{MRT}} \sim \mathcal{CN}\left(0, 2\sigma_{\omega}^2\right)$ where $\sigma_{\omega}^2 = \sigma_v^2\sum_{\substack{i=1\\ i\neq k}}^{K}P_{i,\mathrm{com}} + \sigma_{\eta}^2$ with $\sigma_{\eta}^2 = P_{\mathrm{rad}}\sigma_f^2 + \sigma_n^2$. Fig. 5.2 compares the density functions obtained by approximation (Aprx) with the actual distributions obtained by simulation (Sim) for different values of the number of communication antennas N_C, where the total number of the BS antennas is fixed at $N = 30$. Binary phase shift keying (BPSK) is considered in this figure with $\frac{P_T}{\sigma_n^2} = 10$ dB, $P_{\text{rad}} = 0.3$ units and the number of CUEs is $K = 2$. It is worth noting that the legends for Fig. 5.2 a) and Fig. 5.2 b) are similar, as well as, the legend of Fig. 5.2 d) is the same as Fig. 5.2 c). Since the variables $t_{k,i}$, $\tilde{v}_{k,i}$ and $\tilde{\omega}_{\text{MRT}}$ are complex and symmetric, we plot the real components of the random variables as the imaginary parts have distributions identical to the real parts. As can noted from the figure, the accuracy of CLT considered to approximate the PDF of $t_{k,i}$ starts improving as N_C increases. More specifically, the approximated PDF converges to simulations for $N_C > 8$. It can be also observed from Fig. 5.2 b) that the Gaussian approximation used in Appendix I to approximate the Chi squared distributed random variable z_i is very accurate for $N_C > 4$. As can be seen from Fig. 5.2 b), unlike the other three subfigures, the mean value of z_i increases as N_C increases which can be attributed to the fact that z_i is the envelope of the sum of the power gains of a number of N_C independent paths according to the definition of z_i above (5.29). On the other hand, it can be observed from Fig. 5.2 a) that the mean value of $t_{k,i}$ is 0 since it is a sum of i.i.d random variables with zero mean, and so are $\tilde{v}_{k,i}$ and $\tilde{\omega}_{\text{MRT}}$ as seen from Fig. 5.2 c) and Fig. 5.2 d). Interestingly, as can be depicted from Fig. 5.2 c) and Fig. 5.2 d), the variance of $\tilde{v}_{k,i}$ and $\tilde{\omega}_{\text{MRT}}$ is independent of N_C because, according to their definition, each term is normalized by $\|\mathbf{g}_i\|$ which cancels the impact of N_C. Interestingly, Fig. 5.2 c) and Fig 5.2 d) show that the distributions of $\tilde{v}_{k,i}$ and $\tilde{\omega}_{\text{MRT}}$ are independent of the number of antennas N_C and the approximated densities perfectly captures the characteristics of these random variables.

Since the distribution of $\tilde{\omega}_{\text{MRT}}$ is accurately approximated as a Gaussian density function, **Corrolary 1** can be employed and then the expected value with respect to $\|\mathbf{g}_k\|^2$ is evaluated. Consequently, the KLD for MRT with vector based normalization can be found as

$$\text{KLD}_{k,\text{NIMRT,avg}} = \frac{P_{k,\text{com}}}{2\sigma_\omega^2 M (M-1) \ln 2} \lambda \mathbb{E}\left[\|\mathbf{g}_k\|^2\right] = \frac{\lambda \sigma_g^2}{\sigma_\omega^2 M (M-1) \ln 2} N_C P_{k,\text{com}}, \tag{5.30}$$

where the fact that $\|\mathbf{g}_k\|^2 \sim \text{Gamma}\left(N_C, 2\sigma_g^2\right)$ is used to evaluate $\mathbb{E}\left[\|\mathbf{g}_k\|^2\right]$.

5.4 Relation Between ZF-KLD and SER

For the sake of completeness, in this section we compare the commonly used SER performance evaluation metric with the KLD metric. Towards this purpose, we consider the ZF precoding scheme with instantaneous matrix based power normalization whose received signal is given in (5.24). The SER of most standard modulation schemes, such as MPSK, MPAM, rectangular and nonrectangular MQAM, under AWGN channel can be generally approximated as [76, Table 6.1, pp. 180],

$$\text{SER}_{\text{IZF}|\tilde{\alpha}_{\text{ZF}}} = AQ\left(\sqrt{B\gamma_{\text{IZF}|\tilde{\alpha}_{\text{ZF}}}}\right), \tag{5.31}$$

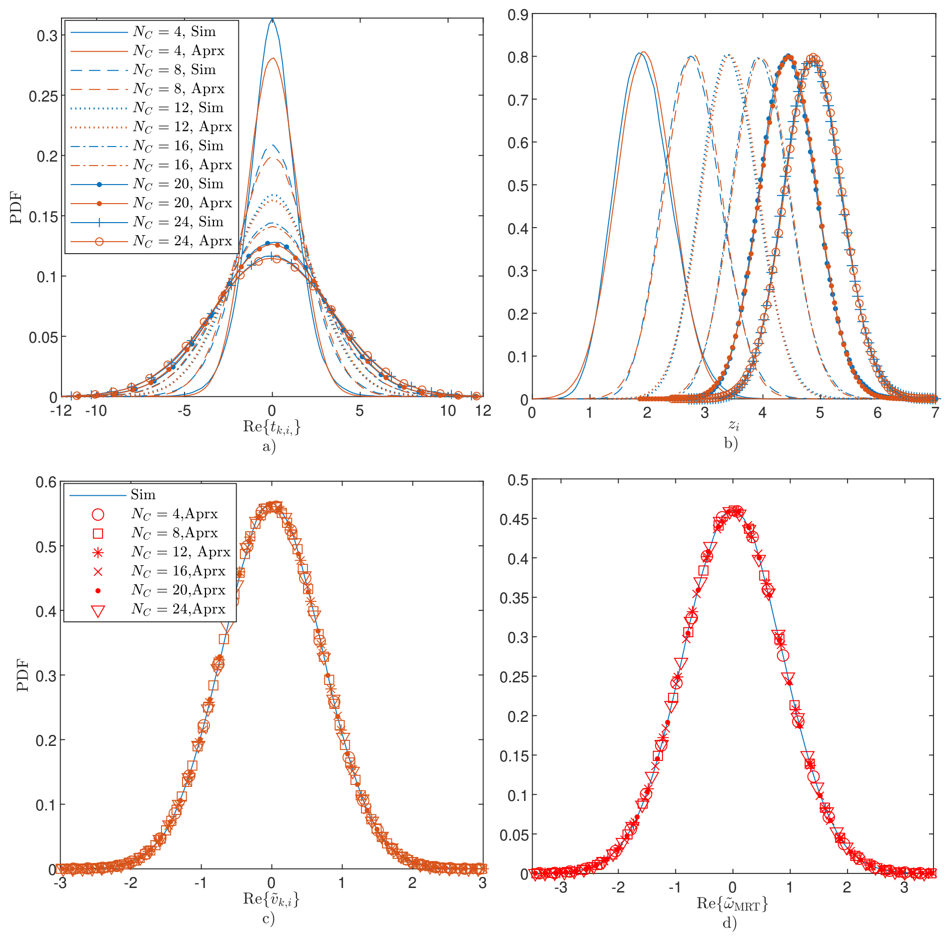

Figure 5.2: The density functions of the approximated random variables: a) The PDF of the real part of $t_{i,k}$, b) The PDF of z_i, c) The PDF of the real part of $\tilde{v}_{i,k}$, and d) The PDF of the real part of interference plus SNR $\tilde{\omega}_{\mathrm{MRT}}$.

where $\gamma_{\mathrm{IZF}|\tilde{\alpha}_{\mathrm{ZF}}} \triangleq \frac{P_{k,\mathrm{com}}}{2\sigma_\eta^2}\tilde{\alpha}_{\mathrm{ZF}}^2$ and $\mathrm{SER}_{\mathrm{IZF}|\tilde{\alpha}_{\mathrm{ZF}}}$ denote the instantaneous SNR and SER, respectively, of an IMZF based precoding system conditioned on $\tilde{\alpha}_{\mathrm{ZF}}$, $Q(\cdot)$ is the tail distribution function of the standard normal distribution, i.e., the Q-function, and the values of A and B are dependent on the modulation scheme and order. Consequently, by comparing (5.25) with (5.31), the KLD in (5.25) can be written in terms of $\mathrm{SER}_{\mathrm{LTZF}|\tilde{\alpha}_{\mathrm{ZF}}}$ as

$$\mathrm{KLD}_{\mathrm{IZF}|\tilde{\alpha}_{\mathrm{ZF}}} = \frac{\lambda}{M(M-1)\ln 2}\frac{1}{B}\left(Q^{-1}\left(\frac{\mathrm{SER}_{\mathrm{IZF}|\tilde{\alpha}_{\mathrm{ZF}}}}{A}\right)\right)^2, \tag{5.32}$$

where $Q^{-1}(\cdot)$ is the inverse Q-function. On the other hand, the average SER can be evaluated by averaging $\mathrm{SER}_{\mathrm{IZF}|\tilde{\alpha}_{\mathrm{ZF}}}$ over the PDF of $\tilde{\alpha}_{\mathrm{ZF}}$, which can be written as

$$\mathrm{SER}_{\mathrm{IZF}} = A\int_0^\infty Q\left(\sqrt{\frac{BP_{k,\mathrm{com}}}{2\sigma_\eta^2}}\tilde{\alpha}_{\mathrm{ZF}}\right) f_{\tilde{\alpha}_{\mathrm{ZF}}}(\tilde{\alpha}_{\mathrm{ZF}})\, d\tilde{\alpha}_{\mathrm{ZF}}. \tag{5.33}$$

By substituting the PDF of $\tilde{\alpha}_{\mathrm{ZF}}$ provided in (5.19) and rewriting the Q-function in terms of the complementary error function erfc, i.e., $Q(x) = \frac{1}{2}\mathrm{erfc}\left(\frac{1}{\sqrt{2}}x\right)$, $\mathrm{SER}_{\mathrm{IZF}}$ can be expressed as

$$\mathrm{SER}_{\mathrm{IZF}} = \frac{A}{\Gamma(N_C-K+1)}\int_0^\infty \tilde{\alpha}_{\mathrm{ZF}}^{2(N_C-K)+1}\mathrm{e}^{-\tilde{\alpha}_{\mathrm{ZF}}^2}\mathrm{erfc}\left(\sqrt{\frac{BP_{k,\mathrm{com}}}{4\sigma_\eta^2}}\tilde{\alpha}_{\mathrm{ZF}}\right) d\tilde{\alpha}_{\mathrm{ZF}}, \tag{5.34}$$

which can be solved using [65, 2.8.5.6, pp. 104] as

$$\mathrm{SER}_{\mathrm{IZF}} = A\left(\frac{1}{2} - \frac{\Gamma(N_C-K+1.5)}{\Gamma(N_C-K+1)}\sqrt{\frac{BP_{k,\mathrm{com}}}{4\pi\sigma_\eta^2}}\,{}_2F_1\left([0.5, N_C-K+1.5]\,; 1.5; -\frac{BP_{k,\mathrm{com}}}{4\sigma_\eta^2}\right)\right), \tag{5.35}$$

where ${}_2F_1([\,\cdot\,,\,\cdot\,];\cdot\,;\cdot)$ is the Gaussian, or ordinary, hypergeometric function. By comparing $\mathrm{SER}_{\mathrm{IZF}|\tilde{\alpha}_{\mathrm{ZF}}}$ with the average KLD in (5.27), it is more convenient to rewrite $\mathrm{SER}_{\mathrm{IZF}|\tilde{\alpha}_{\mathrm{ZF}}}$ as a function of KLD. Therefore, by using (5.27), we obtain $\frac{P_{k,\mathrm{com}}}{2\sigma_\eta^2} = \frac{M(M-1)\ln 2}{\lambda(N_C-K+1)}\mathrm{KLD}_{\mathrm{IZF,avg}}$, and thus $\mathrm{SER}_{\mathrm{IZF}}$ can be rewritten as

$$\begin{aligned}\mathrm{SER}_{\mathrm{IZF}} = A\Bigg(&\frac{1}{2} - \frac{\Gamma(N_C-K+1.5)}{\Gamma(N_C-K+1)}\sqrt{\frac{B\tilde{\lambda}}{2\pi}\mathrm{KLD}_{\mathrm{IZF,avg}}}\\ &\times {}_2F_1\left([0.5, N_C-K+1.5]\,; 1.5; -\frac{B}{2}\tilde{\lambda}\mathrm{KLD}_{\mathrm{IZF,avg}}\right)\Bigg),\end{aligned} \tag{5.36}$$

where $\tilde{\lambda} = \frac{M(M-1)\ln 2}{(N_C-K+1)\lambda}$.

5.5 Radar System with Multiple Targets

For the radar subsystem, we consider the case in which targets are spatially separated such that each target is in a distinct radar bin [41, 66, 67]. It is worth noting that some separation algorithms have been proposed in the literature to separate signals associated with individual targets in the case of unresolvable targets, and thus estimating the number of targets can be achieved accordingly, [38–40]. We assume that the number of possibly existing targets in the environment is known at BS, however, a simple counting method can be performed by employing the detection process in this paper on all radar angular-range-Doppler bins and then counting the number of detected targets. Additionally, we consider that MIMO radar is able to generate multiple beams simultaneously by considering a linear combination of multiple orthogonal signals [21, 68–70]. Let $\Phi = [\phi_1, \phi_2, \cdots, \phi_T]^T$ be a set of T orthonormal baseband waveforms, κ_t with $\sum_{t=1}^{T} \kappa_t = 1$ is a power allocation factor which is used to control the amount of power to be emitted towards a certain target, and $\mathbf{w}_{\mathrm{rad},t}[l] \in \mathbb{C}^{N_R \times 1}, t = \{1, 2, \cdots, T\}$ is a weight vector at the lth signalling period, then the transmitted signals vector at the output of transmitting antennas can be represented as

$$\tilde{\mathbf{s}}_l = \sqrt{\frac{P_{t,\mathrm{rad}}}{N_R}} \sum_{t=1}^{T} \sqrt{\kappa_t} \mathbf{w}_{\mathrm{rad},t} \phi_t = \sqrt{\frac{P_{t,\mathrm{rad}}}{N_R}} \mathbf{W}_{\mathrm{rad}} \operatorname{diag}(\bar{\kappa}) \ \Phi, \tag{5.37}$$

where $\bar{\kappa} \in \mathbb{C}^{1 \times T} = \left[\sqrt{\kappa_1}, \sqrt{\kappa_2}, \cdots, \sqrt{\kappa_T}\right]$ with $\|\bar{\kappa}\|^2 = 1$ is the power allocation vector that is used to control the portion of power emitted towards each target, and $\mathbf{W}_{\mathrm{rad}}[l] \in \mathbb{C}^{N_R \times T} = [\mathbf{w}_{\mathrm{rad},1}[l], \mathbf{w}_{\mathrm{rad},2}[l], \cdots, \check{\mathbf{w}}_{\mathrm{rad},T}[l]]$ with $\mathbf{w}_{\mathrm{rad},t}[l] \in \mathbb{C}^{N_R \times 1}$ is the precoding matrix. In general, the precoding vectors $\mathbf{w}_{\mathrm{rad},t}[l] \, \forall t$ can be designed to optimize the radar subsystem performance or satisfy some desired radar covariance matrix; for example, a radar covariance matrix of $\mathbf{R}_{\mathbf{w}} \triangleq \frac{1}{L} \mathbf{W}_{\mathrm{rad}} \times \mathbf{W}_{\mathrm{rad}}^H = \mathbf{I}_{N_R \times N_R}$ is typically used for omnidirectional radar. Using this signal waveform design for the radar subsystem, the receiver can apply a set of matched filters to separate the signals reflected by different targets by matched-filtering the received signals $\mathbf{y}_{\mathrm{rad}}(t)$ to signal waveforms $\phi_t \forall t = \{1, 2, \cdots, T\}$. Consequently, after matched-filtering $\mathbf{y}_{\mathrm{rad}}$ under hypothesis H_1, the target existence scenario, using the corresponding ϕ_t, the received signal vector in baseband in (5.5) can be rewritten as

$$\mathbf{y}_{\mathrm{rad},t|H_1}[l] = \sqrt{\frac{\kappa_t P_{\mathrm{rad}}}{N_R}} \alpha_t \mathbf{a}_{\mathrm{R}}(\theta_t) \mathbf{a}_{\mathrm{T}}(\theta_t)^T \mathbf{w}_{\mathrm{rad},t} + \mathbf{G}_{\mathrm{rad}} \mathbf{d}_{\mathbf{w}}[l] + \mathbf{n}_{\mathrm{rad}}[l], \tag{5.38}$$

where the last equality is obtained using the fact that $\phi_t \forall t = \{1, 2, \cdots, T\}$ are orthonormal waveforms. Interestingly, as can be observed from the received signal form, the interference and noise free part of $\mathbf{y}_{\mathrm{rad},t}[l] \in \mathbb{C}^{N_R \times 1}$ is a function of the parameters of target t only, and thus targets can be resolved and detected independently of each other.

By employing IC to cancel out or reduce the amount of interference caused by the communication signals reflected by the environment and noting that we consider imperfect cancellation due to channel estimation errors of $\mathbf{G}_{\mathrm{err}}$, then the received signal vector under hypothesis H_1 can be represented as

$$\check{\mathbf{y}}_{\mathrm{rad},t|H_1}[l] = \sqrt{\frac{\kappa_t P_{\mathrm{rad}}}{N_R}} \alpha_t \mathbf{A}(\theta) \mathbf{w}_{\mathrm{rad},t} + \omega_{\mathrm{rad}}[l] + \mathbf{n}_{\mathrm{rad}}[l], \tag{5.39}$$

where $\omega_{\mathrm{rad}}[l] \in \mathbb{C}^{N_R \times 1} \triangleq \mathbf{G}_{\mathrm{err}} \mathbf{d}_{\mathbf{w}}[l] = \mathbf{G}_{\mathrm{err}} \sum_{i=1}^{K} \sqrt{p_i} \mathbf{w}_i d_i[l]$ represents the residue of the communication signal after implementing IC. By assuming that the statistics of channel estimation errors follow a Gaussian distribution [71, 72], i.e., each entry of $\mathbf{G}_{\mathrm{err}}$ is $\mathcal{CN}\left(0, 2\sigma_{\mathrm{err}}^2\right)$ where $2\sigma_{\mathrm{err}}^2$ is the variance of the channel estimator, and noting that every element in ω_{rad} is a sum of independent KN_C random variables, the CLT can be applied to approximate the density of the elements of ω_{rad} for large KN_C. Consequently, the errors caused by imperfect IC are approximately complex Gaussian distributed, $\omega_{\mathrm{rad}} \sim \mathcal{CN}\left(0, 2\sigma_{\omega}^2 \mathbf{I}_{N_R}\right)$ with $\sigma_{\omega}^2 = \sigma_{\mathrm{err}}^2 \sigma_{\mathrm{w}}^2 N_C \times \sum_{i=1}^{K} P_{i,\mathrm{com}}$ where σ_{w}^2 is the variance of the elements of $\mathbf{w}_i$. Hence, the received signal can be expressed as

$$\check{\mathbf{y}}_{\mathrm{rad},t|H_1}[l] = \sqrt{\frac{\kappa_i P_{\mathrm{rad}}}{N_R}} \alpha_t \mathbf{A}(\theta_t) \mathbf{w}_{\mathrm{rad},t} + \tilde{\omega}_{\mathrm{rad}}[l], \tag{5.40}$$

where $\tilde{\omega}_{\mathrm{rad}}[l] \triangleq \omega_{\mathrm{rad}} + \mathbf{n}_{\mathrm{rad}}[l] \sim \mathcal{CN}\left(0, 2\sigma_{\tilde{\omega}}^2 \mathbf{I}_{N_R}\right)$ with $\sigma_{\tilde{\omega}}^2 = \sigma_{\omega}^2 + \sigma_n^2$.

On the other hand, under null hypothesis H_0, i.e., the target absence scenario, the received signals consist of the residues of imperfect IC and AWGN, consequently, the received signals vector is

$$\check{\mathbf{y}}_{\mathrm{rad}|H_0}[l] = \tilde{\omega}_{\mathrm{rad}}[l]. \tag{5.41}$$

After collecting a number of L snapshots, the received signal matrix can be formulated as

$$\check{\mathbf{Y}}_{\mathrm{rad},t|H_1} = \sqrt{\frac{\kappa_i P_{\mathrm{rad}}}{N_R}} \alpha_t \mathbf{a}_{\mathrm{R}}(\theta_t) \mathbf{a}_{\mathrm{T}}(\theta_t)^T \mathbf{W}_{\mathrm{rad},t} + \mathbf{\Omega}_{\mathrm{rad}} \tag{5.42}$$

$$\check{\mathbf{Y}}_{\mathrm{rad},t|H_0} = \mathbf{\Omega}_{\mathrm{rad}}, \tag{5.43}$$

where $\tilde{\mathbf{W}}_{t,\mathrm{rad}} \in \mathbb{C}^{N_R \times L} = [\mathbf{w}_{t,\mathrm{rad}}[1], \mathbf{w}_{t,\mathrm{rad}}[2], \cdots, \mathbf{w}_{t,\mathrm{rad}}[L]]$ and $\mathbf{\Omega}_{\mathrm{rad}} \in \mathbb{C}^{N_R \times L} = [\tilde{\omega}_{t,\mathrm{rad}}[1], \tilde{\omega}_{t,\mathrm{rad}}[2], \cdots, \tilde{\omega}_{t,\mathrm{rad}}[L]]$. By noting that $\check{\mathbf{y}}_{\mathrm{rad},t|H_1}[l] \sim \mathcal{CN}\left(\sqrt{\frac{\kappa_i P_{\mathrm{rad}}}{N_R}} \alpha_t \mathbf{A}(\theta_t) \mathbf{w}_{\mathrm{rad},t}[l], 2\sigma_{\tilde{\omega}}^2 \mathbf{I}_{N_R}\right)$, the log-likelihood function of the received signal matrix $\check{\mathbf{Y}}_{\mathrm{rad},t|H_1}$ can be obtained as

$$\begin{aligned} \ln\left(f\left(\check{\mathbf{Y}}_{\mathrm{rad},t|H_1}; \alpha_t, \theta_t\right)\right) &= -N_R L \ln\left(\pi \sigma_{\tilde{\omega}}^2\right) \\ &\quad - \frac{1}{2\sigma_{\tilde{\omega}}^2} \sum_{l=1}^{L} \left\| \check{\mathbf{y}}_{\mathrm{rad},t|H_1}[l] - \sqrt{\frac{\kappa_i P_{\mathrm{rad}}}{N_R}} \alpha_t \mathbf{A}(\theta_t) \mathbf{w}_{\mathrm{rad},t}[l] \right\|^2. \end{aligned} \tag{5.44}$$

By evaluating the squared norm and neglecting the terms which do not affect the estimation process, the sufficient statistic matrix can be formulated as

$$\tilde{\mathbf{E}}_t = \frac{1}{L} \sum_{l=1}^{L} \check{\mathbf{y}}_{\mathrm{rad},t|H_1}[l] \mathbf{w}_{\mathrm{rad},t}^H[l], \tag{5.45}$$

which, after extracting the independent sufficient statistics, can be simplified to [20, Eq. 15],

$$\mathbf{e}_t = \alpha_t \mathbf{d}_{\mathbf{w}} \left(\theta_t\right) + \tilde{\mathbf{n}}, \tag{5.46}$$

where $\mathbf{d}_{\mathbf{w}} \left(\theta_t\right) = \operatorname{vec}\left\{\mathbf{A} \left(\theta_t\right) \mathbf{U} \mathbf{\Lambda}^{1/2}\right\}$ with $\breve{\mathbf{w}}_{\mathrm{rad},t} [l] = \mathbf{\Lambda}^{-1/2} \mathbf{U}^H \mathbf{w}_{\mathrm{rad},t} [l]$ denotes the equivalent array steering vector which is a function of the signal correlation matrix, and $\tilde{\mathbf{n}} = \dfrac{1}{L} \operatorname{vec}\left\{\sum_{l=1}^{L} \tilde{\omega}_{\mathrm{rad}} [l] \, \breve{\mathbf{w}}^H_{\mathrm{rad},t} [l]\right\} \sim \mathcal{CN}\left(0, 2\sigma^2_{\tilde{\omega}} \mathbf{I}_{N_R}\right)$. Consequently, the generalized likelihood ratio test (GLRT) can be formulated as $\xi\left(\theta_t\right) \underset{H_0}{\overset{H_1}{\lessgtr}} \tau$, where τ is a detection threshold which, according to Neyman-Pearson test, is determined by fixing the false alarm rate at a fixed value, and $\xi\left(\theta_t\right)$ is the generalized likelihood ratio function and given by [73, Ch. 6.5]

$$\xi\left(\theta_t\right) \triangleq \ln\left(\arg\max_{\theta_t,\alpha_t} f\left(\mathbf{e}_t; \alpha_t, \theta_t, H_1\right) / \arg\max_{\theta_t,\alpha_t} f\left(\mathbf{e}_t; H_0\right)\right) = \ln\left(f\left(\mathbf{e}_t; \hat{\alpha}_t, \hat{\theta}_t, H_1\right) / f\left(\mathbf{e}_t; H_0\right)\right), \tag{5.47}$$

where $\left\{\hat{\alpha}_t, \hat{\theta}_t\right\}$ are the maximum likelihood estimates of the target parameters, which can be evaluated as

$$\left\{\hat{\alpha}_t, \hat{\theta}_t\right\} = \arg\max_{\theta_t,\alpha_t} f\left(\mathbf{e}_t; \alpha_t, \theta_t, H_1\right) = \arg\min_{\theta_t,\alpha_t} \left\|\mathbf{e}_t - \alpha_t \mathbf{d}_{\mathbf{w}}\left(\theta_t\right)\right\|^2. \tag{5.48}$$

The generalized likelihood ratio function $\xi\left(\theta_t\right)$ can be derived as [20, Eq. 36]

$$\xi\left(\theta_t\right) = \left|\mathbf{a}_{\mathrm{R}}\left(\hat{\theta}_t\right)^H \tilde{\mathbf{E}}_t \mathbf{a}_{\mathrm{T}}\left(\hat{\theta}_t\right)\right|^2 / \left(N_R \mathbf{a}_{\mathrm{R}}\left(\hat{\theta}_t\right)^H \mathbf{R}_t^T \mathbf{a}_{\mathrm{T}}\left(\hat{\theta}_t\right)\right), \tag{5.49}$$

where $\mathbf{R}_t = \frac{1}{L}\sum_{l=1}^{L} \mathbf{w}_{t,\mathrm{rad}} [l] \, \mathbf{w}^H_{t,\mathrm{rad}} [l]$. After substituting for $\tilde{\mathbf{E}}_t$ as given in (5.45), $\xi\left(\theta_t\right)$ can be written as

$$\xi\left(\theta_t\right) = \left|\mathbf{a}_{\mathrm{R}}\left(\hat{\theta}_t\right)^H \frac{1}{L}\sum_{l=1}^{L} \breve{\mathbf{y}}_{\mathrm{rad},t|H_1} [l] \, \mathbf{w}^H_{\mathrm{rad},t} [l] \, \mathbf{a}_{\mathrm{T}}\left(\hat{\theta}_t\right)\right|^2 / \left(N_R \mathbf{a}_{\mathrm{R}}\left(\hat{\theta}_t\right)^H \mathbf{R}_t^T \mathbf{a}_{\mathrm{T}}\left(\hat{\theta}_t\right)\right). \tag{5.50}$$

Thereafter, by using the law of large numbers, it can be deduced that at $L \longrightarrow \infty$, the estimators of α_t and θ_t are asymptotically consistent estimators, thus $\hat{\theta}_t \overset{asymp.}{\longrightarrow} \theta_t$ and $\hat{\alpha}_t \overset{asymp.}{\longrightarrow} \alpha_t$. Consequently, by substituting for $\breve{\mathbf{y}}_{\mathrm{rad},t|H_1}$ using (5.40) and considering orthogonal signal waveforms with $\mathbf{R}_t = \mathbf{I}_{N_R}$, $\xi\left(\theta_t\right)$ can be reduced to

$$\xi\left(\theta_t\right) = \left|\left(\sqrt{\frac{\kappa_i P_{\mathrm{rad}}}{N_R}} \alpha_t \mathbf{a}_{\mathrm{T}}\left(\theta_t\right)^T \mathbf{R}_t \mathbf{a}_{\mathrm{T}}\left(\hat{\theta}_t\right) + \breve{n}\right)\right|^2,$$

where $\breve{n} \sim \mathcal{CN}\left(0, 2\sigma^2_{\tilde{\omega}}\right)$. Obviously, by using the fact that the squared amplitude of a complex Gaussian distributed random variable is Chi-squared distributed, the sufficient statistics of $\xi\left(\theta_k\right)$ is [20, Eq. 37], [33, Eq. 54], [73, Ch. 6.5]

$$\xi\left(\theta_t\right) \sim \begin{cases} H_1 : \mathcal{X}_2^2\left(\lambda_t\right) \\ H_0 : \mathcal{X}_2^2\left(0\right) \end{cases}, \tag{5.51}$$

where $\mathcal{X}_2^2(\lambda_t)$ denotes a noncentral Chi-squared random variable with 2 degrees of freedom and a noncentrality parameter of $\lambda_t = \frac{|\alpha_t|^2}{\sigma_{\tilde{\omega}}^2}\frac{\kappa_t P_{\mathrm{rad}}}{N_R}\left|\mathbf{a}^H(\theta_t)\mathbf{R}_t\mathbf{a}(\theta_t)\right|^2$, which for orthogonal waveforms (e.g. $\mathbf{R}_t = \mathbf{I}_{N_R}$ where $\mathbf{I}_{N_R}$ is an $N_R \times N_R$ identity matrix), can be reduced to $\lambda_t = \frac{|\alpha_t|^2}{\sigma_{\tilde{\omega}}^2}\kappa_t N_R P_{\mathrm{rad}}$.

5.5.1 KLD from ξ_{H_1} to ξ_{H_0}

By using **Definition 1**, noting that noncentral Chi-squared random variables are strictly positive, substituting $f_\xi(\xi|H_0) = \frac{1}{2}\mathrm{e}^{-0.5\xi}$ and $f_\xi(\xi|H_1) = \frac{1}{2}\mathrm{e}^{-0.5(\xi+\lambda_t)}I_0\left(\sqrt{\lambda_t\xi}\right)$, and using the logarithmic identity $\log_2 x = \frac{\ln x}{\ln 2}$, the relative information from ξ_{H_1} to ξ_{H_0} can be derived as

$$\mathrm{KLD}\left(\xi_{H_0} \parallel \xi_{H_1}\right) = \int_0^\infty f_\xi(\xi|H_0)\log_2\left(\frac{f_\xi(\xi|H_0)}{f_\xi(\xi|H_1)}\right)d\xi = \frac{1}{2\ln 2}\int_0^\infty \mathrm{e}^{-0.5\xi}\ln\left(\frac{1}{\mathrm{e}^{-0.5\lambda_t}I_0\left(\sqrt{\lambda_t\xi}\right)}\right)d\xi. \tag{5.52}$$

Thereafter, using the logarithmic identities $\log_a\left(\frac{x}{y}\right) = \log_a x - \log_a y$ and $\log_a(xy) = \log_a x + \log_a y$, and noting that $\ln(1) = 0$, $\ln(\mathrm{e}^x) = x$ and $\int_0^\infty \mathrm{e}^{-0.5\xi} = 2$, $\mathrm{KLD}\left(\xi_{H_0} \parallel \xi_{H_1}\right)$ can be written as

$$\begin{aligned}\mathrm{KLD}\left(\xi_{H_0} \parallel \xi_{H_1}\right) &= \frac{1}{2}\left(\frac{0.5\lambda_t}{\ln 2}\int_{-\infty}^{\infty}\mathrm{e}^{-0.5\xi}d\xi - \frac{1}{\ln 2}\int_{-\infty}^{\infty}\mathrm{e}^{-0.5\xi}\ln\left(I_0\left(\sqrt{\lambda_t\xi}\right)\right)d\xi\right)\\ &= \frac{1}{2}\left(1.4427\lambda_t - \frac{1}{\ln 2}\int_0^\infty \mathrm{e}^{-0.5\xi}\ln\left(I_0\left(\sqrt{\lambda_t\xi}\right)\right)\right)d\xi.\end{aligned} \tag{5.53}$$

To be able to solve the integral, we make use of the infinite series representation of the modified Bessel function $I_0(x)$ for $0 \le x \le 1$, and an asymptotic approximation for $I_0(x)$ which is very accurate for $x > 1$. It is worth noting that since $I_0(x)$ is sharply increasing as x increases, thus the computation of the infinite series representation is very costly for large values of x. Therefore, the infinite series representation of $I_0(x)$ is employed for small values of x, i.e., $0 \le x \le 1$, while an efficient asymptotic approximation with high accuracy is invoked when $x > 1$ [74, Eq. 9.7.1, pp. 377]. Using the infinite series representation, $I_0\left(\sqrt{\lambda_t\xi}\right)$for $0 \le \xi \le \frac{1}{\lambda_t}$(e.g. the Bessel function argument $x \in [0, 1]$) can be written as [74, Eq. 9.6.10, pp. 375],

$$I_0\left(\sqrt{\lambda_t\xi}\right) = 1 + \sum_{l=1}^{\infty}\frac{\lambda_t^l}{2^{2l}(l!)^2}\xi^l, 0 \le \xi \le \frac{1}{\lambda_t}. \tag{5.54}$$

However, since this representation will be used for small values of $\lambda_t\xi$, the first few terms, i.e., two or three terms, provide a tractable solution with a very accurate approximation. On the other hand, the following approximation is used for $\xi > \frac{1}{\lambda_t}$ [74, Eq. 9.7.1, pp. 377],

$$I_0\left(\sqrt{\lambda_t\xi}\right) \simeq \frac{\exp\left(\sqrt{\lambda_t\xi}\right)}{\sqrt{2\pi}\sqrt[4]{\lambda_t\xi}}\left(1 + \sum_{q=1}^{Q}\left(\frac{1}{\left(\sqrt{\lambda_t\xi}\right)^q}\frac{\prod_{k=1}^{q}\left[(2k-1)^2\right]}{q!8^q}\right)\right), \xi > \frac{1}{\lambda_t}, \tag{5.55}$$

where the results show that using $Q = 5$ provide very accurate approximation for the considered scenarios in this paper. Consequently, by dividing the interval of the integral in (5.53) into two subintervals as discussed above, $\mathrm{KLD}\left(\xi_{H_0} \parallel \xi_{H_1}\right)$ can be given by

$$\mathrm{KLD}\left(\xi_{H_0} \parallel \xi_{H_1}\right) = \frac{1}{2}\left(1.4427\lambda_t - \frac{1}{\ln 2}\left(\mathcal{I}_1 + \mathcal{I}_2\right)\right), \tag{5.56}$$

where

$$\mathcal{I}_1 = \int_0^{\frac{1}{\lambda_t}} \mathrm{e}^{-0.5\xi} \ln\left(I_0\left(\sqrt{\lambda_t \xi}\right)\right) d\xi, \tag{5.57}$$

and

$$\mathcal{I}_2 = \int_{\frac{1}{\lambda_t}}^{\infty} \mathrm{e}^{-0.5\xi} \ln\left(I_0\left(\sqrt{\lambda_t \xi}\right)\right) d\xi. \tag{5.58}$$

By substituting the infinite series representation (5.54) in (5.57), $\mathcal{I}_1$ can be written as

$$\mathcal{I}_1 = \int_0^{\frac{1}{\lambda_t}} \mathrm{e}^{-0.5\xi} \ln\left(1 + \sum_{l=1}^{\infty} \frac{\lambda_t^l}{2^{2l}\left(l!\right)^2}\xi^l\right) d\xi. \tag{5.59}$$

Thereafter, the Taylor series expansion for $\ln(1+x)$ is invoked [75, Eq. 1.511, pp. 53]. However, by noting that for the considered range of ξ, i.e., $\xi < \frac{1}{\lambda_t}$, $\sum_{l=1}^{\infty} \frac{\lambda_t^l}{2^{2l}(l!)^2}\xi^l < 1$, using the first term of Taylor series expansion can be considered, i.e., $\ln(1+x) \approx x$ for $x < 1$. Consequently, using the fact that summation and integration are interchangeable, $\mathcal{I}_1$ can be rewritten as

$$\mathcal{I}_1 = \sum_{l=1}^{\infty} \frac{\lambda_t^l}{2^{2l}\left(l!\right)^2} \int_0^{\frac{1}{\lambda_t}} \mathrm{e}^{-0.5\xi}\xi^l d\xi, \tag{5.60}$$

which, after evaluating the integral and some mathematical manipulations, can be evaluated as

$$\mathcal{I}_1 = \sum_{l=1}^{\infty} \frac{\lambda_t^{0.5l}}{2^{1.5l-1}\left(l+1\right)\left(l!\right)^2} \mathrm{e}^{-\frac{0.25}{\lambda_t}} \mathrm{M}_{0.5l,0.5l+0.5}\left(\frac{0.5}{\lambda_t}\right), \tag{5.61}$$

where $\mathrm{M}_{\cdot,\cdot}(\cdot)$ is the Whittaker-M function.

On the other hand, substituting the approximation given by (5.55) in (5.58) yields

$$\mathcal{I}_2 \approx \sqrt{\lambda_t}\mathcal{I}_{2a} - \left(\left(\frac{1}{2}\ln(2\pi) + \frac{1}{4}\ln(\lambda_t)\right)\mathcal{I}_{2b} + \frac{1}{4}\mathcal{I}_{2c}\right) + \mathcal{I}_{2d}, \tag{5.62}$$

where the derivations of $\mathcal{I}_{2a}$, $\mathcal{I}_{2b}$, $\mathcal{I}_{2c}$ and $\mathcal{I}_{2a}$ are provided in Appendix II.

5.5.2 KLD from ξ_{H_0} to ξ_{H_1}

Similar to the previous subsection, the KLD from ξ_{H_0} to ξ_{H_1}, i.e., $\mathrm{KLD}\left(\xi_{H_1} \parallel \xi_{H_0}\right)$, can be derived with the aid of **Definition 1** as

$$\mathrm{KLD}\left(\xi_{H_1} \parallel \xi_{H_0}\right) = \int_{-\infty}^{\infty} f_\xi\left(\xi|H_1\right) \log_2\left(\frac{f_\xi\left(\xi|H_1\right)}{f_\xi\left(\xi|H_0\right)}\right) d\xi. \tag{5.63}$$

By employing the logarithmic identity $\log\left(\frac{x}{y}\right) = \log x - \log y$, substituting the PDFs of $f_\xi\left(\xi|H_0\right)$ and $f_\xi\left(\xi|H_1\right)$, and using some simple mathematical operations, $\mathrm{KLD}\left(\xi_{H_1} \parallel \xi_{H_0}\right)$ can be found as

$$\mathrm{KLD}\left(\xi_{H_1} \parallel \xi_{H_0}\right) = \frac{-0.5\lambda_t \mathrm{e}^{-0.5\lambda_t}}{2\ln 2}\mathcal{I}_3 + \frac{\mathrm{e}^{-0.5\lambda_t}}{2\ln 2}\mathcal{I}_4 = \frac{-0.5\lambda_t}{\ln 2} + \frac{\mathrm{e}^{-0.5\lambda_t}}{2\ln 2}\mathcal{I}_4, \tag{5.64}$$

where $\mathcal{I}_3 = \int_0^\infty \mathrm{e}^{-0.5\xi} I_0\left(\sqrt{\lambda_t \xi}\right) d\xi$ which has been solved using [65, Eq. 2.15.5.4, pp. 306], and $\mathcal{I}_4$ is given by

$$\mathcal{I}_4 = \int_0^\infty \mathrm{e}^{-0.5\xi} I_0\left(\sqrt{\lambda_t \xi}\right) \ln\left(I_0\left(\sqrt{\lambda_t \xi}\right)\right) d\xi. \tag{5.65}$$

Similar to the procedure applied to evaluate $\mathrm{KLD}\left(\xi_{H_0} \parallel \xi_{H_1}\right)$, the infinite series representation for the modified Bessel function and the asymptotic approximation for $0 \leq \xi \leq \frac{1}{\lambda_t}$ and $\xi > \frac{1}{\lambda_t}$, respectively. Thus the integral $\mathcal{I}_4$ can be tightly approximated as

$$\mathcal{I}_4 = \underbrace{\int_0^{\frac{1}{\lambda_t}} \mathrm{e}^{-0.5\xi} I_0\left(\sqrt{\lambda_t \xi}\right) \ln\left(I_0\left(\sqrt{\lambda_t \xi}\right)\right) d\xi}_{\mathcal{I}_{4a}} + \underbrace{\int_{\frac{1}{\lambda_t}}^\infty \mathrm{e}^{-0.5\xi} I_0\left(\sqrt{\lambda_t \xi}\right) \ln\left(I_0\left(\sqrt{\lambda_t \xi}\right)\right) d\xi}_{\mathcal{I}_{4b}}. \tag{5.66}$$

The evaluation of $\mathcal{I}_{4a}$ and $\mathcal{I}_{4a}$ is provided with details in Appendix III.

5.5.3 The Detection and False Alarm Probabilities

For the sake of completeness, this subsection compares the commonly used detection probability metric with the KLD measure. The detection and false alarm probabilities are respectively defined as

$$P_{\mathrm{D}} \triangleq \int_\tau^\infty f_\xi\left(\xi|H_1\right) d\xi = 1 - F_\xi\left(\tau|H_1\right) = Q_1\left(\sqrt{\lambda_t}, \sqrt{\tau}\right), \tag{5.67}$$

and

$$P_{\mathrm{FA}} \triangleq \int_\tau^\infty f_\xi\left(\xi|H_0\right) d\xi = 1 - F_\xi\left(\tau|H_0\right) = Q_1\left(0, \sqrt{\tau}\right) = \Gamma\left(1, 0.5\tau\right), \tag{5.68}$$

where $F_\xi\left(\xi|H_i\right) \forall i = \{0,1\}$ is the cumulative distribution function (CDF) of ξ under hypothesis H_i, $\Gamma\left(\cdot,\cdot\right)$ is the upper incomplete gamma function, $Q_1\left(\sqrt{\lambda_t}, \sqrt{\tau}\right)$ is the Marcum Q-function, and τ is a predefined threshold which according to Neyman-Pearson lemma is selected to satisfy a certain false alarm constraint, for example, $\tau = 2\Gamma^{-1}(1, P_{\mathrm{FA}})$ with $\Gamma^{-1}(1,\cdot)$ is the inverse incomplete Gamma function. Consequently, the detection probability is found as $P_{\mathrm{D}} = Q_1\left(\sqrt{\lambda_t}, \sqrt{2\Gamma^{-1}(1, P_{\mathrm{FA}})}\right)$. Therefore, by noting that $\lambda_t = \left(Q_1^{-1}\left(P_{\mathrm{D}}, \sqrt{2\Gamma^{-1}(1, P_{\mathrm{FA}})}\right)\right)^2$, the statistics of the test formulated in (5.51) can be rewritten in terms of P_{D} and P_{FA} instead of λ_t by substituting $\lambda_t = \left(Q_1^{-1}\left(P_{\mathrm{D}}, \sqrt{2\Gamma^{-1}(1, P_{\mathrm{FA}})}\right)\right)^2$ in (5.51), and thus (5.52) and (5.63) can be also rewritten as functions of P_{D} and P_{FA}. Subsequently, all KLD equations in Sec. V.A and Sec. V.B can be rewritten in terms of $\{P_{\mathrm{D}}, P_{\mathrm{FA}}\}$.

5.6 KLD for Multi-user Multi-target ISAC System

The KLD measures in the previous section have been evaluated for a single user and a single target scenario. In this section, the weighted sum method is employed to evaluate KLD for multiple CUEs and targets scenario. Accordingly, the weighted sum for the KLD of each of the subsystems $\mathrm{s} \in \{\mathrm{ZF}, \mathrm{MRT}, \mathrm{rad}\}$ which consists of a number of CUEs or targets denoted as $J \in \{K, T\}$ can be formulated as

$$\mathrm{KLD}_{\mathrm{s}} = \sum_{i=1}^{J} c_{\mathrm{s},i} \mathrm{KLD}_{i,\mathrm{s},\mathrm{avg}}, \tag{5.69}$$

where $\sum\limits_{i=1}^{J} c_i = 1$, and for equal weights of $c_i = \frac{1}{J}$, $\mathrm{KLD}_{\mathrm{s}}$ is reduced to

$$\mathrm{KLD}_{\mathrm{s}} = \frac{1}{J} \sum_{i=1}^{J} \mathrm{KLD}_{i,\mathrm{s},\mathrm{avg}}. \tag{5.70}$$

On the other hand, for an ISAC system with multiple CUEs and multiple targets, we introduce a novel performance measure referred to the weighted sum of the relative entropy (WSRE). This performance measure will be very beneficial for ISAC systems as it can be employed to assess the performance of the system holistically as one entity rather than the conventional ways which typically characterize the ISAC system as two distinct subsystems. Additionally, WSRE will be very useful for a system designer to allocate the resources of BS, for example, power and antenna allocation. For a number of K CUEs and a number of T targets, WSRE is defined as

$$\mathrm{WSRE}_{\mathrm{ISAC}} \triangleq \sum_{k=1}^{K} c_{k,\mathrm{com}} \mathrm{KLD}_{k,\mathrm{com},\mathrm{avg}} + \sum_{t=1}^{T} c_{t,\mathrm{rad}} \mathrm{KLD}_{t,\mathrm{rad}}, \tag{5.71}$$

where $\sum_{k=1}^{K} c_{k,\mathrm{com}} + \sum_{t=1}^{T} c_{t,\mathrm{rad}} = 1$. It worth noting that $c_{k,\mathrm{com}}$ and $c_{t,\mathrm{rad}}$ $\forall\{k,t\}$ are design parameters which can be chosen to give some priority for a certain subsystem, CUE or target. In some scenarios in which CUEs and targets have the equal priority, then $c_{k,\mathrm{com}} = c_{t,\mathrm{rad}} = \frac{1}{K+T} \forall\{k,t\}$. Therefore, WSRE is reduced to

$$\mathrm{WSRE}_{\mathrm{ISAC}} = \frac{1}{K+T}\left(\sum_{k=1}^{K}\mathrm{KLD}_{k,\mathrm{com,avg}} + \sum_{t=1}^{T}\mathrm{KLD}_{t,\mathrm{rad}}\right). \tag{5.72}$$

5.7 Numerical Results

This section presents the measured performance of the ISAC system introduced in this paper, which considers a multi-antenna BS that simultaneously transmits data symbols to K CUEs and aims at detecting a number of T targets. Monte Carlo simulation with 10^6 realizations for each run is used to generate the simulation (Sim.) results and the derived formulas in this paper are used to generate the theoretical performance. Unless otherwise stated, a number of 2 CUEs and a single target scenario, a number of $L = 100$ snapshots, the antenna spacing is half the wavelength, i.e., $\Delta = 0.5\lambda_0$, and the total transmit power is normalized to unity, i.e., $P_{\mathrm{T}} = 1$, are considered. The total transmit power P_{T} is distributed among both subsystems with $P_{\mathrm{C}} = P_{\mathrm{T}} - P_{\mathrm{rad}}$ is the power allocated to the communication subsystem, where P_{rad} is the allocated power for the radar subsystem. For Figs. 5.3, 5.4, 5.5, 5.6, a single target located at $\theta = 35^o$ is deployed in the environment, the radar covariance matrix is $\mathbf{R}_s = \mathbf{I}_{N_R}$, and the radar channel pathloss is normalized, i.e., $\alpha_{\mathrm{rad}} = 1$. On the other hand, a number of $T = 3$ targets with $\{\theta_1, \theta_2, \theta_3\} = \{35^o, 100^o, 160^o\}$ and $\{\alpha_{\mathrm{rad},1}, \alpha_{\mathrm{rad},2}, \alpha_{\mathrm{rad},3}\} = \{1, 0.6, 0.3\}$, in addition to a number of $K = 3$ CUEs are considered in Fig. 5.7.

Fig. 5.3 presents the impact of the interference caused from radar subsystem on CUEs and the effect of estimation errors in $\mathbf{G}_{\mathrm{rad}}$ on the detection capability of the radar receiver, where the error in $\mathbf{G}_{\mathrm{rad}}$ is modeled using the variance of channel estimator σ^2_{err}. The total number of BS antennas is 20 which are distributed evenly among the radar and communication subsystems with QPSK signalling employed to modulate CUEs data symbols. The power allocated for radar and communication services are $P_{\mathrm{rad}} = 0.1$ and $P_{\mathrm{C}} = 0.9$ unit power, respectively. Moreover, the achievable performance using IMZF precoding is compared with IVMRT scheme. The simulation results confirm the accuracy of the derived equations in this paper for $\mathrm{KLD}_{\mathrm{IZF}}$, $\mathrm{KLD}_{\mathrm{IVMRT}}$, P_e and $\mathrm{KLD}_{\mathrm{rad}}$. As can be depicted from the figure, the interference caused from a subsystem to the other limits the performance. For example, Fig. 5.3 a) shows that the probability of error for CUEs with IMZF precoding suffers from an error floor at 5×10^{-6} approximately, and $\mathrm{KLD}_{\mathrm{IZF}}$ also reaches an upper bound of about 54 bits for $\frac{P_{\mathrm{T}}}{\sigma_n^2} \gtrsim 30$ dB. On the other hand, the error floor for IVMRT scheme is $\sim 3\times10^{-4}$, and the upper bound of $\mathrm{KLD}_{\mathrm{IVMRT}}$ is almost 10 bits which is reached at $\frac{P_{\mathrm{T}}}{\sigma_n^2} \approx 20$ dB. The superiority of IMZF over IVMRT can be attributed to the fact that MRT generally suffers from inter-user-interference in addition to the interference caused by radar, and thus the total amount of interference a communication user suffers is much larger in MRT based precoding systems. As can be observed from Fig. 5.3 a), the detection capability of a communication system can be interpreted using KLD. More precisely, the relative entropy, or the KLD measure, is inversely proportional

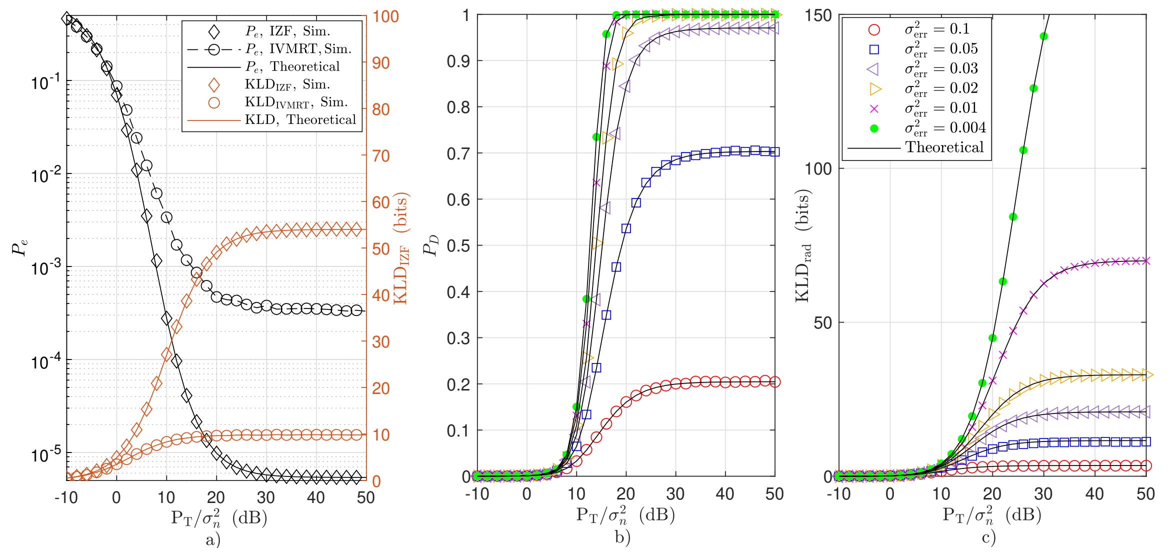

Figure 5.3: The impact of radar-to-CUs interference and the estimation errors in $\mathbf{G}_{\mathrm{rad}}$ on the performance of CUs and radar subsystem, respectively, vs. the transmit SNR P_T/σ_n^2: a) The error rate and KLD of CUs, b) The detection probability P_{D} for the radar subsystem, and c) The KLD for the radar subsystems.

to SER where higher KLD values imply lower SER and thus better detection performance. It is worth noting that there is only one curve for each performance measure in Fig. 5.3 a) because a fixed $P_{\mathrm{C}} = 0.9$ is considered in this figure and the communication subsystem is independent of σ_{err}^2. It can be also seen from Fig. 5.3 b) and Fig. 5.3 c) that the channel estimation errors in $\mathbf{G}_{\mathrm{rad}}$ have a severe effect on the performance of the radar subsystem as the detection probability and KLD significantly decrease as σ_{err}^2 increases. For example, asymptotic detection probabilities of 0.2 and 0.7 are obtained when $\sigma_{\mathrm{err}}^2 = 0.1$ and 0.05, respectively, and KLD of about 3.45 and 11.56 bits for the same values of σ_{err}^2. However, although further decrease in σ_{err}^2 results in huge enhancement for $\mathrm{KLD}_{\mathrm{rad}}$, the improvement in P_{D} is small, for example, a decrease in σ_{err}^2 from 0.01 to 0.004 improves $\mathrm{KLD}_{\mathrm{rad}}$ from 63 to 143 bits at $\frac{P_{\mathrm{T}}}{\sigma_n^2} = 30$ dB, but the improvement in P_D is almost negligible at the same $\frac{P_{\mathrm{T}}}{\sigma_n^2}$. Interestingly, by comparing Fig. 5.3 b) with Fig. 5.3 c), it can be observed that the change in the detection probability is very slow as $\frac{P_{\mathrm{T}}}{\sigma_n^2}$ goes beyond 25 dB unlike KLD that has faster growing rate, which can be attributed to the fact that the detection probability is upper bounded by 1 whereas KLD is not upper bounded.

Figs. 5.4 and 5.5 show the performance of ISAC system with IMZF data precoder for different values of P_{rad}, where σ_{err}^2 is fixed at 0.01. All other system parameters considered for the simulation environment of these figures are similar to Fig. 5.3. It worth noting that different P_{rad} values impose different interference levels at CUEs, as well as, higher P_{rad} implies that less power is allocated to communication service since the total power is fixed. It is clear from these figures that the theoretical analysis agrees with the simulation results. Additionally, it can observed from Fig. 5.4 that increasing the value of P_{rad} can significantly degrade the performance of the communication subsystem by increasing SER and decreasing $\mathrm{KLD}_{\mathrm{IZF}}$. According the results in Fig. 5.4 a), an error floor for SER is obtained even with small amounts of P_{rad}, for example, the error floor is about 5×10^{-6} and substantially increases considerably as P_{rad}

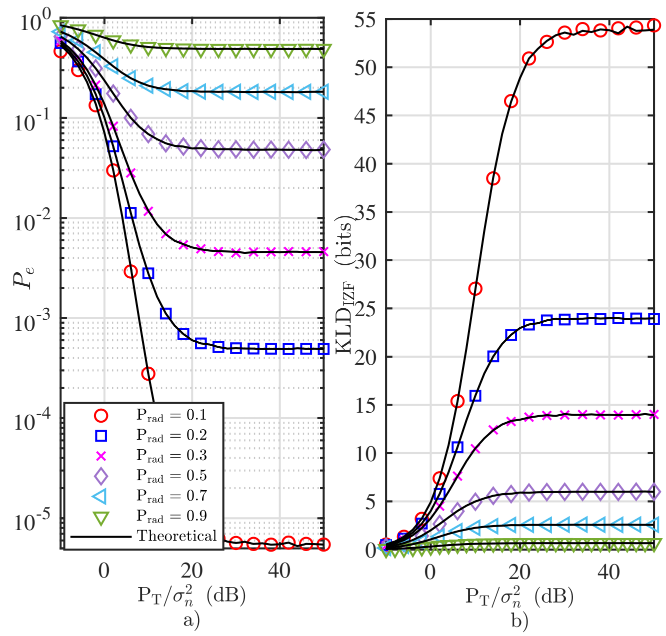

Figure 5.4: The impact of different interference levels on the CUs represented by several values of P_{rad} and plotted vs. the transmit SNR P_T/σ_n^2, where $N = 20$ with $\{N_R, N_C\} = \{10, 10\}$: a) The probability of symbols errors, and b) The KLD for CUs.

increases, for example, the error floor is more that 4.5×10^{-3} when $P_{\text{rad}} \geq 0.3$ unit power. Similarly, Fig. 5.4 b) shows that KLD_{IZF} goes below 15 bits for $P_{\text{rad}} \geq 0.3$ regardless the increase in SNR.

On the other hand, it can be noticed from Fig. 5.5 that increasing P_{rad} can boost the detection capabilities of the radar subsystem by enhancing KLD_{rad}. For example, the upper bound of KLD_{rad} with $P_{\text{rad}} = 0.3$ is about 290 bits, whereas it is 70 and 164 for $P_{\text{rad}} = 0.1$ and $P_{\text{rad}} = 0.2$, respectively.

Fig. 5.6 shows the theoretical detection performance of the communication subsystem against the detection capability of the radar subsystem. Several values for $\frac{P_{\text{T}}}{\sigma_n^2}$, $\frac{P_{\text{T}}}{\sigma_n^2} = \{0, 5, 10, 15, 20\}$ dB, a number of $N = 50$ antennas distributed evenly among both subsystems with 25 antennas each, QPSK signalling for the communication part, and a channel estimator variance of $\sigma_{\text{err}} = 0.01$ are considered in this figure. The amount of power allocated for the radar is varied over $0 < P_{\text{rad}} < 1$, and then the pairs (P_e, P_D) and $(\text{KLD}_{\text{rad}}, \text{KLD}_{\text{IZF}})$ are calculated accordingly. As can be observed from Fig. 5.6 a), both systems suffer from poor detection capabilities regardless the power allocation at $\frac{P_{\text{T}}}{\sigma_n^2} = 0$ dB. The best P_e can be obtained at this SNR level is about 10^{-3} that is obtained at $P_D = 0$, whereas the highest P_D is $\lesssim 0.8$ which occurs at $P_e \approx 1$. In terms of KLD, it can be seen from Fig. 5.6 b) that a KLD_{IZF} of 16 bits is obtained at $\text{KLD}_{\text{rad}} = 0$ and a KLD_{rad} of 13.2 bits is obtained when $\text{KLD}_{\text{IZF}} = 0$ at $\frac{P_{\text{T}}}{\sigma_n^2} = 0$ dB. On the other hand, at mid-range SNR, $\frac{P_{\text{T}}}{\sigma_n^2} = 5$ dB, the capability of the ISAC system in whole starts improving, however, only one of the two subsystems can operate efficiently at this range of SNR. For example, Fig. 5.6 a) depicts that $P_e > 10^{-3}$ is obtained for $P_D > 0.75$ when $\frac{P_{\text{T}}}{\sigma_n^2} = 5$ dB, as well as Fig. 5.6 b) shows that the highest KLD obtained for each subsystem is about 50 bits which occurs when the KLD of the other system is 0 bit at the same value of $\frac{P_{\text{T}}}{\sigma_n^2}$. Nonetheless, the detection capability of both systems is

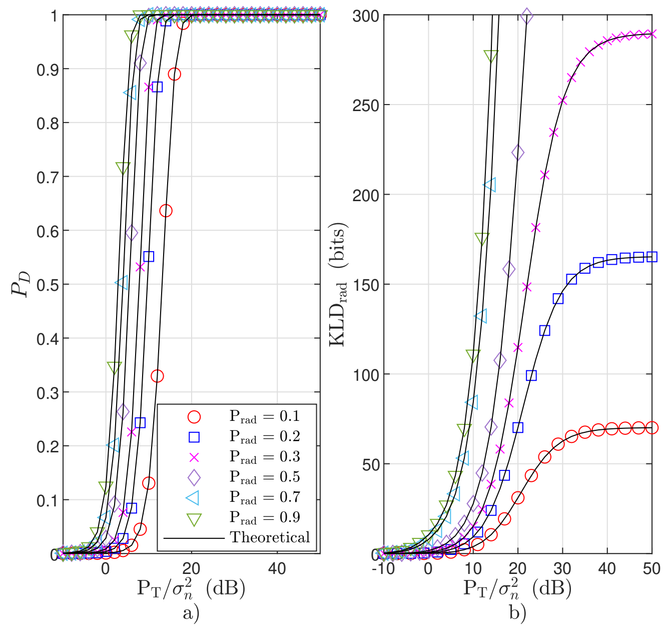

Figure 5.5: The performance of the radar system vs. the transmit SNR P_T/σ_n^2 with $\sigma_{\mathrm{err}}^2 = 0.01$ and several values of P_{rad}, where $N = 20$ with $\{N_R, N_C\} = \{10, 10\}$: a) The probability of detection, and b) The KLD for radar subsystem.

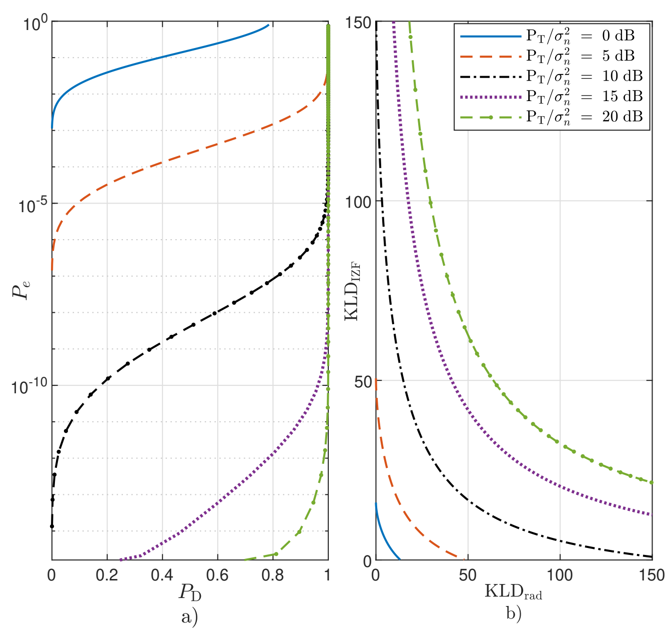

Figure 5.6: The trade-off between the radar and communication subsystems for different values of the transmit SNR $P_{\mathrm{T}}/\sigma_n^2$, where $N = 50$ with $\{N_R, N_C\} = \{25, 25\}$: a) The tradeoff between P_e and P_{D}, and b) The trade-off between $\mathrm{KLD_{IZF}}$ and $\mathrm{KLD_{rad}}$.

superior when $\frac{P_{\mathrm{T}}}{\sigma_n^2} \geq 10$ dB as a detection probability of $P_D \to 1$ can be obtained while maintaining low values for P_e if the value of P_{rad} is properly selected. On the other side, it is clear from Fig. 5.6 b) that a maximum KLD value of about 150 bits can be achieved for each subsystem when $\frac{P_{\mathrm{T}}}{\sigma_n^2} = 10$ dB. To investigate the trade-off of the KLD of the two subsystems at a fixed transmit SNR, let us consider the case of $\frac{P_T}{\sigma_n^2} = 10$ dB. As can be observed from the figure, as one of the KLDs improves, the other one becomes worse. For example, the maximum achievable KLD for each subsystem is about 150 bits which occurs when the KLD of the other subsystem deteriorates to 0.

Fig. 5.7 presents a three dimensional (3D) plot for P_e in (5.36), $\mathrm{KLD_{IZF}}$ in (5.70), P_{D} in (5.67), $\mathrm{KLD_{rad}}$ in (5.70) and $\mathrm{WSRE_{ISAC}}$ in (5.72) vs. P_{rad} and the number of allocated antennas to the radar subsystem, N_R. For this figure, three CUEs denoted as $\mathcal{U}_1, \mathcal{U}_2$ and $\mathcal{U}_3$ using BPSK, QPSK and 8PSK, respectively, and three targets denoted as $\mathcal{T}_1$, $\mathcal{T}_2$ and $\mathcal{T}_3$ with $\{\theta_1, \theta_2, \theta_3\} = \{35^o, 100^o, 160^o\}$ and $\{\alpha_{\mathrm{rad},1}, \alpha_{\mathrm{rad},2}, \alpha_{\mathrm{rad},3}\} = \{1, 0.6, 0.3\}$, are used. The values of $\frac{P_{\mathrm{T}}}{\sigma_n^2}$ and σ_{err}^2 are fixed at 10 dB and 0.01, respectively, the total number of BS antennas is fixed at $N = 50$, and N_R ranges from 1 to 49 with $N_C = N - N_R$. As can be observed from Fig. 5.7 a) and Fig. 5.7 b), SER and $\mathrm{KLD_{IZF}}$ degrade as P_{rad} and/or N_R increase as the resources allocated for the communication subsystem are reduced. Moreover, it can be seen from these two subplots that as the modulation order increases the performance of CUE becomes worse as SER increases and KLD decreases. On the other hand, P_{D} and $\mathrm{KLD_{rad}}$ improve as P_{rad} and/or N_R increase which can be clearly seen in Fig. 5.7 c) and Fig. 5.7 d). In addition, it can be also observed that the detection capability of BS substantially decreases as α_t decreases, which represents the radar cross section (RCS) of the target and the pathloss, i.e., lower α_t implies lower RCS and/or farther target. Fig. 5.7 e) presents a 3D plot for the weighted sum of KLD for both radar and communication subsystems, $\mathrm{WSRE_{ISAC}}$ in (5.72). As can be clearly observed from this subplot, there is a trade-off between the performance of the radar and the communication subsystems. For example, it can be seen from Fig. 5.7 e) that there are two local maximum points: $(P_{\mathrm{rad}}, N_R, \mathrm{KLD_{WSUM}}) \to (0, 1, 116)$ which represents the best scenario for the CUEs, and $(P_{\mathrm{rad}}, N_R, \mathrm{WSRE_{ISAC}}) \to (1, 49, 20)$ which is the best case for the radar subsystem. Although the first scenario provides the global maximum $\mathrm{WSRE_{ISAC}}$, it deteriorates the performance of the radar subsystem. On the other hand, by referring to Fig. 5.7 a) and Fig. 5.7 c), it can be realized that the SER of CUEs at $(P_{\mathrm{rad}}, N_R) \to (1, 49)$ is almost 1 and the detection probability for the radar subsystem is $P_{\mathrm{D}} = 1$. Fig. 5.7 f) shows the trade-off between $\mathrm{KLD_{rad}}$ and $\mathrm{KLD_{IZF}}$ as evaluated using (5.70) for different values of N_R, where the total number of antennas is fixed at $N = 50$. It is worth noting that the total power consumption is fixed for all the results in this figure, i.e., $\frac{P_{\mathrm{T}}}{\sigma_n^2} = 10$ dB, where the portion of power allocated for each subsystem is changed from 0% to 100% to get this trade-off. As can be noticed, for low values of $\mathrm{KLD_{rad}}$, which basically occurs when the allocated P_{rad} is very low, $\mathrm{KLD_{IZF}}$ is significantly high and increases as N_R decreases. By considering a fixed N_R value, it can be noticed that as P_{rad} increases, $\mathrm{KLD_{IZF}}$ exponentially decays until reaching very low values. It is worth noting that the intersection between different curves with different N_R is due to different P_{rad} values. For example, the intersection between the two curves associated with $N_R = 20$ and $N_R = 30$ (e.g. the black-circles line and magenta dashed line) at $(\text{KLD}_{\text{rad}}, \text{KLD}_{\text{IZF}}) = (10, 6.2)$ occurs when the portion of the power allocated to the radar subsystem is 51% and 66% for the cases of $N_R = 30$ and $N_R = 20$, respectively. In other words, an ISAC system with $N_R = 30$ and 51% allocated power for the radar subsystem will provide the same KLD as $N_R = 20$ with 66% allocated radar power.

5.8 Conclusion

An ISAC system which consists of a multi-antenna BS serving CUEs and aims at detecting multiple targets simultaneously was introduced in this paper, where the separated deployment was considered. In addition, ZF and MRT were employed to precode the communication signals. The relative entropy or KLD was derived for both radar and communication subsystems, and a unified performance measure using the sum of weighted KLDs was proposed. In addition, the interference caused by the radar subsystem on CUEs and the impact of imperfect IC on the radar subsystem were analyzed and studied. Moreover, the relation between this performance measure from one side, and SER and detection probability on the other side was investigated. The obtained simulation results confirmed the derived equations where a perfect match was obtained. In addition, the results showed that there is a trade-off between the radar and the communication subsystems where enhancing one negatively impacts the other. Consequently, the system designer should be aware of this trade-off and allocate the power and antenna resources to maximize $\text{WSRE}_{\text{ISAC}}$ under some constraints on KLD_{IZF} and KLD_{rad} to guarantee boosting the performance of the whole system in an efficient way. Moreover, it was revealed that the effect of system imperfections, i.e., interference and imperfect channel estimation for $\mathbf{G}_{\text{rad}}$, result in an error floor in SER and upper bound in P_{D}, KLD_{IZF} and KLD_{rad}. It was also disclosed that MRT based precoding could experience a considerable error floor due to inter-user-interference resulted from MRT, in addition to the interference caused by the radar subsystem.

Future work may include using the derived KLD to allocate the BS resources among the users and targets to maximize $\text{WSRE}_{\text{ISAC}}$ for given constraints on individual KLDs. Moreover, the employment of KLD for the analysis, design and optimization of ISAC systems in which the radar subsystem aims at estimating the targets' parameters is also an interesting research topic.

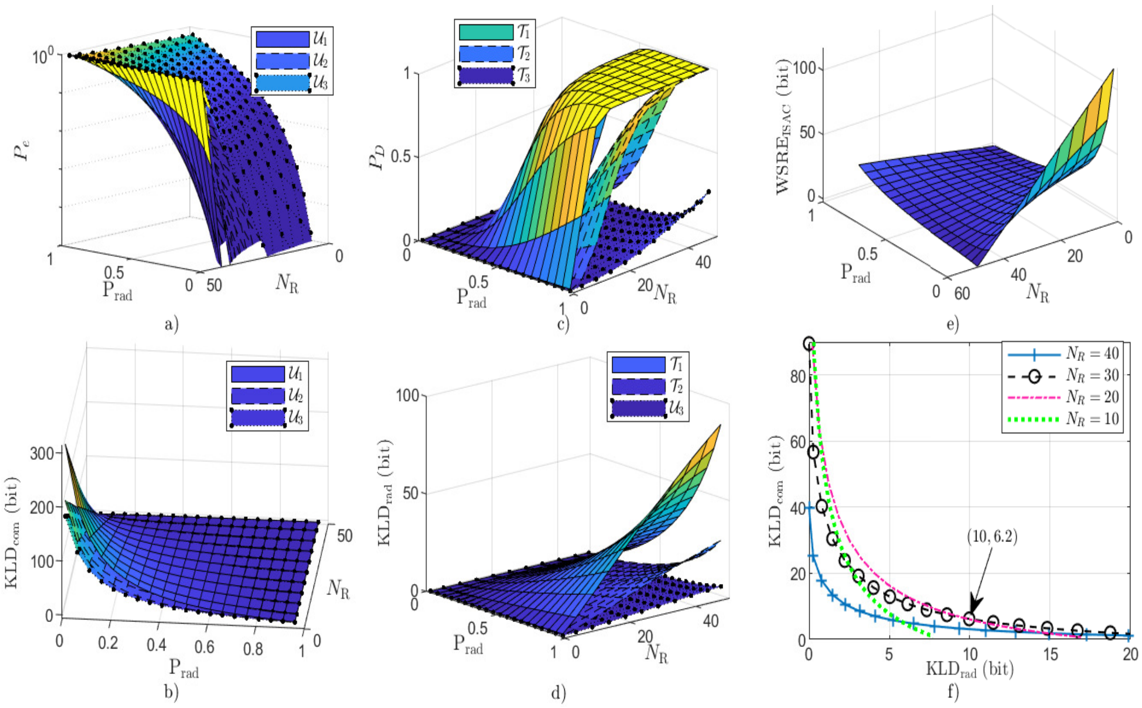

Figure 5.7: A 3D plot for the KLD of ISAC system vs. N_R and P_{rad} where $N = 50$: a) The symbol error rate of CUEs, b) The KLD of CUEs, c) The detection probability P_{D} of the radar subsystem, d) The KLD of the radar subsystem, e) The $\mathrm{WSRE}_{\mathrm{ISAC}}$ of ISAC system, and f) The $\mathrm{WSRE}_{\mathrm{ISAC}}$ of ISAC system viewed from different angle.

5.9 Appendix

5.9.1 Appendix I

Central Limit Theorem (CLT) is applied to approximate the distribution of $t_{k,i} = \sum_{n_c=1}^{N_C} d_i\,[l]\mathbf{g}_{k,n_c}^T \mathbf{g}_{i,n_c}^*$ $\forall i \neq k$ for considerable values of N_C. Therefore, with a normalized signal constellation, $\mathbb{E}\left[|d_i\,[l]|^2\right] = 1$, $t_{k,i} \sim \mathcal{CN}\left(0, 2\sigma_t^2\right)$ with $\sigma_t^2 = 2\sigma_g^4 N_C$. On the other hand, the exact density function of $z_i = \|\mathbf{g}_i\|^2$ is Chi distribution, which can be derived as below. Let us express z_i as $z_i = \sqrt{\sum_{n_c=1}^{N_C} |\mathbf{g}_{i,n_c}|^2}$, which can be rewritten as $z_i = \sigma_g \tilde{z}_i$ where $\tilde{z}_i = \sqrt{\sum_{n_c=1}^{N_C} \left(\frac{\mathbf{g}_{i,n_c,\Re}}{\sigma_g}\right)^2 + \left(\frac{\mathbf{g}_{i,n_c,\Im}}{\sigma_g}\right)^2}$. Thereafter, by using the definition of a Chi distributed random variable, it can be easily shown that $\tilde{z}_i \sim \mathrm{Chi}\,(2N_C)$ with PDF given by

$$f_{\tilde{z}_i}\left(\tilde{z}_i\right) = \frac{1}{2^{N_C-1}\Gamma\left(N_C\right)} \tilde{z}_i^{2N_C-1} \mathrm{e}^{-\frac{1}{2}\tilde{z}_i^2}, \tag{5.73}$$

and then by employing random variable transformation, it can be found that $z_i \triangleq \sigma_g \tilde{z}_i$ is also Chi distributed with PDF given by

$$f_{z_i}\left(z_i\right) = \frac{1}{2^{N_C-1}\Gamma\left(N_C\right)\sigma_g^{2N_C}} z_i^{2N_C-1} \mathrm{e}^{-\frac{1}{2\sigma_g^2} z_i^2}. \tag{5.74}$$

The ratio distribution of independent Gaussian and Chi random variables is a Student-t distribution. However, the analysis for the density of a sum of K Student-t random variables is not tractable. Therefore, to make the analysis tractable, we use the fact that for large value of the degrees of freedom of Chi distribution, which is directly proportional to N_C, the Chi density function can be approximated as real positive Gaussian PDF, i.e., $z_i \sim \mathcal{N}\left(\sigma_g\sqrt{2}\frac{\Gamma(0.5(2N_C+1))}{\Gamma(N_C)}, \left(2N_C - 2\left(\frac{\Gamma(0.5(2N_C+1))}{\Gamma(N_C)}\right)^2\right)\sigma_g^2\right)$. It is worthy noting that the assumption of large N_C is reasonable in multi-user MIMO systems since BS is typically equipped with a large number of antennas. Thereafter, we check the correlation between $t_{k,i}$ and z_i. To begin, the correlation between $t_{k,i}$ and z_i^2 is checked because it is more traceable.

$$\rho_{t_i,z_i^2} = \frac{\mathbb{E}\left[\left(t_{k,i} - \mu_{t_{k,i}}\right)\left(z_i^2 - \mu_{z_i^2}\right)\right]}{\sqrt{\mathrm{var}\left[t_{k,i}\right]\mathrm{var}\left[z_i^2\right]}}. \tag{5.75}$$

By noting that $\mu_{t_{k,i}} = 0$, and then substituting for z_i and $t_{k,i}$ and using the fact that the expectation operator can be distributed over summation and over a product of independent random variables, ρ_{t_i,z_i^2} can be found as

$$\rho_{t_i,z_i^2} = \frac{\sum_{n_{c1}=1}^{N_C}\sum_{n_{c2}=1}^{N_C}\mathbb{E}\left[\mathbf{g}_{i,n_{c1}}^{*}\left|\mathbf{g}_{i,n_{c2}}\right|^2\right]\mathbb{E}\left[\mathbf{g}_{k,n_{c1}}^{T}\right]}{\sqrt{\mathrm{var}\left[t_{k,i}\right]\mathrm{var}\left[z_i\right]}} = 0, \tag{5.76}$$

where the last equality holds as $\mathbf{g}_i$ and $\mathbf{g}_k$ are i.i.d for $i \neq k$ with zero mean (e.g. $\mathbb{E}\left[\mathbf{g}_{k,n_{c1}}^{T}\right] = 0$). Consequently, $t_{k,i}$ and z_i are uncorrelated and approximately Gaussian variables for considerable values of N_C, and thus it can be assumed that they are independent. Next, let us define $\tilde{v}_{k,i}$ can be written as

$$\tilde{v}_{k,i} \triangleq \sqrt{P_{i,\mathrm{com}}}\frac{t_{k,i}}{z_i} = \sqrt{P_{i,\mathrm{com}}}\left(v_{k,i,\Re} + jv_{k,i,\Re}\right), \tag{5.77}$$

where the subscripts $(\cdot)_{\Re}$ and $(\cdot)_{\Im}$ denote the real and imaginary components of a complex number, respectively, $v_{k,i,\Re} = \frac{t_{k,i,\Re}}{z_i}$ and $v_{k,i,\Im} = \frac{t_{k,i,\Im}}{z_i}$. Since $t_{k,i}$ is $\mathcal{N}\left(0, 2\sigma_t^2\right)$ with identically distributed real and imaginary parts, then $t_{k,i,\Re}$ and $t_{k,i,\Im}$ are $\mathcal{N}\left(0, \sigma_t^2\right)$. When $\Pr\left(z_i > 0\right) \to 1$, or $\mu_{z_i} \gg \sigma_{z_i}$, which is a satisfied condition since z_i is a strictly positive random variable in our case, the cumulative distribution function (CDF) of the ratio of two normally distributed random variables, $v_{k,i,\Re} = \frac{t_{k,i,\Re}}{z_i}$, having means of $\mu_{t,\Re} = 0$ and $\mu_z = \sqrt{2}\frac{\Gamma(0.5(2N_C+1))}{\Gamma(N_C)}$, and unequal variance values of $\sigma_t^2 = 2\sigma_g^4 N_C$ and $\sigma_z^2 \triangleq 2N_C - 2\left(\frac{\Gamma(0.5(2N_C+1))}{\Gamma(N_C)}\right)^2$, can be approximated as [76, Eq. (5)],

$$F_{v_{k,i,\Re}}\left(v\right) = \Phi\left(\frac{\mu_z v}{\sigma_t\sigma_z\left(\frac{v^2}{\sigma_t^2} + \frac{1}{\sigma_z^2}\right)^{0.5}}\right), \tag{5.78}$$

where $\Phi\left(x\right) \triangleq \frac{1}{\sqrt{2\pi}}\int_{-\infty}^{x} \mathrm{e}^{-\frac{u^2}{2}} du$ is the CDF of a standard normal distribution, i.e., $\mathcal{N}\left(0, 1\right)$. It is worthy to note that $v_{k,i,\Im}$ have the same CDF as $v_{k,i,\Re}$. Therefore, by using the derivative of $F_{v_{k,i,\Re}}\left(v\right)$, which can be solved using the chain rule and the derivative of $\Phi\left(x\right)$ as $\frac{\partial}{\partial v}\Phi\left(x\right) \triangleq \frac{1}{\sqrt{2\pi}}\mathrm{e}^{-\frac{x^2}{2}}$, the PDF can be found as,

$$\begin{aligned} f_{v_{k,i,\Re}}(v) &\triangleq \frac{\partial}{\partial v} F_{v_{k,i,\Re}}(v) \\ &= \frac{\mu_z}{\sigma_t \sigma_z \sqrt{2\pi}} \left(\frac{v^2}{\sigma_t^2} + \frac{1}{\sigma_z^2}\right)^{-0.5} \left(1 - \frac{v^2}{\sigma_t^2}\left(\frac{v^2}{\sigma_t^2} + \frac{1}{\sigma_z^2}\right)^{-1}\right) \exp\left(-\frac{\mu_z^2 v^2}{2\sigma_z^2\left(v^2 + \frac{\sigma_t^2}{\sigma_z^2}\right)}\right). \end{aligned} \tag{5.79}$$

Interestingly, for typical range of $N_C \gg 1$, $f_{v_{k,i,\Re}}(v)$ tends to take the shape of Gaussian random variable [76, Eq. (5)], consequently, $f_{v_{k,i,\Re}}(v)$ is assumed following $\mathcal{N}\left(\mu_v, \sigma_v^2\right)$ where

$$\mu_v \triangleq \mathbb{E}\left[v_{k,i,\Re}\right] = \mathbb{E}\left[t_{k,i,\Re}\right] \mathbb{E}\left[\frac{1}{z_i}\right] = 0, \tag{5.80}$$

and

$$\sigma_v^2 \triangleq \mathbb{E}\left[\left(v_{k,i,\Re} - \mu_v\right)^2\right] = \mathbb{E}\left[\left(v_{k,i,\Re}\right)^2\right] = \mathbb{E}\left[t_{k,i,\Re}^2\right] \mathbb{E}\left[\frac{1}{z_i^2}\right] = \sigma_t^2 \int_0^\infty \frac{1}{z_i^2} f_z(z)\, dz. \tag{5.81}$$

By using the PDF $f_z(z)$ which has been derived in (5.74), σ_v^2 can be written as

$$\sigma_v^2 = \frac{\sigma_t^2}{2^{N_C-1}\Gamma\left(N_C\right)\sigma_g^{2N_C}} \int_0^\infty z_i^{2N_C-3} \mathrm{e}^{-\frac{1}{2\sigma_g^2} z_i^2}\, dz. \tag{5.82}$$

Thereafter, by employing integration by substitution rule with $y = \frac{1}{2\sigma_g^2} z_i^2$, the value of σ_v^2 can be found as $\sigma_v^2 = \sigma_g^2$. Therefore, $\tilde{v}_{k,i}$ can be approximated as a symmetric complex Gaussian random variable, i.e., $\tilde{v}_{k,i} \sim \mathcal{CN}\left(0, 2P_{i,\mathrm{com}}\sigma_v^2\right)$. Next, we check the correlation between $\tilde{v}_{k,i} \forall i \neq k$. It can be easily realized that $z_i = \|\mathbf{g}_i\| \,\forall i$ are independent, as well as, the correlation coefficient between $t_{k,i} \forall i \neq k$ can be found using similar derivations in (5.76) as

$$\rho_{i,j} = \frac{\mathbb{E}\left[t_{k,i} t_{k,j}^*\right]}{\sqrt{\mathrm{var}\left[t_{k,i}\right] \mathrm{var}\left[t_{k,j}\right]}} = \frac{\sum_{n_{c1}=1}^{N_C} \sum_{n_{c2}=1}^{N_C} \mathbb{E}\left[\mathbf{g}_{i,n_{c1}}^*\right] \mathbb{E}\left[\left|\mathbf{g}_{k,n_{c2}}\right|^2\right] \mathbb{E}\left[\mathbf{g}_{j,n_{c1}}^*\right]}{\sqrt{\mathrm{var}\left[t_{k,i}\right] \mathrm{var}\left[t_{k,j}\right]}} = 0. \tag{5.83}$$

Consequently, since $t_{k,i}$ is complex Gaussian distributed according to CLT and $\rho_{i,j} = 0 \forall i \neq j$, $t_{k,i}$ and $t_{k,j}$ are independent for $i \neq j$. Moreover, since z_i and z_j are independent $\forall i \neq j$, and thus $\tilde{v}_{k,i} = \sqrt{P_{i,\mathrm{com}}} \frac{t_{k,i}}{z_i}$ and $\tilde{v}_{k,j} = \sqrt{P_{j,\mathrm{com}}} \frac{t_{k,j}}{z_j}$ for $i \neq j$ are also independent. Finally, $\omega_{\mathrm{MRT}} = \sum_{\substack{i=1 \\ i \neq k}}^{K} \tilde{v}_{k,i}$ is a sum of $K-1$ independent complex Gaussian random variables each of which $\tilde{v}_{k,i} \sim \mathcal{CN}\left(0, 2P_{i,\mathrm{com}}\sigma_v^2\right)$, thus $\omega_{\mathrm{MRT}} \sim \mathcal{CN}\left(0, 2\sigma_v^2 \sum_{\substack{i=1 \\ i \neq k}}^{K} P_{i,\mathrm{com}}\right)$. Therefore, the equivalent inter-user and radar interference plus noise $\tilde{\omega}_{\mathrm{MRT}} \sim \mathcal{CN}\left(0, 2\sigma_\omega^2\right)$ where $\sigma_\omega^2 = \sigma_v^2 \sum_{\substack{i=1 \\ i \neq k}}^{K} P_{i,\mathrm{com}} + \sigma_\eta^2$ with $\sigma_\eta^2 = P_{\mathrm{rad}}\sigma_f^2 + \sigma_n^2$.

5.9.2 Appendix II

Substituting the approximation given by (5.55) in (5.58) and then performing some mathematical manipulation including some logarithmic and exponential identities such as $\ln\left(\frac{x}{y}\right) = \ln x - \ln y$, $\ln(xy) =$

Table 5.1: The values of I_{2a}, I_{2b},...,I_{2d} that are required to compute KLD($\xi_{H0}||\xi_{H1}$).

$\mathcal{I}_{2a} = \int\limits_{\frac{1}{\lambda_t}}^{\infty} \sqrt{\xi}\mathrm{e}^{-0.5\xi} d\xi$	$\mathcal{I}_{2b} = \int\limits_{\frac{1}{\lambda_t}}^{\infty} \mathrm{e}^{-0.5\xi} d\xi = \frac{2}{\sqrt[2\lambda_t]{\mathrm{e}}}$	$\mathcal{I}_{2c} = \int\limits_{\frac{1}{\lambda_t}}^{\infty} \mathrm{e}^{-0.5\xi} \ln(\xi) \, d\xi$
$\mathcal{I}_{2d} = \int\limits_{\frac{1}{\lambda_t}}^{\infty} \mathrm{e}^{-0.5\xi} \ln\left(1 + \sum_{q=1}^{Q} \left(\frac{1}{\left(\sqrt{\lambda_t \xi}\right)^q} \frac{\prod_{k=1}^{q}\left[(2k-1)^2\right]}{q!8^q}\right)\right) d\xi$		

$\ln x + \ln y$ and $\ln \mathrm{e}^x = x$ yield

$$\mathcal{I}_2 \approx \sqrt{\lambda_t}\mathcal{I}_{2a} - \left(\left(\frac{1}{2}\ln(2\pi) + \frac{1}{4}\ln(\lambda_t)\right)\mathcal{I}_{2b} + \frac{1}{4}\mathcal{I}_{2c}\right) + \mathcal{I}_{2d}, \tag{5.84}$$

where $\mathcal{I}_{2a}$, $\mathcal{I}_{2b}$, $\mathcal{I}_{2c}$ and $\mathcal{I}_{2d}$ are given in Table 5.1.

Thereafter, by using integration by substitution with $y = \sqrt{\xi}$ and then using [77, Eq. 1.3.3.8, pp. 140], $\mathcal{I}_{2a}$ can be found as

$$\mathcal{I}_{2a} = -\sqrt{2\pi}\mathrm{erf}\left(\frac{1}{\sqrt{2\lambda_t}}\right) + \sqrt{2\pi} + \frac{2}{\sqrt[2\lambda_t]{\mathrm{e}}\sqrt{\lambda_t}}. \tag{5.85}$$

Moreover, using integration by parts rule with $dv = \mathrm{e}^{-0.5\xi}$ and $u = \ln(\xi)$ and then using the definition of the exponential integral, $\mathcal{I}_{2c}$ can be found as

$$\mathcal{I}_{2c} = \left(-\frac{2\ln\lambda_t}{\sqrt[2\lambda_t]{\mathrm{e}}} + 2\mathrm{Ei}_1\left(\frac{1}{2\lambda_t}\right)\right). \tag{5.86}$$

To solve $\mathcal{I}_{2d}$, let us consider the first five terms in the summation, i.e., $Q = 5$ which can provide a very good approximation for $\xi \geq \frac{1}{\lambda_t}$. In this case we obtain $\sum_{q=1}^{Q=5}(\cdot) < 1$, and thus Taylor series expansion can be adopted and the first term is sufficient for providing accurate results, i.e., $\ln\left(1 + \sum_{q=1}^{Q=5}(\cdot)\right) \approx \sum_{q=1}^{Q=5}(\cdot)$ for $\sum_{q=1}^{Q=5}(\cdot) < 1$. Thereafter, by using the fact that summation and integration are interchangeable operations, $\mathcal{I}_{2d}$ can be evaluated as [77, Eq. 1.3.2.4, pp. 137]

$$\mathcal{I}_{2d} = \sum_{q=1}^{Q=5} \frac{\prod_{k=1}^{q}\left[(2k-1)^2\right]}{q!8^q\lambda_t^{0.5q}} \frac{1}{0.5^{1-0.5q}} \Gamma\left(1 - 0.5q, \frac{0.5}{\lambda_t}\right), \tag{5.87}$$

where $\Gamma(\cdot,\cdot)$ is the upper incomplete gamma function.

5.9.3 Appendix III

By substituting the infinite series representation provided in (5.54) for the modified Bessel function in (5.66), $\mathcal{I}_{4a}$ can be given by

$$\mathcal{I}_{4a} = \int_0^{\frac{1}{\lambda_t}} \mathrm{e}^{-0.5\xi} \sum_{l_1=0}^{\infty} \frac{\lambda_t^{l_1}}{2^{2l_1}(l_1!)^2}\xi^{l_1} \ln\left(1 + \sum_{l_2=1}^{\infty} \frac{\lambda_t^{l_2}}{2^{2l_2}(l_2!)^2}\xi^{l_2}\right) d\xi. \tag{5.88}$$

Table 5.2: The values of $I_{4b,1}$, $I_{4b,2}$,...,$I_{4b,8}$ that are required to compute KLD($\xi_{H1}||\xi_{H0}$).

$\mathcal{I}_{4b,1} = \int_{\frac{1}{\lambda_t}}^{\infty} \xi^{0.25} \exp\left(-0.5\xi + \sqrt{\lambda_t \xi}\right) d\xi$	$\mathcal{I}_{4b,2} = \int_{\frac{1}{\lambda_t}}^{\infty} \xi^{-0.25} \exp\left(-0.5\xi + \sqrt{\lambda_t \xi}\right) d\xi$
$\mathcal{I}_{4b,3} = \int_{\frac{1}{\lambda_t}}^{\infty} \xi^{-0.25} \ln(\xi) \exp\left(-0.5\xi + \sqrt{\lambda_t \xi}\right) d\xi$	$\mathcal{I}_{4b,4} = \int_{\frac{1}{\lambda_t}}^{\infty} \frac{1}{\xi^{\frac{q_2}{2}+\frac{1}{4}}} \exp\left(-0.5\xi + \sqrt{\lambda_t \xi}\right) d\xi$
$\mathcal{I}_{4b,5} = \int_{\frac{1}{\lambda_t}}^{\infty} \frac{1}{\xi^{\frac{q_1}{2}-\frac{1}{4}}} \exp\left(-0.5\xi + \sqrt{\lambda_t \xi}\right) d\xi$	$\mathcal{I}_{4b,6} = \int_{\frac{1}{\lambda_t}}^{\infty} \frac{1}{\xi^{\frac{q_1}{2}+\frac{1}{4}}} \exp\left(-0.5\xi + \sqrt{\lambda_t \xi}\right) d\xi$
$\mathcal{I}_{4b,7} = \int_{\frac{1}{\lambda_t}}^{\infty} \frac{1}{\xi^{\frac{q_1}{2}+\frac{1}{4}}} \ln(\xi) \exp\left(-0.5\xi + \sqrt{\lambda_t \xi}\right) d\xi$	$\mathcal{I}_{4b,8} = \int_{\frac{1}{\lambda_t}}^{\infty} \frac{1}{\xi^{\frac{q_1}{2}+\frac{q_2}{2}+\frac{1}{4}}} \exp\left(-0.5\xi + \sqrt{\lambda_t \xi}\right) d\xi$

After that, by noting that $\sum_{l_2=1}^{\infty} \frac{\lambda_t^{l_2}}{2^{2l_2}(l_2!)^2}\xi^{l_2} < 1$ for $0 \leq \xi < \frac{1}{\lambda_t}$, the first term of the Taylor series is considered to approximate the logarithmic function and then interchange the summations and integration order, $\mathcal{I}_{4a}$ can be accurately approximated as

$$\mathcal{I}_{4a} \approx \sum_{l_1=0}^{\infty} \frac{\lambda_t^{l_1}}{2^{2l_1}(l_1!)^2} \sum_{l_2=1}^{\infty} \frac{\lambda_t^{l_2}}{2^{2l_2}(l_2!)^2} \int_0^{\frac{1}{\lambda_t}} \mathrm{e}^{-0.5\xi} \xi^{l_1+l_2} d\xi, \tag{5.89}$$

which can be solved as

$$\mathcal{I}_{4a} \approx \sum_{l_1=0}^{\infty} \frac{\lambda_t^{l_1}}{2^{2l_1}(l_1!)^2} \sum_{l_2=1}^{\infty} \frac{\lambda_t^{l_2}}{2^{2l_2}(l_2!)^2} \frac{2^{1+0.5(l_1+l_2)}}{(1+l_1+l_2)\lambda_t^{0.5(l_1+l_2)}} \mathrm{e}^{-\frac{0.25}{\lambda_t}} \mathrm{M}_{0.5(l_1+l_2),0.5(l_1+l_2)+0.5}\left(\frac{0.5}{\lambda_t}\right). \tag{5.90}$$

On the other hand, by substituting the approximation in (5.55) to approximate $\mathcal{I}_{4b}$ given in (5.66) for $\xi > \frac{1}{\lambda_t}$ and using some algorithmic identities such as $\log\left(\frac{x}{y}\right) = \log x - \log y$, $\log(xy) = \log x + \log y$ and $\log(x^y) = y \log x$, then $\mathcal{I}_{4b}$ can be simplified to

$$\begin{aligned}
\mathcal{I}_{4b} \approx & \int_{\frac{1}{\lambda_t}}^{\infty} \mathrm{e}^{-0.5\xi} \frac{\exp\left(\sqrt{\lambda_t\xi}\right)}{\sqrt{2\pi}\sqrt[4]{\lambda_t\xi}} \left(1 + \sum_{q1=1}^{Q}\left(\frac{1}{\left(\sqrt{\lambda_t\xi}\right)^q} \frac{\prod_{k=1}^{q}\left[(2k-1)^2\right]}{q!8^q}\right)\right) \\
& \times\left(\sqrt{\lambda_t\xi} - \ln\left(\sqrt{2\pi}\sqrt[4]{\lambda_t}\right) - 0.25\ln(\xi) + \ln\left(1+\sum_{q2=1}^{Q}\left(\frac{1}{\left(\sqrt{\lambda_t\xi}\right)^q}\frac{\prod_{k=1}^{q}\left[(2k-1)^2\right]}{q!8^q}\right)\right)\right) d\xi \quad (5.91) \\
= & \frac{1}{\sqrt{2\pi}\sqrt[4]{\lambda_t}}\left(\sqrt{\lambda_t}\mathcal{I}_{4b,1} - \ln\left(\sqrt{2\pi}\sqrt[4]{\lambda_t}\right)\mathcal{I}_{4b,2} - 0.25\mathcal{I}_{4b,3} + \mathcal{Q}_{\mathrm{sum},q_2}\mathcal{I}_{4b,4}\right. \\
& \left. + \mathcal{Q}_{\mathrm{sum},q_1} \times \left(\sqrt{\lambda_t}\mathcal{I}_{4b,5} - \ln\left(\sqrt{2\pi}\sqrt[4]{\lambda_t}\right)\mathcal{I}_{4b,6} - 0.25\mathcal{I}_{4b,7} + \mathcal{Q}_{\mathrm{sum},q_2}\mathcal{I}_{4b,8}\right)\right), \quad (5.92)
\end{aligned}$$

where $\mathcal{Q}_{\mathrm{sum},q} = \sum_{q=1}^{Q} \frac{1}{q_1!8^q\sqrt{\lambda_t^q}} \prod_{k=1}^{q}\left[(2k-1)^2\right]$ $\forall q \in \{q_1, q_2\}$, and $\mathcal{I}_{4b,i} \forall i \in \{1, 2, \cdots, 8\}$ are given in Table 5.2. Due to the limited space, we will show the complete solutions for $\mathcal{I}_{4b,1}$ and $\mathcal{I}_{4b,3}$ only, anyway, the other integrals can be solved in a similar way. By using integration by substitution rule with $y = \sqrt{0.5\xi}$ followed by the complete square rule to write the exponents in a more convenient form, i.e., the integrand is multiplied by $\exp\left(\pm\frac{\lambda_t}{2}\right)$, $\mathcal{I}_{4b,1}$ and $\mathcal{I}_{4b,3}$ can be expressed as

$$\mathcal{I}_{4b,1} = 4\,(2)^{0.25} \exp\left(\frac{\lambda_t}{2}\right) \int\limits_{\sqrt{\frac{1}{2\lambda_t}}}^{\infty} y^{1.5} \exp\left(-\left(y-\sqrt{\frac{\lambda_t}{2}}\right)^2\right) dy, \tag{5.93}$$

$$\mathcal{I}_{4b,3} = 4\,(2)^{-0.25} \exp\left(\frac{\lambda_t}{2}\right) \int\limits_{\sqrt{\frac{1}{2\lambda_t}}}^{\infty} y^{0.5} \ln\left(2y^2\right) \exp\left(-\left(y-\sqrt{\frac{\lambda_t}{2}}\right)^2\right) dy. \tag{5.94}$$

Next, with the aid of the series representation of $\exp\left(-x^2\right)$ [75, Eq. 1.211.3, pp. 26] and then interchanging the integration and summation operations, $\mathcal{I}_{4b,1}$ and $\mathcal{I}_{4b,3}$ can be simplified to

$$\mathcal{I}_{4b,1} = 4\,(2)^{0.25} \exp\left(\frac{\lambda_t}{2}\right) \sum_{k=0}^{\infty} \frac{(-1)^k}{k!} \int\limits_{\sqrt{\frac{1}{2\lambda_t}}}^{\infty} y^{1.5} \sum_{l=0}^{\infty} \left(y-\sqrt{\frac{\lambda_t}{2}}\right)^{2k} dy, \tag{5.95}$$

$$\mathcal{I}_{4b,3} = 4\,(2)^{-0.25} \exp\left(\frac{\lambda_t}{2}\right) \sum_{k=0}^{\infty} \frac{(-1)^k}{k!} \int\limits_{\sqrt{\frac{1}{2\lambda_t}}}^{\infty} y^{0.5} \ln\left(2y^2\right) \left(y-\sqrt{\frac{\lambda_t}{2}}\right)^{2k} dy. \tag{5.96}$$

Thereafter, the binomial expansion theorem is invoked and interchanging the summation and integration is applied. Additionally, to make the series converges to the answer quickly, we limit the integration to an upper bound of $y_{\mathrm{U}} = \sqrt{\frac{\lambda_t}{2}} + \frac{4}{\sqrt{2}}$ instead of ∞ as $\exp\left(-\left(y-\sqrt{\frac{\lambda_t}{2}}\right)^2\right) \approx 0$ for $y > \sqrt{\frac{\lambda_t}{2}} + \frac{4}{\sqrt{2}}$. It is worthy to notice that the exponential term has a form similar to a normal distribution with a mean of $\mu = \sqrt{\frac{\lambda_t}{2}}$ and a standard deviation of $\sigma = \frac{1}{\sqrt{2}}$, and thus it can interpreted that more than 99.9999% of the area under the curve is in the range $\mu - 4\sigma \leq y \leq \mu + 4\sigma$. Subsequently, $\mathcal{I}_{4b,1}$ can be evaluated as

$$\begin{aligned}
\mathcal{I}_{4b,1} &= 4\,(2)^{0.25} \exp\left(\frac{\lambda_t}{2}\right) \sum_{k=0}^{\infty} \frac{(-1)^k}{k!} \sum_{l=0}^{2k} (-1)^{2k-l} \binom{2k}{l} \left(\frac{\lambda_t}{2}\right)^{0.5(2k-l)} \int\limits_{\sqrt{\frac{1}{2\lambda_t}}}^{y_{\mathrm{U}}} y^{l+1.5} dy \\
&= 4\,(2)^{0.25} \exp\left(\frac{\lambda_t}{2}\right) \sum_{k=0}^{\infty} \frac{(-1)^k}{k!} \sum_{l=0}^{2k} (-1)^{2k-l} \binom{2k}{l} \left(\frac{\lambda_t}{2}\right)^{0.5(2k-l)} \frac{1}{l+2.5} \left(y_{\mathrm{U}}^{l+2.5} - \left(\frac{1}{2\lambda_t}\right)^{\frac{l+2.5}{2}}\right)
\end{aligned} \tag{5.97}$$

and $\mathcal{I}_{4b,3}$ can be further simplified to

$$\mathcal{I}_{4b,3} = 4\,(2)^{-0.25} \exp\left(\frac{\lambda_t}{2}\right) \sum_{k=0}^{\infty} \frac{(-1)^k}{k!} \sum_{l=0}^{2k} (-1)^{2k-l} \binom{2k}{l} \left(\frac{\lambda_t}{2}\right)^{0.5(2k-l)} \int\limits_{\sqrt{\frac{1}{2\lambda_t}}}^{y_{\mathrm{U}}} y^{l+0.5} \ln\left(2y^2\right) dy. \tag{5.98}$$

Using the logarithmic identities $\log(xy) = \log x + \log y$ and $\log(y^x) = x \log y$, $\mathcal{I}_{4b,3}$ can be written as

$$\mathcal{I}_{4b,3} = 4\,(2)^{-0.25} \exp\left(\frac{\lambda_t}{2}\right) \sum_{k=0}^{\infty} \frac{(-1)^k}{k!} \sum_{l=0}^{2k} (-1)^{2k-l} \binom{2k}{l} \left(\frac{\lambda_t}{2}\right)^{0.5(2k-l)} \times \left(\ln 2 \int_{\sqrt{\frac{1}{2\lambda_t}}}^{y_{\mathrm{U}}} y^{l+0.5} dy + 2 \int_{\sqrt{\frac{1}{2\lambda_t}}}^{y_{\mathrm{U}}} y^{l+0.5} \ln y dy \right). \quad (5.99)$$

Subsequently, with the aid of [77, Eq. 1.6.1.18, pp. 241], the second integral is solved and the final equation can be expressed as

$$\mathcal{I}_{4b,3} = 4\,(2)^{-0.25} \exp\left(\frac{\lambda_t}{2}\right) \sum_{k=0}^{\infty} \frac{(-1)^k}{k!} \sum_{l=0}^{2k} (-1)^{2k-l} \binom{2k}{l} \left(\frac{\lambda_t}{2}\right)^{0.5(2k-l)} \left(\frac{\ln 2}{l+1.5} \left(\left(\sqrt{\frac{\lambda_t}{2}} + \frac{5}{\sqrt{2}} \right)^{l+1.5} - \left(\frac{1}{2\lambda_t}\right)^{\frac{l+1.5}{2}} \right) + 2 \left(y_{\mathrm{U}}^{l+1.5} \left(\frac{\ln(y_{\mathrm{U}})}{l+1.5} - \frac{1}{(l+1.5)^2} \right) - \left(\frac{1}{2\lambda_t}\right)^{\frac{l+1.5}{2}} \left(\frac{-\ln(2\lambda_t)}{2\,(l+1.5)} - \frac{1}{(l+1.5)^2} \right) \right) \right). \quad (5.100)$$

References

[1] D. Evans, "The internet of things: How the next evolution of the internet is changing everything," Cisco IBSG., US, Apr. 2011. [Online]. Available: https://www.cisco.com/c/dam/en_us/about/ac79/docs/innov/IoT_IBSG_04 11FINAL.pdf

[2] M. A. Al-Jarrah, M. A. Yaseen, A. Al-Dweik, O. Dobre, and E. Alsusa, "Decision fusion for IoT-based wireless sensor networks," *IEEE Internet Things J.*, vol. 7, no. 2, pp. 1313-1326, Feb. 2020, doi: 10.1109/JIOT.2019.2954720.

[3] L. Chettri and R. Bera, "A comprehensive survey on internet of things (IoT) toward 5G wireless systems," *IEEE Internet Things J.*, vol. 7, no. 1, pp. 16-32, Jan. 2020, doi: 10.1109/JIOT.2019.2948888.

[4] L. Yang, R. Muresan, A. Al-Dweik and L. Hadjileontiadis, "Image-based visibility estimation algorithm for intelligent transportation systems," *IEEE Access*, vol. 6, pp. 76728-76740, 2018, doi: 10.1109/ACCESS.2018.2884225.

[5] M. Al-Jarrah, E. Alsusa, A. Al-Dweik and D. K. C. So, "Capacity analysis of IRS-based UAV communications with imperfect phase compensation," *IEEE Wireless Commun. Lett.*, vol. 10, no. 7, pp. 1479-1483, July 2021, doi: 10.1109/LWC.2021.3071059.

[6] M. Al-Jarrah, A. Al-Dweik, E. Alsusa, Y. Iraqi and M.-S. Alouini, "On the performance of IRS-assisted multi-layer UAV communications with imperfect phase compensation," *IEEE Trans. Commun.*, vol. 69, no. 12, pp. 8551-8568, Dec. 2021, doi: 10.1109/TCOMM.2021.3113008.

[7] F. Liu, C. Masouros, A. Li, and T. Ratnarajah, "Robust MIMO beamforming for cellular and radar coexistence," *IEEE Wireless Commun. Lett.*, vol. 6, no. 3, pp. 374-377, Jun. 2017.

[8] F. Liu, L. Zhou, C. Masouros, A. Li, W. Luo, and A. Petropulu, "Toward dual-functional radar-communication systems: Optimal waveform design," *IEEE Trans. Signal Process.*, vol. 66, no. 16, pp. 4264-4279, Aug. 2018.

[9] F. Liu, C. Masouros, A. Li, H. Sun, and L. Hanzo, "MU-MIMO communications with MIMO radar: From co-existence to joint transmission," *IEEE Trans. Wireless Commun.*, vol. 17, no. 4, pp. 2755-2770, Apr. 2018.

[10] A. Liu *et al.*, “A survey on fundamental limits of integrated sensing and communication,” *IEEE Commun. Surveys Tuts.*, *Early access*, 2022, doi: 10.1109/COMST.2022.3149272.

[11] J. A. Zhang *et al.*, “An overview of signal processing techniques for joint communication and radar sensing,” *IEEE J. Sel. Topics Signal Process.*, vol. 15, no. 6, pp. 1295-1315, Nov. 2021, doi: 10.1109/JSTSP.2021.3113120.

[12] M. Temiz, E. Alsusa, and M. Baidas, “A dual-functional massive MIMO OFDM communication and radar transmitter architecture,” *IEEE Trans. Veh. Technol.*, vol. 69, no. 12, pp. 14974-14988, Dec. 2020, doi: 10.1109/TVT.2020.3031686.

[13] M. Temiz, E. Alsusa and M. Baidas, “Optimized precoders for massive MIMO OFDM dual radar-communication systems,” *IEEE Trans. Commun.*, vol. 69, no. 7, pp. 4781-4794, Jul. 2021, doi: 10.1109/TCOMM.2021.3068485.

[14] M. A. Al-Jarrah, A. Al-Dweik, S. Ikki, and E. Alsusa, “Spectrum-occupancy aware cooperative spectrum sensing using adaptive detection,” *IEEE Systems J.*, vol. 14, no. 2, pp. 2225-2236, Jun. 2020, doi: 10.1109/JSYST.2019.2922773.

[15] S. Chen, H. Xu, D. Liu, B. Hu, and H. Wang, “A vision of IoT: Applications, challenges, and opportunities with china perspective,” *IEEE Internet Things J.*, vol. 1, no. 4, pp. 349-359, Aug. 2014, doi: 10.1109/JIOT.2014.2337336.

[16] Mohammad A. Al-Jarrah, N. Al-Ababneh, M. Al-Ibrahim, and R. Al-Jarrah, “Cooperative OFDM for semi distributed detection in wireless sensor networks,”*AEU-Int. J. of Electron. Commun.*, vol. 68, no. 10, pp. 1022-1029, 2014.

[17] L. Zhang, L. Zhang, and B. Du, “Deep learning for remote sensing data: A technical tutorial on the state of the art,” *IEEE Geosci. Remote Sens. Mag.*, vol. 4, no. 2, pp. 22-40, Jun. 2016, doi: 10.1109/MGRS.2016.2540798.

[18] M. A. Al-Jarrah, A. Al-Dweik, E. Alsusa, and E. Damiani, “RFID reader localization using hard decisions with error concealment,” *IEEE Sensors J.*, vol. 19, no. 17, pp. 7534-7542, 1 Sept.1, 2019, doi: 10.1109/JSEN.2019.2914914.

[19] E. Fishler, A. Haimovich, R. Blum, L. Cimini, D. Chizhik, and R. Valenzuela, “Spatial diversity in radars—Models and detection performance,” *IEEE Trans. Signal Process.*, vol. 54, no. 3, pp. 823-838, Mar. 2006.

[20] I. Bekkerman and J. Tabrikian, “Target detection and localization using MIMO radars and sonars,” *IEEE Trans. Signal Process.*, vol. 54, no. 10, pp. 3873-3883, Oct. 2006, doi: 10.1109/TSP.2006.879267.

[21] A. Hassanien and S. Vorobyov, “Phased-MIMO radar: A tradeoff between phased-array and MIMO radars,” *IEEE Trans.Signal Process.*, vol. 58, no. 6, pp. 3137-3151, Jun. 2010, doi: 10.1109/TSP.2010.2043976.

[22] H. Godrich, A. Haimovich, and R. Blum, “Target localization accuracy gain in MIMO radar-based systems,” *IEEE Trans. Inf. Theory*, vol. 56, no. 6, pp. 2783-2803, June 2010, doi: 10.1109/TIT.2010.2046246.

[23] B. Friedlander, “On transmit beamforming for MIMO radar,” *IEEE Trans. Aerosp. Electron. Syst.*, vol. 48, no. 4, pp. 3376-3388, Oct. 2012.

[24] N. Fatema, G. Hua, Y. Xiang, D. Peng, and I. Natgunanathan, “Massive MIMO linear precoding: A survey,” *IEEE Sys. J.*, vol. 12, no. 4, pp. 3920-3931, Dec. 2018, doi: 10.1109/JSYST.2017.2776401.

[25] M. Shafi *et al.*, “5G: A tutorial overview of standards, trials, challenges, deployment, and practice,” *IEEE J. Sel. Areas Commun.*, vol. 35, no. 6, pp. 1201-1221, Jun. 2017, doi: 10.1109/JSAC.2017.2692307.

[26] Samsung, “Massive MIMO for new radio,” SAMSUNG, South Korea, Dec. 2020, [Online]. Available: https://images.samsung.com/is/content/samsung/ assets/global/business/networks/insights/white-papers/1208_massive-mimo-for-new-radio/MassiveMIMOforNRTechnicalWhitePaper-v1.2.0.pdf

[27] ZTE, “5G massive MIMO network application,” ZTE, China, Sep. 2020, [Online]. Available: https://res-www.zte.com.cn/mediares/zte/Files/PDF/ white_book/202009101153.pdf

[28] J. Tang, N. Li, Y. Wu, and Y. Peng, “On detection performance of MIMO radar: A relative entropy-based study,” *IEEE Signal Process. Lett.*, vol. 16, no. 3, pp. 184-187, Mar. 2009, doi: 10.1109/LSP.2008.2011704.

[29] B. Tang, J. Tang, and Y. Peng, “MIMO radar waveform design in colored noise based on information theory,” *IEEE Trans. Signal Process.*, vol. 58, no. 9, pp. 4684-4697, Sep. 2010, doi: 10.1109/TSP.2010.2050885.

[30] T. M. Cover and J. A. Thomas, Elements of Information Theory. New York: Wiley, 1991.

[31] B. Tang, M. Naghsh, and J. Tang, “Relative entropy-based waveform design for MIMO radar detection in the presence of clutter and interference,” *IEEE Trans. Signal Process.*, vol. 63, no. 14, pp. 3783-3796, Jul. 2015, doi: 10.1109/TSP.2015.2423257.

[32] M. Al-Jarrah, R. Al-Jarrah, N. Al-Ababneh, “Decision fusion in mobile wireless sensor networks using cooperative multiple symbol differential space time coding”, *AEU-Int. J. Electron. Commun.*, vol. 80, pp. 127-136, 2017.

[33] A. Khawar, A. Abdelhadi and C. Clancy, "Target detection performance of spectrum sharing MIMO radars," *IEEE Sensors J.*, vol. 15, no. 9, pp. 4928-4940, Sep. 2015.

[34] J. Zuk, "Correlated noncoherent radar detection for gamma-fluctuating targets in compound clutter," *IEEE Trans. Aerosp. Electron. Syst*, vol. 58, no. 2, pp. 1241-1256, Apr. 2022, doi: 10.1109/TAES.2021.3113629.

[35] H. Li, F. Wang, C. Zeng, and M. Govoni, "Signal detection in distributed MIMO radar with non-orthogonal waveforms and sync errors," *IEEE Trans. Signal Process.*, vol. 69, pp. 3671-3684, 2021, doi: 10.1109/TSP.2021.3087897.

[36] Z. Liu and A. Nehorai, "Statistical angular resolution limit for point sources," *IEEE Trans. Signal Process.*, vol. 55, no. 11, pp. 5521-5527, Nov. 2007, doi: 10.1109/TSP.2007.898789.

[37] M. El Korso, R. Boyer, A. Renaux, and S. Marcos, "Statistical resolution limit for source localization with clutter interference in a MIMO radar context," *IEEE Trans. Signal Process.*, vol. 60, no. 2, pp. 987-992, Feb. 2012, doi: 10.1109/TSP.2011.2174232.

[38] A. Zaimbashi, "Forward M-ary hypothesis testing based detection approach for passive radar," *IEEE Trans. Signal Process.*, vol. 65, no. 10, pp. 2659-2671, 15 May 2017, doi: 10.1109/TSP.2017.2666778.

[39] L. Wang, W. Zhu, Y. Zhang, Q. Liao, and J. Tang, "Multi-target detection and adaptive waveform design for cognitive MIMO radar," *IEEE Sensors J.*, vol. 18, no. 24, pp. 9962-9970, Dec. 2018, doi: 10.1109/JSEN.2018.2873103.

[40] W. Yi, T. Zhou, Y. Ai, and R. S. Blum, "Suboptimal low complexity joint multi-target detection and localization for non-coherent MIMO radar with widely separated antennas," *IEEE Trans. Signal Process.*, vol. 68, pp. 901-916, 2020, doi: 10.1109/TSP.2020.2968282.

[41] Y. Zhang, L. Wang, J. Tang, and J. Pan, "Multi-hypothesis test for close targets detection in co-located MIMO radar," *J. Eng.*, pp. 5986-5989, May 2019. Online. [Available:] https://doi.org/10.1049/joe.2019.0456.

[42] A. Chiriyath, B. Paul, and D. Bliss, "Radar-communications convergence: Coexistence, cooperation, and co-design," *IEEE Trans. Cogn. Commun. Netw.*, vol. 3, no. 1, pp. 1-12, Mar. 2017, doi: 10.1109/TCCN.2017.2666266.

[43] A. Chiriyath, B. Paul, G. Jacyna, and D. Bliss, "Inner bounds on performance of radar and communications co-existence," *IEEE Trans. Signal Process.*, vol. 64, no. 2, pp. 464-474, Jan.15, 2016, doi: 10.1109/TSP.2015.2483485.

[44] M. Temiz, E. Alsusa, and M. Baidas, “A dual-function massive MIMO uplink OFDM communication and radar architecture,” *IEEE Trans. Cogn. Commun. Netw.*, Early Access, 2021, doi: 10.1109/TCCN.2021.3128599.

[45] P. Kumari, J. Choi, N. González-Prelcic, and R. Heath, “IEEE 802.11ad-based radar: An approach to joint vehicular communication-radar system,” *IEEE Trans. Veh. Technol.*, vol. 67, no. 4, pp. 3012-3027, Apr. 2018, doi: 10.1109/TVT.2017.2774762.

[46] K. Singh, S. Biswas, T. Ratnarajah, and F. Khan, “Transceiver design and power allocation for full-duplex MIMO communication systems with spectrum sharing radar,” *IEEE Trans. Cogn. Commun. Netw.*, vol. 4, no. 3, pp. 556-566, Sep. 2018, doi: 10.1109/TCCN.2018.2830758.

[47] X. Yuan *et al.*, “Spatio-temporal power optimization for MIMO joint communication and radio sensing systems with training overhead,” *IEEE Trans. Veh. Technol.*, vol. 70, no. 1, pp. 514-528, Jan. 2021, doi: 10.1109/TVT.2020.3046438.

[48] C. Xu, B. Clerckx, S. Chen, Y. Mao, and J. Zhang, “Rate-splitting multiple access for multi-antenna joint communication and radar transmissions,” *2020 IEEE Int. Conf. Commun. Workshops (ICC Workshops)*, Dublin, Ireland, 2020, pp. 1-6, doi: 10.1109/ICCWorkshops49005.2020.9145168.

[49] N. Luong, X. Lu, D. Hoang, D. Niyato, and D. Kim, “Radio resource management in joint radar and communication: A comprehensive survey,” *IEEE Commun. Surveys Tuts.*, vol. 23, no. 2, pp. 780-814, Secondquarter 2021, doi: 10.1109/COMST.2021.3070399.

[50] B. Chalise, M. Amin, and B. Himed, “Performance tradeoff in a unified passive radar and communications system,” *IEEE Signal Process. Lett.*, vol. 24, no. 9, pp. 1275-1279, Sep. 2017, doi: 10.1109/LSP.2017.2721639.

[51] C.-C. Ouyang, Y. Liu, and H. Yang, “Fundamental performance of integrated sensing and communications (ISAC) systems,” *arXiv Preprint*, 2022, Online. [Available]: https://arxiv.org/abs/2202.06207.

[52] C.-C. Ouyang, Y. Liu, and H. Yang, “On the performance of uplink ISAC systems,” *arXiv Preprint*, 2022, Online. [Available]: https://arxiv.org/abs/2201.01422.

[53] Z. Xiao and Y. Zeng, “Waveform design and performance analysis for full-duplex integrated sensing and communication,” *IEEE J. Sel. Areas Commun.*, Early access, 2022, doi: 10.1109/JSAC.2022.3155509.

[54] L. Gaudio, M. Kobayashi, B. Bissinger, and G. Caire, “Performance analysis of joint Radar and communication using OFDM and OTFS,” *2019 IEEE Int. Conf. Commun. Workshops (ICC Workshops)*, 2019, pp. 1-6, doi: 10.1109/ICCW.2019.8757044.

[55] M. Ahmadipour, M. Kobayashi, M. Wigger, and G. Caire, “An information-theoretic approach to joint sensing and communication,” *IEEE Trans. Inf. Theory*, IEEE early access, 2022, doi: 10.1109/TIT.2022.3176139.

[56] Z. Yun and M. F. Iskander, “Ray tracing for radio propagation modeling: Principles and applications,” *IEEE Access*, vol. 3, pp. 1089-1100, 2015, doi: 10.1109/ACCESS.2015.2453991.

[57] R. Feng, E. D. Greef, M. Rykunov, H. Sahli, S. Pollin and A. Bourdoux, “Multipath ghost recognition for indoor MIMO radar,” *IEEE Trans. Geosci. Remote Sens.*, vol. 60, Art no. 5104610, pp. 1-10, 2022, doi: 10.1109/TGRS.2021.3109381

[58] J. Chen, S. Guo, H. Luo, N. Li and G. Cui, “Non-line-of-sight multi-target localization algorithm for driver-assistance radar system,” *IEEE Trans. Veh. Technology.*, IEEE early access, 2022, doi: 10.1109/TVT.2022.3227971.

[59] S. Kullback, Information Theory and Statistics. Dover Publications, NY, USA, 1978.

[60] K. Burnham and D. Anderson, Model selection and Multimodel Inference : A Practical Information-Theoretic Approach. Springer-Verlang, USA, 2002.

[61] W. Press, S. Teukolsky, W. Vetterling and B. Flannery, Numerical Recipes: The Art of Scientific Computing, 3rd Edition. Cambridge University Press, USA, 2007.

[62] C. Bishop, Pattern Recognition and Machine Learning. Springer-Verlang, USA, 2006.

[63] A. Stavridis, M. Renzo, and H. Haas, “Performance analysis of multistream receive spatial modulation in the MIMO broadcast channel,” *IEEE Trans. Wireless Commun.*, vol. 15, no. 3, pp. 1808-1820, Mar. 2016, doi: 10.1109/TWC.2015.2496597.

[64] A. Goldsmith, Wireless Communications. Cambridge University Press, 2005.

[65] A. Prudnikov, Y. Brychkov, and O. Marichev, *Integrals Series: Special Functions*, 3rd ed. London, U.K.: Gordon and Breach Science Publishers, 1986.

[66] H. Zhang, B. Zong, and J. Xie, “Power and bandwidth allocation for multi-target tracking in collocated MIMO radar,” *IEEE Trans. Veh. Technol.*, vol. 69, no. 9, pp. 9795-9806, Sep. 2020, doi: 10.1109/TVT.2020.3002899.

[67] H. Zhang, J. Shi, Q. Zhang, B. Zong, and J. Xie, “Antenna selection for target tracking in collocated MIMO radar,” *IEEE Trans. Aerosp. Electron. Sys.*, vol. 57, no. 1, pp. 423-436, Feb. 2021, doi: 10.1109/TAES.2020.3031767.

[68] A. Hassanien and S. Vorobyov, “Transmit energy focusing for DOA estimation in MIMO radar with colocated antennas,” *IEEE Trans. Signal Process.*, vol. 59, no. 6, pp. 2669-2682, Jun. 2011, doi: 10.1109/TSP.2011.2125960.

[69] H. Xu, J. Wang, J. Yuan, and X. Shan, “Colocated MIMO radar transmit beamspace design for randomly present target detection,” *IEEE Signal Process. Lett.*, vol. 22, no. 7, pp. 828-832, Jul. 2015, doi: 10.1109/LSP.2014.2371241.

[70] H. Xu, R. S. Blum, J. Wang, and J. Yuan, “Colocated MIMO radar waveform design for transmit beampattern formation,” *IEEE Trans. Aerosp. Electron. Sys.*, vol. 51, no. 2, pp. 1558-1568, Apr. 2015, doi: 10.1109/TAES.2014.140249.

[71] K. Sayana, J. Zhuang and K. Stewart, IEEE 802.16 Broadband Wireless Access Working Group: Channel Estimation Modeling for System Simulations. Technical Report, no. IEEE C802.16m-07/208, Motorola Inc 600, N US Hwy 45, Libertyville, IL, 2007.

[72] P. Arvidson, Channel Estimation Error Model for SRS in LTE. Technical Report, nO. EAB/FJL-10:0537 Uen, Ericsson, 2010.

[73] S. Kay, Fundementals of Statistical Signal Processing: Part II. Englewood Cliffs, NJ: Prentice-Hall, 1998.

[74] M. Abramowitz and I. Stegun, Handbook of Mathematical Functions with Formulas, New York, 1972.

[75] I. Gradshteyn and I. Ryzhik, Table of Integrals, Series and Products, 7th ed. USA: Academic Press, 2000.

[76] D. Hinkley, “On the ratio of two correlated normal random variables,” *Biometrika*, vol. 56, no. 3, pp. 635–639, Dec. 1969, doi:10.2307/2334671. JSTOR 2334671.

[77] Prudnikov, Y. Brychkov, and O. Marichev, *Integrals Series: Elementary Functions*. 3rd ed. London, U.K.: Gordon and Breach Science Publishers, 1986.

Chapter 6

Performance Analysis of Wireless Mesh Backhauling Using Intelligent Reflecting Surfaces[1]

Abstract

This paper considers the deployment of intelligent reflecting surfaces (IRSs) technology for wireless multi-hop backhauling of multiple basestations (BSs) connected in a mesh topology. The performance of the proposed architecture is evaluated in terms of outage and symbol error probability in Rician fading channels, where closed-form expressions are derived and demonstrated to be accurate for several cases of interest. The analytical results corroborated by simulation, show that the IRS-mesh backhauling architecture has several desired features that can be exploited to overcome some of the backhauling challenges, particularly the severe attenuation at high frequencies. For example, using IRS with four elements, $N = 4$ provides a symbol error rate of about 10^{-5} at a signal-to-noise ratio of about 0 dB, even for a large number of hops. Moreover, the obtained analytical results corroborated by Monte Carlo simulation show that the gain obtained by increasing N decreases significantly for $N > 5$. For example, increasing N from 1 to 2 provides about 8 dB of gain, while the increase from 3 to 4 provides about 4 dB. Moreover, the degradation caused by the relaying process becomes negligible when the number of IRS elements $N = 3$.

[1]**M. A. Al-Jarrah**, E. Alsusa, A. Al-Dweik and M.-S. Alouini, "Performance analysis of wireless mesh backhauling using intelligent reflecting surfaces," *IEEE Trans. Wireless Commun.*, vol. 20, no. 6, pp. 3597-3610, Jun. 2021, doi: 10.1109/TWC.2021.3052370.

Index Terms

6G, wireless backhauling, mesh backhauling, intelligent reflecting surfaces (IRSs), symbol error rate, outage probability, Rician channel.

6.1 Introduction

Current wireless communication networks such as the fourth and fifth generations, (4G) and (5G) respectively, have to support more than 6 billion users with a considerable proportion running applications that require high data rates [1–3], that severely strain the available spectrum. Moreover, the demand for data services is continuously increasing as shown by the latest statistics of wireless networks, which revealed that data traffic for mobile users grew 68% in 2019, reaching 38 Exabyte (EB) per month as compared to 27 EB per month in 2018 [1, 2]. Ericsson predicts that the mobile data traffic will show an upsurge of 27% annually till 2025. Network densification (NeDe) is one of the prominent techniques that can be used to improve the capacity of wireless networks, and it is an integral part of the 5G architecture [4, 5]. The main concept of NeDe is to deploy a large number of small cells with low power to complement the macro cell functionality in areas with poor signal quality, such as indoor environments and urban areas with tall buildings [6, 7]. The term small-cell covers a variety of cell types such as mini-cells, micro-cells, pico-cells, femto-cells, and mobile-small cell. Wireless coverage at the street level is a key solution in urban areas where the access points are placed on poles and walls [8, 9].

While indoor small-cell backhauling is typically based on wired technologies, outdoor small cells backhauling is mostly performed through wireless technologies, which may increase the macro cell base station (BS) backhauling traffic rate to several gigabit/s (Gbps) [10]. Although existing fiber infrastructure provides reliable and large capacity communications with rates that may reach terabit/s, installing new fiber infrastructure has limitations such as the high installation and maintenance cost, considerable installation time, and trenching is prohibitively expensive and might be impossible in some areas. For example, according to [11,12], about 85% of the fiber links cost is due to trenching and installation. Consequently, high dense small cells with wireless backhauling, which is the main focus in this work, are widely considered to combat the wired solutions limitations. The main advantages of wireless over wired backhauling are the scalability, flexibility, cost efficiency, and low-complexity maintenance process. To reduce the traffic load on the macro BS, wireless mesh backhauling is indispensable, and is considered an integral technology of the current 5G, future sixth generation (6G) and $6G^{+}$ cellular communication networks [8, 9]. Moreover, wireless backhauling is the key enabler for the integrated access and backhauling (IAB) technology, which is a promising approach to reduce the deployment cost in ultra-dense networks by utilizing a portion of the available radio resources for wireless backhauling [13–16]. Recently, wireless backhauling has been investigated and standardized by the 3rd Generation Partnership Project (3GPP) Rel-16 and Rel-17, the

European Commission (EC) and Ericsson [8, 10, 17], and has attracted extensive research attention in the quest to develop efficient backhauling solutions.

One of the prominent efforts on wireless backhauling is the Telecom Infra Project (TIP), which consists of more than 500 member organizations that devote their efforts to accelerate the development of new infrastructure solutions for future networks [18, 19, 21, 22, 62]. Wireless backhauling can be realized with several network topologies such as ring, tree and mesh, with the later being the most attractive because it provides backhauling with low-cost, flexible configuration, maintainable, and long distance coverage [23–26]. However, wireless backhauling suffers from some limitations as compared to optical fiber, particularly the relatively low capacity, disruptive interference, and severe signal attenuation at high frequencies. Therefore, several researchers have proposed transmission schemes and technologies to overcome one or more of the wireless backhauling limitations. Examples for such solutions include millimeter-wave (mmWave) transmission, free-space optical (FSO), interference management protocols [27–31] and massive multiple-input-multiple-output (mMIMO) [32–36].

The lack of spectrum supporting wide channel bandwidths has been identified as a potential bottleneck for wireless backhaul. This has given spectrum administrators the opportunity to introduce wider channels in currently used frequencies. An additional possibility is to open new frequency bands such as the 90 GHz band [10]. The European Telecommunications Standards Institute (ETSI) and TIP recommend mmWave communications as a core technology [18, 19, 62]. Realistic experiments have been conducted for one Gbps average peak user throughput for a maximum range of 250 m [19]. In addition, the TIP backhaul team has proposed different methods for assessing the performance of mmWave, and provided a guidance for the installation process [21, 22].

Intelligent reflecting surfaces (IRSs), also called metasurfaces, have been introduced recently with the aim of controlling the propagation medium to enhance the quality of service (QoS) by boosting the energy and spectral efficiencies of wireless networks. The IRS technology is expected to play a significant role in the future, where smartness, energy efficiency and spectral efficiency are the main requirements for the forthcoming wireless networks. IRS applies a large number of passive antenna elements which introduce a phase-shift to the received signals, and reflect them back to the destination. For efficient transmission, multiple reflectors are used to target a certain destination, and the introduced phase shifts are selected to ensure that the reflected signals add coherently at the receiver. As a result, the signal-to-noise ratio (SNR) increases considerably, and consequently, the spectral efficiency is boosted [37]- [52]. In the context of wireless backhauling, particularly when small cells are deployed in urban areas, using IRSs is crucial to improve the signal quality in the absence of line-of-sight (LoS) connectivity between certain BSs. In this case, a virtual LoS can be created by inserting IRS panels between such BSs, where the locations of IRS panels are selected to ensure a strong LoS for transmitter-IRS and IRS-receiver paths. Such scenarios are expected when the small cells are deployed at the street level in urban areas [8]. Moreover, even if

LoS exists, IRS can significantly boost the signal quality by focusing the radiated energy towards the destination BS.

6.1.1 Related Work

IRS has recently attracted extensive research attention. For example, the authors of [37, 38] presented detailed IRS technology overview, and discussed state-of-art solutions and theoretical performance limits. Energy-efficient approaches for the transmit power allocation and the phase shifts of the IRS elements is introduced in [39], where an accurate model for IRS power consumption is presented. A realistic implementation in outdoor environments has shown that the methods proposed in [39] for IRS power allocation may provide up to 300% higher energy efficiency when compared to multi-antenna and amplify-and-forward systems. Joint active and passive beamforming is considered in [5], where some recommendations are provided for optimal deployment. Other research efforts are dedicated to study the performance of IRS with other existing signalling and communication technologies such as index modulation (IM) [41], space-shift-keying (SSK) [42], and non-orthogonal multiple access (NOMA) [45]. In [43], IRS assisted MIMO is investigated, where efficient algorithms for the phase shifts at the IRS and precoding at the transmitter are proposed to minimize the symbol error rate (SER). Since the optimum values for the phase shifts depend on the instantaneous channel side information (CSI), channel modeling and estimation are considered in [44]- [47]. In [49], the far-field pathloss model is derived for IRS based links using optical physics techniques, and it is shown that each reflecting element acts as a diffuse scatterer. A practical IRS implementation is introduced in [50], where a high-gain and low-cost IRS with 256 reflecting elements is designed, in which positive intrinsic negative (PIN) diodes are used to design 2-bit phase shifters, and it was shown that a gain of 19.1 dBi can be achieved using mmWave. In [51], the joint design of the beamforming matrix and phase shift matrix at the BS and IRS is investigated using deep reinforcement learning algorithms. An overview about holographic MIMO surfaces is provided in [53] including the hardware architectures for reconfiguring the surfaces.

6.1.2 Motivation and Contribution

Future mobile networks are expected to confine more of the radio communication needs of current users, and support many new users and industries, with applications that require ultra high data rates. Examples for such applications include holographic communication, online gaming, and streaming of super high definition immersive 3D videos, etc. To be able to support such applications for a large number of users, the network should be able to handle traffic volumes in the range of terrabit/s per square kilometer, coming from a massive simultaneous connections [10]. Consequently, the backhaul traffic between the base stations (BSs) is expected to experience enormous data rate and traffic volume increase, and thus the design of a backhaul that satisfies such scenarios is indispensable.

This work focuses on the wireless portion of the backhaul network where data volumes are forwarded to a nearby BS which has a fiber connection with the corenetwork. Since the link to the fiber-connected BS may have multiple hops, the analysis is generalized to multiple hop scenario, where IRS panels with N reflectors are deployed between communicating BSs in each hop to enhance the connection reliability. The obtained analytical results corroborated by Monte Carlo simulation demonstrate that the gain achieved by increasing the number of IRS elements is inversely proportional to the number of IRS elements N, particularly for $N > 5$. Moreover, the degradation caused by the relaying process becomes negligible when the number of IRS elements is more than 3. The contribution of this paper can be summarized as follows:

1. Although IRSs have been considered widely in the recent literature [37,38], to the best of the authors' knowledge, there is no work reported that considers the application of IRS in wireless backhauling with multiple hops, where BSs relay the traffic until it arrives to the core network.

2. Because wireless backhauling typically requires LoS connectivity to avoid severe signal fading, the channel gain is assumed to follow the Rician fading model.

3. An accurate approximation for the probability density function (PDF) of the received SNR is derived.

4. Analytical expressions are derived for the SER and outage probability (OP) for single and multi hop scenarios.

5. Because some of the analytical results are represented in terms of infinite series, numerical results for the truncation error are presented to demonstrate the convergence behavior of the derived solution. The obtained results showed that using about 30 terms in the summations provides a truncation error of less than 10^{-7} for most cases of interest.

6.1.3 Paper organization

The rest of the paper is organized as follows. Sec. 6.2 presents the system model with IRS based wireless backhauling. A derivation for an accurate approximation for the PDF of the received SNR per hop is introduced in Sec. 6.3. The derivations for the SER and OP are provided in Secs. 6.4 and 6.5, respectively. Sec. 6.6 shows and discusses the numerical results of the proposed system whereas the conclusion and future work are provided in Sec. 6.7.

6.2 System Model

This work considers a heterogenous wireless network where a macro cell is overlaid with multiple small cells. The macro BS (mBS) and small-cells BS (sBS) are configured in a mesh topology. In such networks

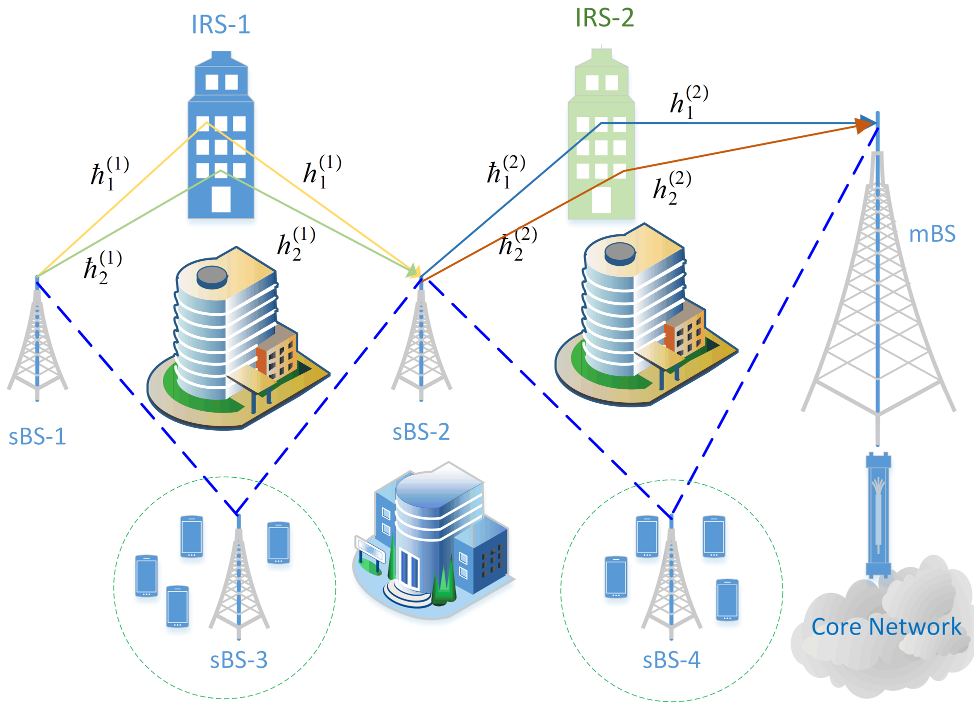

Figure 6.1: Example for a two-hop backhauling using IRS in a mesh network with IBA. The mesh network consists of four sBSs and one mBS.

[54], each sBS might be able to communicate with multiple other sBSs and choose a particular route to backhaul its data to the core network. Fig. 7.1 shows a simplified mesh network with IBA using four sBSs and one mBS. As shown in the figure, some routes may only be utilized through IRS. Once a particular route is selected, the sBSs cooperate, act as relays, to route the backhaul traffic to the mBS, and then to the core network. Therefore, the traffic of a particular sBSs may arrive to the mBS through multiple hops, where the signal in each hop is decoded and forwarded to the next sBS, or to the mBS. The route selection process is typically performed to optimize certain performance parameters such as delay, interference, power, energy or load balance [55–59]. Therefore, the number of hops is generally a random variable which has been the subject of some studies dedicated to model the hop count [60], [61]. To provide LoS links between adjacent sBSs, IRS panels, each of which consists of N reflecting elements, are placed between each two BSs. The backhaul links are realized using a single broadband antenna at each BS. Using the region three-dimensional maps, advanced ray tracing techniques [62] can be used to predict the CSI between adjacent BSs and the IRS, which allow selecting the optimum location for the IRS panels'. The channel fading is considered to be Rician to capture the LoS signal component and other small reflections from the surrounding environment. The LoS is considered only between the BSs and the IRS, while the direct path between BSs is typically blocked by large buildings or other obstacles.

In each hop, a sBS transmits its backhaul traffic to one of the adjacent sBSs, or to the mBS, through an IRS panel, where each reflecting element introduces a phase shift φ_n and amplitude gain β_n. The process is repeated L times until the data arrive at the corenetwork or mBS. It is worth noting that an IRS panel can be shared by multiple BSs simultaneously, where the available reflecting elements can be assigned to BSs that have LoS link with the IRS panel. However, an IRS element can be assigned only to one BS to avoid interference.

In this work, we initially consider the single hop scenario, and then the model is extended to multiple hops. Consequently, the hop index is dropped unless it is necessary to include it. Given that a particular sBS transmits a data symbol s, the signal reflected from the nth IRS element can be expressed as

$$x_n = \sqrt{P_0} H_n \hbar_n s,\ n \in \{1, 2, \ldots, N\} \tag{6.1}$$

where $H_n = \beta_n \mathrm{e}^{j\varphi_n}$, φ_n is the phase shift and $\beta_n \leq 1$ is the reflection coefficient of the nth IRS element, P_0 is the sBS transmission power, and the channel coefficient $\hbar_n \triangleq |\hbar_n| \mathrm{e}^{j\theta_n} \sim \mathcal{CN}\left(m_n, 2\sigma_n^2\right)$. In urban environments, sBSs do not typically have LoS link with each other due to the dense and large structures in such environments. Therefore, IRSs can be deployed in specific locations such that a LoS connection is established between the IRS and each of the concerned sBSs. Therefore, the PDF of the channel envelop $\alpha_n \triangleq |\hbar_n|$ can be considered Rician [63],

$$f\left(\alpha_n\right) = \frac{2(1+K_n)}{\Omega_n} \alpha_n \, \mathrm{e}^{-K_n} \, \mathrm{e}^{-\frac{(1+K_n)}{\Omega_n} \alpha_n^2} \times I_0 \left(2\alpha_n \sqrt{\frac{K_n(1+K_n)}{\Omega_n}}\right) \tag{6.2}$$

where $I_0\left(\cdot\right)$ is the modified Bessel function of the first kind and zero order, $\Omega_n \triangleq \mathrm{E}\left[\alpha_n^2\right] = \mu_n^2 + 2\sigma_n^2$, $\mu_n = |m_n|$, the average channel fading $m_n \geq 0$, and $K_n = \frac{\mu_n^2}{2\sigma_n^2}$ is the Rician factor that determines the link quality, $K_n \in (0, \infty)$. For small values of K_n, the channel fading becomes severe, which indicates that the LoS signal component is weak. However, according to some experimental measurements, it has been shown that the received signal amplitude in urban and suburban areas follows the Rician distribution with $K_n \gtrsim 9$ dB due to strong LoS propagation [64]- [69]. The first moment of α_n with parameters K_n and Ω_n is given by [70]

$$\mathrm{E}\left[\alpha_n\right] = \tfrac{1}{2}\sqrt{\frac{\pi\Omega_n}{1+K_n}} \; {}_1F_1\left(-\frac{1}{2}, 1, -K_n\right) \tag{6.3}$$

where $\mathrm{E}\left[\cdot\right]$ denotes the expected value and ${}_1F_1\left(\cdot,\cdot,\cdot\right)$ is the confluent hypergeometric function of the first kind.

In the reflecting phase, the signal will go through a second fading channel h_n before arriving to the destination BS. Therefore, the received signal at the destination BS is given by

$$\begin{aligned} y &= \sqrt{P_0} \sum_{n=1}^{N} \beta_n h_n \hbar_n \mathrm{e}^{j\varphi_n} s + w \\ &= \sqrt{P_0} \sum_{n=1}^{N} \beta_n \left|\hbar_n\right| \left|h_n\right| \mathrm{e}^{j(\theta_n + \zeta_n + \varphi_n)} s + w. \end{aligned} \tag{6.4}$$

where the channel coefficient $h_n \triangleq |h_n| \mathrm{e}^{j\zeta_n} \sim \mathcal{CN}\left(\bar{m}_n, 2\bar{\sigma}_n^2\right)$ and w is the additive white Gaussian noise

(AWGN), $w \sim \mathcal{CN}\left(0, \sigma_w^2\right)$. By selecting $\varphi_n = -\left(\theta_n + \zeta_n\right)$, all the reflected signal components are added coherently in the channel, and thus, the received signal at BS can be rewritten as

$$y = \sqrt{P_0} \sum_{n=1}^{N} \beta_n \varpi_n s + w. \tag{6.5}$$

where $|\hbar_n| \, |h_n| \triangleq \varpi_n$. Therefore, ϖ_n is formed by the product of two Rician random variables, and hence, its PDF is given by [71, eq. 6.67]

$$f_{\varpi_n}\left(\varpi_n\right) = \frac{\mathrm{e}^{-\left(K_n + \bar{K}_n\right)}}{\sigma_n^2 \bar{\sigma}_n^2} \varpi_n \sum_{i=0}^{\infty} \sum_{l=0}^{\infty} \frac{\bar{K}_n^l K_n^i}{\left(i! l!\right)^2} \left(\frac{\varpi_n}{2 \bar{\sigma}_n \sigma_n}\right)^{i+l} \times \mathcal{K}_{i-l}\left(\frac{\varpi_n}{\sigma_n \bar{\sigma}_n}\right) \tag{6.6}$$

where $\bar{K}$ is the Rician factor for channel h_n and $\mathcal{K}_m\left(\cdot\right)$ is the modified Bessel function of the second kind with order m.

6.3 SNR Distribution

To derive the SER and OP, the SNR distribution should be evaluated. Towards this goal, the following two subsections present the PDF derivation of the instantaneous SNR at the destination BS for a single and multiple reflectors, respectively.

6.3.1 Single Reflector ($N = 1$)

Based on the received signal in (6.5), the instantaneous SNR of the received signal at the BS for a signal reflected from the nth reflector, can be written as

$$\gamma_n = \mathcal{P} \beta_n^2 \varpi_n^2 \tag{6.7}$$

where $\mathcal{P} \triangleq P_0/\sigma_w^2$. Using $f_{\varpi_n}\left(\varpi_n\right)$ given in (6.6), the PDF of γ_n can be obtained by applying random variable transformation. Consequently, $f_{\gamma_n}\left(\gamma_n\right)$ can be written as

$$f_{\gamma_n}\left(\gamma_n\right) = C_n \sum_{i=0}^{\infty} \sum_{l=0}^{\infty} D_{i,l}^n \gamma_n^{\frac{i+l}{2}} \mathcal{K}_{i-l}\left(E_n \sqrt{\gamma_n}\right) \tag{6.8}$$

where

$$E_n = \frac{2}{\beta_n} \sqrt{\frac{\left(1 + K_n\right)\left(1 + \bar{K}_n\right)}{\Omega_n \, \bar{\Omega}_n \mathcal{P}}} \tag{6.9}$$

$$C_n = \frac{E_n^2}{2} \mathrm{e}^{-\left(K_n + \bar{K}_n\right)} \tag{6.10}$$

$$D_{i,l}^n = \frac{K_n^i \bar{K}_n^l}{\left(i! l!\right)^2} \left(\frac{E_n}{2}\right)^{i+l}. \tag{6.11}$$

6.3.2 Multiple Reflectors($N > 1$)

Based on the received signal in (6.5), the instantaneous SNR for $N > 1$ can be written as

$$\gamma = \left(\sqrt{\mathcal{P}}\sum_{n=1}^{N}\beta_n\varpi_n\right)^2. \tag{6.12}$$

Unlike the single reflector case, deriving a closed-form expression for the PDF of γ is intractable. Consequently, an approximate PDF will be derived to enable analytical performance evaluation. To this end, the cascaded channels for the nth reflector can be written as $Z_n = \hbar_n h_n \triangleq Z_n^I + jZ_n^Q$, where $Z_n^I = \hbar_n^I h_n^I - \hbar_n^Q h_n^Q$ and $Z_n^Q = \hbar_n^I h_n^Q + \hbar_n^Q h_n^I$, $\left\{\hbar_n^I, \hbar_n^Q, h_n^I, h_n^Q\right\} \sim \mathcal{N}\left(\left\{\bar{m}_n^I, \bar{m}_n^Q, m_n^I, m_n^Q\right\}, \left\{\bar{\sigma}_n^2, \bar{\sigma}_n^2, \sigma_n^2, \sigma_n^2\right\}\right)$. In general, the product of two independent Gaussian random variables $X \sim \mathcal{N}\left(m_X, \sigma_X^2\right)$ and $Y \sim \mathcal{N}\left(m_Y, \sigma_Y^2\right)$ is not Gaussian [72]. However, if $\left\{\frac{\mu_X}{\sigma_X}, \frac{\mu_Y}{\sigma_Y}\right\} \gg 1$, then the PDF of the product can be approximated by $\mathcal{N}\left(m_X m_Y, m_X^2\sigma_Y^2 + m_Y^2\sigma_X^2\right)$ [73, 74]. For Rician fading channels, such condition can be satisfied when the Rician factors $\left\{\bar{K}, K\right\} \gg 1$ dB, and thus the approximation is very accurate for strong LoS environments. Consequently, the PDFs of Z_n^I and Z_n^Q can be approximated as $Z_n^I \sim \mathcal{N}\left(m_{Z_n^I}, \sigma_{Z_n}^2\right)$ and $Z_n^Q \sim \mathcal{N}\left(m_{Z_n^Q}, \sigma_{Z_n}^2\right)$. Given that $\sigma_n^I = \sigma_n^Q = \sigma_n$ and $\bar{\sigma}_n^I = \bar{\sigma}_n^Q = \bar{\sigma}_n$, the statistics of Z_n^I and Z_n^Q are given by

$$m_{Z_n^I} = m_n^I\bar{m}_n^I - m_n^Q\bar{m}_n^Q \tag{6.13}$$

$$\sigma_{Z_n^I}^2 = \mu_n^2\bar{\sigma}_n^2 + \bar{\mu}_n^2\sigma_n^2 \tag{6.14}$$

$$m_{Z_n^Q} = m_n^I\bar{m}_n^Q + m_n^Q\bar{m}_n^I \tag{6.15}$$

$$\sigma_{Z_n^Q}^2 = \mu_n^2\bar{\sigma}_n^2 + \bar{\mu}_n^2\sigma_n^2. \tag{6.16}$$

Therefore, $\sqrt{\mathcal{P}}\beta_n Z_n^I \sim \mathcal{N}\left(\sqrt{\mathcal{P}}\beta_n m_{Z_n^I}, \beta_n^2\mathcal{P}\sigma_{Z_n}^2\right)$ and $\sqrt{\mathcal{P}}\beta_n Z_n^Q \sim \mathcal{N}\left(\beta_n\sqrt{\mathcal{P}}m_{Z_n^Q}, \beta_n^2\mathcal{P}\sigma_{Z_n}^2\right)$. Consequently, the PDF of Z_n can be approximated as $Z_n \sim \mathcal{CN}\left(m_{Z_n}, 2\sigma_{Z_n}^2\right)$, where $m_{Z_n} = m_{Z_n^I} + jm_{Z_n^Q}$ and $\sigma_{Z_n}^2 = \sigma_{Z_n^I}^2 = \sigma_{Z_n^Q}^2$. In addition, as can be noted from the statistics of Z_n^I and Z_n^Q in (6.13)-(6.16), Z_n^I and Z_n^Q have the same variance but different mean values. Consequently, the distribution of ϖ_n can be approximated by a Rician PDF with mean and variance that are given by

$$\begin{aligned}\mu_{Z_n} &= \left|m_{Z_n}\right|^2\\ &= \bar{\mu}_n\mu_n\end{aligned} \tag{6.17}$$

$$\sigma_{Z_n}^2 = \mu_n^2\bar{\sigma}_n^2 + \bar{\mu}_n^2\sigma_n^2. \tag{6.18}$$

Consequently, the Rician PDF parameters Ω_{ϖ_n} and K_{ϖ_n} can be written as

$$\begin{aligned}\Omega_{\varpi_n} &= \mu_{Z_n}^2 + 2\sigma_{Z_n}^2 \\ &= \bar{\mu}_n^2 \mu_n^2 + 2\left(\mu_n^2 \bar{\sigma}_n^2 + \bar{\mu}_n^2 \sigma_n^2\right)\end{aligned} \tag{6.19}$$

$$K_{\varpi_n} = \frac{\bar{K}_n K_n}{\bar{K}_n + K_n}. \tag{6.20}$$

Based on (6.20), a cascaded channel of two Rician channels having Rician factors $\bar{K}$ and K can be approximated as a Rician channel with Rician factor $K_{\varpi_n} < \min\left(\bar{K}_n, K_n\right)$ given that $\bar{K}_n$ and K_n are large.

By simple random variable transformation, the PDF of $\lambda_n{=}\sqrt{\mathcal{P}}\beta_n\varpi_n$ can be found as Rician with the following distribution.

$$f_{\lambda_n}\left(\lambda_n\right) = \frac{2(1+K_{\lambda_n})}{\Omega_{\lambda_n}\,\mathrm{e}^{K_{\lambda_n}}}\lambda_n\,\mathrm{e}^{-\frac{(1+K_{\lambda_n})}{\Omega_{\lambda_n}}\lambda_n^2} \times I_0\left(2\lambda_n\sqrt{\frac{K_{\lambda_n}(1+K_{\lambda_n})}{\Omega_{\lambda_n}}}\right) \tag{6.21}$$

where $K_{\lambda_n} = K_{\varpi_n}$ and $\Omega_{\lambda_n} = \Omega_{\varpi_n}\mathcal{P}\beta_n^2$. However, the distribution of the sum of multiple Rician random variables, $\Lambda = \sum_n \lambda_n$, does not have a closed form expression. Therefore, an accurate closed-form approximation will be used as described in [75] to enable analytical performance evaluation. It is worth noting that there is a typo in [75, Eq. 5], where the first term should be $1/\sqrt{2\pi\sigma_{\lambda_n}^2}$ instead of $1/\sqrt{2\pi}$. To simplify the discussion, it is assumed that $\beta_n = \beta\ \forall n$, and a new variable is defined as $\check{P}_0 \triangleq \beta^2 P_0$ and $\check{\mathcal{P}} \triangleq \check{P}_0/\sigma_w^2$, to simplify the notation. Finally, by simple random variable transformation for the distribution of Λ given in [75], the distribution of $\gamma{=}\Lambda^2$ can be provided as

$$f_\gamma\left(\gamma\right) = \frac{1}{\sigma_{\lambda_n}\sqrt{8\pi N\check{\mathcal{P}}\gamma}}\,\mathrm{e}^{-\frac{\left(\sqrt{\frac{\gamma}{\check{\mathcal{P}}}}-\mu_{\lambda_n}N\right)^2}{2N\sigma_{\lambda_n}^2}} + f_c\left(\gamma\right) \tag{6.22}$$

where μ_{λ_n} and $\sigma_{\lambda_n}^2$ are the mean and variance of λ_n, respectively, and $f_c\left(\gamma\right)$ is a correction

$$f_c\left(\gamma\right) = \frac{a_0}{2a_1\sqrt{\check{\mathcal{P}}\gamma}}\Psi_{(\gamma)}\left(\Psi_{(\gamma)}^2 - 3\right)\mathrm{e}^{-\frac{1}{2}\Psi_{(\gamma)}^2} \tag{6.23}$$

where $\Psi_{(\gamma)} = \left(\sqrt{\frac{\gamma}{\check{\mathcal{P}}}} - \sqrt{N}a_2\right)/\sqrt{N}a_1$, and the coefficients a_0, a_1 and a_2 are used to control the amplitude, spread and shift, respectively. In [75], the values of these coefficients depend on the Rician factor K and the number of random variables N. The method for evaluating the coefficients is introduced in [75], which is based on the least squares fitting with the exact cumulative distribution function (CDF). A table is provided in [75] for certain cases, however, these coefficients can be evaluated using nonlinear curve-fitting in least-squares sense, where the exact CDF can be obtained by convolving N Rician PDFs and then performing numerical integration.

6.3.3 The SNR Gain

The SNR improvement gained by increasing N can be measured using the effective SNR of the received signal, which can be defined for the lth hop as

$$\bar{\gamma}_{N,l} \triangleq \mathrm{E}\left[\gamma\right] \tag{6.24}$$

Substituting (6.12) into (6.24) gives

$$\begin{aligned}\bar{\gamma}_{N,l} &= \mathcal{P}\,\mathrm{E}\left[\left(\sum_{n=1}^{N}\beta_n\varpi_n\right)^2\right]\\ &= \mathcal{P}\,\mathrm{E}\left[\sum_{n=1}^{N}\left(\beta_n^2\left|\hbar_n\right|^2\left|h_n\right|^2+2\sum_{k>n}^{N}\beta_n \quad \times\left|\hbar_n\right|\left|h_n\right|\beta_k\left|\hbar_k\right|\left|h_k\right|\right)\right]\\ &= \mathcal{P}\sum_{n=1}^{N}\left(\beta_n^2\Omega_n\bar{\Omega}_n+2\sum_{k>n}^{N}\beta_k\beta_n \quad \times\mathrm{E}\left[\left|\hbar_n\right|\right]\mathrm{E}\left[\left|h_n\right|\right]\mathrm{E}\left[\left|\hbar_k\right|\right]\mathrm{E}\left[\left|h_k\right|\right]\right)\end{aligned} \tag{6.25}$$

where the expected value of the channel envelope is given in (6.3). For independent and identically distributed (i.i.d.) channels and equal reflection coefficients, $\beta_n = \beta\ \forall n$, then $\bar{\gamma}_N$ can be expressed as

$$\begin{aligned}\bar{\gamma}_{N,l} &= \mathcal{P}\ \beta^2 N\left(\Omega^2+(N-1)\,\beta^2\mathrm{E}^4\left[\alpha\right]\right)\\ &= \mathcal{P}\ \beta^2 N^2\left(\frac{\Omega^2-\beta^4\mathrm{E}^4\left[\alpha\right]}{N}+\beta^2\mathrm{E}^4\left[\alpha\right]\right)\end{aligned} \tag{6.26}$$

For large value of N, $\beta^2\mathrm{E}^4\left[\alpha\right] \gg \frac{\Omega^2-\beta^4\mathrm{E}^4[\alpha]}{N}$, and thus,

$$\bar{\gamma}_{N,l} \approx \mathcal{P}\ \beta^4\mathrm{E}^4\left[\alpha\right]\ N^2. \tag{6.27}$$

Therefore, the effective received SNR for large number of reflectors becomes linearly proportional to N^2. It is also worth noting that $\mathrm{E}\left[\alpha\right]$ is an increasing function versus the Rician factor K, which implies that increasing K provides additional improvement to $\bar{\gamma}_{N,l}$.

6.4 Symbol Error Rate (SER) Analysis

To evaluate the SER of signalling over fading channels, the general method is to model the channel as conditionally Gaussian, obtain the SER, and then to eliminate the conditioning by averaging the conditional SER over the instantaneous SNR γ. Therefore, the average SER $\bar{P}_S$ can be computed as

$$\bar{P}_S = \int_0^\infty P_S\left(\gamma\right) f_\gamma\left(\gamma\right) d\gamma. \tag{6.28}$$

For most widely used modulation schemes such as quadrature amplitude modulation (QAM) and phase shift keying (PSK), the conditional SER for a given γ in the presence of AWGN can be approximated as

$$P_S(\gamma) \simeq AQ\left(\sqrt{B\gamma}\right) \tag{6.29}$$

where $Q(\cdot)$ is the complementary cumulative distribution function of the Gaussian distribution, and the values of A and B depend on the modulation scheme [76, Table 6.1, pp. 167]. The values of A and B can be selected such that (6.29) can be used to evaluate the bit error rate (BER).

6.4.1 Single Reflector ($N = 1$), Single Hop ($L = 1$)

The SER for the single reflector case can be obtained by substituting (6.8) and (6.29) into (6.28), and defining $\sqrt{\gamma} \triangleq y$, which yields

$$\bar{P}_S = 2AC_n \sum_{i=0}^{\infty}\sum_{l=0}^{\infty} D_{i,l}^{n} \int_0^{\infty} y^{i+l+1} Q\left(\sqrt{B}y\right) \mathcal{K}_{i-l}(Ey)\, dy. \tag{6.30}$$

As can be noted that the closed form for the integral is very difficult to obtain. Therefore, approximating either the Q-function or the modified Bessel function can result in a solvable integration. However, to make the integration feasible, tight and tractable approximation for $Q(x)$, which has been proposed in [84], is applied. The approximation is based on a truncated series and given by

$$Q(x) \simeq \frac{\mathrm{e}^{-\frac{x^2}{2}}}{1.135\sqrt{\pi}} \sum_{i=1}^{n_a} \frac{(-1)^{i+1}\, 1.98^i}{i!\; 2^{\frac{i+1}{2}}} x^{i-1} \tag{6.31}$$

where the number of terms in the summation n_a can be selected depending on the desired tightness. Substituting (6.31) in (6.30) yields

$$\bar{P}_S = \frac{2AC_n}{1.135\sqrt{\pi}} \sum_{i=0}^{\infty}\sum_{l=0}^{\infty} D_{i,l}^{n} \sum_{k=1}^{n_a} \frac{(-1)^{k+1}\, 1.98^k B^{\frac{k-1}{2}}}{2^{\frac{k+1}{2}}\, k!} \times \int_0^{\infty} y^{i+l+k} \mathrm{e}^{-\frac{By^2}{2}} \mathcal{K}_{i-l}(E_n y)\, dy. \tag{6.32}$$

The integral can be solved as described in [78, eq. (2.16.8.4)], which yields the SER in (6.33), where $\mathcal{W}$ is the Whittaker hypergeometric function.

$$\bar{P}_S = \frac{AC_n \mathrm{e}^{\frac{E_n^2}{4B}}}{1.135\sqrt{\pi}E_n} \sum_{i=0}^{\infty}\sum_{l=0}^{\infty} D_{i,l}^{n} \sum_{k=1}^{n_a} \frac{(-1)^{k+1}\, 1.98^k B^{\frac{k-1}{2}} \left(\frac{B}{2}\right)^{-\frac{i+l+k}{2}}}{2^{\frac{k+1}{2}}\, k!} \Gamma\left(i+\frac{k+1}{2}\right)\Gamma\left(l+\frac{k+1}{2}\right)\mathcal{W}_{-\frac{i+l+k}{2},\frac{i-l}{2}}\left(\frac{E_n^2}{2B}\right) \tag{6.33}$$

6.4.2 Multiple Reflectors ($N \geq 2$), Single Hop ($L = 1$)

The average SER $\bar{P}_S$ for this case can be derived by substituting (6.29) and (6.22) into (6.28), which after some manipulations, as shown in Appendix I, gives

$$\bar{P}_S = A\left(\frac{1}{\sigma_{\lambda_n}\sqrt{2\pi N}}T_1 + \frac{a_0}{a_1}\left[T_2 - 3T_3\right]\right) \tag{6.34}$$

where the integrals T_1, T_2 and T_3 are evaluated in Appendix I and the final solutions are given by

$$T_1 = \frac{\mathrm{e}^{-\frac{\mu_{\lambda_n}^2 N}{2\sigma_{\lambda_n}^2}}}{1.135\sqrt{\pi}}\sum_{k=1}^{n_a}\left(\frac{(-1)^{k+1}\,1.98^k}{2^{\frac{k+1}{2}}k!}\left(B\check{\mathcal{P}}\right)^{\frac{k-1}{2}}\frac{\Gamma(k)}{\rho_n^k}\times\mathrm{e}^{\frac{\mu_{\lambda_n}^2}{4\rho_n^2\sigma_{\lambda_n}^4}}\mathcal{D}_{-k}\left(\frac{-\mu_{\lambda_n}}{\sigma_{\lambda_n}^2\rho_n}\right)\right) \tag{6.35}$$

$$T_2 = \sqrt{\frac{N}{2\pi}}a_1\,\mathrm{e}^{-\frac{1}{2}\acute{a}}\left(\sqrt{\frac{\pi}{2}}\left(2+\acute{a}\right) - \mathrm{e}^{\frac{\nu^2}{8\delta}}\sum_{k=1}^{3}\omega_k\mathcal{D}_{-k}\left(\frac{\nu}{\sqrt{2\delta}}\right)\right) \tag{6.36}$$

$$T_3 = \frac{1}{2}\sqrt{\frac{N}{\pi}}a_1\,\mathrm{e}^{-\frac{1}{2}\acute{a}}\left(\sqrt{\pi} - \frac{1}{\sqrt{\delta}}\,\mathrm{e}^{\frac{\nu^2}{8\delta}}\mathcal{D}_{-1}\left(\frac{\nu}{\sqrt{2\delta}}\right)\right) \tag{6.37}$$

where $\acute{a} = a_2^2/a_1^2$, $\rho_n = \sqrt{\frac{1}{\sigma_{\lambda_n}^2 N} + B\check{\mathcal{P}}}$, $\delta = \frac{1}{2}\left(1 + \frac{1}{Na_1^2 B\check{\mathcal{P}}}\right)$, $\nu = \frac{-a_2}{a_1^2\sqrt{NB\check{\mathcal{P}}}}$, $\omega_1 = (2+\acute{a})\frac{1}{\sqrt{2\delta}}$, $\omega_2 = \frac{2\nu}{2\delta}$ and $\omega_3 = \frac{\delta^{\frac{-3}{2}}}{\sqrt{2}a_1^2 NB\check{\mathcal{P}}}$, and $\mathcal{D}_{-n}(\cdot)$ is the parabolic cylindrical function.

6.4.3 Single and Multiple Reflectors ($N > 1$), Multiple Hops ($L \geq 2$)

To extend the SER analysis for the general case where $\{N, L\} \geq 2$, we define the vector $\hat{\mathbf{s}} = [\hat{s}_1, \hat{s}_2, \ldots, \hat{s}_L]$, which contains the decoded symbols of each hop. Given that symbol s_0 is transmitted over a route of L total number of hops, the SER can be expressed as

$$\begin{aligned}\bar{P}_{S|L} &= \Pr\left(s_0 \neq \hat{s}_L\right)\\ &= \sum_{s_0}\Pr\left(\hat{s}_L \neq s_0|s_0\right)\Pr\left(s_0\right)\\ &= \frac{1}{M}\sum_{s_0}\sum_{\hat{\mathbf{s}}\in\mathbb{S}}\Pr\left(\hat{s}_1|s_0\right)\prod_{l=2}^{L}\Pr\left(\hat{s}_l|\hat{s}_{l-1}\right)\end{aligned} \tag{6.38}$$

where M is the modulation order, $\Pr(\hat{s}_1|s_0)$ is the conditional probability for the first hop, and $\Pr(\hat{s}_l|\hat{s}_{l-1})$ is the conditional probability for the remaining $L-1$ hops. The vector $\hat{\mathbf{s}} \in \mathbb{S}$, where $\mathbb{S}$ is the set of all vectors that has $\hat{s}_L \neq s_0$. Evaluating (7.61) can be performed using the approach described in [79, 80], which for the special case of binary phase shift keying (BPSK) is given by

$$\bar{P}_{S|L} = \frac{1}{2} - \frac{1}{2}\prod_{l=1}^{L}\left(1 - 2\bar{P}_{S,l}\right) \tag{6.39}$$

where $\bar{P}_{S,l}$ is the average symbol/bit error rate for the lth hop.

6.4.4 Performance Analysis with Random L

The routing protocol for a mesh network is typically designed to optimize the network parameters, i.e., maximize the total traffic, minimize the average error rate or the outage probability. In addition, most of the routing strategies permit a certain maximum limit for the number of hops based on QoS measures such as latency and time delay. Accordingly, the number of hops in a mesh network is a random variable, where the probability mass function (PMF) of the hop count depends on the system parameters and the adopted routing technique [60, 61]. For example, empirical and analytical PMFs have been compared in [60] for unit disk planar network (UDPN) and unit disk linear network (UDLN) routing protocols where the furthest neighbor (FN) and nearest neighbor (NN) strategies are considered. On the other hand, different path selection strategies for IAB are discussed in [61] including the highest quality first (HQF), wired first (WF), position aware (PA) and the maximum local rate (MLR). In this paper, the WF routing strategy is adopted [61]. According to the WF approach, if the sBS has a link with a wired mBS with SNR greater than a certain threshold, then this link is selected. Otherwise, the sBS selects the link with the highest SNR by employing HQF strategy. The same process is repeated by the receiving sBS to select the appropriate BS for the next hop. Therefore, the WF strategy tends to select paths with low number of hops. In general, given the PMF of the number of hops, the probability of error can be expressed as

$$\bar{P}_S = \sum_{L=1}^{L_{\max}} \Pr\left(L\right) \bar{P}_{S|L} \tag{6.40}$$

where $\Pr\left(L\right)$ is the probability that the message travels over a route with L hops.

6.5 Outage Probability

The OP is defined as the probability that the SNR is below a certain threshold γ_{th}, will be also denoted as χ for notational simplicity,

$$\bar{P}_O = \int_0^{\chi} f_\gamma\left(\gamma\right) d\gamma. \tag{6.41}$$

6.5.1 Single Reflector $(N = 1)$, Single Hop $(L = 1)$

By substituting (6.8) into (6.41), and applying the series expansion of the modified Bessel function, the OP can be found as

$$\bar{P}_O = C_n \sum_{i=0}^{\infty} \sum_{l=0}^{\infty} D_{i,l}^n \int_0^{\chi} \gamma^{\frac{i+l}{2}} \mathcal{K}_{i-l}\left(E_n\sqrt{\gamma}\right) d\gamma. \tag{6.42}$$

By substituting $y = \gamma/\chi$, and after some simplifications $\bar{P}_{O,1}$ can be expressed as

$$\bar{P}_O = C_n \sum_{i=0}^{\infty} \sum_{l=0}^{\infty} D_{i,l}^n \chi^{\frac{i+l}{2}+1} \int_0^{1} y^{\frac{i+l}{2}} \mathcal{K}_{i-l}\left(E_n\sqrt{y\varkappa}\right) dy. \tag{6.43}$$

Based on [81, Eq. 6.592.2], $\bar{P}_O$ can be solved in a closed-form in terms of the Meijer G function,

$$\bar{P}_O = C_n \sum_{i=0}^{\infty}\sum_{l=0}^{\infty}\frac{2^{i-l-1}}{E_n^{i-l}} D_{i,l}^{n} \chi^{l+1} G_{1,3}^{2,1}\left(\frac{\chi E_n^2}{4}\middle| \begin{matrix} -l \\ i-l, 0, -l-1 \end{matrix}\right) \tag{6.44}$$

6.5.2 Multiple Reflectors ($N \geq 2$), Single Hop ($L = 1$)

The OP for this case is derived by substituting (6.22) in (6.41) and evaluating the integral. The resultant expression can be written as

$$\bar{P}_O = \bar{P}_O^{(a)} + \bar{P}_O^{(b)} - \bar{P}_O^{(c)} \tag{6.45}$$

where the expressions of $\bar{P}_O^{(a)}$, $\bar{P}_O^{(b)}$ and $\bar{P}_O^{(c)}$ are given by

$$\bar{P}_O^{(a)} = \frac{1}{2}\left(\operatorname{erf}\left(\frac{\mu_{\lambda_n}\sqrt{N}}{\sqrt{2}\sigma_{\lambda_n}}\right) - \operatorname{erf}\left(\frac{-\check{\chi} + \mu_{\lambda_n} N}{\sqrt{2N}\sigma_{\lambda_n}}\right)\right) \tag{6.46}$$

$$\bar{P}_O^{(b)} = \frac{a_0 \, \mathrm{e}^{-\frac{1}{2}\acute{a}}}{a_1^2\sqrt{N}}\left(N\left(a_2^2 + 2a_1^2\right) + \Gamma_{\text{th}}\, \mathrm{e}^{-\frac{\check{\chi}^2 - 2\sqrt{N}a_2\check{\chi}}{2Na_1^2}}\right) \tag{6.47}$$

$$\bar{P}_O^{(c)} = 3a_0\sqrt{N}\, \mathrm{e}^{-\frac{1}{2}\acute{a}}\left(1 - \mathrm{e}^{-\check{\chi}\left(\frac{\check{\chi} - 2\sqrt{N}a_2}{2Na_1^2}\right)}\right) \tag{6.48}$$

where $\operatorname{erf}(\cdot)$ is the error function, $\check{\chi} = \sqrt{\frac{\chi}{\mathcal{P}}}$ and $\Gamma_{\text{th}} = -Na_2^2 + 2\sqrt{N}a_2\check{\chi} - \check{\chi}^2 - 2Na_1^2$. Multiple reflectors ($N \geq 2$), multiple hops ($L \geq 2$)

Given that the signal will undergo L hops, the outage event occurs if one or more of the L hops go through an outage. Therefore, OP can be formulated as [82, 83],

$$\bar{P}_{O|L} = 1 - \prod_{l=1}^{L}\left(1 - \bar{P}_{O,l}\right) \tag{6.49}$$

where $\bar{P}_{O,l}$ is the OP for the lth hop, which is given by (6.44) and (6.45) for $N = 1$ and $N \geq 2$, respectively.

6.5.3 Outage Probability with Random L

Similar to Sec. 6.4.4, the effect of a random number of hops on the outage probability can be computed as

$$\bar{P}_O = \sum_{L=1}^{L_{\max}} \Pr(L)\, \bar{P}_{O|L} \tag{6.50}$$

where $\Pr(L)$ is the probability that the message travels over a route with L hops.

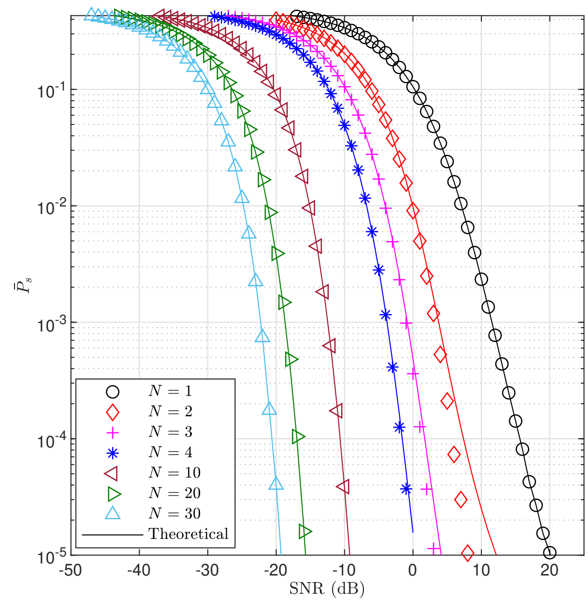

Figure 6.2: SER using BPSK for various values of N, $K = 10$ dB and $L = 1$.

6.6 Numerical Results

This section presents the analytical and simulation results for OP and SER of the considered system. The simulation results are obtained using Monte Carlo simulation, where each simulation run consists of 10^7 realizations. The links TxBS-IRS and IRS-RxBS are considered i.i.d. flat Rician fading channels where $K_n = \bar{K}_n = K$, unless mentioned otherwise. The average transmission power of the TxBS P_0 and the reflection coefficient β are normalized to unity, i.e., $\beta = P_0 = 1$, and the SNR is defined as $\mathcal{P} = P_0/\sigma_w^2$.

Figs. 6.2 and 6.3 show the SER for the single hop case, $L = 1$, using various values of N using BPSK and quadrature phase shift keying (QPSK), respectively, and using $K = 10$ dB. As can be noted from the two figures, the analytical and simulation results for the single reflector case, $N = 1$, match very well for the considered range of SNR because the cascaded channel PDF is exact, and the only approximation used is for the Q-function. For the multiple reflectors case, the PDF approximation of the cascaded channel resulted in some discrepancies for the $N = 2, 3$ cases, at high SNRs. Such results are obtained because the approximation error is relatively more significant for $N < 4$, particularly at high SNRs where the effect of the AWGN is small when compared to the approximation error. As can be noted from the figures, increasing the number of reflectors N effectively improves the SNR, or equivalently, it enhances the SER considerably. Nevertheless, the improvement gained by increasing N decreases for large values of N. For example, the gain obtained using $N = 2$ as compared to the case of $N = 1$ is about 8 dB at $\bar{P}_S = 10^{-4}$, increasing N from 2 to 3 provides only and additional 6 dB, and so forth. Such behavior is obtained because SNR increases nonlinearly versus N. As an example, for the special case where $\{\beta_n, \varpi_n\} = 1\ \forall n$ in (6.5), the SNR improvement becomes $2\log_{10}(N)$. Interestingly, increasing N to 30 provides about 36 dB of SNR improvement. The significant SNR improvement can be exploited to increase the modulation

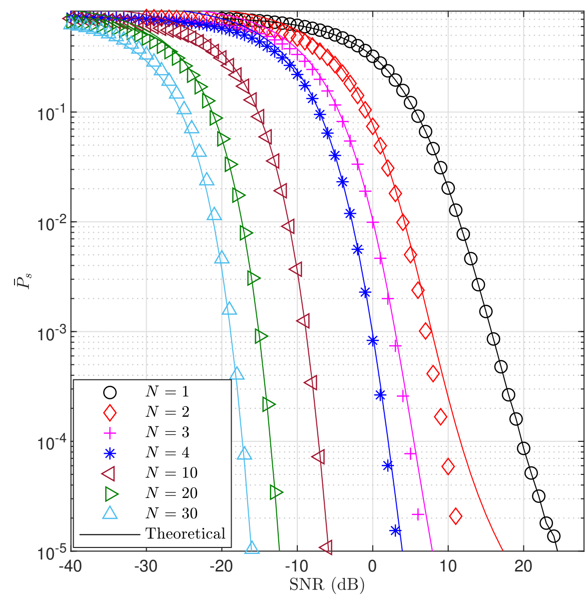

Figure 6.3: SER using QPSK using various values of N, $K = 10$ dB and $L = 1$.

order, and thus enhance the spectral efficiency.

Fig. 7.5a shows the analytical and simulated SER versus SNR using QPSK for various values of N and K. As can be noted from the figure, the derived approximation matches the simulation results very well for high values of K for the considered SNR range. For small K values, the difference between the approximated and simulation results is noticeable for $N = 10$, and it decreases by increasing N. It can be also noted that the approximation error becomes less significant at low SNRs because the performance in such regions is dominated by the AWGN. The impact of the channel quality on SER decreases by increasing N, which is demonstrated by the condensed SER curves for large values of N.

Fig. 6.5 presents the analytical and simulated SER using BPSK for various values of N and L, where the transmitted power per each TxBS and the Rician factor K are fixed at 0 and 10 dB, respectively. The results show the high accuracy of the approximations used because $K \gg 1$ dB. The figure also shows the SER for a random number of hops. The number of possible hops takes a value from the set $\{1, 2, 3, 4, 5, 6\}$ with probabilities $\{0.75, 0.15, 0.05, 0.025, 0.015, 0.01\}$, where this model corresponds to the WF routing policy proposed in [61] with gNodeB BSs density of 30 gNB/km^2. As can be seen from the figure, the SER for a random number of hops is bounded by the SER of $L_{\max} = 1$ and 6, but closer to $L_{\max} = 1$ because the considered routing protocol tends to select the path with minimum number of hops.

Fig. 6.6 presents the results of the OP for various values of γ_{th}, i.e., χ, and N. The Rician factor $K = 10$ dB, $\gamma_{\text{th}} = [5, 10, 15]$ dB, and $N = [10, 20]$. As the figure shows, derived OP shows an excellent match with simulation results for all of the considered scenarios. Clearly, increasing γ_{th} for a given value of N deteriorates OP, however, the degradation can be compensated by increasing N. It is interesting to note that increasing γ_{th} by a certain value degrades $\bar{P}_O$ approximately by the same value. For example,

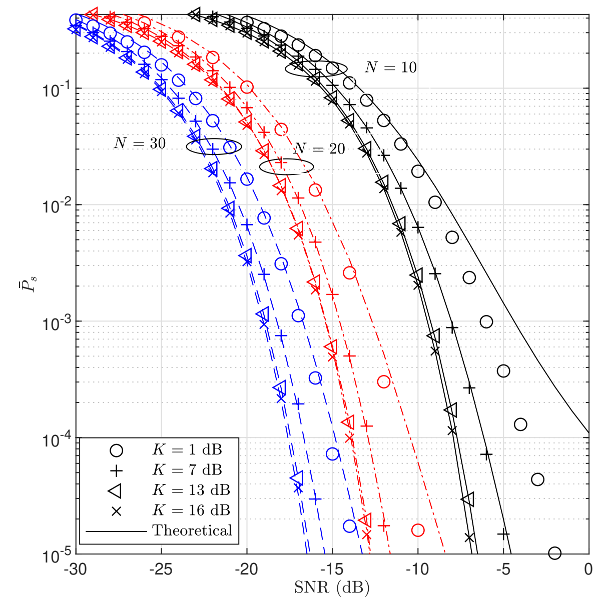

Figure 6.4: SER using QPSK for various values of N and K, $L = 1$.

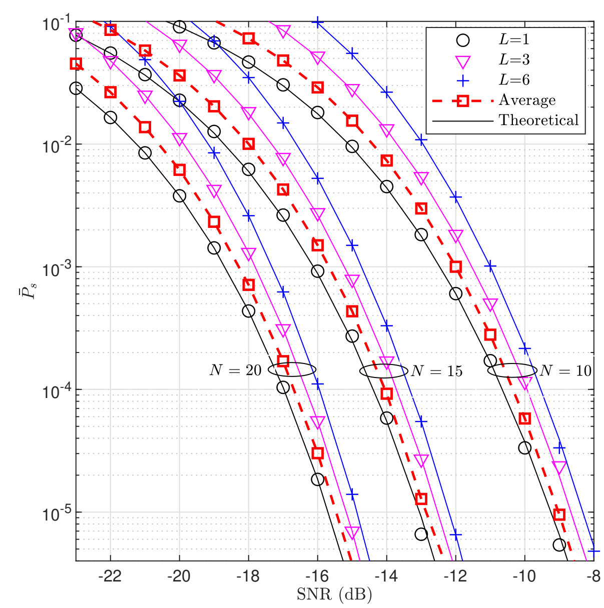

Figure 6.5: SER versus SNR using BPSK for fixed and random values of L, $K = 10$ dB.

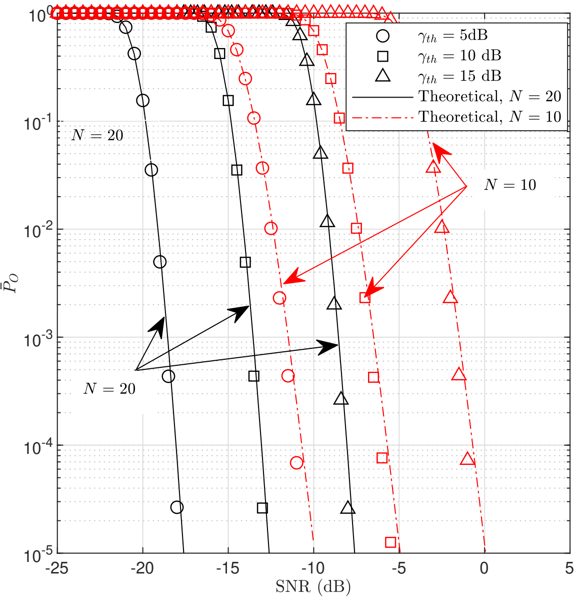

Figure 6.6: The OP for various values of N and γ_{th}, $K = 10$ dB and $L = 1$.

when $N = 10$, increasing γ_{th} from 5 to 10 dB increases the SNR required to achieve $\bar{P}_O = 10^{-5}$ from -5 to -10 dB.

Fig. 7.5b shows the OP versus SNR for various values of K, where $N = 10$, $L = 1$, and $\gamma_{\text{th}} = 10$ dB. As shown in the figure, the difference between the analytical and simulation results is about 0.3 dB at $\bar{P}_O = 10^{-4}$, it decreases by decreasing SNR. The approximation becomes more accurate for larger values of K. The figure also shows the impact of K on $\bar{P}_O$, where increasing K can significantly improve $\bar{P}_O$, particularly when K has originally small values. For example, the SNR required to obtain $P_O = 10^{-5}$ can be reduced by about 2.5 dB when K increases from 4 dB to 7 dB, while the gain is reduced to less than 1 dB when K increases from 16 dB to 20 dB.

Fig. 6.8 presents the analytical and simulated OP for various values of L and N, $K = 10$ dB and $\gamma_{\text{th}} = 5$ dB. As can be noticed from the figure, the analytical and simulation results match very well for $N = 1$ because $\bar{P}_O$ is exact for this case, and for $N \geq 5$ because the approximation accuracy improves versus N. Moreover, it can be noted that increasing N improves $\bar{P}_O$ significantly, and dilutes the degradation caused by increasing L. More specifically, the effect of N becomes negligible for $N \geq 10$.

Fig. 6.9 shows the normalized truncation error that results when using a small number of terms in the summations used to evaluate the BER in (6.33) and (6.34), which is defined as

$$\text{TE} \triangleq \frac{\left|\bar{P}_e|_{50} - \bar{P}_e|_{l_{\max}}\right|}{\bar{P}_e|_{50}} \tag{6.51}$$

where $l_{\max}$ is the number of terms used in the summations, and $\bar{P}_e|_{50}$ is the probability of error for $l_{\max} = 50$. The $\bar{P}_e|_{50}$ is taken as the reference because TE for $l_{\max} > 50 \approx 0$. The results are obtained for various values of the number of reflectors N and SNR values. As can be noted from the figure, TE

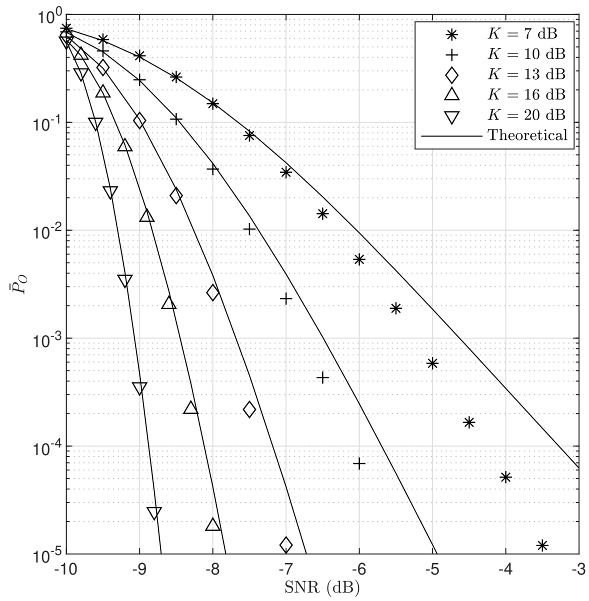

Figure 6.7: OP for various values of K, where $N = 10$, $\gamma_{\rm th} = 10$ dB and $L = 1$.

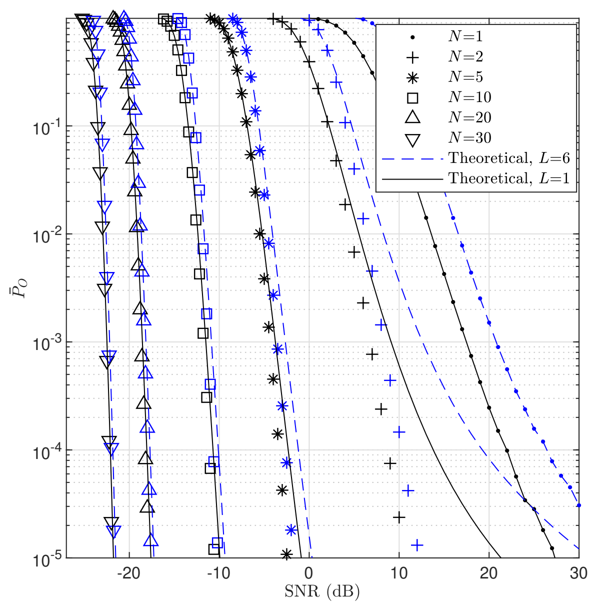

Figure 6.8: OP for various values of N, $L = 1$ and 6, $K = 10$ dB and $\gamma_{\rm th} = 5$ dB.

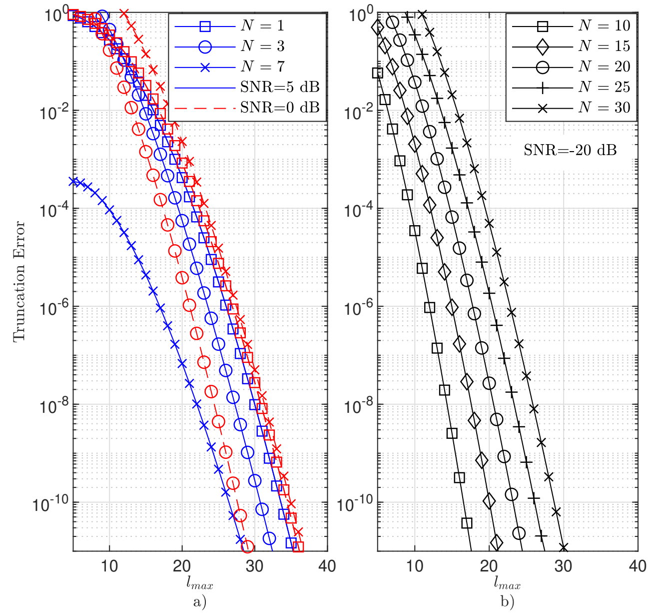

Figure 6.9: The truncation error for various values of N and SNR.

decreases as $l_{\max}$ increases, and it becomes less than 10^{-7} for $l_{\max} \geq 30$.

Fig. 6.10 shows the theoretical and simulated effective SNR $\bar{\gamma}_N$ versus N for $K = 0$, 10 and 30 dB, $\sigma_w^2 = -10$ dB, $\Omega = 1$, and all channels are considered i.i.d. As can be seen from the figure, the relation between $\bar{\gamma}_N$ in dB and N is nonlinear due to the log function. Moreover, the figure shows that increasing K improves $\bar{\gamma}_N$.

Fig. 6.11.a and Fig. 6.11.b show the outage probability versus N and L, respectively, using SNR$=$ -34.5 dB, $K = 20$ dB, $\Omega = 1$, and $\gamma_{\text{th}} = 5$ dB. The results in Fig. 6.11.a show that using $L > 10$ may provide $\bar{P}_O > 10^{-2}$ for $N < 98$. Therefore, using large number of hops should be avoided unless the number of elements in each IRS is large. Moreover, it can be noted that $\bar{P}_O$ decreases sharply for $N > 98$. For the case of Fig. 6.11.b, it can be noted that $\bar{P}_O$ increases severely for $L < 20$, and then the increase becomes moderate. Moreover, it can be seen that $\bar{P}_O$ is very sensitive to the variations of N.

6.7 Conclusion and Future Work

This paper have investigated the performance of the promising IRS technology for wireless mesh backhauling, where data traffics for each BS reaches the corenetwork through multiple wireless hops. The proposed system model was analyzed for the single hop, and then generalized to multiple hops. The system performance was evaluated in terms of SNR, SER and OP were exact and approximated analytical expressions were derived for IRS systems over Rician fading channels. The analytical results were verified using Mote Carlo simulation, and the extensive comparisons confirmed the accuracy of the derived solutions, particularly when the number of reflectors N and the Rician K factors are high. In addition, the results showed that the proposed IRS based backhauling can be considered as an attractive solution

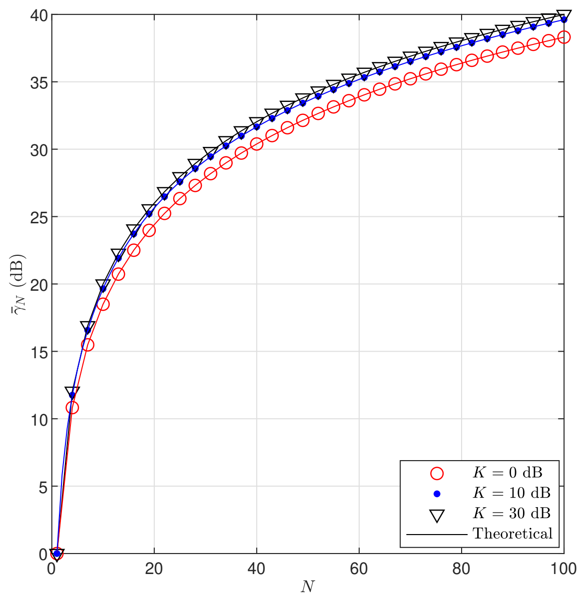

Figure 6.10: The effective received signal SNR $\bar{\gamma}_N$ in dB.

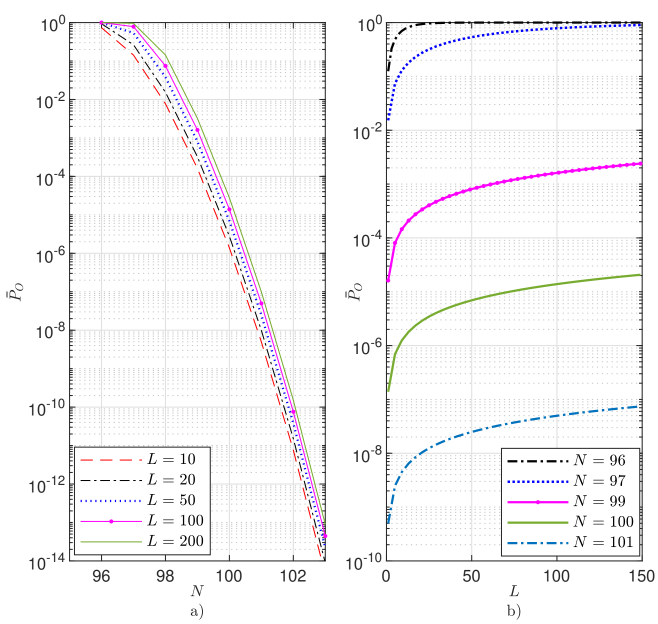

Figure 6.11: The outage probability versus the number of hops L and number of reflectors N.

for wireless backhauling because it can boost the effective SNR, and reduce OP and SER considerably. Consequently, IRS is an energy and spectrum efficiency enabler for wireless backhauling.

Our Future work will focus on investigating the IRS backhauling system in multihop scenarios where the channel estimation and compensation at each hop is imperfect, and the limitations for the timing alignment and its impact on the bandwidth will be evaluated. In addition, the design of routing protocols and path selection mechanisms based on the derived formulas will be performed to minimize the OP for a given energy constraint will be considered. The use of multi IRSs between adjacent BSs will be also considered.

Appendix I: Evaluating T_1, T_2 and T_3

The SER for $N \geq 2$ is obtained by substituting (6.23) in (6.22), and thus the complete expression $f_\gamma(\gamma)$ is easily obtained. The obtained $f_\gamma(\gamma)$ and (6.29) are then substituted in (6.28), where the result is expressed in (6.52).

$$\bar{P}_S = A\left(\frac{1}{\sigma_{\lambda_n}\sqrt{2\pi N}}\frac{1}{2\sqrt{\check{\mathcal{P}}}}\int_0^\infty \mathrm{e}^{-\frac{\left(\sqrt{\frac{\gamma}{\check{\mathcal{P}}}}-\mu_{\lambda_n}N\right)^2}{2N\sigma^2_{\lambda_n}}}\frac{Q\left(\sqrt{B\gamma}\right)}{\sqrt{\gamma}}d\gamma + \frac{a_0}{a_1}\int_0^\infty \frac{Q\left(\sqrt{B\gamma}\right)}{2\sqrt{\check{\mathcal{P}}\gamma}}\Psi_{(\gamma)}\left(\Psi^2_{(\gamma)}-3\right)\mathrm{e}^{-\frac{1}{2}\Psi^2_{(\gamma)}}\,d\gamma\right) \tag{6.52}$$

After some mathematical manipulations, the resulting integral can be expressed as

$$\bar{P}_S = A\left(\frac{1}{\sigma_{\lambda_n}\sqrt{2\pi N}}T_1 + \frac{a_0}{a_1}\left[T_2 - 3T_3\right]\right) \tag{6.53}$$

where

$$T_1 = \frac{1}{2\sqrt{\check{\mathcal{P}}}}\int_0^\infty \frac{Q\left(\sqrt{B\gamma}\right)}{\sqrt{\gamma}}\,\mathrm{e}^{-\frac{\left(\sqrt{\frac{\gamma}{\check{\mathcal{P}}}}-\mu_{\lambda_n}N\right)^2}{2N\sigma^2_{\lambda_n}}}\,d\gamma \tag{6.54}$$

$$T_2 = \frac{1}{2\sqrt{\check{\mathcal{P}}}}\int_0^\infty \frac{\Psi^3_{(\gamma)}}{\sqrt{\gamma}}Q\left(\sqrt{B\gamma}\right)\mathrm{e}^{-\frac{1}{2}\Psi^2_{(\gamma)}}\,d\gamma \tag{6.55}$$

$$T_3 = \frac{1}{2\sqrt{\check{\mathcal{P}}}}\int_0^\infty Q\left(\sqrt{B\gamma}\right)\frac{\Psi_{(\gamma)}}{\sqrt{\gamma}}\,\mathrm{e}^{-\frac{1}{2}\Psi^2_{(\gamma)}}\,d\gamma \tag{6.56}$$

These three integrals are solved individually in the three subsections below.

6.7.1 Evaluating the Integral T_1

By substituting $y = \sqrt{\frac{\gamma}{\check{\mathcal{P}}}}$, the integral T_1 in (6.54) is reduced to

$$T_1 = \int_0^\infty Q\left(\sqrt{B\check{\mathcal{P}}}y\right)\mathrm{e}^{-\frac{1}{2N}\left(\frac{y-N\mu_{\lambda_n}}{\sigma_{\lambda_n}}\right)^2}\,dy. \tag{6.57}$$

The approximation of the Q-function provided in (6.31) is applied, and then the resulting integral can be written as

$$T_1 = \frac{\mathrm{e}^{-\frac{\mu_{\lambda_n}^2 N}{2\sigma_{\lambda_n}^2}}}{1.135\sqrt{\pi}} \sum_{i=1}^{n_a} \frac{(-1)^{i+1}\, 1.98^i}{2^{\frac{i+1}{2}}\, i!} \left(B\check{\mathcal{P}}\right)^{\frac{i-1}{2}} \times \int_0^\infty y^{i-1}\, \mathrm{e}^{-\frac{1}{2}\left(\frac{1}{N\sigma_{\lambda_n}^2}+B\check{\mathcal{P}}\right)y^2 + \frac{\mu_{\lambda_n}}{\sigma_{\lambda_n}^2}y}\, dy \tag{6.58}$$

which can be solved as [81, 3.462.1]

$$T_1 = \frac{\mathrm{e}^{-\frac{\mu_{\lambda_n}^2 N}{2\sigma_{\lambda_n}^2}}}{1.135\sqrt{\pi}} \sum_{i=1}^{n_a} \frac{(-1)^{i+1}\, 1.98^i}{2^{\frac{(i+1)}{2}}\, i!} \left(B\check{\mathcal{P}}\right)^{\frac{i-1}{2}} \frac{\Gamma(i)}{\rho_n^i} \times \mathrm{e}^{\frac{\mu_{\lambda_n}^2}{4\rho_n^2 \sigma_{\lambda_n}^4}}\, \mathcal{D}_{-i}\left(\frac{-\mu_{\lambda_n}}{\sigma_{\lambda_n}^2 \rho_n}\right) \tag{6.59}$$

where $\rho_n = \sqrt{\frac{1}{\sigma_{\lambda_n}^2 N} + B\check{\mathcal{P}}}$, $\Gamma(\cdot)$ is the Gamma function, and $\mathcal{D}_{-n}(\cdot)$ is the parabolic cylinder function.

6.7.2 Evaluating the Integral T_2

By substituting $x = \sqrt{\gamma}$, the integral T_2 in (6.55) is reduced to

$$T_2 = \frac{1}{\sqrt{\check{\mathcal{P}}}} \int_0^\infty \Psi_{(x^2)}^3\, \mathrm{e}^{-\frac{1}{2}\Psi_{(x^2)}^2}\, Q\left(\sqrt{B}x\right) dx. \tag{6.60}$$

The definition of the Q-function is then substituted in (6.60), i.e., $Q(x) \triangleq \frac{1}{\sqrt{2\pi}} \int_x^\infty \mathrm{e}^{-\frac{y^2}{2}} dy$, and thus T_2 can be written as

$$T_2 = \frac{1}{\sqrt{2\pi\check{\mathcal{P}}}} \int_0^\infty \int_{\sqrt{B}x}^\infty \Psi_{(x^2)}^3\, \mathrm{e}^{-\frac{1}{2}\Psi_{(x^2)}^2}\, \mathrm{e}^{-\frac{y^2}{2}}\, dy dx. \tag{6.61}$$

Subsequently, by changing the order of the integrals, thus T_2 can be rewritten as

$$\begin{aligned} T_2 &= \frac{1}{\sqrt{2\pi\check{\mathcal{P}}}} \int_0^\infty \int_0^{\frac{y}{\sqrt{B}}} \Psi_{(x^2)}^3\, \mathrm{e}^{-\frac{1}{2}\Psi_{(x^2)}^2}\, \mathrm{e}^{-\frac{y^2}{2}}\, dx dy \\ &= \frac{1}{\sqrt{2\pi\check{\mathcal{P}}}} \int_0^\infty \mathrm{e}^{-\frac{y^2}{2}}\, T_{2,1} dy \end{aligned} \tag{6.62}$$

where $T_{2,1}$ is given by

$$T_{2,1} = \int_0^{\frac{y}{\sqrt{B}}} \Psi_{(x)}^3\, \mathrm{e}^{-\frac{1}{2}\Psi_{(x)}^2}\, dx. \tag{6.63}$$

Therefore, $T_{2,1}$ should be solved first, then the result is substituted in (6.62) to solve T_2. By using the change of variables $\Psi_{(x^2)} = \left(\sqrt{\frac{x^2}{\check{\mathcal{P}}}} - \sqrt{N}a_2\right) / \left(\sqrt{N}a_1\right)$ in (6.63), $T_{2,1}$ can be written as

$$T_{2,1} = \sqrt{N\check{\mathcal{P}}}a_1 \int_{\frac{-a_2}{a_1}}^{\Psi_{(y^2/B)}^2} \Psi_{(x)}^3\, \mathrm{e}^{-\frac{1}{2}\Psi_{(x^2)}^2}\, d\Psi_{(x^2)} \tag{6.64}$$

which can be solved as [81]

$$T_{2,1} = \sqrt{N\check{\mathcal{P}}}a_1 \left((2+\acute{a})\, \mathrm{e}^{-\frac{1}{2}\acute{a}} \left(2 + \Psi^2_{\left(\frac{y^2}{B}\right)} \right) - \mathrm{e}^{-\frac{1}{2}\Psi^2_{\left(\frac{y^2}{B}\right)}} \right). \tag{6.65}$$

Consequently, (6.65) is substituted in (6.62), and thus T_2 is reduced to

$$T_2 = \sqrt{\frac{N}{2\pi}} a_1 \left((2+\acute{a})\, \mathrm{e}^{-\frac{1}{2}\acute{a}} \int_0^\infty \mathrm{e}^{-\frac{y^2}{2}} dy - \int_0^\infty \left(2 + \Psi^2_{\left(\frac{y^2}{B}\right)} \right) \mathrm{e}^{-\frac{y^2}{2} - \frac{1}{2}\Psi^2_{\left(\frac{y^2}{B}\right)}} dy \right). \tag{6.66}$$

By using the definition of the Q-function, it can be easily shown that $\int_0^\infty \mathrm{e}^{-\frac{y^2}{2}} = \sqrt{\frac{\pi}{2}}$. After some algebraic operations, T_2 can be simplified to (6.67).

$$T_2 = \sqrt{\frac{N}{2\pi}} a_1 \Bigg((2+\acute{a})\, \mathrm{e}^{-\frac{1}{2}\acute{a}} \sqrt{\frac{\pi}{2}} - (2+\acute{a})\, \mathrm{e}^{-\frac{1}{2}\acute{a}} \int_0^\infty \mathrm{e}^{\left(-\delta y^2 - \nu y\right)} dy - 2\nu\, \mathrm{e}^{-\frac{1}{2}\acute{a}} \int_0^\infty y\, \mathrm{e}^{\left(-\delta y^2 - \nu y\right)} dy \\ - \frac{\mathrm{e}^{-\frac{1}{2}\acute{a}}}{N a_1^2 B \check{\mathcal{P}}} \int_0^\infty y^2 \mathrm{e}^{\left(-\delta y^2 - \nu y\right)} dy \Bigg) \tag{6.67}$$

Thereafter, the integration can be evaluated in closed form as given in (6.7.2) [81, 3.462.1].

$$T_2 = \sqrt{\frac{N}{2\pi}} a_1\, \mathrm{e}^{-\frac{1}{2}\acute{a}} \Bigg(\sqrt{\pi}\,(2+\acute{a}) - \mathrm{e}^{\frac{\nu^2}{8\delta}} \Bigg[(2+\acute{a}) \frac{1}{\sqrt{\delta}} \mathcal{D}_{-1}\left(\frac{\nu}{\sqrt{2\delta}}\right) + \frac{\nu\sqrt{2}}{\delta} \mathcal{D}_{-2}\left(\frac{\nu}{\sqrt{2\delta}}\right) \\ + \frac{\delta^{\frac{-3}{2}}}{N a_1^2 B \check{\mathcal{P}}} \mathcal{D}_{-3}\left(\frac{\nu}{\sqrt{2\delta}}\right) \Bigg] \Bigg) \tag{6.68}$$

Finally, the expression in (6.7.2) can be written using the summation notation, where the result is expressed in (6.36) where δ and ν are defined below (6.37).

6.7.3 Evaluating the Integral T_3

The steps followed to evaluate T_3 is very quiet similar to the procedure used to evaluate T_2, and therefore the derivation of T_3 is not included for the sake of brevity.

References

[1] Ericsson. (2019) Mobility report. [Online]. Available: `https://www.ericsson.com/4acd7e/assets/local/mobility-report/documents/2019/emr-november-2019.pdf`.

[2] Cisco. (2020) Cisco annual internet report. [Online]. Available: `https://www.cisco.com/c/en/us/solutions/collateral/executiveperspectives/annual-internet-report/white-paper-c11-741490.html`.

[3] E. Calvanese Strinati *et al.*, "6G: The next frontier: From holographic messaging to artificial intelligence using subterahertz and visible light communication," *IEEE Veh. Technol. Mag.*, vol. 14, no. 3, pp. 42-50, Sep. 2019.

[4] J. Rygaard, "Digitization, densification and why you should care," Nokia, Tech. Rep., Feb. 2017. [Online]. Available: `https:www.nokia.com/blog/digitization-densification-care`

[5] X. Ge, S. Tu, G. Mao, C. Wang, and T. Han, "5G ultra-dense cellular networks," *IEEE Wireless Commun.*, vol. 23, no. 1, pp. 72-79, Feb. 2016.

[6] M. Mirahmadi, A. Al-Dweik, and A. Shami, "Interference modeling and performance evaluation of heterogeneous cellular networks," *IEEE Trans. Commun.*, vol. 62, no. 6, pp. 2132–2144, Jun. 2014.

[7] J. G. Andrews, H. Claussen, M. Dohler, S. Rangan, and M. C. Reed, "Femtocells: Past, present, and future," *IEEE J. Sel. Areas Commun.*, vol. 30, no. 3, pp. 497–508, 2012.

[8] H. Ronkainen, J. Edstam, A. Ericsson and C. Östberg, "Integrated access and backhaul: a new type of wireless backhaul in 5G," *Ericsson Technology Review*, July 2020. [Online]. Available: `https://www.ericsson.com/en/reports-and-papers/ericsson-technology-review/articles/introducing-integrated-access-and-backhaul`. Accessed 16 Sep. 2020.

[9] C. Madapatha *et al.*, "On integrated access and backhaul networks: Current status and potentials," *IEEE Open J. Commun. Soc.*, vol. 1, pp. 1374-1389, 2020.

[10] RSPG Report on Spectrum Issues on Wireless Backhaul, Radio Spectrum Policy Group, European Commission, Directorate-General for Communications Networks, Content and Technology, RSPG15-607, June 2015.

[11] H. Willebrand and B. Ghuman, “Fiber optics without fiber,” *IEEE Spectrum*, vol. 38, no. 8, pp. 40–45, Aug. 2001.

[12] GSMA, “Mobile backhaul: An overview,” GSMA.com, available: `https://www.gsma.com/futurenetworks/wiki/mobile-backhaul-anoverview`, accessed Oct. 2020.

[13] W. Abderrahim, O. Amin, M. Alouini and B. Shihada, “Latency-aware offloading in integrated satellite terrestrial networks,” *IEEE Open J. Commun. Soc.*, vol. 1, pp. 490-500, 2020.

[14] Y. Liu, A. Tang and X. Wang, “Joint incentive and resource allocation design for user provided network under 5G integrated access and backhaul networks,” *IEEE Trans. Netw. Sci. Eng.*, vol. 7, no. 2, pp. 673-685, Apr. 2020.

[15] C. Saha and H. S. Dhillon, “Millimeter wave integrated access and backhaul in 5G: performance analysis and design insights,” *IEEE J. Sel. Areas Commun.*, vol. 37, no. 12, pp. 2669-2684, Dec. 2019.

[16] M. Polese *et al.*, “Integrated Access and Backhaul in 5G mmWave Networks: Potential and Challenges,” *IEEE Commun. Mag.*, vol. 58, no. 3, pp. 62-68, Mar. 2020.

[17] 3GPP R1-1913600, “RAN1 agreements for Rel-16 IAB,” 3rd Generation Partnership Project (3GPP), Tech. Rep. Meeting #99, Reno, USA, Nov. 2019.

[18] N. Kim and D. Cho, “A novel synchronous duplexing method for long distance wireless backhaul system,” *IEEE Wireless Commun. Lett.*, vol. 8, no. 3, pp. 761-764, Jun. 2019.

[19] “Terragraph virtual fiber for high speed fixed broadband,” Telecom infra project, White Paper, 2018. [Online]. Available: `https://terragraph.com/wp-content/uploads/2019/02/Terragraph_MikebudaTrial_Whitepaper.pdf`

[20] M. Coldrey, “Maturity and field proven experience of millimetre wave transmission,” Sophia Antipolis, France, ETSI White Paper, Sep. 2015. [Online]. Available: `https://www.etsi.org/images/files/ETSIWhitePapers/etsi_wp10_field_pr-oven_experience_of_mwt_20150923.pdf`

[21] “Telecom infra project mmWave radio link aspects,” Telecom infra project, White Paper, 2018. [Online]. Available: `https://telecominfraproject.com/wp-content/uploads/TIP-mmWave_Radio-Link-Aspects_October-2018_vF.pdf`

[22] “Telecom infra project customer premises equipment (CPE) market adoption requirements,” Telecom infra project, White paper, 2018. [Online]. Available: `https://telecominfraproject.com/wp-content/uploads/TIP-mmWave-CPE-Market-Adoption-Requirements_October-2018_vF.pdf`

[23] O. Tipmongkolsilp, S. Zaghloul and A. Jukan, "The evolution of cellular backhaul technologies: Current issues and future trends," *IEEE Commun. Surveys Tuts.*, vol. 13, no. 1, pp. 97-113, First Quarter 2011.

[24] K. Zheng, L. Zhao, J. Mei, M. Dohler, W. Xiang, and Y. Peng, "10 Gb/s hetsnets with millimeter-wave communications: Access and networking - challenges and protocols," *IEEE Commun. Mag.*, vol. 53, no. 1, pp. 222-231, Jan. 2015.

[25] R. Favraud, C. Chang, and N. Nikaein, "Autonomous self-backhauled LTE mesh network with QoS guarantee," *IEEE Access*, vol. 6, pp. 4083-4117, 2018.

[26] Y. Yu, T. Hsieh, and A. Pang, "Millimeter-wave backhaul traffic minimization for CoMP over 5G cellular networks," *IEEE Trans. Veh. Technol.*, vol. 68, no. 4, pp. 4003-4015, Apr. 2019.

[27] M. Alzenad, M. Shakir, H. Yanikomeroglu, and M. Alouini, "FSO-based vertical backhaul/fronthaul framework for 5G+ wireless networks," *IEEE Commun. Mag.*, vol. 56, no. 1, pp. 218-224, Jan. 2018.

[28] S. Samarakoon, M. Bennis, W. Saad, and M. Latva-aho, "Backhaul-aware interference management in the uplink of wireless small cell networks," *IEEE Trans. Wireless Commun.*, vol. 12, no. 11, pp. 5813-5825, Nov. 2013.

[29] L. Sanguinetti, A. Moustakas, and M. Debbah, "Interference management in 5G reverse TDD HetNets with wireless backhaul: A large system analysis," *IEEE J. Sel. Areas Commun.*, vol. 33, no. 6, pp. 1187-1200, Jun. 2015.

[30] P. Liu and A. Springer, "Space shift keying for LOS communication at mmWave frequencies," *IEEE Wireless Commun. Lett.*, vol. 4, no. 2, pp. 121-124, April 2015.

[31] E. Panayirci, A. Yesilkaya, T. Cogalan, H. Poor, and H. Haas, "Physical-layer security with optical generalized space shift keying," *IEEE Trans. Commun.*, vol. 68, no. 5, pp. 3042-3056, May 2020.

[32] Q.-U.-A Nadeem, A. Kammoun, M. Debbah, and M. Alouini, "3D massive MIMO systems: Modeling and performance analysis," *IEEE Trans. Wireless Commun.*, vol. 14, no. 12, pp. 6926-6939, Dec. 2015.

[33] H. Tabassum, A. Sakr, and E. Hossain, "Analysis of massive MIMO-enabled downlink wireless backhauling for full-duplex small cells," *IEEE Trans. Commun.*, vol. 64, no. 6, pp. 2354-2369, Jun. 2016.

[34] M. Feng, S. Mao, and T. Jiang, "Joint frame design, resource allocation and user association for massive MIMO heterogeneous networks with wireless backhaul," *IEEE Trans. Wireless Commun.*, vol. 17, no. 3, pp. 1937-1950, Mar. 2018.

[35] P. Anokye, R. Ahiadormey, C. Song, and K. Lee, "Achievable sum-rate analysis of massive MIMO full-duplex wireless backhaul links in heterogeneous cellular networks," *IEEE Access*, vol. 6, pp. 23456-23469, 2018.

[36] A. Bonfante *et al.*, "5G massive MIMO architectures: self-backhauled small cells versus direct access," *IEEE Trans. Veh. Technol.*, vol. 68, no. 10, pp. 10003-10017, Oct. 2019.

[37] E. Basar, M. Di Renzo, J. De Rosny, M. Debbah, M.-S. Alouini and R. Zhang, "Wireless communications through reconfigurable intelligent surfaces," *IEEE Access*, vol. 7, pp. 116753-116773, 2019.

[38] M. Di Renzo *et al.*, "Smart radio environments empowered by reconfigurable AI meta-surfaces: An idea whose time has come," *EURASIP J. Wireless Commun. Netw.*, vol. 2019, p. 129, May 2019.

[39] C. Huang, A. Zappone, G. Alexandropoulos, M. Debbah, and C. Yuen, "Reconfigurable intelligent surfaces for energy efficiency in wireless communication," *IEEE Trans. Wireless Commun.*, vol. 18, no. 8, pp. 4157–4170, Aug. 2019.

[40] Q. Wu and R. Zhang, "Intelligent reflecting surface enhanced wireless network via joint active and passive beamforming," *IEEE Trans. Wireless Commun.*, vol. 18, no. 11, pp. 5394-5409, Nov. 2019.

[41] E. Basar, "Reconfigurable intelligent surface-based index modulation: A new beyond MIMO paradigm for 6G," *IEEE Trans. Commun.*, vol. 68, no. 5, pp. 3187-3196, May 2020.

[42] A. Canbilen, E. Basar, and S. Ikki, "Reconfigurable intelligent surface-assisted space shift keying,"*IEEE Wireless Commun. Lett.*, vol. 9, no. 9, pp. 1495-1499, Sep. 2020.

[43] J. Ye, S. Guo, and M.-S. Alouini, "Joint reflecting and precoding designs for SER minimization in reconfigurable intelligent surfaces assisted MIMO systems," *IEEE Tran. Wireless Commun.*, vol. 19, no. 8, pp. 5561-5574, Aug. 2020.

[44] D. Mishra and H. Johansson, "Channel estimation and low-complexity beamforming design for passive intelligent surface assisted MISO wireless energy transfer, " *IEEE Int. Conf. Acoustics, Speech and Signal Process. (ICASSP)*, Brighton, United Kingdom, 2019, pp. 4659-4663.

[45] Z. Ding and H. V. Poor, "A simple design of IRS-NOMA transmission," *IEEE Commun. Lett.*, vol. 24, no. 5, pp. 1119-1123, May 2020.

[46] Z. He and X. Yuan, "Cascaded channel estimation for large intelligent metasurface assisted massive MIMO," *IEEE Wireless Commun. Lett.*, vol. 9, no. 2, pp. 210-214, Feb. 2020.

[47] Q.-U.-A. Nadeem, A. Kammoun, A. Chaaban, M. Debbah, M.-S. Alouini, "Intelligent reflecting surface assisted wireless communication: Modeling and channel estimation," *IEEE Open J. Commun. Soc.* IEEE early Access, 2020.

[48] Q. U. Nadeem, A. Kammoun, A. Chaaban, M. Debbah, and M. -S. Alouini, "Asymptotic max-min SINR analysis of reconfigurable intelligent surface assisted MISO systems," *IEEE Trans. Wireless Commun.*, IEEE early access, 2020.

[49] Ö. Özdogan, E. Björnson, and E. Larsson, “Intelligent reflecting surfaces: Physics, propagation, and pathloss modeling,” *IEEE Wireless Commun. Lett.*, vol. 9, no. 5, pp. 581-585, May 2020.

[50] L. Dai *et al.*, “Reconfigurable intelligent surface-based wireless communication: Antenna design, prototyping and experimental results,” *IEEE Access*, vol. 8, pp. 45913-45923, 2020.

[51] C. Huang, R. Mo, and C. Yuen, “Reconfigurable intelligent surface assisted multiuser MISO systems exploiting deep reinforcement learning,” *IEEE J. Sel. Areas Commun.*, vol. 38, no. 8, pp. 1839-1850, Aug. 2020.

[52] M. Al-Jarrah, A. Al-Dweik, E. Alsusa, Y. Iraqi, and M.-S. Alouini, “IRS-assisted UAV communications with imperfect phase compensation,” *TechRxiv. Preprint.* [Online]. Available : `https://doi.org/10.36227/techrxiv.13153211.v1`

[53] C. Huang *et al.*, “Holographic MIMO surfaces for 6G wireless networks: Opportunities, challenges, and trends,” *IEEE Wireless Commun.*, vol. 27, no. 5, pp. 118-125, Oct. 2020.

[54] D. Benyamina, A. Hafid and M. Gendreau, “Wireless mesh networks design-a survey,” *IEEE Commun. Surveys & Tuts.*, vol. 14, no. 2, pp. 299-310, Second Quarter 2012.

[55] A. Akhtar, M. Nakhai, and A. Aghvami, “Power aware cooperative routing in wireless mesh networks,” *IEEE Commun. Lett.*, vol. 16, no. 5, pp. 670-673, May 2012.

[56] Z. Yuan, J. Song, and Z. Han, “Interference aware routing using network formation game in cognitive radio mesh networks,” *IEEE J. Sel. Areas Commun.*, vol. 31, no. 11, pp. 2494-2503, Nov. 2013.

[57] A. Akhtar, M. Nakhai, and A. Aghvami, “Energy-efficient adaptive routing in wireless ad hoc and mesh networks,” *IET Networks*, vol. 1, no. 4, pp. 249-256, Dec. 2012.

[58] Y. Chai and X. Zeng, “Delay- and interference-aware routing for wireless mesh network,” *IEEE Syst. J.*, vol. 14, no. 3, pp. 4119-4130, Sep. 2020.

[59] Y. Chai and X. Zeng, “Load balancing routing for wireless mesh network with energy harvesting,” *IEEE Commun. Lett.*, vol. 24, no. 4, pp. 926-930, Apr. 2020.

[60] G. Rahmatollahi and G. Abreu, “Closed-form hop-count distributions in random networks with arbitrary routing,” *IEEE Trans. Commun.*, vol. 60, no. 2, pp. 429-444, Feb. 2012.

[61] M. Polese, M. Giordani, A. Roy, D. Castor, and M. Zorzi, “Distributed path selection strategies for integrated access and backhaul at mmWaves,” *2018 IEEE Global Commun. Conf. (GLOBECOM)*, Abu Dhabi, United Arab Emirates, 2018, pp. 1-7.

[62] K. Hammad, “Radio resource management optimization for next generation wireless networks,”, PhD Thesis, Western University, London, ON, Canada, 2016.

[63] M. Al-Jarrah, K. Park, A. Al-Dweik, and M. Alouini, “Error rate analysis of amplitude-coherent detection over Rician fading channels with receiver diversity,” *IEEE Trans. Wireless Commun.*, vol. 19, no. 1, pp. 134-147, Jan. 2020.

[64] R. Dana, “Statistics of sampled Rician fading,” DNA-TR-92–98 Tech. Rep., Feb. 1993.

[65] M. Samimi, G. MacCartney, S. Sun and T. S. Rappaport, “28 GHz millimeter-wave ultrawideband small-scale fading models in wireless channels,” *IEEE 83rd Veh. Technol. Conf.*e (VTC Spring), Nanjing, 2016, pp. 1-6.

[66] I. Hemadeh, K. Satyanarayana, M. El-Hajjar, and L. Hanzo, “Millimeter-wave communications: Physical channel models, design considerations, antenna constructions, and link-budget,” *IEEE Commun. Surveys Tuts.*, vol. 20, no. 2, pp. 870-913, Secondquarter 2018.

[67] L. Wang, B. Ai, D. He, H. Yi, Z. Zhong, and J. Kim, “Channel characterisation in rural railway environment at 28 GHz,” *IET Microw. Antennas Propag.*, vol. 13, no. 8, pp. 1052-1059, Jul. 2019.

[68] K. Guan *et al.*, “Channel characterization for intra-wagon communication at 60 and 300 GHz bands,” *IEEE Trans. Veh. Technol.*, vol. 68, no. 6, pp. 5193-5207, Jun. 2019.

[69] D. Yan *et al.*, “Channel characterization for vehicle-to-infrastructure communications in millimeter-wave band,” *IEEE Access*, vol. 8, pp. 42325-42341, 2020.

[70] J. Proakis, Digital Communications. 3rd Ed. New York: McGraw-Hill, 1995.

[71] M. K. Simon, “Probability Distributions Involving Gaussian Random Variables: A Handbook for Engineers and Scientists ”Norwell, MA: Kluwer Academic, 2002.

[72] N. O’Donoughue and J. Moura, “On the product of independent complex Gaussians,” *IEEE Trans. Signal Process.*, vol. 60, no. 3, pp. 1050-1063, March 2012.

[73] A. Seijas-Macias and A. Oliveira. “An approach to distribution of the product of two normal variables,” *Discussiones Mathematicae Probability and Statistics*, vol. 32, no. 1-2, pp. 87-99, 2012.

[74] A Saci, A Al-Dweik, and A Shami, “Direct data detection of OFDM signals over wireless channels,” *IEEE Trans. Veh. Technol.*, vol. 69, no. 11, pp. 12432-12448, Nov. 2020.

[75] J. A. Lopez-Salcedo, “Simple closed-form approximation to Ricean sum distributions,” *IEEE Signal Process. Lett.*, vol. 16, no. 3, pp. 153-155, Mar. 2009.

[76] A. Goldsmith, Wireless Communications. Cambridge University Press, 2005.

[77] Y. Isukapalli and B. Rao, “An analytically tractable approximation for the Gaussian Q-function,” *IEEE Commun. Lett.*, vol. 12, no. 9, pp. 669-671, Sep. 2008.

[78] A. Prudnikov, Y. Brychkov, and O. Marichev, Integrals and Series, vol. 2 Special Functions. Gordon and Breach Science Publishers, UK, 3rd edition, 1986.

[79] K. Dhaka, R. Mallik and R. Schober, "Performance analysis of decode-and-forward multi-hop communication: A difference equation approach," *IEEE Trans. Commun.*, vol. 60, no. 2, pp. 339-345, Feb. 2012.

[80] A. Muller and J. Speidel, "Exact symbol error probability of M-PSK for multihop transmission with regenerative relays," *IEEE Commun. Lett.*, vol. 11, no. 12, pp. 952-954, Dec. 2007.

[81] I. Ryzhik and I. Gradshteyn, Table of Integrals, Series and Products, 7th Ed. San Diego, CA, USA: Academic Press, 2007.

[82] O. Badarneh and F. Almehmadi, "Performance of multihop wireless networks in α-μ fading channels perturbed by an additive generalized Gaussian noise," *IEEE Commun. Lett.*, vol. 20, no. 5, pp. 986-989, May 2016.

[83] D. Dixit and P. Sahu, "Exact closed-form ABER for multi-hop regenerative relay systems over κ-μ fading," *IEEE Wireless Commun. Lett.*, vol. 6, no. 2, pp. 246-249, Apr. 2017.

Chapter 7

On the Performance of IRS-Assisted Multi-Layer UAV Communications with Imperfect Phase Compensation[1]

Abstract

This work presents the symbol error rate (SER) and outage probability analysis of multi-layer unmanned aerial vehicles (UAVs) wireless communications assisted by intelligent reflecting surfaces (IRS). In such systems, the UAVs may experience high jitter, making the estimation and compensation of the end-to-end phase for each propagation path prone to errors. Consequently, the imperfect phase knowledge at the IRS should be considered. The phase error is modeled using the von Mises distribution and the analysis is performed using the Sinusoidal Addition Theorem (SAT) to provide accurate results when the number of reflectors $L \leq 3$, and the Central Limit Theorem (CLT) when $L \geq 4$. The achieved results show that accurate phase estimation is critical for IRS based systems, particularly for a small number of reflecting elements. For example, the SER at 10^{-3} degrades by about 5 dB when the von Mises concentration parameter $\kappa = 2$ and $L = 30$, but the degradation for the same κ surges to 25 dB when $L = 2$. The air-to-air (A2A) channel for each propagation path is modeled as a single dominant line-of-sight (LoS) component, and the results are compared to the Rician channel. The obtained results reveal that the considered A2A model can be used to accurately represent the A2A channel with Rician fading.

[1] **M. A. Al-Jarrah**, A. Al-Dweik, E. Alsusa, Y. Iraqi, and M.-S. Alouini, "On the performance of IRS-assisted multi-layer UAV communications with imperfect phase compensation," *IEEE Trans. Commun.*, vol. 69, no. 12, pp. 8551-8568, Dec. 2021, doi: 10.1109/TCOMM.2021.3113008.

Index Terms

Bit error rate (BER), outage probability, Rician fading, intelligent reflecting surfaces (IRS), imperfect phase estimation, sinusoidal addition theorem (SAT), unmanned aerial vehicle (UAV), flying network, von Mises density, 6G.

7.1 Introduction

Intelligent reflecting surfaces (IRS), also called metasurfaces, is an emerging technology that has recently received extensive attention [1–13]. The main aim of IRS is controlling the propagation medium to improve the quality of wireless signals by increasing their total energy. The IRS technology is expected to play a significant role in future wireless networks, such as sixth generation (6G), because of its positive impact on energy and spectral efficiency. IRS consist of a large number of passive antenna elements that can introduce phase-shifts to wireless signals before reflecting them to their destination. For efficient transmission, multiple reflectors are used for a certain destination, and the introduced phase shifts are selected such that the reflected signals add coherently in the channel. As a result, the signal-to-noise ratio (SNR) increases considerably, which allows using high modulation orders to improve the spectral efficiency. Recently, holographic multiple-input-multiple-output surfaces, which are capable of shaping electromagnetic waves according to desired objectives, have gained significant attention [14].

Likewise, the use of unmanned aerial vehicles (UAVs) as flying networks has recently attracted a substantial attention in both academic and industrial sectors. Because of their autonomy, flexibility and cost efficiency, there has been a significant growth in the deployment of UAVs in many applications including surveillance, localization and tracking, remote sensing, search and rescue missions, aerial imaging, and military applications. In addition, UAVs can be integrated with base stations (BSs) to construct cost and energy efficient flying BSs. These flying BSs can provide integrated access and backhaul (IAB) solutions with significantly improved coverage, capacity and connectivity. Furthermore, UAV based IAB can assist the terrestrial cellular network that may suffer from congestion due to extremely high traffic or physical failure due to emergencies such as storms and earthquakes [1,15,17–21]. However, UAV design and deployment are typically confronted with serious regulatory and technical hurdles [22]. In terms of regulations, the aviation regulation authorities in most countries impose strict constraints on UAVs' weight, speed, altitude and permitted flying sites. Technically speaking, the UAV engine energy consumption drastically affects the UAV flying time, and thus, limits the UAV maneuvering capability. Therefore, optimizing the trajectory and UAV placement have received great attention as potential solutions to improve the UAV performance in terms of coverage, connectivity and networking capabilities, as reported in [23] and the references listed therein. More recently, multi-layer UAV networks have been considered to mitigate the regulatory and technical UAV limitations [22]. In multi-layer UAV network structures, a quasi-stationary

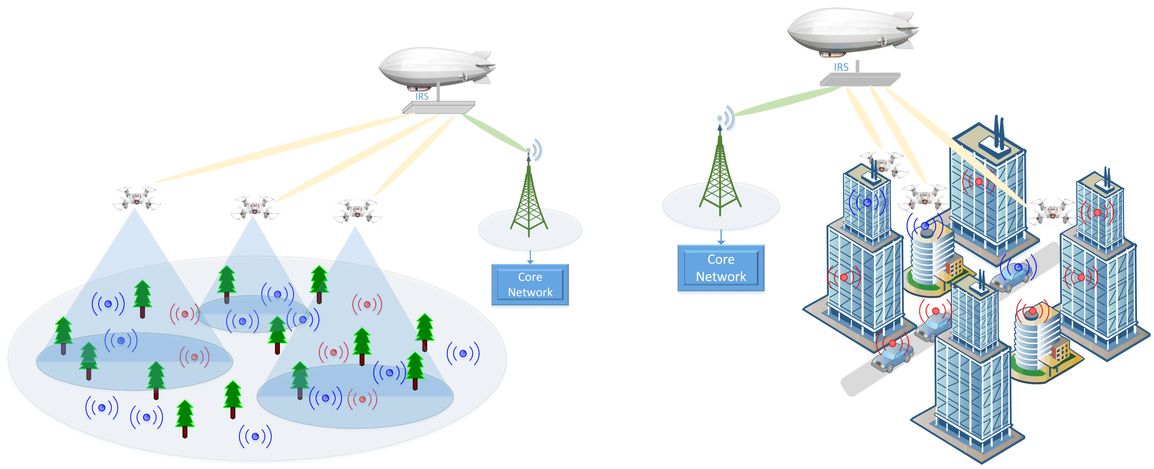

(a) Rural and farming areas (b) Urban areas

Figure 7.1: IRS-assisted two-layer flying network examples in rural and urban areas.

UAV, such as a balloon, is placed at higher altitudes to serve smaller UAVs with lower altitudes, and hence, increase the probability of LoS connectivity and the UAV link to the core network without the need for the UAV to change its location considerably [22, 24, 25]. Fig. 7.1 shows an example for a two-layer UAV networks in rural and urban scenarios.

Although IRS may lead to significant SNR gain, such gain is highly dependent on the system capability to accurately estimate and compensate the end-to-end phase for each IRS element, which is one of the main challenges for IRS technology. Therefore, channel estimation, phase shift design, and performance evaluation with imperfect phase have received extensive attention [13, 26–33]. The phase estimation and compensation problem becomes more critical when IRS is integrated with flying nodes. In such contexts, UAV assisted communications may employ IRS to improve the signal quality in the absence of LoS connectivity between certain UAVs due to Skyscrapers, as in the case of urban areas [12, 34–42], or to provide efficient IAB as in the case of rural areas. Nevertheless, imperfect conditions such as UAVs jittering [43], channel estimation errors and phase noise imply that the IRS might be provided with inaccurate phase information. To model the effect of UAV jittering, a uniformly distributed random variable is assumed in [43]. Hence, performance analysis of IRS based systems while considering imperfect co-phasing process is crucial.

7.1.1 Related Work

Existing research work on IRS has covered a broad range of topics such as, but not limited to, power and energy optimization [1, 8, 13, 36, 44], physical layer security [7], resource allocation with non orthogonal multiple access (NOMA) [9], full duplex cognitive radio [5], and symbol-level precoding [11]. The integration of IRS and simultaneous wireless information and power transfer (SWIPT) is considered in [4]. Gao *et al.* considered the design of distributed IRS with passive reflecting beamforming that exploits statistical channel state information (CSI) and analyzed the ergodic achievable rate. Xie *et al.* [3] formulated and solved a joint optimization problem for the coordinated transmit and reflective beamforming for maximizing the minimum weighted received signal-to-interference-plus-noise ratio (SINR) at users subject to transmit power constraints. In [45], IRS is used to enhance the coverage of TeraHertz (THz) waveforms by using multi-hop transmission with multiple IRS panels, where deep reinforcement learning is employed to design the beamforming matrices.

The integration of IRS and UAVs has also been considered in the literature. For example, Lu *et al.* [12] proposed deploying flying platforms such as balloons or UAVs equipped with IRS to serve terrestrial users. The presented results show that flying IRS has an extra degree of freedom because of the capability of relocating the IRS to optimize certain system parameters such as maximizing the SNR. Moreover, it is shown that flying IRS require less number of elements to achieve a certain gain as compared to terrestrial IRS. Ma *et al.* [34] used the IRS to direct the signal to the UAV to increase its received signal strength. The obtained results show that significant signal improvement can be obtained using a small number of reflectors given that the location of the IRS and phase of the reflected signals are optimized. Ge *et al.* [35] considered a system where a single UAV transmits to multiple terrestrial IRS. The work focused on the optimal design of beamforming at the UAV, IRS and the UAV's trajectory to maximize the received power at the ground users. Mohamed and Aïssa [36] considered the downlink of a multi-antenna BS that communicates to a single antenna user via an IRS-UAV platform. The work evaluates the advantage of the IRS to maximize the total energy efficiency of the system by jointly optimizing the beamforming vector at the BS and the phase shifts matrix of the IRS. Various optimization techniques under the assumption of perfect CSI. Several other articles have considered integrated IRS-UAV [37–42] to minimize the transmit power, maximize the SNR, maximize the spectral efficiency, or maximize the sum rate. Nevertheless, they did not consider the error or outage probability analysis, or the impact of imperfect phase estimation and control process.

The impact of the phase modeling, estimation and compensation has been considered by Abeywickrama *et al.* [13], who proposed a more practical phase model that considers the correlation between the phase and amplitude of the individual reflected signals. The authors formulated an optimization problem to minimize the total transmit power by jointly designing the transmit and IRS beamforming. Although the phase model is interesting, the phase estimation and control processes are considered perfect. Moreover, the error and outage probabilities are not considered. The CSI estimation and discrete phase model are considered in [26], where the presented results, in terms of the achievable rate, demonstrate the significant impact of using a discrete phase. Hu *et al.* [27] considered the imperfect phase scenario by introducing user location uncertainty. The objective of this work is to minimize the transmit power subject to quality of service (QoS) constraint. CSI estimation has also been considered in [28–33], though the focus of these works is mostly on evaluating the CSI estimates accuracy, rather than evaluating its impact on the system performance. In [46], a channel estimation framework is introduced based on parallel factor decomposition, where iterative algorithms such as alternating least squares and vector approximate message passing are employed to estimate the unknown channel matrices. In [47], the achievable capacity of IRS-based UAV communications with imperfect phase compensation is evaluated.

The error probability analysis of IRS based systems with perfect phase estimation and compensation is considered in [48–54], and with imperfect phase information in [55,56] . The work in [55] approximated the composite fading channel, for a large number of reflectors, by a direct fading channel with Nakagami distribution. By deriving the distribution of the instantaneous signal-to-noise ratio (SNR), the bit error rate (BER) of the system is approximated using [57, Eq. 4]. Although the derived BER is generally accurate for large number of reflectors, it is not the case for small number of reflectors where the accuracy starts to degrade when the number of reflectors is less than 16. The work in [56] considered a more general model where the Central Limit Theorem (CLT) is used to approximate the composite double Nakagami channel distribution with von Mises phase errors, when a large number of reflectors is used. For a small number of reflectors, the Sinusoidal Addition Theorem (SAT) [58, 59] was used to evaluate the distribution of the received signal envelope. Nevertheless, the phase error for this case is considered to be uniform [56, Eq. 13, Eq. 14]. It is worth noting that both [55] and [56] considered only the BER analysis.

7.1.2 Motivation and Main Contributions

As can be noted from the surveyed literature, integrating IRS with flying networks using UAVs has a strong potential to improve UAVs connectivity in various applications. The extra degree of freedom that UAVs have can enable optimizing the IRS link by selecting the most suitable placement for the IRS-UAV. Nevertheless, achieving the ultimate gain using IRS is highly dependent on the reliability of the phase estimation and co-phasing processes. Practically speaking, both operations are not perfect, and thus, the ultimate gain promised by the IRS technology may not be guaranteed, which is particularly critical for IRS-UAV configurations. Therefore, this work analyzes the performance of a two-layer IRS assisted UAV communications under a more realistic scenario, where the phase estimation and co-phasing processes are imperfect. The phase error is modeled using the von Mises distribution, and the channels are considered to have a dominant LoS component. Unlike [47], which evaluates the achievable ergodic capacity, this paper evaluates the system performance in terms of symbol error rate (SER) and outage probability, where exact closed-form expressions are derived for a small number of reflecting elements, and accurate approximations are derived for large number of reflectors. In addition, this work considers a multi-layer UAV network with multiple hops, whereas [47] considers only the single hop scenario. It is worth noting that this paper considers the von Mises distribution to model the phase error, and thus it generalizes the derivations of the envelope distribution in [58, 59] where the phase error is considered to be uniformly distributed. Moreover, [58,59] consider a single hop system with a small number of reflections and without IRS. The obtained results show that the gain achieved using IRS depends strongly on the reliability of the

Table 7.1: Nomenclature.

Symbol	Definition	Symbol	Definition
s	Complex data symbol	ψ	Channel phase, Tx$\rightarrow$IRS
r	Received passband signal at IRS	y	Received passband signal at Rx
T_s	Symbol duration	$\hbar_i$	Channel attenuation, IRS$\rightarrow$Rx
$p(t)$	Pulse shape	ϕ_i	Channel phase, IRS$\rightarrow$Rx
L	Number of IRS elements	z	AWGN at Rx
f_c	Carrier frequency	σ_z^2	AWGN variance
a	Amplitude of data symbol, $\lvert s \rvert$	ζ_L	Signal phase at Rx
φ	Phase of data symbol, $\tan^{-1}\left(\frac{\Im\{s(\ell)\}}{\Re\{s(\ell)\}}\right)$	B_L	Signal amplitude at Rx
τ_i	Time delay of the i	d	Decision variable at Rx
h	Channel attenuation, Tx$\rightarrow$IRS	μ	Phase error mean
τ	Channel delay, Tx$\rightarrow$IRS	κ	Phase error shape parameter
P_e	Conditional SER	$I_0(\cdot)$	The modified Bessel function
$\mathcal{K}$	Rician fading factor	$\bar{P}_e$	Average SER

Table 7.2: Frequently used definitions.

$\alpha = j(b_2^2 - A_1^2 - A_2^2)$	$\mathcal{A}_1 = 2\sqrt{A_1 A_2}$	$K = \frac{\kappa_2}{2A_1A_2}$
$\acute{\alpha} = j(b_3^2 - b_2^2 - A_3^2)$	$\mathcal{A}_2 = (A_1 - A_2)^2$	$\acute{K} = \frac{\kappa_3}{2A_3b_2}$
$\breve{\alpha} = b_3^2 - b_2^2 - A_3^2$	$\mathcal{A}_3 = (A_1 + A_2)^2$	$\theta_i = \psi_i + \phi_i$
$\tilde{\alpha} = -j\alpha$	$v = -K\left(\sin\left(\epsilon_1\right) + j\cos\left(\epsilon_1\right)\right)$	$A_i = g_i \hbar_i h_i$
$\beta = -2\lvert A_1 A_2 \rvert$	$\acute{v} = -\acute{K}(\sin(\zeta_2) + j\cos(\zeta_2))$	$\epsilon_i = \hat{\theta}_i - \theta_i$
$\mathcal{B}(b_2) \triangleq \mathcal{B} = \sqrt{\alpha^2 + \beta^2}$	$I_0^{(2)}(\boldsymbol{\kappa}) = I_0(\kappa_1)I_0(\kappa_2)$	$\lambda = K\sin\left(\epsilon_1\right)$
$\mathcal{B}_2(b_2) \triangleq \mathcal{B}_2 = \frac{\tilde{\alpha}}{2A_1A_2}$	$I_0^{(3)}(\boldsymbol{\kappa}) = I_0(\kappa_1)I_0(\kappa_2)I_0(\kappa_3)$	$\acute{\lambda} = \acute{K}\sin(\zeta_2)$
$\mathcal{B}_3(b_3) \triangleq \mathcal{B}_3 = \frac{\breve{\alpha}}{2A_3b_2}$	$\acute{\mathcal{B}}(b_3) \triangleq \acute{\mathcal{B}} = \sqrt{\acute{\alpha}^2 + \acute{\beta}^2}$	$\acute{\beta} = -2\lvert A_3 b_2 \rvert$

co-phasing process, particularly when the number of reflectors is small. For a large number of reflectors, the system sensitivity to the co-phasing process decreases significantly.

7.1.3 Notations

For the readers' convenience, the nomenclature and main symbol definitions are given in Tables 7.1 and 7.2, respectively. In Table 7.2 $j \triangleq \sqrt{-1}$.

7.1.4 Paper Organization

The rest of the paper is organized as follows. Sec. 7.2 presents the system and channel models. Sec. 7.3 presents the derivation of the signal envelope distribution for different number of reflectors. Secs. 7.4 and 7.5 present the SER and outage probability analysis. Numerical and simulation results are presented in Sec. 7.7, and finally the paper is concluded in Sec. 7.8.

7.2 System and Channel Models

This work considers an IRS-assisted multi-layer UAV network where each device is equipped with a single antenna. As depicted in Fig. 7.1, a BS located at $\mathbf{p}_{\mathrm{BS}} = [x_{\mathrm{BS}}, y_{\mathrm{BS}}, \mathrm{h}_{\mathrm{BS}}]$, where h_{BS} is the height of the BS, aims at improving the transmission to users with poor channel conditions by creating virtual LoS links through a multi-layer network of UAVs. The top layer consists of an IRS panel carried by a UAV and located at $\mathbf{p}_{\text{IRS}} = [x_{\text{IRS}}, y_{\text{IRS}}, z_{\text{IRS}}]$. The IRS panel reflects the BS signal to a low-altitude UAV (LA-UAV) located at $\mathbf{p}_{\text{UAV}} = [x_{\text{UAV}}, y_{\text{UAV}}, z_{\text{UAV}}]$, which decodes-and-forwards (DF) the received data to ground users (GUs). The direct path between the BS and LA-UAVs is considered blocked because the UAV is far from the BS as shown in Fig. 7.1a, or due to obstacles such as skyscrapers in urban areas as shown in Fig. 7.1b.All UAVs are considered to have hovering capability. It is worth noting that this scenario is widely adopted in the literature as reported in [1, 15, 17–21] and the references listed therein. Therefore, the channel between the BS and ith IRS element can be modeled as flat fading link, and thus, the passband signal at the ith IRS element can be written as

$$\begin{aligned} r_i(t) &= \sqrt{P_t} h_i s \cos\left[\omega_{\text{c}} t - \psi_i\right] \\ &= \sqrt{P_t} h_i a \cos\left[\omega_{\text{c}} t + \varphi - \psi_i\right], \; i = [1, 2, \ldots, L] \end{aligned} \tag{7.1}$$

where P_t is the transmission power, $s \in \mathcal{S}$ is the complex information symbol, $s = a e^{j\varphi}$, $\omega_{\text{c}} \triangleq 2\pi f_{\text{c}}$ is the angular carrier frequency, f_{c} is the carrier frequency in Hz, h_i is the envelope of channel fading coefficient between the transmitter and the ith IRS element, ψ_i is the phase introduced by the channel, and , and $z\,(t)$ is the additive white Gaussian noise (AWGN). The phases $\psi_i \; \forall i$ are typically modeled as mutually independent and identically distributed (i.i.d.) random variables that are uniformly distributed over $[-\pi, \pi)$ [60]. Each IRS element shifts the signal phase by a value $\theta_i \in [-\pi, \pi)$ and attenuates the signal by a factor g_i. The phase shifts are typically evaluated at the BS based on the channel estimates and sent to the IRS panel through a dedicated control channel. Therefore, the reflected L signals received by a LA-UAV from the IRS can be written as [47]

$$y\,(t) = \sqrt{P_t} \sum_{i=1}^{L} g_i \hbar_i h_i a \cos\left[\omega t + \varphi - \psi_i - \phi_i + \theta_i\right] + z\,(t) \tag{7.2}$$

where $\hbar_i$ is the channel attenuation between the ith IRS element and LA-UAV, and $\phi_i \in [-\pi, \pi)$ is the phase shift caused by the channel. To maximize the received SNR, the value of θ_i is selected such that $\theta_i = \psi_i + \phi_i$, $^{[R_{1,1}]}$ $\psi_i \in [-\pi, \pi)$. Thus, $y\,(t)$ can be written as

$$y(t) = \sqrt{P_t} B_L \cos\left[\omega_c t + \varphi\right] + z\,(t) \tag{7.3}$$

where $B_L = \sum_{i=1}^{L} g_i \hbar_i h_i a$. For IRS phase estimation and compensation, we consider the protocol proposed in [61], where the cascaded channel associated with each IRS element is estimated separately from other reflectors, and the phase estimation and compensation processes are performed prior to data transmission. Consequently, the phase estimates for the L reflectors can be considered mutually independent. Moreover, the estimated phases will generally be different from the phases during the data transmission interval, and the phase difference is proportional to the number of IRS elements for which the phase will be estimated and compensated. As such, it is practically infeasible to estimate and compensate the phases ψ_i and ϕ_i perfectly because of the UAVs' jitter while hovering and the AWGN. Therefore, $y(t)$ with imperfect phase estimation and compensation should be written as

$$y(t) = \sqrt{P_t} \sum_{i=1}^{L} g_i \hbar_i h_i a \cos\left[\omega t + \varphi - \psi_i - \phi_i + \hat{\theta}_i\right] + z(t) \tag{7.4}$$

where $\hat{\theta}_i = \hat{\psi}_i + \hat{\phi}_i$, $\hat{\psi}_i$ and $\hat{\phi}_i$ are the estimated and compensated ψ_i and ϕ_i, respectively. Thus,

$$y(t) = \sqrt{P_t} a \sum_{i=1}^{L} A_i \cos\left[\omega t + \varphi + \epsilon_i\right] + z(t) \tag{7.5}$$

where $\epsilon_i = \hat{\theta}_i - \theta_i$, $g_i \hbar_i h_i \triangleq A_i \in (-\infty, \infty)$, and $\epsilon_i \in [-\pi, \pi)$. According to the SAT [58, 59], the sum of weighted sinusoidals with different phase values can be represented as a single sinusoid with phase ζ_L and amplitude B_L. Therefore,

$$y(t) = \sqrt{P_t} a B_L \cos(\omega t + \varphi + \zeta_L),\ t \geq 0 \tag{7.6}$$

where

$$B_L^2 = \|\mathbf{A}\|^2 + 2 \sum_{L \geq j > k \geq 1} A_j A_k \cos(\epsilon_j - \epsilon_k) \tag{7.7}$$

$$\zeta_L = \tan^{-1}\left[\frac{\sum_{i=1}^{L} A_i \sin(\epsilon_i)}{\sum_{i=1}^{L} A_i \cos(\epsilon_i)}\right] \tag{7.8}$$

and $\|\cdot\|$ is the Euclidian norm.

At the receiving LA-UAV, the carrier signal will be removed and the data symbol during the ℓth signaling period can be expressed as

$$y \triangleq \tfrac{1}{T_s} \int_0^{T_s} 2y(t) \mathrm{e}^{-j(\omega t + \hat{\zeta}_L)}\, dt = \sqrt{P_t} s B_L \mathrm{e}^{j\left(\zeta_L - \hat{\zeta}_L\right)} + z \tag{7.9}$$

where $\hat{\zeta}_L$ is an estimate of the accumulated phase offset ζ_L, and $z \sim \mathcal{CN}\left(0, \sigma_z^2\right)$ is the AWGN. According to the European Telecommunications Standards Institute (ETSI), each data resource block (RB) in the fifth generation new radio (5G-NR) includes large number of pilot symbols that can be used for channel estimation [62, 63]. Therefore, ζ_L can be estimated accurately at the receiving UAV. Moreover, $\hat{\zeta}_L$ is used locally at the receiver and will not be sent to the IRS, and hence, it is less prone to errors. Consequently, we can assume that $\hat{\zeta}_L \approx \zeta_L$, which reduces y to

$$y = \sqrt{P_t} B_L s + z. \tag{7.10}$$

At the LA-UAV, maximum likelihood detection (MLD) can be applied to extract the transmitted symbol s, such that

$$\hat{s} = \arg\max_{s \in \mathcal{S}} \left| y - \sqrt{P_t} B_L s \right|^2. \tag{7.11}$$

The LA-UAV forwards $\hat{s}$ to a GU located at $\mathbf{p}_{\mathrm{GU}} = [x_{\mathrm{GU}}, y_{\mathrm{GU}}, 0]$ where the channel is denoted as $\tilde{h}$. The received signal at the GU can be written as

$$x = \sqrt{P_{\mathrm{U}}} \tilde{h} \hat{s} + w \tag{7.12}$$

where P_{U} is the UAV transmit power. Similar to the detection method at the LA-UAV, the GU detects the transmitted symbol using MLD, which in the absence of SER information is given by [64]

$$\hat{s}_{\mathrm{GU}} = \arg\max_{s \in \mathcal{S}} \left| x - \sqrt{P_{\mathrm{U}}} \tilde{h} s \right|^2. \tag{7.13}$$

7.2.1 Channel Model for BS-IRS-UAV

The elements of $\mathbf{A}_L = [A_1, ..., A_L]$ depend on the channel model. For air-to-air channels (A2A), the signal typically has a strong LoS and a small number of weak reflected components, and thus, such channels can be modeled using the Rician fading [66–72]. According to the general Rician channel model, the instantaneous channel coefficient can be represented as

$$\breve{h}_i = \rho_{\text{t-r},i} \sqrt{\frac{1}{1 + \mathcal{K}_{\breve{h}}}} \left(\sqrt{\mathcal{K}_{\breve{h}}} \breve{h}_{i,\mathrm{LoS}} + \breve{h}_{i,\mathrm{nLoS}} \right) \tag{7.14}$$

where $\breve{h}_i \in \{h_i, \hbar_i, \tilde{h}\}$, $\rho_{\text{t-r},i}$ is the pathloss which depends on the distance between a transmitter t and a receiver r, $\breve{h}_{i,\mathrm{LoS}}$ is the LoS component which can be considered deterministic, $\breve{h}_{i,\mathrm{nLoS}}$ is the non-LoS component which is typically modeled as a complex Gaussian random variable, and $\mathcal{K}_{\breve{h}}$ is the Rice factor. However, because the spacing between reflectors is very small as compared to the distance between transceivers, the distance between the BS and any IRS element can be assumed equal. Similarly, the distance between any reflector and the small drone can be assumed equal for all reflectors. Therefore, the subscript i in ρ_i can be omitted, and for given transmitter and receiver locations in 3D Cartesian coordinates as $\mathbf{p}_t = [x_t, y_t, z_t]$ and $\mathbf{p}_r = [x_r, y_r, z_r]$, respectively, ρ can be represented by

$$\rho_{\text{t-r}} \triangleq \frac{c}{4\pi f_c} d_{\text{t-r}}^{-\varrho/2} = \frac{c}{4\pi f_c} \left\| \mathbf{p}_t - \mathbf{p}_r \right\|^{-\varrho/2} \tag{7.15}$$

where c is the speed of light, $d_{\text{t-r}}$ is the distance between the transmitter and receiver, and ϱ is the pathloss exponent.

However, as the measurements indicate, the Rice factor $\mathcal{K}$ for A2A channel is about 20 dB, and the received signal power may remain constant for long time periods [66–72]. Consequently, the channel coefficients h_i's are not suffering from small scale fading, and the large scale fading is dominated by the free space path loss. Similarly, for a sufficiently high BS, $\mathrm{h_{BS}}$ is large, $\hbar_i$ can be assumed dominated by the LoS term. Mathematically, by referring to (7.14), for large values of the Rice factor ($\mathcal{K}_{\check{h}} \to \infty$), $\sqrt{\mathcal{K}_{\check{h}}}\check{h}_{i,\mathrm{LoS}} \gg \check{h}_{i,\mathrm{nLoS}}$, and thus A_i can be approximated as,

$$A_i = g_i \left(\frac{c}{4\pi f_c}\right)^2 \|\mathbf{p}_{\mathrm{BS}} - \mathbf{p}_{\mathrm{IRS}}\|^{-\varrho/2} \|\mathbf{p}_{\mathrm{UAV}} - \mathbf{p}_{\mathrm{IRS}}\|^{-\varrho/2} \sqrt{\frac{\mathcal{K}_h \mathcal{K}_{\hbar}}{(1+\mathcal{K}_h)(1+\mathcal{K}_{\hbar})}} h_{i,\mathrm{LoS}} \hbar_{i,\mathrm{LoS}}. \tag{7.16}$$

Nevertheless, the obtained results in Sec. 7.7 show that the constant fading coefficients model can be used to closely approximate the Rician fading channel with high $\mathcal{K}$ values, i.e., $\mathcal{K} \geq 20$ dB.

7.2.2 Channel Model for UAV-GU

Unlike BS-UAV and UAV-UAV channels, it is very likely that the GU detects some reflected signals from surroundings, and thus this channel is modeled as Rician channel with limited Rice factor

$$\tilde{h} = \frac{c}{4\pi f_c} \|\mathbf{p}_{\mathrm{UAV}} - \mathbf{p}_{\mathrm{GU}}\|^{-\varrho/2} \sqrt{\frac{1}{1+\mathcal{K}_{\tilde{h}}}} \left(\sqrt{\mathcal{K}_{\tilde{h}}}\tilde{h}_{i,\mathrm{LoS}} + \tilde{h}_{i,\mathrm{nLoS}}\right) \tag{7.17}$$

Since the top layer, i.e., BS-IRS-UAV link, is the main interest of this paper, Secs. III, IV and V focus on the derivations of the PDF of the received signal envelope, SER and outage probability for this layer, respectively. Nevertheless, the derivations for the SER and outage probability for the multi-layer network scenario are provided in Sec. VI.

7.3 PDF of the Signal Envelope B_L

For given values of A_1, A_2, ..., A_L, the PDF of B_L can be computed as [58, 59]

$$f_{B_L}(b_L) = \frac{b_L}{\pi} \int_{-\infty}^{\infty} \mathrm{e}^{-jb_L^2 t} \int_{-\pi}^{\pi} \mathrm{e}^{jt\{b_{L-1}^2 + A_L^2 + 2A_L b_{L-1} \cos(\epsilon_L - \zeta_{L-1})\}} \times f_{\epsilon}(\boldsymbol{\epsilon}) d\boldsymbol{\epsilon} dt \tag{7.18}$$

where $\boldsymbol{\epsilon} = [\epsilon_1, \epsilon_2, \ldots, \epsilon_L]$ are the phase errors for the L reflecting elements. The PDF $f_{B_L}(b_L)$ is derived in [58, 59] for the uniform phase $\epsilon_i \sim \mathcal{U}[-\pi, \pi]$ $\forall i$, and has been used to model fading, interference and jamming in wireless systems [60, 73, 74]. However, when the SAT is used to model phase estimation errors, the uniform phase model is not applicable for such scenarios [75], because the phase error generally follows the von Mises distribution with mean μ and shape parameter κ [47, 76],

$$f_{\epsilon_i}(\epsilon_i) = \frac{\mathrm{e}^{\kappa_i \cos(\epsilon_i - \mu_i)}}{2\pi I_0(\kappa_i)} \tag{7.19}$$

where $I_q(.)$ is the modified Bessel function of the first kind and order q. It is worth noting that the values of κ_i and μ_i depend on the accuracy of phase estimation and compensation process, where μ_i

represents the bias of the estimator whereas κ_i is inversely proportional to the mean-squared error (MSE) of phase estimation and compensation. For example, high values of κ_i are obtained when accurate phase compensation with low MSE is performed. In [43], the phase error caused by UAV jitter is modeled as a uniformly distributed random variable, whereas this work considers von Mises distribution which is more general. In this paper, we assume that the phase compensation error caused by all kinds of possible imperfections, such as UAV jittering, air turbulence effects, phase noise, and channel estimation process, is represented by ϵ_i with parameter κ_i. As can be noted from (8.5), the uniform PDF is a special case of the von Mises PDF with $\kappa = 0$, which corresponds to the worst case phase error. For large values of κ, the PDF becomes concentrated around μ, which indicates small phase errors, and setting $\mu = 0$ implies that the phase error is unbiased. Although in theory $\kappa \in [0, \infty)$, typical values of κ occupy a smaller bounded range. For example, least square channel estimation (LSCE) using a single pilot symbol provides $\kappa = [1.25, 3, 8, 25, 250]$ for SNR $= [-5, 0, 5, 10, 20]$, respectively.

In the following subsections, the exact PDF $f_{B_L}(b_L)$ is derived for the cases of $L = 2$, 3, and the PDFs for $L \geq 4$ are approximated using the CLT. It is worth noting that considering the cases with small number of IRS elements is crucial for several applications such as resource allocation for multiuser IRS where each user can be assigned a wide range of IRS elements [77]. Consequently, this paper considers a wide range of reflecting elements including $L = \{2, 3\}$ as well as $L \geq 4$. Moreover, for all scenarios, the phase error will be considered unbiased, $\mu_i = 0\ \forall i$, and the values of κ_i are considered unequal deterministic variables. Additionally, the phase errors $\epsilon_i\ \forall i$ are i.i.d. von Mises random variables.

7.3.1 The Signal Envelope PDF for $L = 2$, $f_{B_2}(b_2)$

For $L = 2$, $\zeta_{L-1} = \zeta_1 = \epsilon_1$ and $b_1 = A_1$. Substituting these terms in (7.18) and rearranging the order of integrals give

$$f_{B_2}(b_2) = \frac{b_2}{4\pi^3 I_0^{(2)}(\boldsymbol{\kappa})} \int_{-\infty}^{\infty} \mathrm{e}^{-jt(b_2^2 - A_1^2 - A_2^2)} \int_{-\pi}^{\pi} \mathrm{e}^{\kappa_1 \cos(\epsilon_1)} \left[\int_{-\pi}^{\pi} \mathrm{e}^{2jtA_1A_2\cos(\epsilon_2 - \epsilon_1) + \kappa_2 \cos(\epsilon_2)} d\epsilon_2 \right] d\epsilon_1 dt. \tag{7.20}$$

It should be noted that when the distributions of phase errors are not uniform, it cannot be assumed that one of these errors is zero as reported in [58, 59], which implies that there is an additional integration that should be solved for the von Mises PDFs. The integral inside the brackets can be evaluated with respect to ϵ_2 as [78, 3.338.4],

$$\begin{aligned} \mathcal{I}_2 &= \int_{-\pi}^{\pi} \mathrm{e}^{2jtA_1A_2\cos(\epsilon_2 - \epsilon_1) + \kappa_2 \cos(\epsilon_2)} d\epsilon_2 \\ &= 2\pi I_0 \left(2\left|A_1A_2\right| \sqrt{-t^2 + K^2 + 2jtK\cos(\epsilon_1)} \right). \end{aligned} \tag{7.21}$$

By substituting (7.21) in (7.20) and rearranging the integrals order, $f_{B_2}(b_2)$ can be obtained as

$$f_{B_2}(b_2) = \frac{b_2}{4\pi^3 I_0^{(2)}(\boldsymbol{\kappa})} \int_{-\pi}^{\pi} \mathrm{e}^{\kappa_1 \cos(\epsilon_1)} \left[\int_{-\infty}^{\infty} \mathrm{e}^{-jt\tilde{\alpha}} \mathcal{I}_2 dt \right] d\epsilon_1. \tag{7.22}$$

The integral inside the brackets, $\mathcal{I}_3$, can be evaluated using the following tabulated integral [78, 6.616.1],

$$\int_0^{\infty} \mathrm{e}^{-\alpha x} J_0\left(\beta\sqrt{x^2+2\lambda x}\right) dx = \frac{1}{\sqrt{\alpha^2+\beta^2}} \mathrm{e}^{\lambda\left(\alpha-\sqrt{\alpha^2+\beta^2}\right)} \tag{7.23}$$

which after some straightforward manipulations can be written as,

$$\int_{-\infty}^{\infty} \mathrm{e}^{-\alpha x} I_0\left(-j\beta\sqrt{x^2+2\lambda x}\right) dx = \frac{1}{\sqrt{\alpha^2+\beta^2}} \left[\mathrm{e}^{\lambda\left(\alpha-\sqrt{\alpha^2+\beta^2}\right)} + \mathrm{e}^{\lambda\left(\alpha+\sqrt{\alpha^2+\beta^2}\right)} \right]. \tag{7.24}$$

By using the change of variable $x = t + v$,

$$\int_{-\infty}^{\infty} \mathrm{e}^{-\alpha x} I_0\left(-j\beta\sqrt{x^2+2\lambda x}\right) dx = \mathrm{e}^{-\alpha v} \int_{-\infty}^{\infty} \mathrm{e}^{-\alpha t} I_0\left(-j\beta\sqrt{t^2+2t(v+\lambda)+v^2+2\lambda v}\right) dt. \tag{7.25}$$

Therefore, $\mathcal{I}_3$ can be evaluated as

$$\mathcal{I}_3 = \mathrm{e}^{\alpha v} \frac{2\pi}{\mathcal{B}} \left[\mathrm{e}^{\lambda(\alpha-\mathcal{B})} + \mathrm{e}^{\lambda(\alpha+\mathcal{B})} \right], \qquad \alpha^2+\beta^2 \geq 0. \tag{7.26}$$

By noting that $v + \lambda = -jK\cos(\epsilon_1)$ and $v^2 + 2\lambda v = -K^2$, $f_{B_2}(b_2)$ can be expressed as

$$\begin{aligned}
f_{B_2}(b_2) &= \frac{b_2}{2\pi^2 \mathcal{B} I_0^{(2)}(\boldsymbol{\kappa})} \left[\int_{-\pi}^{\pi} \mathrm{e}^{[(K\tilde{\alpha}+\kappa_1)\cos(\epsilon_1) - K\mathcal{B}\sin(\epsilon_1)]} + \int_{-\pi}^{\pi} \mathrm{e}^{[(K\tilde{\alpha}+\kappa_1)\cos(\epsilon_1) + K\mathcal{B}\sin(\epsilon_1)]} \right] d\epsilon_1 \\
&= \frac{b_2}{\pi \mathcal{B} I_0^{(2)}(\boldsymbol{\kappa})} \left[I_0\left[\sqrt{(K\tilde{\alpha}+\kappa_1)^2 + [K\mathcal{B}]^2}\right] + I_0\left[\sqrt{(K\tilde{\alpha}+\kappa_1)^2 + [K\mathcal{B}]^2}\right] \right] \\
&= \frac{2b_2}{\pi \mathcal{B} I_0^{(2)}(\boldsymbol{\kappa})} I_0\left[\sqrt{(2KA_1A_2\mathcal{B}_2+\kappa_1)^2 + K^2\left(-4A_1^2A_2^2\mathcal{B}_2^2 + 4A_1^2A_2^2\right)}\right] \\
&= \frac{2b_2}{\pi \mathcal{B} I_0^{(2)}(\boldsymbol{\kappa})} I_0\left[\sqrt{(\kappa_1-\kappa_2)^2 + \frac{\kappa_2\kappa_1}{A_1A_2}\left(b_2^2 - \mathcal{A}_2\right)}\right]
\end{aligned} \tag{7.27}$$

which, after some algebraic simplifications, can be simplified to

$$f_{B_2}(b_2) = \frac{2b_2 I_0\left[\sqrt{(\kappa_1-\kappa_2)^2 + \frac{\kappa_2\kappa_1}{A_1A_2}\left(b_2^2-\mathcal{A}_2\right)}\right]}{\pi\sqrt{\left(\mathcal{A}_3 - b_2^2\right)\left(b_2^2-\mathcal{A}_2\right)} I_0^{(2)}(\boldsymbol{\kappa})}, \; |\mathcal{B}_2| \leq 1. \tag{7.28}$$

The condition $|\mathcal{B}_2| \leq 1$ can be solved as $\left|\frac{b_2^2 - A_1^2 - A_2^2}{2A_1A_2}\right| \leq 1$, which gives $B_{2,\mathrm{m}} \leq b_2 \leq B_{2,\mathrm{M}}$, where $B_{2,\mathrm{m}} = |A_1 - A_2|$ and $B_{2,\mathrm{M}} = A_1 + A_2$. It can be noted that $f_{B_2}(b_2)$ derived in [58, 59] is just a special case of (7.28) with $\kappa_i = 0 \; \forall i$.

Fig. 7.2a shows the PDF of $f_{B_2}(b_2)$ for different values of κ, where the individual signal amplitudes are $A_i = 1 \; \forall i$. As can be noted from the figure, the derived formula in (7.28) matches the simulation results

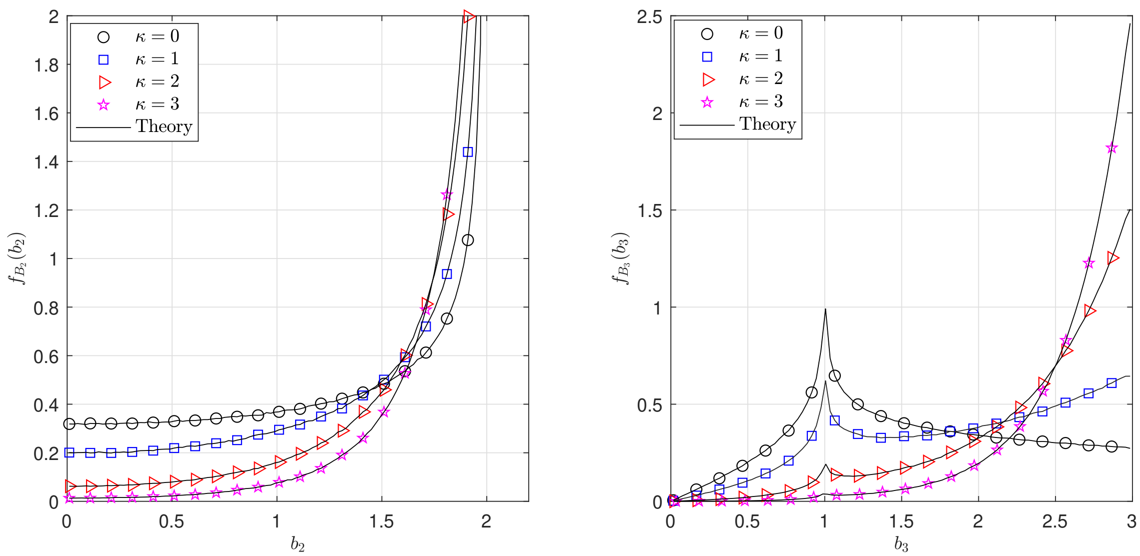

(a) $L = 2$

(b) $L = 3$

Figure 7.2: The PDF of the signal envelope for different values of κ for $L = 2, 3$, $A_i = 1\ \forall i$.

for all the considered values of κ, including $\kappa = 0$, which corresponds to the uniformly distributed phase errors. The figure shows that large phase errors may drive the amplitude B_2 below the $\min\{A_1, A_2\}$, which implies that the error rate would be worse than the case without IRS. Increasing the value of κ makes the envelope more concentrated around $A_1 + A_2$, which implies that the IRS will provide a gain of about 6 dB in terms of SNR.

7.3.2 The Signal Envelope PDF for $L = 3$, $f_{B_3}(b_3)$

Using the same assumptions of $L = 2$, $f_{B_3}(b_3)$ can be expressed as

$$f_{B_3}(b_3) = \frac{b_3}{8\pi^4 I_0^{(3)}(\boldsymbol{\kappa})} \int_{-\infty}^{\infty} \mathrm{e}^{-jb_3^2 t} \int_{-\pi}^{\pi}\int_{-\pi}^{\pi}\int_{-\pi}^{\pi} \mathrm{e}^{jt\{b_2^2 + A_3^2 + 2A_3 b_2 \cos(\epsilon_3 - \zeta_2)\}} \mathrm{e}^{\sum_{i=1}^{L} \kappa_i \cos(\epsilon_i)} d\epsilon_1 d\epsilon_2 d\epsilon_3 dt. \tag{7.29}$$

where $b_2^2 = A_1^2 + A_2^2 + 2A_1A_2\cos(\epsilon_2 - \epsilon_1)$ and $\zeta_2 = \tan^{-1}\left[\frac{A_1\sin(\epsilon_1) + A_2\sin(\epsilon_2)}{A_1\cos(\epsilon_1) + A_2\cos(\epsilon_2)}\right]$. Hence, the constraint $|\mathcal{B}_2| \leq 1$ is also applicable. By substituting the identity $\cos(\epsilon_3 - \zeta_2) = \cos(\epsilon_3)\cos(\zeta_2) + \sin(\epsilon_3)\sin(\zeta_2)$ and evaluating the integral with respect to ϵ_3, $f_{B_3}(b_3)$ can be written as

$$\begin{aligned} f_{B_3}(b_3) &= \frac{b_3}{4\pi^3 I_0^{(3)}(\boldsymbol{\kappa})} \int_{-\infty}^{\infty} \mathrm{e}^{-jt\left(b_3^2 - A_3^2\right)} \int_{-\pi}^{\pi}\int_{-\pi}^{\pi} \mathrm{e}^{jtb_2^2} \mathrm{e}^{\kappa_1\cos(\epsilon_1) + \kappa_2\cos(\epsilon_2)} \\ &\qquad \times I_0\left[\sqrt{\left[2jtA_3b_2\cos(\zeta_2) + \kappa_3\right]^2 + \left[2jtA_3b_2\sin(\zeta_2)\right]^2}\right] d\epsilon_1 d\epsilon_2 dt \\ &= \frac{b_3}{4\pi^3 I_0^{(3)}(\boldsymbol{\kappa})} \int_{-\pi}^{\pi} \mathrm{e}^{\kappa_1\cos(\epsilon_1)} \int_{-\pi}^{\pi} \frac{1}{\acute{\mathcal{B}}} \mathrm{e}^{\kappa_2\cos(\epsilon_2)} \\ &\qquad \times \left[\mathrm{e}^{-\acute{K}\sin(\zeta_2)\acute{\mathcal{B}} + \check{a}\acute{K}\cos(\zeta_2)} + \mathrm{e}^{\acute{K}\sin(\zeta_2)\acute{\mathcal{B}} + \check{a}\acute{K}\cos(\zeta_2)}\right] \mathbf{1}_{\{|\mathcal{B}_3| \leq 1\}} d\epsilon_2 d\epsilon_1 \end{aligned} \tag{7.30}$$

where $\mathbf{1}_{\{\cdot\}}$ is the indicator function of the set $\{\cdot\}$. Thus,

$$f_{B_3}(b_3) = \frac{b_3}{2\pi^3 I_0^{(3)}(\boldsymbol{\kappa})} \int_{-\pi}^{\pi}\int_{-\pi}^{\pi} \frac{1}{\acute{\mathcal{B}}} \mathrm{e}^{\kappa_1 \cos(\epsilon_1)+\kappa_2 \cos(\epsilon_2)} \left[\mathrm{e}^{\acute{K}\check{\alpha}\cos(\zeta_2)} \cosh\left(\acute{K}\sin(\zeta_2)\acute{\mathcal{B}}\right)\right] \mathbf{1}_{\{|\mathcal{B}_3|\leq 1\}} d\epsilon_1 d\epsilon_2. \tag{7.31}$$

As can be noted from (7.31), deriving $f_{B_3}(b_3)$ in a closed-form is intractable. Fig. 7.2b shows $f_{B_3}(b_3)$ for various values of κ, where high values of κ make the PDF to be mostly concentrated close to the maximum amplitude, i.e., $B_{3,\mathrm{M}} = A_1 + A_2 + A_3$. For the perfect phase estimation case, the anticipated gain provided by the IRS will be about 9.5 dB. Nevertheless, for low values of κ, the signal will experience fading, which may cause severe increase in the probability of error. In such scenarios, the error probability without IRS may become less than that with IRS.

7.3.3 The Signal Envelope PDF $f_{B_L}(b_L)$ for $L \geq 4$

As can be observed from the derivations for the case of $L = 3$, the exact solution for the PDF of the received SNR is not feasible when $L \geq 4$. Therefore, the CLT can be invoked to approximate the PDF $f_{B_L}(b_L)$ when $L \geq 4$. By referring to B_L^2 in (7.7), which is obtained by using the SAT, it is easier to compute $f_{B_L^2}\left(b_L^2\right)$. Moreover, because the values of B_L are bounded by $B_{L,\mathrm{m}} \leq b_L \leq B_{L,\mathrm{M}}$, it will be more accurate to use the truncated Gaussian distribution [79] to derive the PDF using CLT. By defining $y_L \triangleq b_L^2$ for notational simplicity, we obtain

$$f_{Y_L}(y_L) = \frac{1}{\varpi_L\sqrt{2\pi\sigma_{Y_L}^2}} \exp\left(-\frac{(y_L - m_{Y_L})^2}{2\sigma_{Y_L}^2}\right) \tag{7.32}$$

where ϖ_L is the truncated PDF normalization factor, and m_{Y_L} and $\sigma_{Y_L}^2$ are the mean and variance of the Gaussian PDF, which are given by

$$m_{Y_L} = \sum_{i=1}^{L} A_i^2 + 2\sum_{L\geq j>k\geq 1} A_j A_k \frac{I_1(\kappa_j)\, I_1(\kappa_k)}{I_0(\kappa_j) I_0(\kappa_k)} \tag{7.33}$$

and

$$\sigma_{Y_L}^2 \triangleq \mathbb{E}\left[Y_L^2\right] - m_{Y_L}^2 \tag{7.34}$$

The complete derivations of m_{Y_L}, $\mathbb{E}\left[Y_L^2\right]$ and $\sigma_{Y_L}^2$ are given in Appendix II.

The truncated PDF normalization factor ϖ_L can be written as [79, pp. 20]

$$\varpi_L = \Phi\left(\frac{B_{L,\mathrm{M}} - m_{Y_L}}{\sigma_{Y_L}}\right) - \Phi\left(\frac{B_{L,\mathrm{m}} - m_{Y_L}}{\sigma_{Y_L}}\right) \tag{7.35}$$

where $\Phi(\cdot)$ is the cumulative distribution function of the standard normal distribution. It is worthy to observe that ϖ_L is approximately a unity for high values of m_{Y_L}, where this condition is satisfied when a very large number of reflectors is deployed.

7.4 SER Analysis for BS-IRS-UAV Link

In general, the SER of communication systems over fading channels can be expressed as,

$$\bar{P}_{\mathrm{e}} = \int_0^{\infty} (P_{\mathrm{e}}|b_L)\ f_{B_L}(b_L)\ db_L \tag{7.36}$$

where $f_{B_L}(b_L)$ is the probability density function (PDF) of the signal envelope B_L and $P_{\mathrm{e}}|b_L$ is the conditional SER given $B_L = b_L$.

7.4.1 One Reflector, $L = 1$

In this case, $b_1 = \beta_1 h_1 \hbar_1 \triangleq A_1$, hence the channel is deterministic and based on (8.6), the instantaneous SNR is $\gamma_1 = A_1^2/\sigma_z^2$. Therefore, the SER can be expressed as

$$\bar{P}_{\mathrm{e}} = C_1 Q\left(\sqrt{C_2\gamma_1}\right) \tag{7.37}$$

where $Q(\cdot)$ is the tail distribution function of the standard normal distribution, and C_1 and C_2 are constants that depend on the modulation scheme [80, Table 6.1, pp. 179].

7.4.2 Two Reflectors, $L = 2$

Because the phase compensation errors at the two reflectors are i.i.d random variables, then the instantaneous SNR $\gamma_2 = \frac{b_2^2}{\sigma_z^2}$ is also random. Therefore, the average SER $\bar{P}_{\mathrm{e}}$ can be expressed as

$$\begin{aligned}\bar{P}_{\mathrm{e}} &= C_1 \int_{B_{2,\mathrm{m}}}^{B_{2,\mathrm{M}}} Q\left(b_2\sqrt{\frac{C_2}{\sigma_z^2}}\right) f_{B_2}(b_2)db_2 \\ &= \frac{2C_1}{\pi I_0^{(2)}(\boldsymbol{\kappa})} \int_{B_{2,\mathrm{m}}}^{B_{2,\mathrm{M}}} \frac{b_2 Q\left(b_2\sqrt{\frac{C_2}{\sigma_z^2}}\right)}{\sqrt{\left(\mathcal{A}_3 - b_2^2\right)\left(b_2^2 - \mathcal{A}_2\right)}} I_0\left[\sqrt{\left(\kappa_1-\kappa_2\right)^2 + \frac{\kappa_2\kappa_1}{A_1A_2}\left(b_2^2-\mathcal{A}_2\right)}\right] db_2.\end{aligned} \tag{7.38}$$

By substituting $x = \sqrt{b_2^2 - \mathcal{A}_2}$, and noting that $B_{2,\mathrm{m}} = |A_1 - A_2|$ and $B_{2,\mathrm{M}} = (A_1 + A_2)$, then

$$\bar{P}_{\mathrm{e}} = \frac{2C_1}{\pi I_0^{(2)}(\boldsymbol{\kappa})} \int_0^{\mathcal{A}_1} \frac{Q\left(\sqrt{\frac{C_2}{\sigma_z^2}\left(x^2+\mathcal{A}_2\right)}\right)}{\sqrt{-x^2+\mathcal{A}_1^2}} I_0\left[\sqrt{\left(\kappa_1-\kappa_2\right)^2 + \frac{\kappa_2\kappa_1}{A_1A_2}x^2}\right] dx. \tag{7.39}$$

Evaluating the integral in (7.39) is intractable due to the Bessel function. Therefore, we use the infinite series representation of $I_0(\cdot)$, which gives

$$\bar{P}_{\mathrm{e}} = \frac{2C_1}{\pi I_0^{(2)}(\boldsymbol{\kappa})} \sum_{m=0}^{\infty} \frac{1}{2^{2m}(m!)^2} \int_0^{\mathcal{A}_1} \frac{Q\left(\sqrt{\frac{C_2}{\sigma_z^2}\left(x^2+\mathcal{A}_2\right)}\right)}{\sqrt{-x^2+\mathcal{A}_1^2}} \left[\left(\kappa_1-\kappa_2\right)^2 + \frac{\kappa_2\kappa_1}{A_1A_2}x^2\right]^m dx. \tag{7.40}$$

Using the binomial theorem, (7.40) can be expressed as

$$\bar{P}_{\mathrm{e}} = \frac{2C_1}{\pi I_0^{(2)}(\boldsymbol{\kappa})} \sum_{m=0}^{\infty} \frac{1}{2^{2m}\left(m!\right)^2} \sum_{k=0}^{m} \binom{m}{k} \left(\kappa_1 - \kappa_2\right)^{2(m-k)} \left(\frac{\kappa_2\kappa_1}{A_1 A_2}\right)^k \int_0^{\mathcal{A}_1} \frac{Q\left(\sqrt{\frac{C_2}{\sigma_z^2}\left(x^2+\mathcal{A}_2\right)}\right)}{\sqrt{-x^2+\mathcal{A}_1^2}} x^{2k} dx. \tag{7.41}$$

However, the integral in (7.41) does not have a closed-form solution except for the special case when $A_1 = A_2 \triangleq A$. Consequently, $\bar{P}_{\mathrm{e}}$ is reduced to

$$\bar{P}_{\mathrm{e}} = \frac{2C_1}{\pi I_0^{(2)}(\boldsymbol{\kappa})} \sum_{m=0}^{\infty} \frac{1}{2^{2m}\left(m!\right)^2} \sum_{k=0}^{m} \binom{m}{k} \left(\kappa_1 - \kappa_2\right)^{2(m-k)} \left(\frac{\kappa_2\kappa_1}{A^2}\right)^k \int_0^{\mathcal{A}_1} \frac{Q\left(\sqrt{\frac{C_2}{\sigma_z^2}}x\right)}{\sqrt{-x^2+\mathcal{A}_1^2}} x^{2k} dx \tag{7.42}$$

which can be evaluated as [81, 2.8.3.1, pp. 102],

$$\begin{aligned}\bar{P}_{\mathrm{e}} = {} & \frac{C_1}{\pi I_0^{(2)}(\boldsymbol{\kappa})} \sum_{m=0}^{\infty} \frac{1}{2^{2m}\left(m!\right)^2} \sum_{k=0}^{m} \binom{m}{k} \left(\kappa_1 - \kappa_2\right)^{2(m-k)} \left(\frac{\kappa_2\kappa_1}{A^2}\right)^k \\ & \times \left\{ \frac{\mathcal{A}_1^{2k}}{2} \mathrm{B}\left(k+\tfrac{1}{2}, \tfrac{1}{2}\right) - \sqrt{\frac{C_2}{2\pi\sigma_z^2}} \mathcal{A}_1^{2k+1} \mathrm{B}\left(k+1, \tfrac{1}{2}\right) {}_2F_2\left(\left[k+1, \tfrac{1}{2}\right]; \left[k+\tfrac{3}{2}, \tfrac{3}{2}\right]; -\frac{\mathcal{A}_1^2 C_2}{2\sigma_z^2}\right)\right\}\end{aligned} \tag{7.43}$$

where ${}_2F_2\left(\cdot\right)$ is the hypergeometric function and $\mathrm{B}\left(\cdot,\cdot\right)$ is the beta function, $\mathrm{B}\left(\alpha,\beta\right) = \frac{\Gamma(\alpha)\Gamma(\beta)}{\Gamma(\alpha+\beta)}$.

For the general case of $A_1 \neq A_2$, the integral can be solved using the Q-function approximation [82]

$$Q\left(x\right) \simeq \sum_{l=1}^{N} \delta_l \exp\left(-\varepsilon_l x^2\right), \; x > 0 \tag{7.44}$$

where δ_l and ε_l are constants evaluated to minimize the approximation error, where their values can be found in [82]. Using the Q-function approximation, (7.41) can be simplified to

$$\begin{aligned}\bar{P}_{\mathrm{e}} = {} & \frac{2C_1}{\pi I_0^{(2)}(\boldsymbol{\kappa})} \sum_{m=0}^{\infty} \frac{1}{2^{2m}\left(m!\right)^2} \sum_{k=0}^{m} \binom{m}{k} \left(\kappa_1 - \kappa_2\right)^{2(m-k)} \left(\frac{\kappa_2\kappa_1}{A_1 A_2}\right)^k \sum_{l=1}^{N} \delta_l \exp\left(-\frac{C_2\mathcal{A}_2}{\sigma_z^2}\varepsilon_l\right) \\ & \times \int_0^{\mathcal{A}_1} \frac{\exp\left(-\frac{\varepsilon_l C_2}{\sigma_z^2}x^2\right)}{\sqrt{-x^2+\mathcal{A}_1^2}} x^{2k} dx.\end{aligned} \tag{7.45}$$

Substituting $u = x^2$ yields

$$\begin{aligned}\bar{P}_{\mathrm{e}} = {} & \frac{C_1}{\pi I_0^{(2)}(\boldsymbol{\kappa})} \sum_{m=0}^{\infty} \frac{1}{2^{2m}\left(m!\right)^2} \sum_{k=0}^{m} \binom{m}{k} \left(\kappa_1 - \kappa_2\right)^{2(m-k)} \left(\frac{\kappa_2\kappa_1}{A_1 A_2}\right)^k \sum_{l=1}^{N} \delta_l \exp\left(-\frac{C_2\mathcal{A}_2}{\sigma_z^2}\varepsilon_l\right) \\ & \times \int_0^{\mathcal{A}_1^2} \frac{\exp\left(-\frac{\varepsilon_l C_2}{\sigma_z^2}u\right)}{\sqrt{-u+\mathcal{A}_1^2}} u^{k-0.5} du.\end{aligned} \tag{7.46}$$

Thereafter, [19, 2.3.6.1, pp. 324] is used to solve the integral, which gives,

$$\bar{P}_{\mathrm{e}} = \frac{C_1}{\pi I_0^{(2)}(\boldsymbol{\kappa})} \sum_{m=0}^{\infty} \frac{1}{2^{2m}(m!)^2} \sum_{k=0}^{m} \binom{m}{k} (\kappa_1 - \kappa_2)^{2(m-k)} \left(\frac{\kappa_2 \kappa_1}{A_1 A_2}\right)^k \sum_{l=1}^{N} \delta_l \exp\left(-\frac{C_2 \mathcal{A}_2}{\sigma_z^2}\varepsilon_l\right)$$
$$\times \mathrm{B}(k+0.5, 0.5)(4A_1A_2)^k \; {}_1F_1\left(k+0.5, k+1, -\mathcal{A}_1^2 \frac{\varepsilon_l C_2}{\sigma_z^2}\right). \quad (7.47)$$

7.4.3 Three Reflectors, $L = 3$

Similar to the $L = 2$ case, the SER for $L = 3$ can be computed as,

$$\bar{P}_{\mathrm{e}} = C_1 \int_{B_{3,\mathrm{m}}}^{B_{3,\mathrm{M}}} Q\left(b_3 \sqrt{\frac{C_2}{\sigma_z^2}}\right) f_{B_3}(b_3) db_3 \quad (7.48)$$

where $B_{3,\mathrm{m}}$ and $B_{3,\mathrm{M}}$ are the minimum and maximum values of B_3. As can be noted from (7.31), evaluating $\bar{P}_{\mathrm{e}}$ in a closed-form is infeasible because $f_{B_3}(b_3)$ does not have a closed-form solution. Consequently, the SER can be obtained numerically after substituting (7.31) into (7.48).

7.4.4 Number of Reflectors $L \geq 4$

Because $B_{L,\mathrm{m}} \leq B_L \leq B_{L,\mathrm{M}}$, then $Y_L = B_L^2$ is bounded as $B_{L,\mathrm{m}}^2 \leq Y_L \leq B_{L,\mathrm{M}}^2$. Therefore,

$$\bar{P}_{\mathrm{e}} = \int_{B_{L,\mathrm{m}}^2}^{B_{L,\mathrm{M}}^2} P_{\mathrm{e}} \, f_{Y_L}(y_L) dy_L = \frac{C_1}{\varpi_L \sqrt{2\pi\sigma_{Y_L}^2}} \int_{B_{L,\mathrm{m}}^2}^{B_{L,\mathrm{M}}^2} Q\left(\sqrt{\frac{C_2}{\sigma_z^2} y_L}\right) \exp\left(-\frac{(y_L - \mu_{Y_L})^2}{2\sigma_{Y_L}^2}\right) dy_L. \quad (7.49)$$

To be able to solve the integral, the Q-function approximation in [84] is applied, and thus

$$\bar{P}_{\mathrm{e}} = \frac{C_1 \;\; \exp\left(-\frac{\mu_{Y_L}^2}{2\sigma_{Y_L}^2}\right)}{1.135\pi\varpi_L \sqrt{2\sigma_{Y_L}^2}} \sum_{i=1}^{n_a} \frac{(-1)^{i+1} 1.98^i}{i! \; 2^{\frac{i+1}{2}}} \left(\frac{C_2}{\sigma_z^2}\right)^{\frac{i-1}{2}} \times \int_{B_{L,\mathrm{m}}^2}^{B_{L,\mathrm{M}}^2} y_L^{\frac{i-1}{2}} \exp\left(-\frac{y_L^2}{2\sigma_{Y_L}^2} + \left(\frac{\mu_{Y_L}}{\sigma_{Y_L}^2} - \frac{C_2}{2\sigma_z^2}\right) y_L\right) dy_L. \quad (7.50)$$

The integral in (7.50) can be solved recursively [19, 1.3.3.19, pp. 140], and the solution is given in terms of the error function or Q-function. However, when $B_{L,\mathrm{m}}^2 \to 0$ and $B_{L,\mathrm{M}}^2 \to \infty$, $\bar{P}_{\mathrm{e}}$ can be given as [19, 2.3.15.3, pp. 343]

$$\bar{P}_{\mathrm{e}} = Z \sum_{i=1}^{n_a} \frac{(-1)^{i+1}}{1.98^{-i} \; i!} \Gamma\left(\frac{i+1}{2}\right) \left(\frac{\sigma_{Y_L} C_2}{2\sigma_z^2}\right)^{\frac{i}{2}} D_{-\left(\frac{i+1}{2}\right)}\left(\sigma_{Y_L}\left(\frac{C_2}{2\sigma_z^2} - \frac{\mu_{Y_L}}{\sigma_{Y_L}^2}\right)\right) \quad (7.51)$$

where

$$Z = \frac{C_1 \sigma_z}{2 \times 1.135\pi\varpi_L \sqrt{C_2 \sigma_{Y_L}}} \exp\left(\frac{\sigma_{Y_L}^2}{4}\left(\frac{\mu_{Y_L}}{\sigma_{Y_L}^2} - \frac{C_2}{2\sigma_z^2}\right)^2 - \frac{\mu_{Y_L}^2}{2\sigma_{Y_L}^2}\right) \quad (7.52)$$

and $D_{(\cdot)}(\cdot)$ is the parabolic cylinder function.

7.5 Outage Probability Analysis for BS-IRS-UAV Link

For $L = 1$, the channel gain is fixed and the outage process depends only on the signal power. For $L \geq 2$, the derivation of the outage probability is presented below.

7.5.1 Two Reflectors, $L = 2$

Given that the instantaneous SNR threshold $\gamma_O \triangleq b_O^2/\sigma_z^2$, then the envelope threshold is $b_O = \sqrt{\sigma_z^2 \gamma_O}$. Therefore, the outage probability can be derived as

$$\bar{P}_O = \begin{cases} \int_{B_{2,\mathrm{m}}}^{b_O} f_{B_2}(b_2) db_2, & b_O > B_{2,\mathrm{m}} \\ 1, & b_O \leq B_{2,\mathrm{m}} \end{cases} \tag{7.53}$$

where $\bar{P}_O|_{b_O > B_{2,\mathrm{m}}}$ can be computed as

$$\bar{P}_O = \frac{2}{\pi I_0^{(2)}(\boldsymbol{\kappa})} \int_{B_{2,\mathrm{m}}}^{b_O} \frac{b_2 I_0 \left[\sqrt{(\kappa_1 - \kappa_2)^2 + \frac{\kappa_2 \kappa_1}{A_1 A_2}\left(b_2^2 - \mathcal{A}_2\right)}\right]}{\sqrt{\left(\mathcal{A}_3 - b_2^2\right)\left(b_2^2 - \mathcal{A}_2\right)}} db_2. \tag{7.54}$$

Substituting $x = \sqrt{b_2^2 - \mathcal{A}_2}$ and noting that $B_{2,\mathrm{m}}^2 = \mathcal{A}_2$ give

$$\bar{P}_O = \frac{2}{\pi I_0^{(2)}(\boldsymbol{\kappa})} \int_0^{\sqrt{b_O^2 - \mathcal{A}_2}} \frac{I_0 \left[\sqrt{(\kappa_1 - \kappa_2)^2 + \frac{\kappa_2 \kappa_1}{A_1 A_2} x^2}\right]}{\sqrt{-x^2 + \mathcal{A}_1^2}} dx. \tag{7.55}$$

Using the infinite series representation of the Bessel function gives

$$\bar{P}_O = \frac{2}{\pi I_0^{(2)}(\boldsymbol{\kappa})} \sum_{m=0}^{\infty} \frac{1}{2^{2m} (m!)^2} \int_0^{\sqrt{b_O^2 - \mathcal{A}_2}} \frac{\left((\kappa_1 - \kappa_2)^2 + \frac{\kappa_2 \kappa_1}{A_1 A_2} x^2\right)^m}{\sqrt{-x^2 + \mathcal{A}_1^2}} dx. \tag{7.56}$$

Then, by applying the binomial series expansion,

$$\bar{P}_O = \frac{2}{\pi I_0^{(2)}(\boldsymbol{\kappa})} \sum_{m=0}^{\infty} \frac{1}{2^{2m} (m!)^2} \sum_{l=0}^{m} \binom{m}{l} (\kappa_1 - \kappa_2)^{2(m-l)} \left(\frac{\kappa_2 \kappa_1}{A_1 A_2}\right)^l \int_0^{\sqrt{b_O^2 - \mathcal{A}_2}} \frac{x^{2l}}{\sqrt{-x^2 + \mathcal{A}_1^2}} dx \tag{7.57}$$

which can be solved using [19, 1.2.48.8, pp. 97] as

$$\bar{P}_O = \frac{2}{\pi I_0^{(2)}(\boldsymbol{\kappa})} \sum_{m=0}^{\infty} \frac{1}{2^{2m} (m!)^2} \left(\bar{P}_O|_{l=0} + \bar{P}_O|_{l \geq 1}\right) \tag{7.58}$$

where $\bar{P}_O|_{l=0} = (\kappa_1 - \kappa_2)^{2m} \arcsin\left(\frac{B_O}{\mathcal{A}_1}\right)$, $B_O = \sqrt{b_o^2 - \mathcal{A}_2}$, and

$$\bar{P}_O|_{l\geq 1} = \sum_{l=1}^{m} \binom{m}{l} (\kappa_1 - \kappa_2)^{2(m-l)} \left(\frac{\kappa_2\kappa_1}{A_1 A_2}\right)^l \left\{\left[B_O^{2l-1} + \sum_{k=1}^{l-1} H_{k,l}\mathcal{A}_1^{2k} B_O^{2l-2k-1}\right]\right.$$
$$\left. \times \frac{-1}{2l}\sqrt{\mathcal{A}_1^2 - B_O^2} + \frac{\mathcal{A}_1^{2l}(2l-1)!!}{2^l l!} arcsin\left(\frac{B_O}{\mathcal{A}_1}\right)\right\} \tag{7.59}$$

where $H_{k,l} = \frac{(2l-1)(2l-3)\cdots(2l-2k+1)}{2^k(l-1)(l-2)\cdots(l-k)}$, and $(\cdot)!!$ is the double factorial.

7.5.2 Three Reflectors, $L = 3$

The outage probability for this case can be derived as described in (7.53) except that $B_{2,m}$ is replaced by $B_{3,m}$. Similar to the SER, the outage probability for this case will be evaluated numerically because $f_{B_3}(b_3)$ in (7.31) does not have a closed-form representation.

7.5.3 Number of Reflectors $L \geq 4$

In this case, the PDF obtained using the CLT can be used to derive $\bar{P}_O$ as

$$\begin{aligned}
\bar{P}_O &= \int_{B_{L,\mathrm{m}}^2}^{b_O^2} f_{Y_L}(y_L) dy_L \\
&= \frac{1}{\sigma_{Y_L}\varpi_L\sqrt{2\pi}} \int_{B_{L,\mathrm{m}}^2}^{b_O^2} \exp\left(-\frac{1}{2}\left(\frac{y_L - \mu_{Y_L}}{\sigma_{Y_L}}\right)^2\right) dy_L \\
&= \frac{1}{\varpi_L} Q\left(\frac{B_{L,\mathrm{m}}^2 - \mu_{Y_L}}{\sigma_{Y_L}}\right) - \frac{1}{\varpi_L} Q\left(\frac{b_O^2 - \mu_{Y_L}}{\sigma_{Y_L}}\right).
\end{aligned} \tag{7.60}$$

7.6 End-to-End performance for Multi-Layer UAV Network

In this section, the SER and outage probability derivations are extended for the general case of multi-layer UAV network. A multi-layer network can be observed as a network with N number of hops. In this work, we assume DF relaying is employed at the receiving node in each hop. Moreover, we consider the network architecture in Fig. 7.1 where the top layer consists of BS-IRS-UAV link which is already analyzed above. The remaining $N - 1$ layers could be a combination of UAV-IRS-UAV, which can be analyzed similar to the top layer, and simple point-to-point links. The performance analysis for the latter case, i.e., point-to-point links, is already provided in the literature, for instance, a point-to-point system with perfect phase knowledge can be found in [80] whereas with imperfect phase is investigated in [85]. Thus, we will not include the analysis here for the sake of brevity. Nevertheless, interested readers are recommended to refer to these articles and the references therein for more details.

7.6.1 SER for N Hops

Let us define the vector $\hat{\mathbf{s}} = [\hat{s}_1, \hat{s}_2, \ldots, \hat{s}_N]$, which contains the decoded symbols of the receiver in each hop. Given that symbol s_0 is transmitted by the BS over a route of N total number of hops, the SER at the destination node, which is the GU, can be expressed as [48]

$$\begin{aligned}
\bar{P}_{e,\mathrm{GU}} &= \Pr\left(s_0 \neq \hat{s}_N\right) \\
&= \sum_{s_0} \Pr\left(\hat{s}_N \neq s_0 | s_0\right) \Pr\left(s_0\right) \\
&= \frac{1}{M} \sum_{s_0} \sum_{\hat{\mathbf{s}} \in \mathbb{S}} \Pr\left(\hat{s}_1 | s_0\right) \prod_{l=2}^{N} \Pr\left(\hat{s}_n | \hat{s}_{n-1}\right)
\end{aligned} \tag{7.61}$$

where M is the modulation order, $\Pr\left(\hat{s}_1 | s_0\right)$ is the conditional probability for the first hop (BS-IRS-UAV link), $\Pr\left(\hat{s}_n | \hat{s}_{n-1}\right)$ is the conditional probability for each of the remaining $N-1$ hops, and $\mathbb{S}$ is a set of all possible combinations for the vector $\hat{\mathbf{s}}$ with $\hat{s}_N \neq s_0$.

7.6.2 Outage Probability for N Hops

The outage event in multiple hops based communication system occurs if one or more of the hops suffers from outage, and thus the outage probability can be given by [48]

$$\bar{P}_{O,\mathrm{GU}} = 1 - \prod_{n=1}^{N} \left(1 - \bar{P}_{O,n}\right) \tag{7.62}$$

where $\bar{P}_{O,n}$ is the OP for the nth hop.

7.7 Numerical Results

This section presents the numerical results obtained from the derived formulae, and compares them to Monte Carlo simulation results using various configurations. The performance of the considered UAV-IRS system is evaluated in terms of SER and outage probability. Each simulation point is obtained using 10^7 realizations. The average transmission power for all scenarios is normalized to unity, and the SNR in dB is defined as $\mathrm{SNR} \triangleq -10 \log_{10}\left(\sigma_z^2\right)$. The phase estimates are considered unbiased, i.e., $\mu = 0$, and $\kappa_i = \kappa\ \forall i$ is considered for all figures. For the outage probability, the SNR threshold has been set at $\gamma_O = 10$ dB for all scenarios. The modulation used is BPSK, and hence, the SER and bit error rate (BER) are equal. The analytical SER results for $L = 2$ are obtained using (7.43) and (7.47) for equal and unequal received signal amplitudes, respectively. On the other hand, the outage probability for $L = 2$ is obtained using (7.59). Unless it is specified otherwise, the SER for $L = 3$ is obtained using (7.48) while and outage probability is obtained (7.53) and replacing $B_{2,m}$ with $B_{3,m}$. For $L \geq 4$, the SER is obtained using (7.51) and the outage probability is obtained using (7.60). In all infinite summations, we consistently use the

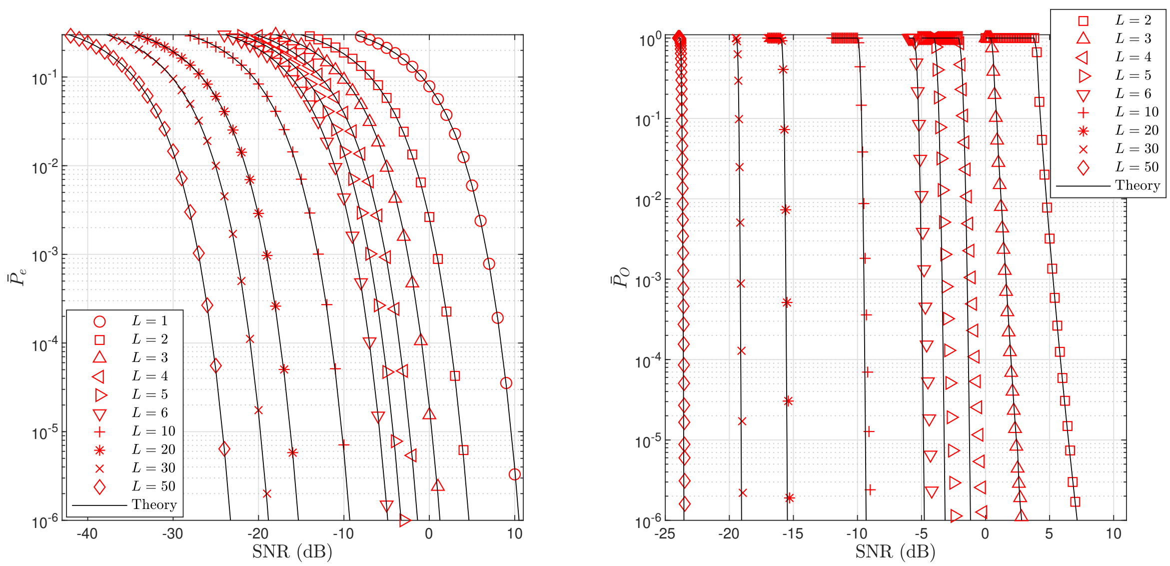

(a) SER

(b) Outage probability

Figure 7.3: Analytical and simulated SER and outage probability of the system for various number of reflecting elements L, where $\kappa = 20$, and $A_i = 1\ \forall i$.

first 30 terms.

Fig. 7.3 shows the analytical and simulated SER and outage probability of the considered system for various values of L where $\kappa = 20$, and $A_i = 1\ \forall i$. As can be noted from Fig. 7.3a, the derived SER expressions match very well the simulation results, including the SER case for $L \geq 4$, which is derived based on the CLT. In addition, the results show the considerable SER enhancement caused by using IRS. However, the obtained SNR gain decreases as L increases. For example, the SNR gain is about 6 dB using $L = 10$ as compared to $L = 20$, while the gain is only 3.5 dB when increasing L from 20 to 30. The same behavior is obtained for $L = 1, 2, 3$.

Fig. 7.3b shows the outage probability of the system where the SNR threshold $\gamma_O = 10$ dB. According to the figure, a perfect match between simulations and analysis is obtained for $L \leq 3$ and $L \geq 20$. However, for the remaining cases, i.e., $4 \leq L < 20$, a small mismatch can be noted when $\bar{P}_O$ is below 10^{-3}. The small difference is due to the CLT, which becomes more accurate by increasing L. Moreover, it can be observed that using IRS can significantly enhance the outage probability. Nevertheless, the outage probability curves are very steep at high values of L because the received signal power distribution is very narrow, and thus, small SNR changes may cause significant change in the outage probability.

Fig. 7.4 shows the analytical and simulated system SER and outage probability for various values of L, and two cases for A_i. In case 1, $A_i = 1\ \forall i$, and in Case 2, $\{A_1, A_2, A_3\} = \{5, 3, 2\}$ and $A_4, A_5, \ldots, A_{30} = 1$. For all cases in the figure $\kappa = 20$. As can be noted from Fig. 7.4a, the SER analytical results match very well the simulation results for all the considered scenarios. The results are presented for the unequal amplitudes as well to evaluate the impact of the signal amplitude on $\bar{P}_{\mathrm{e}}$. For example, there is a gain of about 10 dB in favor of Case 2 as compared to Case 1 when $L = 3$; however, this gain decreases to about 1.9 dB when $L = 30$. This implies that the link quality has a significant effect on the system performance

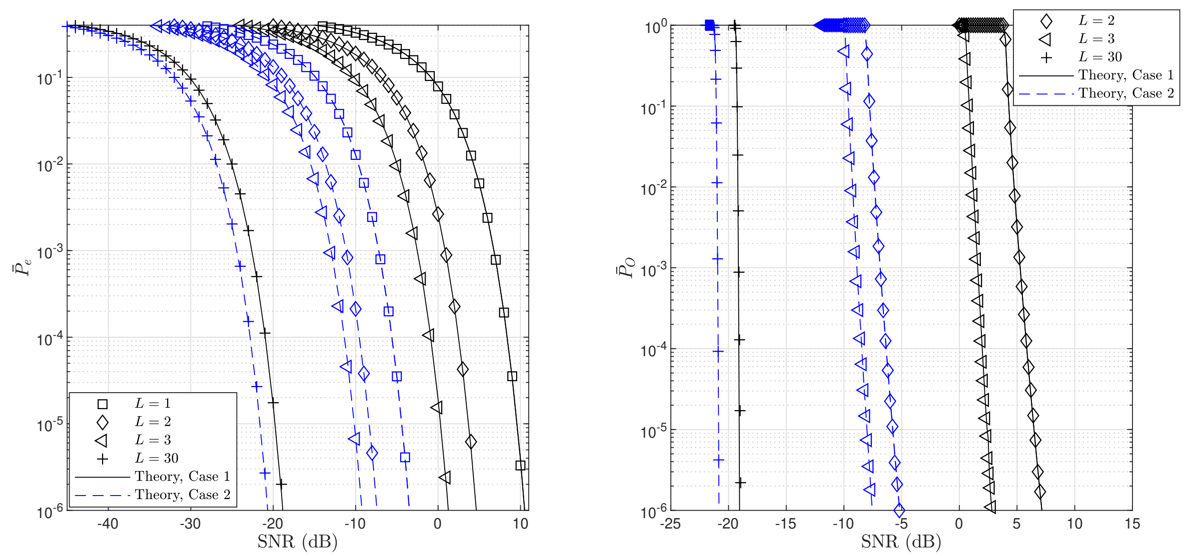

(a) SER

(b) Outage probability

Figure 7.4: Analytical and simulated SER and outage probability for various values of L with equal and unequal A_i, and for $\kappa = 20$.

in addition to the number of reflectors L. Fig. 7.4b shows the outage probability. As can be observed from the figure, the obtained analysis perfectly matches the simulation results. The figure also shows that the outage probability is inversely proportional to the link quality.

Fig. 7.5a shows the SER for different values of κ and L using $A_i = 1\ \forall i$. The SER for $L = 1$ is used as a benchmark, and it is not affected by κ since the receiver is assumed to know the overall signal phase accurately. As can be noted from the figure, the analysis matches the simulation results for all cases except for $L = 3$ with $\kappa \leq 5$, where some mismatch is resulted from the multiple discontinuities in b_3^2 that appear at low κ values. It can be also noted that large values of κ correspond to small phase errors, and thus, better SER is obtained as κ increases for a given L. The figure also shows that the SER degradation versus κ depends on L. For small values of L the SER is very sensitive to κ. Consequently, for a particular value of κ, increasing L does not necessarily improve the system performance. Such observation is critical for resource allocation problems where different users have different values of κ. The same observations and conclusions can be generally made for the outage probability in Fig. 7.5b.

Fig. 7.6 shows the SER and outage probability for various values of L, $A_i = 1\ \forall i$, and $\kappa = 5$. All the results in the figure are obtained using the CLT given in (7.51) and (7.60) for the SER and outage probability, respectively. As can be noted from Fig. 7.6a, the simulation results deviate significantly from the theoretical results obtained using CLT when $L < 4$. However, the mismatch decreases for $L \geq 4$ and becomes negligible for $L \geq 6$. Therefore, the accurate analysis for the cases of $L = 2$ and 3 is necessary to provide accurate analytical results for such cases. The outage probability results in Fig. 7.6b show a higher deviation between the simulation and analytical results obtained suing the CLT, particularly for $L < 10$. Moreover, it can be noted that the deviation becomes more apparent for $\bar{P}_O < 10^{-3}$.

Fig. 7.7 is produced using the same settings of Fig. 7.6 except that $\kappa = 20$. As can be noted from

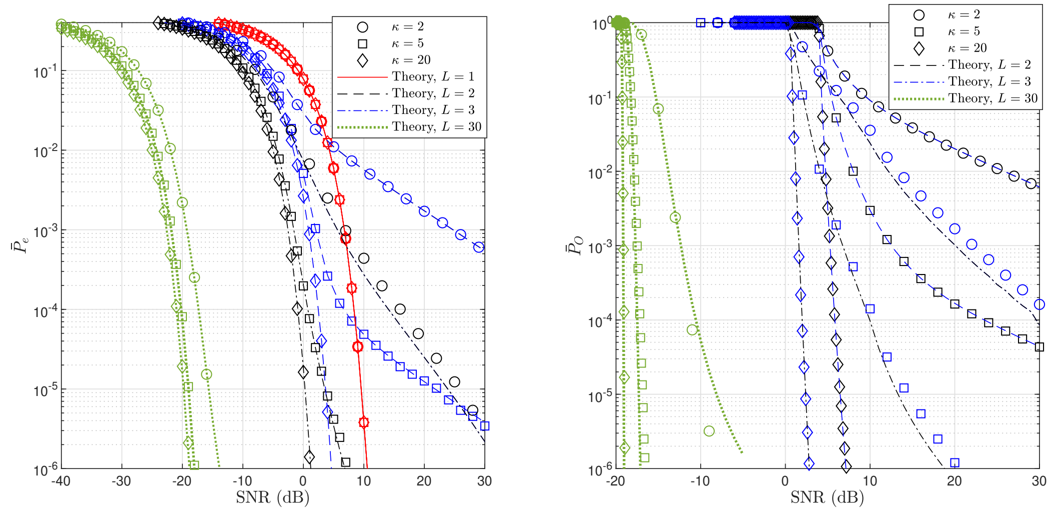

(a) SER (b) Outage probability

Figure 7.5: SER and outage probability for various values of κ and L using $A_i = 1$ $\forall i$.

Fig. 7.7a, the CLT in this case gives near perfect match even for $L = \{1, 2, 3\}$. Such performance is obtained because at high values of κ the PDF of the envelope becomes mostly concentrated around $B_{L,\mathrm{M}}$, and hence, averaging the conditional SER over the PDF will be mostly dependent on the mean and variance of the PDF rather than the actual shape of the PDF. For the outage probability the scenario is different because outage computation involves integration over the PDF itself with no averaging operation. Therefore, it can be noted from the results in Fig. 7.7b the CLT does not provide accurate results for $L < 10$.

Fig. 7.8 shows the SER versus SNR for the cases where the signals have fixed and random amplitudes. For the random amplitudes, the fading factor is modeled as Rician distribution with parameters Ω and $\mathcal{K}$ i.e., $A_i \sim \mathcal{R}(\Omega, \mathcal{K})$. For fair comparison, we set $\Omega = 1$ for each of the L signals in the Rician case and $A_i = 1$ $\forall i$ for the fixed amplitudes case. As can be noted from the figure, the SER performance for the Rician model converges to the fixed amplitude model when L or $\mathcal{K}$ increases. For example, it can be noted that $\bar{P}_e|\,(A_i = 1) \approx \bar{P}_e|\,(A_i \sim \mathcal{R}(1, 20))$. Moreover, the SNR gain obtained by increasing $\mathcal{K}$ becomes less important as L increases. For example, at $\bar{P}_e = 10^{-5}$, the SNR gain obtained by increasing $\mathcal{K}$ from 5 to 20 dB is 27 dB when $L = 2$, while it is almost 4 dB when $L = 20$.

Fig. 7.9 shows the SER and outage probability for a 3-layer UAV network. The first layer consists of a BS-IRS-UAV link with a fixed $\kappa = 20$, $\mathcal{K}_h = 20$ dB, and $\mathcal{K}_{\hbar} = 20$ dB. The second and third layers are UAV-UAV with $\mathcal{K}_{\check{h}} = 20$ and UAV-GU links, respectively, with a perfect phase knowledge at the receiving nodes. The other system parameters that appear in (7.16) and (7.17) are summarized as follows: $c = 3 \times 10^8 m/s$, $f_c = 1$ GHz, $\varrho = 2$, $g_i = 1$, $h_{i,\mathrm{LoS}} = 1$, $\hbar_{i,\mathrm{LoS}} = 1$, $\tilde{h}_{i,\mathrm{LoS}} = 1$, and $\tilde{h}_{i,\mathrm{nLoS}} = 1$. Moreover, the locations of the nodes in 3D Cartesian coordinates measured in meters are $\mathbf{p}_{\mathrm{BS}} = [0, 0, 50]$, $\mathbf{p}_{\mathrm{IRS}} = [50, 50, 400]$, $\mathbf{p}_{\mathrm{UAV}_1} = [300, 1000, 200]$, $\mathbf{p}_{\mathrm{UAV}_2} = [4000, 4000, 150]$, and $\mathbf{p}_{\mathrm{GU}} = [5100, 6200, 0]$. The transmission power of each transmitting node is normalized to 1, and the receiver in each hop applies DF

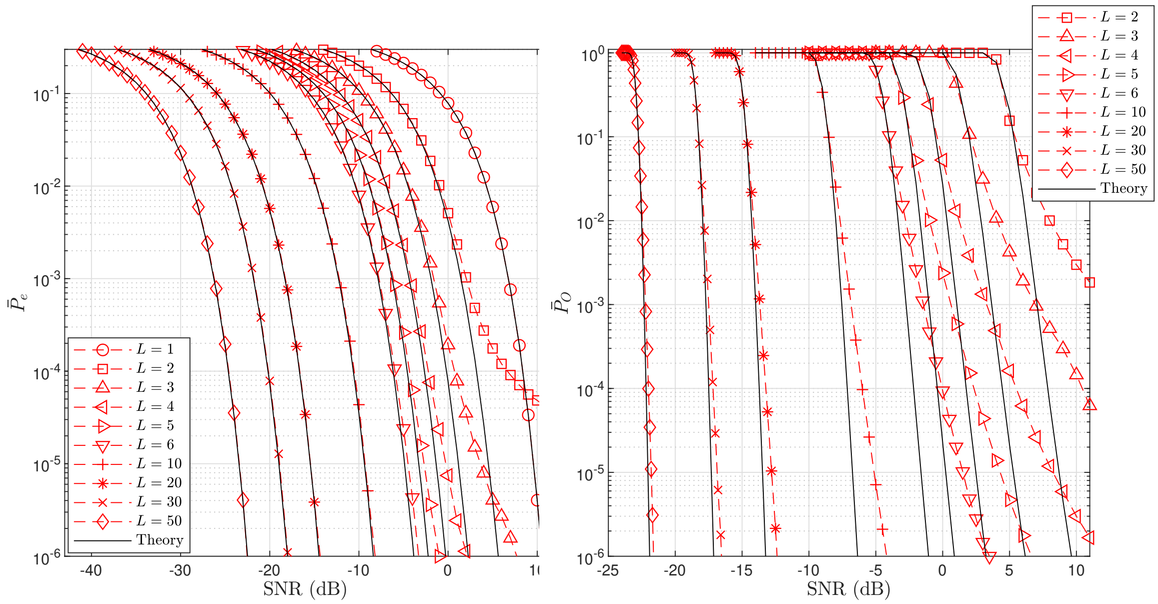

(a) SER

(b) Outage probability

Figure 7.6: The SER and outage probability for different values of L, where the CLT is applied for all L, and $\kappa = 5$.

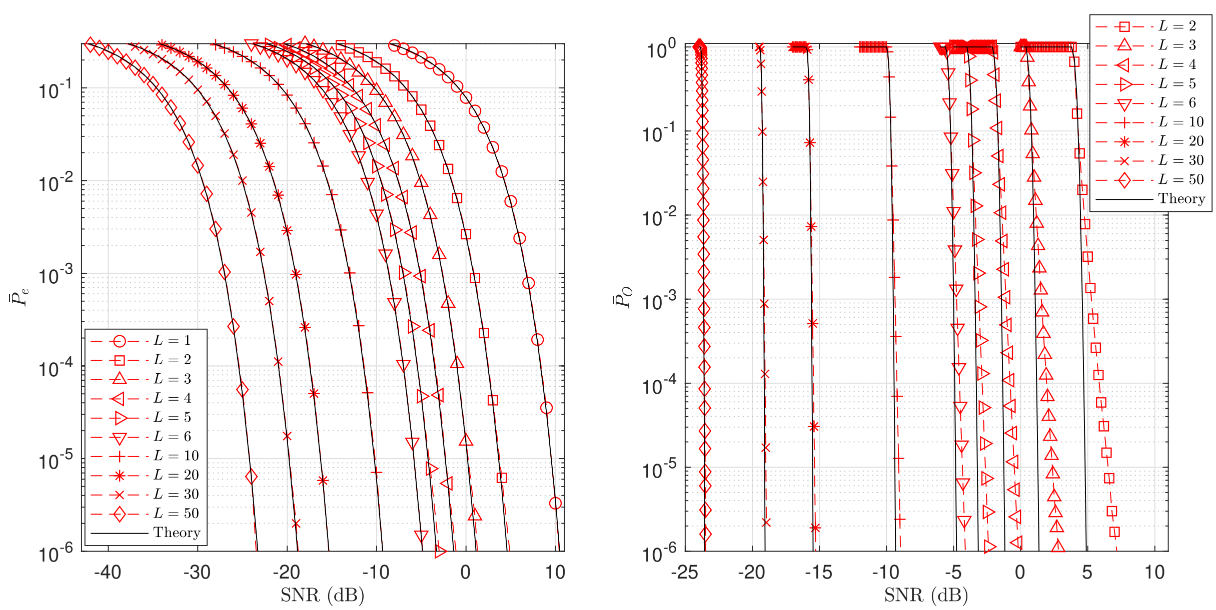

(a) SER

(b) Outage probability

Figure 7.7: The SER and outage probability for different values of L, where the CLT is applied for all L, and $\kappa = 20$.

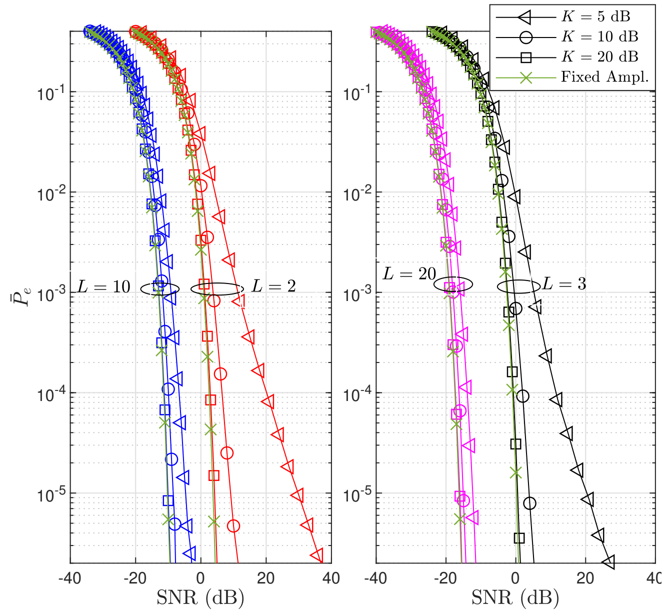

Figure 7.8: The SER for Rician distributed amplitudes, i.e., $A_i \sim \mathcal{R}(\Omega, \mathcal{K})$.

relaying protocol and employs 2 antennas to achieve full duplex transmissions. The noise samples at the receivers are assumed i.i.d with zero mean and a variance of σ_z^2, and the average SNR in this figure is defined as SNR $\triangleq P_{r,\mathrm{GU}}/\sigma_z^2$ where $P_{r,\mathrm{GU}}$ is the amount of received power at GU. As can be observed from the Fig. 7.9a, at low and moderate SNR, the decrease rate in SER is high as the SNR and number of reflecting elements L increase. However, at high SNR, the rate of the decrease in SER becomes less sharp and the effect of L becomes negligible. This behavior is attributed to the fact that the SER is affected by the three hops and the worst hop dominates the SER. The effect of $\mathcal{K}_{\breve{h}}$ becomes more important at high SNR as the link between UAV_2 and GU dominates the SER performance at high SNR. It can be also noticed from Fig. 7.9b that the effect of $\mathcal{K}_{\breve{h}}$ is very significant as the outage probability suffers from high error floors at low values of $\mathcal{K}_{\breve{h}}$; however, the error floor disappears, or lower than 10^{-6} when $\mathcal{K}_{\breve{h}} = 15$ dB.

7.8 Conclusion and Future Work

This paper has presented an investigation into the SER and outage performance of IRS assisted UAV-UAV communications when phase compensation at the reflectors is imperfect. The derived expressions were provided for $L = \{1, 2, 3\}$ using SAT, and CLT when $L \geq 4$. The results gave an insight on the interplay between the number of elements, phase errors and system performance. It was demonstrated that IRS significantly improve the performance of UAV-UAV communications, particularly for large values of L. More interestingly, it was shown that increasing the number of reflectors provides some form of immunity against phase error. On the other hand, when L is small, the degradation due to large phase errors may surpass the IRS gain, hence it is paramount that the system designer is aware of the amount of phase

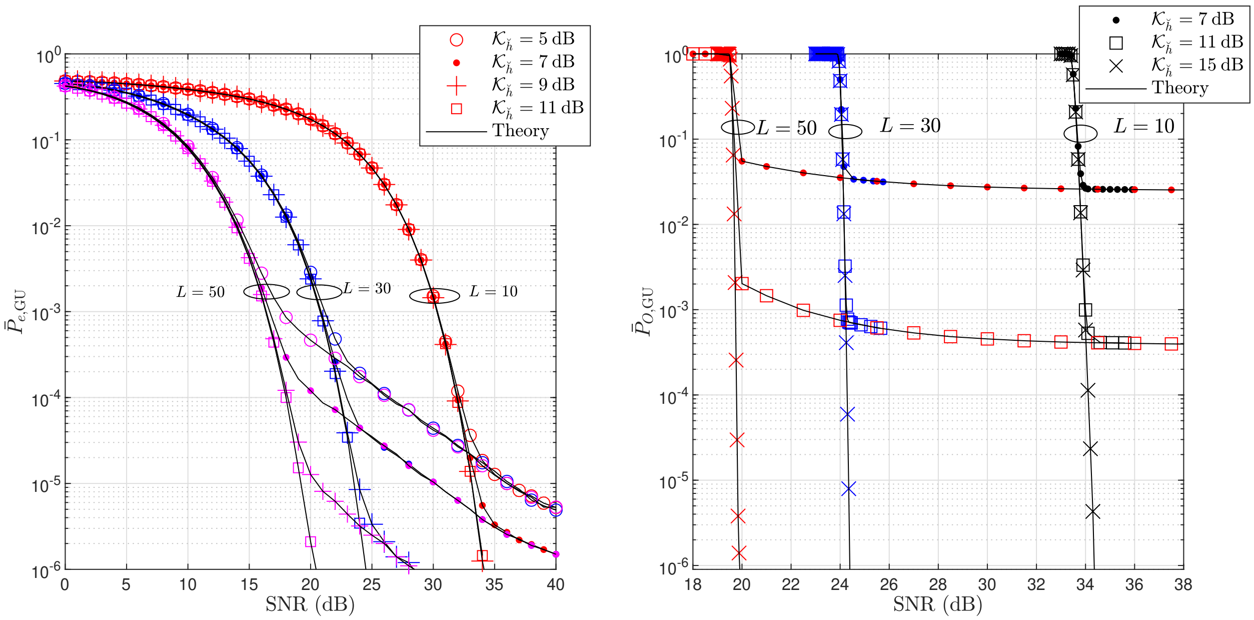

(a) Average SER

(b) Average outage probability

Figure 7.9: The SER and outage probability for a 3-layer UAV network with different values of $\mathcal{K}_{\breve{h}}$.

error. In addition, the results revealed that the accuracy of the CLT approximation improves as L and κ increase. Finally, it was found that the nonfading amplitudes model can be used to accurately model the fading amplitudes with Rician fading given that the Rician factor, or the number of reflectors, is large.

Our future work will focus on finding the relation between κ_i and the compensated phase MSE caused by phase noise, UAV jittering, and phase estimation errors. Moreover, we will consider the case where the phase errors of certain IRS elements are correlated. In such scenarios, splitting the IRS large panels into several small distributed panels may improve the system performance. However, the number and location of the distributed IRS panels should be optimized [65].

Appendix I

The expected value of $\cos(n\phi_j)$ can be expressed as

$$\mathbb{E}\left[\cos(n\phi_j)\right] = \frac{1}{2\pi I_0(\kappa_j)} \int_{-\pi}^{\pi} \cos(n\phi_j)\, \mathrm{e}^{\kappa_j \cos(\phi_j)} d\phi_j \tag{7.63}$$

By dividing the interval of the integral into two subintervals, $[-\pi, 0]$ and $(0, \pi]$, $\mathbb{E}\left[\cos(n\phi_j)\right]$ and substituting $\theta = \phi_j$ in the first integral, and noting that $\cos(-\theta) = \cos\theta$ yields

$$\begin{aligned}\mathbb{E}\left[\cos(n\phi_j)\right] &= \frac{1}{2\pi I_0(\kappa_j)} \left(-\int_{-\pi}^{0} \cos(n\theta)\, \mathrm{e}^{\kappa_j \cos(\theta)} d\theta + \int_{0}^{\pi} \cos(n\phi_j)\, \mathrm{e}^{\kappa_j \cos(\phi_j)} d\phi_j \right) \\ &= \frac{1}{\pi I_0(\kappa_j)} \int_{0}^{\pi} \cos(n\phi_j)\, \mathrm{e}^{\kappa_j \cos(\phi_j)} d\phi_j. \end{aligned} \tag{7.64}$$

Using the modified Bessel function definition, $I_n(x) = \frac{1}{\pi}\int_0^{\pi} \cos(n\theta)\, \mathrm{e}^{x\cos(\theta)} d\theta$, $\mathbb{E}[\cos(n\phi_j)]$ can be written as

$$\mathbb{E}[\cos(n\phi_j)] = \frac{I_n(\kappa_j)}{I_0(\kappa_j)}. \tag{7.65}$$

On the other hand, the expected value of $\cos(n\phi_j)$ can be expressed as

$$\mathbb{E}[\sin(n\phi_j)] = \frac{1}{2\pi I_0(\kappa_j)} \int_{-\pi}^{\pi} \sin(n\phi_j)\, \mathrm{e}^{\kappa_j \cos(\phi_j)} d\phi_j = 0 \tag{7.66}$$

where the last equality is obtained by substituting $\theta = -\phi_j$ and noting that $\sin(-\theta) = -\sin\theta$ while $\cos(-\theta) = \cos\theta$.

Appendix II

This Appendix derives m_{Y_L} and $\sigma^2_{Y_L}$ based on the CLT. By computing the expected value of (7.7) and noting that ϕ_i's are mutually independent, then $m_{Y_L} = \mathbb{E}\left[B_L^2\right]$ can be evaluated as

$$\begin{aligned} m_{Y_L} &= \mathbb{E}\left[||\mathbf{A}||^2\right] + 2 \sum_{L\geq j>k\geq 1} \mathbb{E}[A_j A_k \cos(\phi_j - \phi_k)] \\ &= \sum_{i=1}^{L} \mathbb{E}\left[A_i^2\right] + 2 \sum_{L\geq j>k\geq 1} \mathbb{E}[A_j]\, \mathbb{E}[A_k]\, \mathbb{E}[\cos(\phi_j - \phi_k)]. \end{aligned} \tag{7.67}$$

After some mathematical manipulations and given that $A_i\ \forall i$ is deterministic, then m_{Y_L} can be computed with the aid of (7.65) and (7.66) as

$$\begin{aligned} m_{Y_L} &= \sum_{i=1}^{L} A_i^2 + 2 \sum_{L\geq j>k\geq 1} A_j A_k \left(\mathbb{E}[\cos\phi_j]\, \mathbb{E}[\cos\phi_k] + \mathbb{E}[\sin\phi_j]\, \mathbb{E}[\sin\phi_k]\right) \\ &= \sum_{i=1}^{L} A_i^2 + 2 \sum_{L\geq j>k\geq 1} A_j A_k \frac{I_1(\kappa_j)\, I_1(\kappa_k)}{I_0(\kappa_j) I_0(\kappa_k)}. \end{aligned} \tag{7.68}$$

By using the variance definition $\sigma^2_{Y_L} \triangleq \mathbb{E}\left[Y_L^2\right] - m^2_{Y_L}$,

where

$$\mathbb{E}\left[Y_L^2\right] = \mathbb{E}\left[\left(||\mathbf{A}||^2 + 2 \sum_{L\geq j>k\geq 1} A_j A_k \cos(\phi_j - \phi_k)\right)^2\right] \tag{7.69}$$

By taking the square value for the term inside the bracket and noting that the expected value can be distributed over the sum, $\mathbb{E}\left[Y_L^2\right]$ can be found as

$$\mathbb{E}\left[Y_L^2\right] = \left(||\mathbf{A}||^2\right)^2 + \underbrace{4\mathbb{E}\left[\left(\sum_{L\geq j>k\geq 1} A_j A_k \cos\left(\phi_j - \phi_k\right)\right)^2\right]}_{T_1} + \underbrace{4||\mathbf{A}||^2 \sum_{L\geq j>k\geq 1} A_j A_k \mathbb{E}\left[\cos\left(\phi_j - \phi_k\right)\right]}_{T_2}$$

By noting that $\cos(x-y) = \cos(x)\cos(y) + \sin(x)\sin(y)$ and using Appendix I, then T_2 becomes

$$T_2 = 4||\mathbf{A}||^2 \sum_{L\geq j>k\geq 1} A_j A_k \mathbb{E}\left[\cos\left(\phi_j - \phi_k\right)\right] = 4||\mathbf{A}||^2 \sum_{L\geq j>k\geq 1} A_j A_k \frac{I_1\left(\kappa_j\right) I_1\left(\kappa_k\right)}{I_0(\kappa_j) I_0(\kappa_k)}. \tag{7.70}$$

Similarly, the term T_1 can be split into two terms, $T_1 = T_{1,1} + T_{1,2}$. By evaluating and expanding the term inside the expectation, and using the identity $\cos^2(x) = 0.5(1+\cos(2x))$, then $T_{1,1}$ becomes

$$T_{1,1} = 4 \sum_{L\geq j>k\geq 1} A_j^2 A_k^2 \mathbb{E}\left[\cos^2\left(\phi_j - \phi_k\right)\right] = 2 \sum_{L\geq j>k\geq 1} A_j^2 A_k^2 \left(1 + \mathbb{E}\left[\cos\left(2\phi_j - 2\phi_k\right)\right]\right). \tag{7.71}$$

By employing the cosine of difference of two angles trigonometric identity, and then using the results obtained in Appendix I, $T_{1,1}$ can be evaluated as

$$\begin{aligned} T_{1,1} &= 2 \sum_{L\geq j>k\geq 1} A_j^2 A_k^2 \left(1 + \mathbb{E}\left[\cos\left(2\phi_j\right)\cos\left(2\phi_k\right) + \sin\left(2\phi_j\right)\sin\left(2\phi_k\right)\right]\right) \\ &= 2 \sum_{L\geq j>k\geq 1} A_j^2 A_k^2 \left(1 + \frac{I_2\left(\kappa_j\right)}{I_0(\kappa_j)} \frac{I_2\left(\kappa_j\right)}{I_0(\kappa_j)}\right), \end{aligned} \tag{7.72}$$

and $T_{1,2}$ can be derived as

$$T_{1,2} = \sum_{1\leq k\leq L} \sum_{1\leq j<k} \sum_{\substack{1\leq i\leq L \\ i\neq k}} \sum_{1\leq l<i} 4A_j A_k A_i A_l E_{k,j,i,l} + \sum_{1\leq k\leq L} \sum_{1\leq j<k} \sum_{1\leq i\leq L} \sum_{\substack{1\leq l<i \\ l\neq j}} 4A_j A_k A_i A_l E_{k,j,i,l}, \tag{7.73}$$

where $E_{k,j,i,l} = \mathbb{E}\left[\cos\left(\phi_j - \phi_k\right)\cos\left(\phi_i - \phi_l\right)\right]$. By noting that $\phi_j \neq \phi_k$ and $\phi_i \neq \phi_l$, considering all possibilities for the equality conditions between ϕ_j and $\{\phi_i, \phi_l\}$, and between ϕ_k and $\{\phi_i, \phi_l\}$, and employing the results in Appendix I, $E_{k,j,i,l}$ can be expressed as

$$E_{k,j,i,l} = \begin{cases} \prod_{k=1}^{4} \frac{I_1(\kappa_k)}{I_0(\kappa_k)}, & i\neq k, i\neq j, l\neq k, l\neq j \\ 1 + \prod_{k=1}^{2} \frac{I_2(\kappa_k)}{I_0(\kappa_k)}, & i\neq k, i=j, l=k, l\neq j \\ \frac{1}{2}\frac{I_1(\kappa_k)I_1(\kappa_l)}{I_0(\kappa_k)I_0(\kappa_l)}\left(1+\frac{I_2(\kappa_i)}{I_0(\kappa_i)}\right), & i\neq k, i=j, l\neq k, l\neq j \\ \frac{1}{2}\frac{I_1(\kappa_j)I_1(\kappa_i)}{I_0(\kappa_j)I_0(\kappa_i)}\left(1+\frac{I_2(\kappa_k)}{I_0(\kappa_k)}\right), & i\neq k, i\neq j, l=k, l\neq j \\ \frac{1}{2}\frac{I_1(\kappa_k)I_1(\kappa_i)}{I_0(\kappa_k)I_0(\kappa_i)}\left(1+\frac{I_2(\kappa_j)}{I_0(\kappa_j)}\right), & i\neq k, i\neq j, l\neq k, l=j \\ \frac{1}{2}\frac{I_1(\kappa_j)I_1(\kappa_l)}{I_0(\kappa_j)I_0(\kappa_l)}\left(1+\frac{I_2(\kappa_k)}{I_0(\kappa_k)}\right), & i=k, i\neq j, l\neq k, l\neq j \end{cases} \tag{7.74}$$

References

[1] Q. Wu and R. Zhang, “Intelligent reflecting surface enhanced wireless network via joint active and passive beamforming,” *IEEE Trans. Wireless Commun.*, vol. 18, no. 11, pp. 5394-5409, Nov. 2019.

[2] Q. Wu and R. Zhang, “Towards smart and reconfigurable environment: Intelligent reflecting surface aided wireless network,” *IEEE Commun. Mag.*, vol. 58, no. 1, pp. 106-112, Jan. 2020.

[3] H. Xie, J. Xu, and Y. Liu, “Max-min fairness in IRS-aided multi-cell MISO systems via joint transmit and reflective beamforming,” *ICC 2020 - 2020 IEEE Int. Conf. Commun. (ICC)*, Dublin, Ireland, 2020, pp. 1-6.

[4] Y. Tang, G. Ma, H. Xie, J. Xu, and X. Han, “Joint transmit and reflective beamforming design for IRS-assisted multiuser MISO SWIPT systems,” *ICC 2020 - 2020 IEEE Int. Conf. Commun. (ICC)*, Dublin, Ireland, 2020, pp. 1-6.

[5] D. Xu, X. Yu, Y. Sun, D. Ng, and R. Schober, “Resource allocation for IRS-assisted full-duplex cognitive radio systems,” *IEEE Trans. Commun.*, vol. 68, no. 12, pp. 7376-7394, Dec. 2020.

[6] Y. Gao, J. Xu, W. Xu, D. Ng, and M.-S. Alouini, “Distributed IRS with statistical passive beamforming for MISO communications,” *IEEE Wireless Commun. Lett.*, vol. 10, no. 2, pp. 221-225, Feb. 2021.

[7] X. Yu, D. Xu, Y. Sun, D. Ng, and R. Schober, “Robust and secure wireless communications via intelligent reflecting surfaces,” *IEEE J. Sel. Areas Commun.*, vol. 38, no. 11, pp. 2637-2652, Nov. 2020.

[8] G. Yu, X. Chen, C. Zhong, D. Ng, and Z. Zhang, “Design, analysis, and optimization of a large intelligent reflecting surface-aided B5G cellular internet of things,” *IEEE Internet Things J.*, vol. 7, no. 9, pp. 8902-8916, Sep. 2020.

[9] J. Zuo, Y. Liu, Z. Qin, and N. Al-Dhahir, “Resource allocation in intelligent reflecting surface assisted NOMA systems,” *IEEE Trans. Commun.*, vol. 68, no. 11, pp. 7170-7183, Nov. 2020.

[10] X. Mu, Y. Liu, L. Guo, J. Lin, and N. Al-Dhahir, “Exploiting intelligent reflecting surfaces in NOMA networks: Joint beamforming optimization,” *IEEE Trans. Wireless Commun.*, vol. 19, no. 10, pp. 6884-6898, Oct. 2020.

[11] R. Liu, H. Li, M. Li, and Q. Liu, “Symbol-level precoding design for IRS-assisted MU-MISO systems,” *2020 IEEE Wireless Commun. Netw. Conf. (WCNC)*, Seoul, Korea (South), 2020, pp. 1-6.

[12] H. Lu, Y. Zeng, S. Jin, and R. Zhang, “Enabling panoramic full-angle reflection via aerial intelligent reflecting surface,” *2020 IEEE Int. Conf. Commun. Workshops (ICC Workshops)*, Dublin, Ireland, 2020, pp. 1-6.

[13] S. Abeywickrama, R. Zhang, Q. Wu, and C. Yuen, “Intelligent reflecting surface: Practical phase shift model and beamforming Optimization,” *IEEE Trans. Commun.*, vol. 68, no. 9, pp. 5849-5863, Sep. 2020.

[14] C. Huang *et al.*, “Holographic MIMO surfaces for 6G wireless networks: Opportunities, challenges, and trends,” *IEEE Wireless Commun. Mag.*, vol. 27, no. 5, pp. 118-125, Oct. 2020.

[15] Y. Zeng and R. Zhang, “Energy-efficient UAV communication with trajectory optimization,” *IEEE Trans. Wireless Commun.*, vol. 16, no. 6, pp. 3747-3760, Jun. 2017.

[16] A. Fotouhi *et al.*, “Survey on UAV cellular communications: Practical aspects, standardization advancements, regulation, and security challenges,” *IEEE Commun. Surveys Tuts.*, vol. 21, no. 4, pp. 3417–3442, Fourthquarter 2019.

[17] X. Wang and M. C. Gursoy, “Coverage analysis for energy-harvesting UAV-assisted mmwave cellular networks,” *IEEE J. Sel. Areas Commun.*, vol. 37, no. 12, pp. 2832–2850, 2019.

[18] Y. Zeng, Q. Wu, and R. Zhang, “Accessing from the sky: A tutorial on UAV communications for 5G and beyond,” *Proc. IEEE*, vol. 107, no. 12, pp. 2327-2375, Dec. 2019.

[19] L. Zhu, J. Zhang, Z. Xiao, X. Cao, X.-G. Xia, and R. Schober, “Millimeter-wave full-duplex UAV relay: Joint positioning, beamforming, and power control,” *IEEE J. Sel. Areas Commun.*, vol. 38, no. 9, pp. 2057-2073, Sep. 2020.

[20] S. Khairy, P. Balaprakash, L. Cai, and Y. Cheng, “Constrained deep reinforcement learning for energy sustainable multi-UAV based random access IoT networks with NOMA,” *IEEE J. Sel. Areas Commun.*, vol. 39, no. 4, pp. 1101-1115, Apr. 2021.

[21] C. Liu, W. Feng, Y. Chen, C.-X. Wang, and N. Ge, “Cell-free satellite-UAV networks for 6G wide-area internet of things,” *IEEE J. Sel. Areas Commun.*, vol. 39, no. 4, pp. 1116-1131, Apr. 2021.

[22] Y. Huo, X. Dong, T. Lu, W. Xu, and M. Yuen, "Distributed and multilayer UAV networks for next-generation wireless communication and power transfer: A feasibility study," *IEEE Internet Things J.*, vol. 6, no. 4, pp. 7103-7115, Aug. 2019.

[23] A. Ahmed, M. Naeem, and A. Al-Dweik, "Joint optimization of sensors association and UAVs placement in IoT applications with practical network constraints," *IEEE Access*, vol. 9, pp. 7674-7689, 2021.

[24] I. Bor-Yaliniz and H. Yanikomeroglu, "The new frontier in RAN heterogeneity: Multi-tier drone-cells," *IEEE Commun. Mag.*, vol. 54, no. 11, pp. 48–55, Nov. 2016.

[25] S. Sekander, H. Tabassum, and E. Hossain, "Multi-tier drone architecture for 5G/B5G cellular networks: Challenges, trends, and prospects," *IEEE Commun. Mag.*, vol. 56, no. 3, pp. 96–103, Mar. 2018.

[26] C. You, B. Zheng, and R. Zhang, "Channel estimation and passive beamforming for intelligent reflecting surface: Discrete phase shift and progressive refinement," *IEEE J. Sel. Areas Commun.*, vol. 38, no. 11, pp. 2604-2620, Nov. 2020.

[27] X. Hu, C. Zhong, M.-S. Alouini, and Z. Zhang, "Robust design for IRS-aided communication systems with user location uncertainty," *IEEE Wireless Commun. Lett.*, vol. 10, no. 1, pp. 63-67, Jan. 2021.

[28] D. Xu, X. Yu, Y. Sun, D. Ng, and R. Schober, "Resource allocation for IRS-assisted full-duplex cognitive radio systems," *IEEE Trans. Commun..*, vol. 68, no. 12, pp. 7376-7394, Dec. 2020

[29] V. Jamali *et al.*, "Power efficiency, overhead, and complexity tradeoff in IRS-Assisted communications-quadratic-phase-shift design," *IEEE Commun. Lett.*, IEEE Early Access, 2020, doi: 10.1109/LCOMM.2021.3058063.

[30] Z. Beixiong and R. Zhang, "Intelligent reflecting surface-enhanced OFDM: Channel estimation and reflection optimization." *IEEE Wireless Commun. Lett.*, vol. 9, no.4, pp. 518-522, 2019.

[31] Q.-U.-A. Nadeem *et al.*, "Intelligent reflecting surface-assisted multi-user MISO communication: Channel estimation and beamforming design," *IEEE Open J. Commun. Soc.*, vol. 1, pp. 661-680, 2020.

[32] P. Wang, J. Fang, H. Duan, and H. Li, "Compressed channel estimation for intelligent reflecting surface-assisted millimeter wave systems," *IEEE Signa Process. Lett.*, vol. 27, pp. 905-909, 2020.

[33] Z. Wan, Z. Gao, and M.-S. Alouini, "Broadband channel estimation for intelligent reflecting surface aided mmWave massive MIMO systems," *ICC 2020-2020 IEEE Int. Conf. Commun. (ICC)*, Dublin, Ireland, 2020, pp. 1-6.

[34] D. Ma, M. Ding, and M. Hassan, "Enhancing cellular communications for UAVs via intelligent reflective surface," *2020 IEEE Wireless Commun. Netw. Conf. (WCNC)*, Seoul, Korea (South), 2020, pp. 1-6.

[35] L. Ge, P. Dong, H. Zhang, J. Wang, and X. You, "Joint beamforming and trajectory optimization for intelligent reflecting surfaces-assisted UAV communications," *IEEE Access*, vol. 8, pp. 78702-78712, 2020.

[36] Z. Mohamed and S. Aïssa, "Leveraging UAVs with intelligent reflecting surfaces for energy-efficient communications with cell-edge users," *2020 IEEE Int. Conf. Commun. Workshops (ICC Workshops)*, Dublin, Ireland, 2020, pp. 1-6.

[37] Y. Cai, Z. Wei, S. Hu, D. Ng, and J. Yuan, "Resource allocation for power-efficient IRS-assisted UAV communications," *2020 IEEE Int. Conf. Commun. Workshops (ICC Workshops)*, Dublin, Ireland, 2020, pp. 1-7.

[38] M. Hua, L. Yang, Q. Wu, C. Pan, C. Li, and A. Swindlehurst, "UAV-assisted intelligent reflecting surface symbiotic radio system," *arXiv preprint arXiv:2007.14029*, Jul. 2020.

[39] W. Zhiqiang, C. Yuanxin, S. Zhuo, N. Kwan, and Y. Jinhong, "Sum-rate maximization for IRS-assisted UAV OFDMA communication systems," *GLOBECOM 2020-2020 IEEE Global Commun. Conf.*, Taipei, Taiwan, 2020, pp. 1-7.

[40] T. Shafique, H. Tabassum, and E. Hossain, "Optimization of wireless relaying with flexible UAV-borne reflecting surfaces," *IEEE Trans. Commun.*, vol. 69, no. 1, pp. 309-325, Jan. 2021.

[41] Q. Zhang, W. Saad, and M. Bennis, "Reflections in the sky: Millimeter wave communication with UAV-carried intelligent reflectors," *2019 IEEE Global Commun. Conf. (GLOBECOM)*, 2019, pp. 1-6.

[42] S. Li, B. Duo, X. Yuan, Y. Liang, and M. Di Renzo, "Reconfigurable intelligent surface assisted UAV communication: Joint trajectory design and passive beamforming," *IEEE Wireless Commun. Lett.*, vol. 9, no. 5, pp. 716-720, May 2020.

[43] L. Liu, S. Zhang, and R. Zhang, "CoMP in the sky: UAV placement and movement optimization for multi-user communications," *IEEE Trans. Commun.*, vol. 67, no. 8, pp. 5645-5658, Aug. 2019.

[44] C. Huang, A. Zappone, G. Alexandropoulos, M. Debbah, and C. Yuen, "Reconfigurable intelligent surfaces for energy efficiency in wireless communication," *IEEE Trans. Wireless Commun.*, vol. 18, no. 8, pp. 4157-4170, Aug. 2019.

[45] C. Huang *et al.*, "Multi-hop RIS-empowered Terahertz communications: A DRL-based hybrid beamforming design," *IEEE J. Sel. Areas Commun.*, vol. 39, no. 6, pp. 1663-1677, Jun. 2021.

[46] L. Wei *et al.*, "Channel estimation for RIS-empowered multi-user MISO wireless communications," *IEEE Trans. Commun.*, IEEE Early Access, 2021, doi: doi: 10.1109/TCOMM.2021.3063236.

[47] M. Al-Jarrah, E. Alsusa, A. Al-Dweik, and D. So, "Capacity analysis of IRS-based UAV communications with imperfect phase compensation," *IEEE Wireless Commun. Lett.*, IEEE Early Access, 2021, doi: 10.1109/LWC.2021.3071059.

[48] M. Al-Jarrah, A. Al-Dweik, E. Alsusa, and M.-S. Alouni, "Performance analysis of wireless mesh backhauling using intelligent reflecting surface," *IEEE Trans. Wireless Commun.*, IEEE Early Access, 2021, doi: 10.1109/TWC.2021.3052370.

[49] J. Ye, S. Guo, and M.-S. Alouini, "Joint reflecting and precoding designs for SER minimization in reconfigurable intelligent surfaces assisted MIMO systems," *IEEE Trans. Wireless Commun.*, vol. 19, no. 8, pp. 5561-5574, Aug. 2020.

[50] L. Yang, F. Meng, Q. Wu, D. da Costa, and M.-S. Alouini, "Accurate closed-form approximations to channel distributions of RIS-aided wireless systems," *IEEE Wireless Commun. Lett.*, vol. 9, no. 11, pp. 1985-1989, Nov. 2020.

[51] V. Thirumavalavan and T. Jayaraman, "BER analysis of reconfigurable intelligent surface assisted downlink power domain NOMA system," *2020 Int. Conf. Commun. Syst. Netw. (COMSNETS)*, Bengaluru, India, 2020, pp. 519-522.

[52] A. Boulogeorgos and A. Alexiou, "Performance analysis of reconfigurable intelligent surface-assisted wireless systems and comparison with relaying," *IEEE Access*, vol. 8, pp. 94463-94483, 2020.

[53] E. Basar *et al.*, "Wireless communications through reconfigurable intelligent surfaces," *IEEE Access*, vol. 7, pp. 116753-116773, 2019.

[54] I. Yildirim, F. Kilinc, E. Basar and G. Alexandropoulos, "Hybrid RIS-empowered reflection and decode-and-forward relaying for coverage extension," *IEEE Commun. Lett.*, vol. 25, no. 5, pp. 1692-1696, May 2021.

[55] M. Badiu and J. Coon, "Communication through a large reflecting surface with phase errors," *IEEE Wireless Commun. Lett.*, vol. 9, no. 2, pp. 184-188, Feb. 2020.

[56] R. Ferreira, M. Facina, F. De Figueiredo, G. Fraidenraich, and E. De Lima, "Bit error probability for large intelligent surfaces under double-Nakagami fading channels," *IEEE Open J. Commun. Soc.*, vol. 1, pp. 750-759, 2020.

[57] Z. Wang and G. Giannakis, "What determines average and outage performance in fading channels?," *Glob. Telecommun. Conf., 2002. GLOBECOM '02. IEEE*, Taipei, Taiwan, 2002, pp. 1192-1196.

[58] Y. Maghsoodi and A. Al-Dweik, “Exact formulae for error-rate analysis of synchronous FHSS networks using envelope characteristic functions of sums of stochastic signals,” *IEEE Trans. Veh. Technol.*, vol. 57, pp. 974-985, Mar. 2008.

[59] Y. Maghsoodi and A. Al-Dweik, “Exact amplitude distributions of sums of stochastic sinusoidals and their application in bit error rate analysis,”*arXiv preprint arXiv:1911.04746*, 2019.

[60] A. Al-Dweik, B. Sharif, and C. Tsimenidis, “Accurate BER analysis of OFDM systems over static frequency-selective multipath fading channels,” *IEEE Trans. Broadcast.*, vol. 57, no. 4, pp. 895-901, Dec. 2011.

[61] Z. He and X. Yuan, “Cascaded channel estimation for large intelligent metasurface assisted massive MIMO,” *IEEE Trans. Veh. Technol.*, vol. 68, no. 1, pp. 797-811, Jan. 2019.

[62] “*NR; Physical Channels and Modulation V15.6.0*, 3GPP Standard TS 38.211, 2020. [Online]. Available: `https://bit.ly/2xO4Qrt`

[63] S. Damjancevic, E. Matus, D. Utyansky, P. van der Wolf, and G. Fettweis, “Channel estimation for advanced 5G/6G use cases on a vector digital signal processor,” *IEEE Open J. Circuits Syst.*, vol. 2, pp. 265-277, 2021.

[64] M. A. Al-Jarrah, A. Al-Dweik, M. Kalil, and S. S. Ikki, “Decision fusion in distributed cooperative wireless sensor networks,” *IEEE Wireless Commun. Lett.*, vol. 9, no. 2, pp. 210-214, Feb. 2020.

IEEE Trans. Commun., vol. 69, no. 5, pp. 3313-3351, May 2021.

[65] $^{[R_{3,5}]}$ S. Zhang and R. Zhang, “Intelligent reflecting surface aided multi-user communication: Capacity region and deployment strategy,” *IEEE Trans. Commun.*, IEEE Early Access, 2021, doi: 10.1109/TCOMM.2021.3079128.

[66] N. Goddemeier and C. Wietfeld, “Investigation of air-to-air channel characteristics and a UAV specific extension to the Rice model,” *2015 IEEE Globecom Workshops (GC Wkshps)*, San Diego, CA, 2015, pp. 1-5.

[67] B. Du, R. Xue, L. Zhao, and V. Leung, ”Coalitional graph game for air-to-air and air-to-ground cognitive spectrum sharing,” *IEEE Trans. Aerosp. Electron. Syst.*, vol. 56, no. 4, pp. 2959-2977, Aug. 2020.

[68] F. Ono *et al.*, “Measurements on C-band air-to-air channel for coexistence among multiple unmanned aircraft systems,” *2017 Int. Conference on Unmanned Aircraft Systems (ICUAS)*, Miami, FL, USA, 2017, pp. 1160-1164.

[69] K. Takizawa, F. Ono, H. Tsuji, and R. Miura, "Air-to-air radio channel measurement at 2.3 GHz for unmanned aircraft services," *2013 16th Int. Symp. on Wireless Personal Multimedia Communications (WPMC)*, Atlantic City, NJ, 2013, pp. 1-5.

[70] C. Yan, L. Fu, J. Zhang, and J. Wang, "A comprehensive survey on UAV communication channel modeling," *IEEE Access*, vol. 7, pp. 107769-107792, 2019.

[71] K. Takizawa, F. Ono, M. Suzuki, H. Tsuji, and R. Miura, "Measurement on S-band radio propagation characteristics for unmanned aircraft systems," *The 8th European Conf. Antennas and Propag. (EuCAP 2014)*, The Hague, 2014, pp. 3068-3072.

[72] E. Haas, "Aeronautical channel modeling," *IEEE Trans. Veh. Technol.*, vol. 51, no. 2, pp. 254-264, March 2002.

[73] A. Al-Dweik and B. Sharif, "Exact performance analysis of synchronous FH-MFSK wireless networks," *IEEE Trans. Veh. Technol.*, vol. 58, no. 7, pp. 3771-3776, Sep. 2009.

[74] A. Al-Dweik and A. Shami, "Multitone jamming rejection of frequency hopped OFDM systems in wireless channels," *2012 IEEE Veh. Technol. Conf. (VTC Fall)*, Quebec City, QC, 2012, pp. 1-6.

[75] A. Saci, A. Al-Dweik, A. Shami, and Y. Iraqi, "One-shot blind channel estimation for OFDM systems over frequency-selective fading channels," *IEEE Trans. Commun.*, vol. 65, no. 12, pp. 5445-5458, Dec. 2017.

[76] M. Al-Jarrah, K.-H. Park, A. Al-Dweik, and M.-S. Alouni,"Error rate analysis of amplitude-coherent detection over Rician fading channels with receiver diversity," *IEEE Trans. Wireless Commun.*, vol. 19, no. 1, pp. 134-147, 2020.

[77] Y. Yang, S. Zhang and R. Zhang, "IRS-Enhanced OFDMA: Joint Resource Allocation and Passive Beamforming Optimization,"*IEEE Wireless Commun. Lett.*, vol. 9, no. 6, pp. 760-764, June 2020.

[78] I. Gradshteyn and I. Ryzhik, *Table of integrals, series, and products.* 7th Ed., Academic Press, USA, 2007.

[79] J. Burkardt. "The truncated normal distribution." Department of Scientific Computing Website, Florida State University, 2014.

[80] A. Goldsmith, *Wireless Communications.* Cambridge University Press, 2005.

[81] A. Prudnikov, Y. Brychkov, and O. Marichev, *Integrals and Series: Special Functions.* Gordon and Breach Science Publishers, UK, 3rd edition, 1986.

[82] I. Tanash and T. Riihonen, "Global minimax approximations and bounds for the Gaussian Q-function by sums of exponentials," *IEEE Trans. Commun.*, vol. 68, no. 10, pp. 6514-6524, Oct. 2020.

[83] A. Prudnikov, Y. Brychkov, and O. Marichev, *Integrals and Series: Elementary Functions.* Gordon and Breach Science Publishers, UK, 3rd edition, 1986.

[84] Y. Isukapalli and B. Rao, “An analytically tractable approximation for the Gaussian Q-function,” *IEEE Commun. Lett.*, vol. 12, no. 9, pp. 669-671, Sep. 2008.

[85] A. Chandra, A. Patra, and C. Bose, “Performance analysis of PSK systems with phase error in fading channels: A survey,” *Phys. Commun.*, vol. 4, no. 1, pp. 63-82, Mar. 2011.

Chapter 8

Capacity Analysis of IRS-Based UAV Communications with Imperfect Phase Compensation[1]

Abstract

This paper presents the capacity analysis of unmanned aerial vehicles (UAVs) communications supported by flying intelligent reflecting surfaces (IRSs). In the considered system, some of the UAVs are equipped with an IRS panel that applies certain phase-shifts to the incident waves before being reflected to the receiving UAV. In contrast to existing work, this letter considers the effect of imperfect phase knowledge on the system capacity, where the phase error is modeled as a von Mises random variable with parameter κ. Analytical results, corroborated by Monte Carlo simulations, show that the achievable capacity is dependent on the phase error, however, the capacity loss becomes negligible at high signal-to-noise ratio (SNR) and when $\kappa \geq 6$.

Index Terms

Wireless backhauling, IRS, capacity, imperfect phase compensation, UAV, flying network.

8.1 Introduction

Because of their autonomy, flexibility, three dimensional mobility, and cost efficiency, unmanned aerial vehicles (UAVs) are receiving an increasing attention from industrial and academic researchers. UAVs

[1]**M. A. Al-Jarrah**, E. Alsusa, A. Al-Dweik, and D. K. C. So,"Capacity analysis of IRS-based UAV communications with imperfect phase compensation," *IEEE Wireless Commun. Lett.*, vol. 10, no. 7, pp. 1479-1483, Jul. 2021, doi: 10.1109/LWC.2021.3071059.

have been considered for several applications such as surveillance, tracking, search and rescue missions, and remote sensing [1, 2]. They can also support existing cellular networks that experience temporary congestion or damage caused by environmental disasters such as earthquakes and storms. Recently, flying base-stations (BSs), or UAV based BS (UAV-BS), have been introduced to provide integrated access and backhaul (IAB) with wide coverage area, high capacity and ultimate connectivity. Moreover, the deployment of flying networks of various types of UAVs, including low altitude drones (LAD) and high altitude airships (HAA), is expected to provide reliable and high transmission rate communications as reported in [3–5]. Some challenges for the deployment of LADs and HAAs are discussed in [3], where practical solutions are provided to ensure reliable connectivity.

Recently, intelligent reflecting surfaces (IRSs) have been proposed to control the wireless medium between transceivers. In IRS aided communications, a panel of programmable reflectors, which are able to apply phase shift to the incident waves and reflect them to the receiver, are used to enhance the signal quality at the receiver. The values of the phase-shifts for all reflectors are computed such that the reflected signals add coherently in the medium, and consequently the signal-to-noise ratio (SNR) can be significantly increased. The phase values are typically computed by the BS and sent to the programmable IRS through a control channel [6–8].

The achievable capacity and coverage probability with a limited number of reflectors are discussed in [9] under ideal and arbitrary phase compensation. The results in [9] showed that the capacity achieved with arbitrary phase shifts is very poor relative to the ideal case. However, ideal phase compensation is practically infeasible due to the phase estimation and quantization errors. Consequently, investigating the scenario of non-ideal phase compensation is necessary to explore the performance limits of IRS based communication systems [10–12]. In [10], the capacity limit of multiple-input multiple-output (MIMO) IRS systems is characterized by optimizing the reflection coefficients matrix of the IRS system aiming at maximizing the system capacity. In [11], the impact of a finite number of possible phase shifts on the achievable ergodic capacity (EC) is investigated, where the capacity bounds as a function of channel statistics are derived based on Jensen's inequality, and the phase quantization error is modeled as the derivative of the actual phase value. In [13], the bit error rate (BER) is derived where a statistical model is employed to characterize the phase compensation error caused by imperfect channel estimation and phase quantization. In addition to being considered separately, the synergy of IRSs and UAVs is considered as a promising solution for supporting reliable wireless communications in future generations such as the sixth generation (6G) and beyond [5, 14]. Fig. 8.1 depicts an example where IRS panels are attached to HAAs with hovering ability to support data exchange between small drones and a main BS. However, the wobbling of UAVs makes the assumption that the phase is perfectly compensated unrealistic. Consequently, evaluating the link capacity where IRS-UAV is incorporated with imperfect phase compensation is indispensable. Although similar system model is introduced in [5], the probability

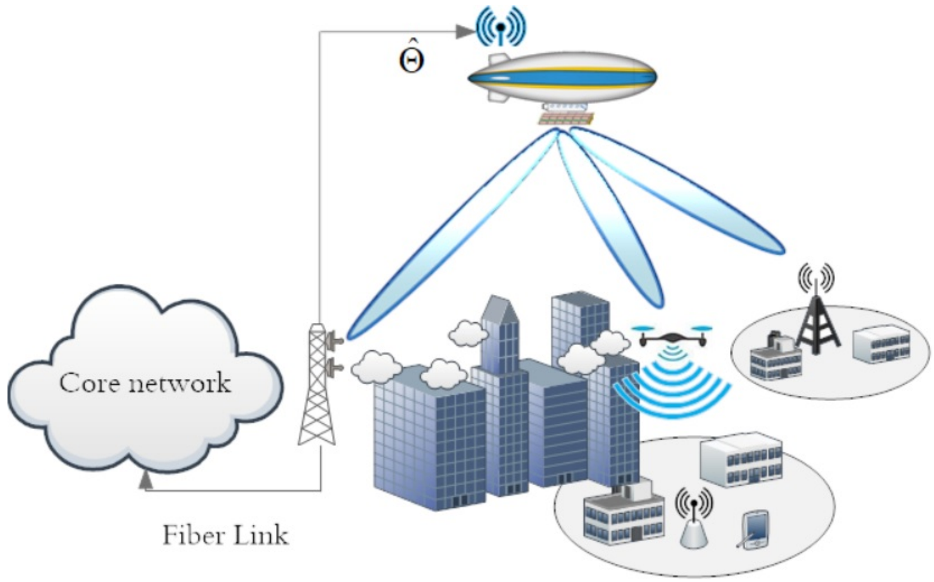

Figure 8.1: IRS assisted flying networks.

density function (PDF) of the received SNR, outage probability and BER have been analyzed, whereas the achievable EC has not been evaluated. Accordingly, the main contribution of this letter is the derivation of the achievable EC of flying IRS (FIRS) assisted UAV communications while considering the impact of imperfect phase compensation. Unlike [11], which considers the phase error as the derivative of the correct phase, we model the phase error using the von Mises PDF. The obtained results show that the phase compensation error has a significant impact on the achievable capacity at low values of κ and SNR, however, the performance degradation becomes negligible at high values of SNR and κ.

The rest of the letter is organized as follows. Sec. II presents the system model of a flying network supported by an IRS. The derivation of the achievable capacity is parovided in Sec. III, while Sec. IV shows the numerical results. Conclusion and future work are provided in Section V.

8.2 System Model

As shown in Fig. 8.1, this work considers an IRS attached to HAA that is deployed to provide efficient wireless backhauling to terrestrial users. In addition, a flying BS represented as a drone is deployed to provide alternative line-of-sight (LoS) paths to users which may suffer from blockage. The IRS panel consists of L elements each of which applies a phase shift $\hat{\theta}_i$, attenuates the signal by a coefficient g_i, and then reflects the signal to the destination drone. The phase compensation is assumed imperfect due to IRS phase noise and non-ideal phase estimation process, which becomes more challenging due to UAV wobbling. Given that the transmitted symbol is $s = |s|\, e^{j\varphi}$, and the cascaded channel envelope is $|h_i|$ with total phase shift θ_i, the received signal at the drone can be written as

$$\tilde{r}\left(t\right) = |s| \sum_{i=1}^{L} A_i \cos\left(\omega_c t + \varphi + \epsilon_i\right) + z\left(t\right) \tag{8.1}$$

where ω_c is the carrier angular frequency, $A_i = g_i |h_i|$, $\epsilon_i = \hat{\theta}_i - \theta_i$ is the phase compensation error, and $z(t)$ is the additive white Gaussian noise (AWGN). Using the sinusoidal addition theorem (SAT) [15], $\tilde{r}(t)$ can be written as

$$\tilde{r}(t) = |s| B_L \cos(\omega_c t + \varphi + \zeta_L) + z(t), \, t \geq 0 \tag{8.2}$$

where and ζ_L are the equivalent channel envelope and phase, respectively,

$$B_L^2 = \|\mathbf{A}\|^2 + 2 \sum_{L \geq j > k \geq 1} A_j A_k \cos(\epsilon_j - \epsilon_k), \tag{8.3}$$

$$\zeta_L = \tan^{-1}\left(\sum_{i=1}^{L} A_i \sin(\epsilon_i) \Big/ \sum_{i=1}^{L} A_i \cos(\epsilon_i)\right) \tag{8.4}$$

and $\|\cdot\|$ is the Euclidian norm. The elements of $\mathbf{A} = [A_1, \ldots, A_L]$ depend on the channel model. For air-to-air channels, the signal typically has a strong LoS component and a small number of weak scattered components; thus, the small scale fading of such channels follows the Rician distribution. However, according to experimental measurements, the Rician factor K for ground-to-air and air-to-air channels is more than 15 dB, and the received signal power may remain constant for long time periods [2,4,5,16,17]. Therefore, it can be assumed that the channel coefficients A_i's do not experience small scale fading, and that free space pathloss dominates the received signal power. Nevertheless, the obtained results in Sec. IV show that the constant fading coefficients model can be used to closely approximate the Rician fading channel with considerable values of K. It is worthy to note that the analysis provided here are valid for both BS-FIRS-UAV and BS-FIRS-BS links with sufficiently high BSs, where these links are shown in Fig. 1 in elliptical shape. The von Mises, or circular normal, distribution is typically used to model the random phase error ϵ_i [13], where the PDF is given by

$$f_{\epsilon_i}(\epsilon_i) = 1/(2\pi I_0(\kappa_i)) \, e^{\kappa_i \cos(\epsilon_i - \mu_i)} \tag{8.5}$$

where μ_i and κ_i are the mean and shape parameter of ϵ_i. For unbiased estimators, the mean of ϵ_i is typically $\mu_i = 0 \; \forall i$.

In slow fading channels, the accumulated phase offset ζ_L can be perfectly estimated by the receiving drone, and consequently the baseband representation of the received signal can be expressed as

$$r = B_L s + z \tag{8.6}$$

where $z \sim \mathcal{CN}\left(0, \sigma_z^2\right)$ is the AWGN.

8.3 The Achievable Capacity

The provided derivations consider a single user scenario. However, if the total number of reflectors is distributed among users with fixed assignment and orthogonal resource blocks are assigned to users [18], the analysis can be applied for multi-user system by adding the individual user's rates.

8.3.1 Single Reflector $(L = 1)$

In this case, the received signal envelope is deterministic, and thus the instantaneous SNR is $\gamma_1 = \frac{A_1^2}{\sigma_z^2}$. Consequently, the capacity normalized to the bandwidth W is

$$R_1 \triangleq C_1/W = \log_2\left(1 + \gamma_1\right) \tag{8.7}$$

where C_1 indicates the capacity for the case $L = 1$.

8.3.2 Two Reflectors $(L = 2)$

Given the instantaneous normalized rate for the $L = 2$ case $R\left(b_2\right) = \log_2\left(1 + \frac{b_2^2}{\sigma_z^2}\right)$, where b_2 is the channel envelope when $L = 2$, and the PDF of the signal envelope $f_{B_2}(b_2)$ in [5, eq. (22)], the average rate can be expressed as

$$\begin{aligned} \bar{R}_2 &= \int_0^\infty R\left(b_2\right) f_{B_2}(b_2) db_2 \\ &= \frac{2}{\pi\tilde{\kappa}} \int_{|\mathcal{A}_1|}^{\mathcal{A}_2} \frac{b_2 R\left(b_2\right) I_0\left(\sqrt{\left(\kappa_1 - \kappa_2\right)^2 + \frac{\kappa_1\kappa_2}{A_1A_2}\left(b_2^2 - \mathcal{A}_1^2\right)}\right)}{\sqrt{-\left(b_2^2 - \mathcal{A}_2^2\right)}\sqrt{\left(b_2^2 - \mathcal{A}_1^2\right)}} db_2 \end{aligned} \tag{8.8}$$

where $|\mathcal{A}_1| \leq b_2 \leq \mathcal{A}_2$, $\tilde{\kappa} = I_0(\kappa_1)I_0(\kappa_2)$, $\mathcal{A}_1 = A_1 - A_2$ and $\mathcal{A}_2 = A_1 + A_2$. By using the infinite series definition for the modified Bessel function, $\bar{R}_2$ can be written as

$$\bar{R}_2 = \frac{2}{\pi\tilde{\kappa}} \int_{|\mathcal{A}_1|}^{\mathcal{A}_2} \frac{b_2 R\left(b_2\right)}{\sqrt{-\left(b_2^2 - \mathcal{A}_2^2\right)}\sqrt{\left(b_2^2 - \mathcal{A}_1^2\right)}} \times \sum_{m=0}^{\infty} \frac{1}{2^{2m}(m!)^2} \left(\left(\kappa_1 - \kappa_2\right)^2 + \frac{\kappa_1\kappa_2}{A_1A_2}\left(b_2^2 - \mathcal{A}_1^2\right)\right)^m db_2. \tag{8.9}$$

To simplify the analysis, the binomial theorem is applied to find the algebraic expansion for the last term of the integrand in (8.9), and thus $\bar{R}_2$ can be expressed as

$$\bar{R}_2 = \frac{2}{\pi\tilde{\kappa}} \sum_{m=0}^{\infty} \frac{1}{2^{2m}\left(m!\right)^2} \sum_{n=0}^{m} \mathcal{T}_{m,n} \times \int_{|\mathcal{A}_1|}^{\mathcal{A}_2} b_2 R\left(b_2\right) \frac{\left(b_2^2 - \mathcal{A}_1^2\right)^{n-0.5}}{\sqrt{-\left(b_2^2 - \mathcal{A}_2^2\right)}} db_2 \tag{8.10}$$

where $\mathcal{T}_{m,n} = \binom{m}{n} \left(\kappa_1 - \kappa_2\right)^{2(m-n)} \left(\frac{\kappa_1\kappa_2}{A_1A_2}\right)^n$.

Using the integration by substitution rule with $y = b_2^2 - \mathcal{A}_1^2$, and the logarithmic identity $\log_k x = \frac{\ln x}{\ln k}$

yields

$$\bar{R}_2 = \frac{1}{\pi\tilde{\kappa}\ln 2}\sum_{m=0}^{\infty}\frac{1}{2^{2m}\left(m!\right)^2}\sum_{n=0}^{m}\mathcal{T}_{m,n}\times\int_0^{\mathcal{A}_3^2}\frac{y^{n-0.5}}{\sqrt{-y+\mathcal{A}_3^2}}\ln\left(\frac{y}{\sigma_z^2}+\frac{\sigma_z^2+\mathcal{A}_1^2}{\sigma_z^2}\right)dy \tag{8.11}$$

where $\mathcal{A}_3 = \sqrt{4A_1A_2}$.

The integral in (8.11) can be solved using [19, 2.6.10.31, pp. 502], and consequently $\bar{R}_2$ can be found as

$$\begin{aligned}\bar{R}_2 = \frac{1}{\pi\tilde{\kappa}\ln 2}\sum_{m=0}^{\infty}\frac{1}{2^{2m}\left(m!\right)^2}\sum_{n=0}^{m}\mathcal{T}_{m,n}\Bigg\{&\mathcal{A}_3^{2n}\ln\left(\nu\right)\mathrm{B}\left(n+0.5,0.5\right)+\frac{\mathcal{A}_3^{2(n+1)}}{\sigma_z^2\nu}\mathrm{B}\left(n+1.5,0.5\right)\\ &\times {}_3F_2\left(\left[n+1.5,1,1\right],\left[2,n+2\right],-\frac{\mathcal{A}_3^2}{\nu\sigma_z^2}\right)\Bigg\}\end{aligned} \tag{8.12}$$

where $\nu = \frac{\sigma_z^2+\mathcal{A}_1^2}{\sigma_z^2}$ and $\mathrm{B}\left(a,b\right)\triangleq\frac{\Gamma(a)\Gamma(b)}{\Gamma(a+b)}$ is the beta function.

8.3.3 Three Reflectors ($L = 3$)

As reported in [5], the PDF $f_{B_3}(b_3)$ does not have a closed-form expression. Therefore, the capacity will be evaluated using the same approach of $L = 2$, but the integrals will be solved numerically.

8.3.4 Central Limit Theorem (CLT) for $L \geq 4$

Since the derivation of closed-form expressions for the PDF when $L \geq 4$ is not feasible, the CLT is invoked. With the aid of SAT, B_L^2 in (8.3) can be rewritten as $B_L^2{=}B_{L,\mathcal{I}}^2{+}B_{L,\mathcal{Q}}^2$, where $B_{L,\mathcal{I}}{=}\sum_{i=1}^{L}A_i\cos\epsilon_i$ and $B_{L,\mathcal{Q}} = \sum_{i=1}^{L}A_i\sin\epsilon_i$. Since A_i and ϵ_i are independent $\forall i$, CLT can be applied for large values of L to evaluate the distributions of $B_{L,\mathcal{I}}$ and $B_{L,\mathcal{Q}}$. Accordingly, the distribution functions of $B_{L,\mathcal{I}}$ and $B_{L,\mathcal{Q}}$ can be found as $\mathcal{N}\left(\mu_{\mathcal{I}},\sigma_{\mathcal{I}}^2\right)$ and $\mathcal{N}\left(\mu_{\mathcal{Q}},\sigma_{\mathcal{Q}}^2\right)$, respectively. By noting that $\mathrm{E}\left[\cos\left(n\theta_i\right)\right]{=}\frac{I_n(\kappa_i)}{I_0(\kappa_i)}$ and $\mathrm{E}\left[\sin\left(n\theta_i\right)\right]{=}0$ [5, Appendix I], $\mu_{\mathcal{Q}}{\triangleq}\mathrm{E}\left[B_{\mathcal{Q}}\right]=0$ can be obtained whereas $\mu_{\mathcal{I}}$ can be found as $\mu_{\mathcal{I}} = \mathrm{E}\left[B_{\mathcal{I}}\right]{=}\sum_{i=1}^{L}A_i\frac{I_1(\kappa_i)}{I_0(\kappa_i)}$. The second moment for $B_{\mathcal{I}}$ can be evaluated as $E\left[B_{\mathcal{I}}^2\right]=\mathrm{E}\left[\sum_{i=1}^{L}A_i\cos\phi_i\right]^2$. Using the expansion for squared summation and, then evaluating the expected value yields

$$\mathrm{E}\left[B_{\mathcal{I}}^2\right]{=}\sum_{i=1}^{L}\frac{A_i^2}{2}\left(1{+}\frac{I_2\left(\kappa_i\right)}{I_0(\kappa_i)}\right){+}2\sum_{i<j}^{L}A_iA_j\frac{I_1\left(\kappa_i\right)I_1\left(\kappa_j\right)}{I_0(\kappa_i)I_0(\kappa_j)}. \tag{8.13}$$

Similarly, $\mathrm{E}\left[B_{\mathcal{Q}}^2\right]$ can be derived as

$$\mathrm{E}\left[B_{\mathcal{Q}}^2\right]{\triangleq}\mathrm{E}\left[\sum_{i=1}^{L}A_i\sin\phi_i\right]^2{=}\sum_{i=1}^{L}\frac{A_i^2}{2}\left(1-\frac{I_2\left(\kappa_i\right)}{I_0(\kappa_i)}\right). \tag{8.14}$$

Consequently, $\sigma_{\mathcal{I}}^2$ and $\sigma_{\mathcal{Q}}^2$ can be found using the well known formula $\sigma_{\mathcal{I}|\mathcal{Q}}^2\triangleq\mathrm{E}\left[B_{\mathcal{I}|\mathcal{Q}}^2\right]-\mathrm{E}^2\left[B_{\mathcal{I}|\mathcal{Q}}\right]$.

Using the definition of the correlation coefficient, and then employing the product of two summations rule to find $\mathrm{E}[B_{L,\mathcal{I}}B_{L,\mathcal{Q}}]$, the correlation between $B_{L,\mathcal{I}}$ and $B_{L,\mathcal{Q}}$ is

$$\rho_{\mathcal{I},\mathcal{Q}} = \frac{1}{\sigma_{\mathcal{I}}\sigma_{\mathcal{Q}}}\sum_{i=1}^{L}\sum_{j=1}^{L} A_i A_j \mathrm{E}[\cos\epsilon_i \sin\epsilon_j]. \tag{8.15}$$

For $i \neq j$, $\mathrm{E}[\cos\epsilon_i \sin\epsilon_j] = \mathrm{E}[\sin\epsilon_j]\,\mathrm{E}[\cos\epsilon_i] = 0$. On the other hand, when $i = j$, the trigonometric identity $\cos\epsilon_i \sin\epsilon_i = 0.5\sin(2\epsilon_i)$ can be applied, which implies that $\mathrm{E}[\cos\epsilon_i \sin\epsilon_j] = 0$ as well . Since $B_{L,\mathcal{I}}$ and $B_{L,\mathcal{Q}}$ are Gaussian distributed according to CLT and they are uncorrelated, $B_{L,\mathcal{I}}$ and $B_{L,\mathcal{Q}}$ are independent random variables. For a special case when the phase error is uniformly distributed, $\kappa = 0$, $\mu_{\mathcal{I}} = \mu_Q = 0$ and $\mathrm{E}\left[B_{\mathcal{I}}^2\right] = \mathrm{E}\left[B_{\mathcal{Q}}^2\right] = \sum_{i=1}^{L} A_i^2/2$. Therefore, the propagation environment follows Rayleigh channel model when $\kappa = 0$. For the general case when $\kappa > 0$, B_L is the envelope of a complex Gaussian with different values for the variance of the in-phase and quadrature components with one of the components has non-zero mean. The PDF of such random variable is given in [20, eq. (8)]. However, the form provided in [20] contains infinite sum of modified Bessel functions product with different orders, which makes the distribution untraceable. An accurate approximation for the PDF of $|B_L|^2$ has been derived in [13], where the PDF is approximated as Gamma random variable with shape parameter $\alpha = \mu_{\mathcal{I}}^2/4\sigma_{\mathcal{I}}^2$ and inverse scale factor $\beta = 1/4\sigma_{\mathcal{I}}^2$. By denoting $y = B_L^2$ and using the gamma distribution function, the achievable EC can be expressed as

$$\begin{aligned}\bar{R}_{\mathrm{CLT}} &= \int_0^\infty R(b_L)\, f_{B_L}(b_L) db_L \\ &= \frac{\beta^\alpha}{\Gamma(\alpha)\ln 2}\int_0^\infty y^{\alpha-1}\mathrm{e}^{-\beta y}\ln\left(1+\frac{y}{\sigma_z^2}\right)dy.\end{aligned} \tag{8.16}$$

By using [19, eq. (2.6.23.4), pp. 530], $\bar{R}_{\mathrm{CLT}}$ can be found in closed-form as

$$\bar{R}_{\mathrm{CLT}} = \frac{\beta^\alpha}{\Gamma(\alpha)\ln 2}\left(\frac{\pi\sigma_z^{2\alpha}\,{}_1F_1\left(\alpha;\alpha+1;\beta\sigma_z^2\right)}{\alpha\sin(\alpha\pi)} - \Gamma(\alpha)\,\beta^{-\alpha}\left\{\ln\left(\beta\sigma_z^2\right) - \Psi(\alpha) + \frac{\beta\sigma_z^2}{1-\alpha}\,{}_2F_2\left([1,1],[2,2-\alpha],\beta\sigma_z^2\right)\right\}\right) \tag{8.17}$$

where $\Psi(\cdot)$ is the digamma function which is defined as $\Psi(\alpha) = \Gamma(\alpha)/\Gamma'(\alpha)$.

For high SNR, $\frac{y}{\sigma_z^2} \gg 1$ and thus $\bar{R}_{\mathrm{CLT}}$ can be reduced to

$$\bar{R}_{\mathrm{CLT,H}} = \frac{\beta^\alpha}{\Gamma(\alpha)\ln 2}\int_0^\infty y^{\alpha-1}\mathrm{e}^{-\beta y}\ln\left(\frac{y}{\sigma_z^2}\right)dy. \tag{8.18}$$

By using the logarithmic identity $\ln\frac{x}{y} = \ln x - \ln y$ and evaluating the resulting integral using [19, eq. (2.6.21.2), pp. 527] and [19, eq. (2.3.3.1), pp. 322], $\bar{R}_{\mathrm{CLT}}$ can be found as

$$\bar{R}_{\mathrm{CLT,H}} = (\Psi(\alpha) - \ln\beta - \ln\sigma_z^2)/\ln 2. \tag{8.19}$$

By comparing the derived $\bar{R}_{\mathrm{CLT}}$ in (8.19) with the formula in (8.17), it can be realized that (8.19) is more

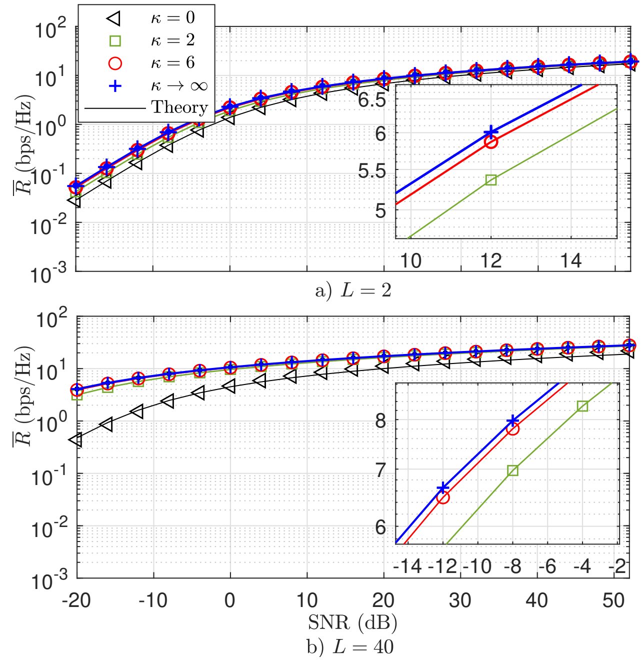

Figure 8.2: The achievable $\bar{R}$ for $L = \{2, 40\}$ for different values of κ, where $A_i = 1 \forall i$.

tractable and has less computational complexity.

8.4 Numerical Results

This section presents the achievable capacity for the considered system model. The analytical results obtained from the derived formulae are compared to Monte Carlo simulation results with 10^7 realizations. To evaluate the impact of phase error compensation, the results are also compared to the cases of ideal and arbitrary phase compensation, which are respectively referred as $\kappa \to \infty$ and $\kappa = 0$. The average transmission power is normalized to unity, and the SNR in dB is defined as SNR$= -10 \log_{10} \left(\sigma_z^2\right)$. Unbiased phase estimators with equal variance are considered, i.e., $\mu = 0$ and $\kappa_i = \kappa \ \forall i$. For the infinite summation in (13), the first 30 terms have been considered.

Fig. 8.2a shows the achievable normalized EC $\bar{R}$ in bps/Hz for different values of κ when the number of reflectors is L=2 and A_1=A_2 =1. As can be observed from the figure, the derived equation for $\bar{R}_2$ matches the simulation results. As expected, the phase compensation errors negatively affect the achievable rate, and as κ increases, i.e., channel estimation and compensation improves, the achievable rate improves. For example, when the SNR is 0 dB, the capacity achieved with $\kappa \to \infty$, ideal phase shift, is about 1.7 times the capacity when $\kappa = 0$, i.e., arbitrary phase compensation. However, the capacity loss decreases as κ increases. For example, the capacity loss is less than 0.5 dB when $\kappa = 6$ as compared to the ideal case. Moreover, the figure shows that the effect of κ becomes negligible when $\kappa \geq 6$, which implies that near-ideal performance for $L = 2$ can be achieved by designing a phase estimation and compensation processes satisfying the condition $\kappa \geq 6$.

Fig. 8.2b shows the achievable $\bar{R}$ for different values of κ when the number of reflectors $L = 40$, where

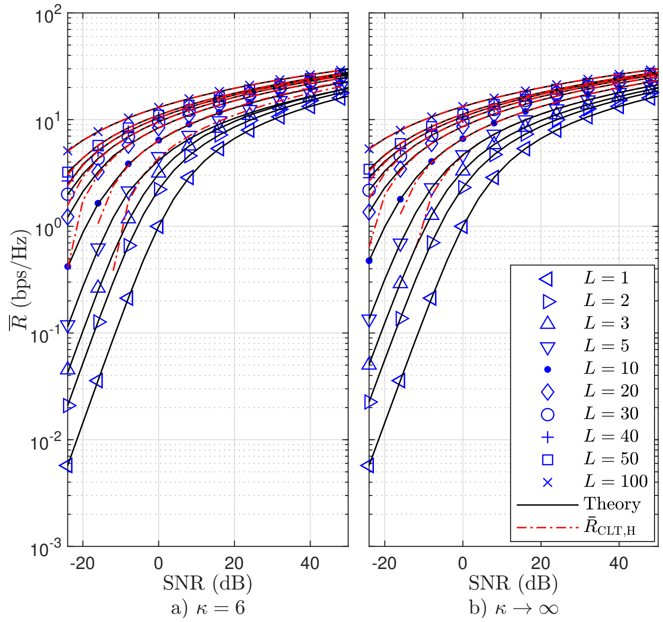

Figure 8.3: The achievable $\bar{R}$ for different numbers of reflectors L, $A_i = 1 \forall i$.

$A_i = 1\ \forall i$. The obtained results show a perfect match for the derived CLT based equation for a wide range of κ values, except for the case of $\kappa = 0$. Similar to Fig. 8.2a, the impact of κ decreases as its value increases and becomes negligible when $\kappa \geq 6$. However, by comparing Fig. 8.2b with Fig. 8.2a, it can be realized that when $L = 40$, the arbitrary phase compensation causes significant capacity loss as compared to the ideal case. For example the difference between the arbitrary and ideal scenarios in Fig. 8.2b is about 20 dB at $\bar{R} = 10$ bps/Hz.

Figs. 8.3a and 8.3b show the impact of increasing the number of reflectors L on the achievable rate $\bar{R}$ when the phase compensation error parameter $\kappa = 6$ and $\kappa \to \infty$, respectively. As can noticed, a perfect match between simulation and theoretical results is obtained, and the asymptotic capacity derived in (8.19) for $L \geq 4$ converges to the exact formula in (8.17) when $\bar{R} \gtrsim 3$ bps/Hz. By comparing Fig. 8.3a with Fig. 8.3b, it can be observed that the effect of phase compensation errors is negligible when $\kappa = 6$. It is worth noting that the case of $L = 1$ is not affected by κ, as discussed in Sec. III. The figure shows that $\bar{R}$ significantly improves by increasing L. For example, at SNR $= 0$ dB, the value of $\bar{R}$ increases by 10-fold when L is increased from 1 to 50. Moreover, by comparing $L = 1$ with other cases, it is realized that deploying IRS with phase compensation error statistics of $\kappa = 6$ can enhance the system capacity considerably.

Fig. 8.4 shows the achievable normalized rate $\bar{R}$ for double Rician, i.e., $\{|\hbar_i|, |h_i|\} \sim \mathcal{R}(\Omega, K)$ for $\Omega = 1$ and different values of the Rician factor K. It is noteworthy that the case of $K \to \infty$ is equivalent to the deterministic channel scenario with $A_i = 1 \forall i$. The figure shows that the impact of the Rician factor is negligible when $K \geq 15$ dB. For example, the achievable rate when $K = 15$ dB is almost the same as the deterministic channel scenario, $(K \to \infty)$. In addition, the impact of K becomes less important for

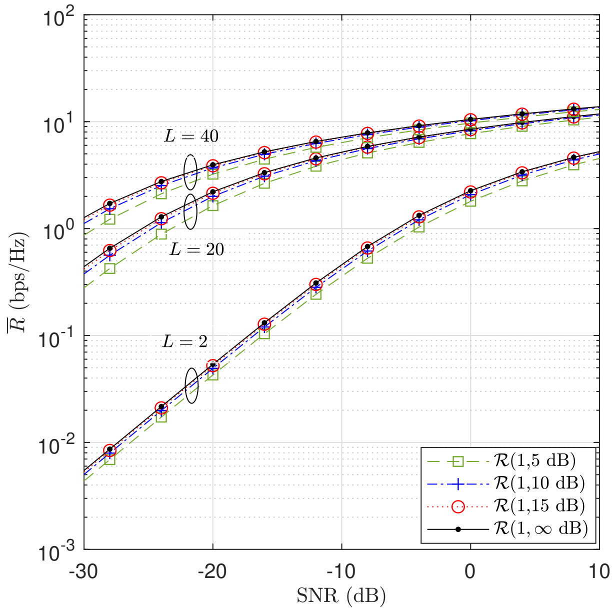

Figure 8.4: The achievable $\bar{R}$ with Rician fading channel $\mathcal{R}(\Omega, K)$ for $\Omega = 1$ and different values of K, where $\kappa = 10$.

small values of L and the rate is mainly determined by the number of reflectors L.

8.5 Conclusion And Future Work

The normalized EC achieved by employing FIRS to support UAV based communications was derived taking into account imperfect phase compensation. The phase compensation error was modeled using von Mises distribution, and the capacity was derived for $L = 1$ and 2 in closed-forms, whereas numerical integration and CLT were applied when $L = 3$ and $L \geq 4$, respectively. The obtained results demonstrated that capacity degradation due to phase errors is inversely proportional to SNR, which is more apparent for large L values. Interestingly, the capacity deterioration is negligible for $\kappa \geq 6$. It was also shown that increasing L enhances the capacity even when the phase compensation is not ideal. Moreover, it was proven that the effect of the Rician factor K becomes negligible when $K \geq 15$ dB.

The study of UAVs mobility effects on the achievable EC is an interesting future extension to the current work.

References

[1] N. Tafintsev *et al.*, "Aerial access and backhaul in mmWave B5G systems: Performance dynamics and optimization," *IEEE Commun. Mag.*, vol. 58, no. 2, pp. 93-99, Feb. 2020.

[2] C. Yan, L. Fu, J. Zhang, and J. Wang, "A comprehensive survey on UAV communication channel modeling," *IEEE Access*, vol. 7, pp. 107769-107792, 2019.

[3] Y. Huo, X. Dong, T. Lu, W. Xu, and M. Yuen, "Distributed and multilayer UAV networks for next-generation wireless communication and power transfer: A feasibility study," *IEEE IoT J.*, vol. 6, no. 4, pp. 7103-7115, Aug. 2019.

[4] B. Du, R. Xue, L. Zhao, and V. Leung, "Coalitional graph game for air-to-air and air-to-ground cognitive spectrum Sharing," *IEEE Trans. Aerosp. Electron. Syst.*, vol. 56, no. 4, pp. 2959-2977, Aug. 2020.

[5] M. Al-Jarrah, A. Al-Dweik, E. Alsusa, Y. Iraqi, and M.-S. Alouini, "IRS-assisted UAV communications with imperfect phase compensation," submitted to *IEEE Trans. Wireless Commun.* [Online]. Available: `https://doi.org/10.36227/techrxiv.13153211.v1`

[6] E. Basar *et al.*, "Wireless communications through reconfigurable intelligent surfaces," *IEEE Access*, vol. 7, pp. 116753-116773, 2019.

[7] M. Al-Jarrah, A. Al-Dweik, E. Alsusa, and M.-S. Alouni, "Performance analysis of wireless mesh backhauling using intelligent reflecting surface," *IEEE Trans. Wireless Commun.*. Early access, doi: 10.1109/TWC.2021.3052370.

[8] W. Shi, X. Zhou, L. Jia, Y. Wu, F. Shu, and J. Wang, "Enhanced secure wireless information and power transfer via intelligent reflecting surface," *IEEE Commun. Lett.*, Early access, doi: 10.1109/LCOMM.2020.3043475.

[9] T. Van Chien, L. Tu, S. Chatzinotas, and B. Ottersten, "Coverage probability and ergodic capacity of intelligent reflecting surface-enhanced communication systems," *IEEE Commun. Lett.*, vol. 25, no. 1, pp. 69-73, Jan. 2021.

[10] S. Zhang and R. Zhang, "Capacity characterization for intelligent reflecting surface aided MIMO communication," *IEEE J. Sel. Areas Commun.*, vol. 38, no. 8, pp. 1823-1838, Aug. 2020.

[11] D. Li, "Ergodic capacity of intelligent reflecting surface-assisted communication systems with phase errors," *IEEE Commun. Lett.*, vol. 24, no. 8, pp. 1646-1650, Aug. 2020.

[12] J. Sánchez, P. Ramírez-Espinosa and F. López-Martínez, "Physical layer security of large reflecting surface aided communications with phase errors," *IEEE Wireless Commun. Lett.*, doi: 10.1109/LWC.2020.3029816.

[13] M. Badiu and J. Coon, "Communication through a large reflecting surface with phase errors," *IEEE Wireless Commun. Lett.*, vol. 9, no. 2, pp. 184-188, Feb. 2020.

[14] T. Shafique, H. Tabassum and E. Hossain, "Optimization of wireless relaying with flexible UAV-borne reflecting surfaces," *IEEE Trans. Commun.*, vol. 69, no. 1, pp. 309-325, Jan. 2021.

[15] Y. Maghsoodi and A. Al-Dweik, "Error-rate analysis of FHSS networks using exact envelope characteristic functions of sums of stochastic signals," *IEEE Trans. Veh. Technol.*, vol. 57, no. 2, pp. 974-985, Mar. 2008.

[16] D. W. Matolak and R. Sun, "Unmanned aircraft systems: Air-ground channel characterization for future applications," *IEEE Veh. Technol. Mag.*, vol. 10, no. 2, pp. 79-85, Jun. 2015.

[17] D. W. Matolak and R. Sun, "Air–ground channel characterization for unmanned aircraft systems—Part I: Methods, measurements, and models for over-water settings," *IEEE Trans. Veh. Technol.*, vol. 66, no. 1, pp. 26-44, Jan. 2017.

[18] S. Zhang and R. Zhang, "Intelligent reflecting surface aided multi-user communication: Capacity region and deployment strategy," *arXiv Preprint.* Online. [Available:] `https://arxiv.org/abs/2009.02324`

[19] A. Prudnikov, Yu. A. Brychkov, and O. Marichev, *Integrals and Series, vol. 1 Elementary Functions.* Gordon and Breach Science Publishers, UK, 3rd edition, 1986.

[20] V. Aalo, G. Efthymoglou, and C. Chayawan, "On the envelope and phase distributions for correlated gaussian quadratures," *IEEE Commun. Lett.*, vol. 11, no. 12, pp. 985-987, Dec. 2007.

Chapter 9

Conclusions and Future Plan

To conclude, this thesis is generally concerned in the performance evaluation of wireless communication systems such as sensor networks, integrated sensing and communication systems and intelligent reflecting surfaces. Simulations corroborated by analytical results have been provided for several operating scenarios. In this chapter, conclusions about the achieved work so far are provided, as well as, interesting work to be explored in future is discussed.

9.1 Conclusions

In **Chapter 2**, target localization problem using RFID network has been investigated using a number of tags deployed in the region of interest with fixed and known positions. A reader, which represents the target, sends interrogation signal which is received by the tags which respond to the reader after harvesting a certain amount of the received power. Then the reader employs the maximum likelihood estimation based on the received signals strength from the tags, after correcting the measurements using majority voting algorithm, to estimate its location giving the positions of the tags in prior. The performance of the proposed localization method has been evaluated using simulations and theoretical derivations, where the theoretical derivations have been carried out using CRLB. The obtained results have shown that CLRB provides a good performance limit of the localization method, and the RMSE of the estimator approaches CRLB when SNR and number of RFID tags are large [1]. **Chapter 3** has presented a joint location and orientation estimation algorithm for a mobile robot using a network of wireless sensors. The mobile robot is equipped with directional antennas and the directivity of those antennas is utilized for the estimation process. Error concealment methods, such as the local majority voting and connected graph algorithms, have been also used to enhance the accuracy of the obtained results. The obtained experimental and simulation results have displayed that the proposed approach can efficiently estimate the location and orientation of the mobile robot with high accuracy, especially at high signal-to-noise-ratio (SNR) [2]. As well as, **Chapter 4** has explored the decision fusion problem in clustered WSNs over IoT infrastructure, where multiple sensors transmit their decisions about a certain phenomenon to a remote fusion center over a wide area network. The proposed ILA fusion rule managed to reduce the decision fusion error probability performance while maintaining the low computational complexity. The performance of the ILA rule is evaluated and compared to other well-established fusion rules in the literature in terms of the detection probability, false alarm probability and global fusion probability of error. The obtained results have shown the robustness of ILA rule where it managed to outperform all other considered suboptimal fusion rules, and its performance has converged to the optimal rule under many operating conditions [3]. In **Chapter 5**, a modern and emerging technology called ISAC has been investigated, in which a MIMO base-station aims at providing sensing services in addition to the conventional data communication services. The separated deployment has been considered, in which the base-station antennas are distributed among the two subsystems; the sensing and communication subsystems. Performance analysis for the introduced ISAC system haveb been provided based on the information theoretical framework of Kullback-Leibler divergence. It worths noting that with this analysis, a unified performance evaluation for ISAC systems has been obtained holistically. Multiple targets have been assumed, and ZF and MRT precoding methods have been assumed for the data communication subsystem in downlink. Theoretical results corroborated by simulations showed that the derived relative entropy is very accurate and can perfectly characterize both subsystems [4].

Furthermore, **Chapters 7** through **9** have explored the emerging IRS technology and its applications in wireless communications, more specifically, wireless backhauling [5–7]. **Chapter 6** introduced a multi-hop wireless backhauling where each hop is assisted by a panel of IRS wherever the LoS between communicating base-stations is dropped. The performance of the introduced system model has been evaluated by simulations and derived equations for the bit error rate and outage probability, where the communication link is modeled as Rician fading channel. The obtained results showed that the IRS-mesh backhauling architecture has several desired features that can be exploited to overcome some of the backhauling challenges, particularly the severe attenuation at high frequencies [5]. In **Chapter 7**, the symbol error rate (SER) and outage probability analysis of multi-layer unmanned aerial vehicles (UAVs) wireless communications assisted by intelligent reflecting surfaces (IRS) have been investigated. The non-ideal channel estimation at the base-station, which results in erronous phase compensation errors at IRS, has been considered. Such imperfect conditions may rise in UAV communications since UAVs generally suffer from jitter while hovering. The phase compensation error at IRS was modeled using the von Mises distribution and the analysis was performed by using the Sinusoidal Addition Theorem (SAT) when the number of reflectors $L \leq 3$, and Central Limit Theorem (CLT) when $L \geq 4$. The obtained results showed that accurate phase estimation is critical for IRS based systems, particularly for a small number of reflecting elements [6]. Moreover, **Chapter 8** has explored the achievable capacity for unmanned aerial vehicles (UAVs) communications supported by flying IRSs taking into account the effect of imperfect phase knowledge on the system capacity. Similar to **Chapter 8**, the phase error was modeled as a von

Mises random variable with parameter κ. Theoretical and simulation results showed that the achievable capacity is dependent on the quality of the compensated phase by IRS, however, the capacity loss becomes negligible at high signal-to-noise ratio (SNR) and when $\kappa \geq 6$ [7].

9.2 Future Work

The problem of multiple target localization can be a significant improvement for the system model considered in **Chapters 2** and **3**. Accordingly, the derivation for the generalized maximum likelihood estimator can be performed, and the performance evaluation for the estimator based on the new system model can be performed. Moreover, the employment of relevant machine learning tools to perform data fusion rather than the statistical tools used in the current work (e.g. the likelihood ratio test) can be considered at future. As well as, a comparison between the currently used algorithms and machine learning algorithms can be performed in terms of achievable performance, computational complexity and the possibility of practical implementation. On the other hand, the unified performance framework derived in **Chapter 5** can be utilized for optimizing the network resources. Therefore, resource allocation algorithms based on the derived relative information can be introduced to allocate the resources among radar and communication subsystems.

Moreover, the derived expressions in this thesis can be considered to efficiently design wireless communication systems depending on the application of interest. For instance, the design may include proposed algorithms for the placement of IRS panels and/or portable BSs aiming at optimizing the system performance, for examples, maximizing the achievable rate, minimizing OP or minimizing SER. The current work studies point-to-point links with single antennas at the transceivers, whereas multi-user with multi-antenna BSs will be considered at future. In addition, the joint design of precoding matrix at a multi-antenna BS and phase shift design of IRS for multi-user multiple input single output (MISO) system. The design of spectral efficient non-orthogonal multiple access (MAC) algorithms for the BSs is also an interesting field of research, as well.

Furthermore, modern wireless technologies can be explore and investigated in the future. For instance, non-orthogonal MAC schemes like NOMA and rate-splitting multiple access (RSMA) would improve the spectral efficiency of the system, especially for highly dense small cells systems, and thus they could be interesting areas of study. As well as, the design of efficient routing algorithms for wireless networks is an important aspect which can be considered in future, where data packets select the best path among all possible routes in mesh backhauling topology. This routing algorithm can be formulated with the aim of maximizing the system capacity under energy constraints. Finally, the deployment of UAVs with hybrid links to assist wireless backhauling would be considered at future as a strong candidate for 6G networks. For example, radio frequency (RF) links between a micro BS and an UAV, while the UAV is connected to the main BS through a free-space optical (FSO) link.

References

[1] **M. A. Al-Jarrah**, A. Al-Dweik, E. Alsusa and E. Damiani, “RFID reader localization using hard decisions with error concealment,” *IEEE Sensors. J.*, vol. 19, no. 17, pp. 7534-7542, Sep. 2019, doi: 10.1109/JSEN.2019.2914914.

[2] **M. A. Al-Jarrah**, A. Al-Dweik, N. T. Ali and E. Alsusa, “Joint estimation of location and orientation in wireless sensor networks using directional antennas,” *IEEE Sensors. J.*, vol. 20, no. 23, pp. 14347-14359, Dec. 2020, doi: 10.1109/JSEN.2020.3008393.

[3] **M. A. Al-Jarrah**, M. A. Yaseen, A. Al-Dweik, O. A. Dobre and E. Alsusa, “Decision fusion for IoT-based wireless sensor networks,” *IEEE IoT. J.*, vol. 7, no. 2, pp. 1313-1326, Feb. 2020, doi: 10.1109/JIOT.2019.2954720.

[4] **M. A. Al-Jarrah**, E. Alsusa and C. Masouros, “A unified performance framework for integrated sensing-communications based on KL-divergence,” Submitted to *IEEE Trans. Wireless Commun.*, Sep. 2022.

[5] **M. A. Al-Jarrah**, E. Alsusa, A. Al-Dweik and M.-S. Alouini, “Performance Analysis of Wireless Mesh Backhauling Using Intelligent Reflecting Surfaces,” *IEEE Trans. Wireless Commun.*, vol. 20, no. 6, pp. 3597-3610, Jun. 2021, doi: 10.1109/TWC.2021.3052370.

[6] **M. A. Al-Jarrah**, A. Al-Dweik, E. Alsusa, Y. Iraqi, and M.-S. Alouini, “On the Performance of IRS-Assisted Multi-Layer UAV Communications with Imperfect Phase Compensation,” *IEEE Trans. Commun.*, vol. 69, no. 12, pp. 8551-8568, Dec. 2021, doi: 10.1109/TCOMM.2021.3113008.

[7] **M. A. Al-Jarrah**, E. Alsusa, A. Al-Dweik, and D. K. C. So, “Capacity Analysis of IRS-Based UAV Communications With Imperfect Phase Compensation,” *IEEE Wireless Commun. Lett.*, vol. 10, no. 7, pp. 1479-1483, Jul. 2021, doi: 10.1109/LWC.2021.3071059.